The Last Stages of Accretion in Young Objects

by

Thanawuth Thanathibodee

A dissertation submitted in partial fulfillment
of the requirements for the degree of
Doctor of Philosophy
(Astronomy and Astrophysics)
in the University of Michigan
2021

Doctoral Committee:

Professor Nuria P. Calvet, Chair
Professor Edwin A. Bergin
Professor Lee W. Hartmann
Professor Enrico Landi
Dr. James C. Muzerolle, Space Telescope Science Institute

Thanawuth Thanathibodee
thanathi@umich.edu
ORCID iD: 0000-0003-4507-1710

ACKNOWLEDGMENTS

The work included in this Dissertation is made possible by contributions from many of my collaborators. In particular, I want to thank Nuria Calvet for being a very supportive and understanding advisor. She is always available to provide guidance and support for my professional and personal development and always sees the best in me, even when I seem to have forgotten it. Under her mentorship, I have learned a great deal about star formation and how to be a scientist. I would also like to thank my dissertation committee members, Lee Hartmann, James Muzerolle, Enrico Landi, and Ted Bergin, for their feedback and suggestions in this work.

I want to thank James Muzerolle for teaching me how to run the magnetospheric code, which was used extensively in this work. I am very grateful to César Briceño, Jesús Hernández, and Karina Maucó for teaching me how to observe and analyze data from large telescopes. I also want to acknowledge Brandon Molina and Javier Serna, whose works contribute significantly to this Dissertation. I appreciate the help from Paco Holguin during several nights of the FIRE observations. In addition, I would like to thank my co-authors whose works and comments have resulted in significant improvements to this Dissertation; including, Jaehan Bae, Greg Herzceg, Mark Reynolds, Ramiro Franco Hernández, Megan Reiter, Melissa McClure, Catherine Clark, and Laura Ingleby. The works included here significantly benefited from discussions with A. Katherina Vivas, Catherine Espaillat, Charles Cowley, Jerome Bouvier, Kevin Luhman, Marina Kounkel, Michael Meyer, Susan Edwards, and Zhaohuan Zhu.

This Dissertation is supported in part by the Rackham One-Term Dissertation Fellowship, NASA grant NNX17AE57G, and Hubble Space Telescope grant HST-GO-14190.001-A. I am grateful to the telescope operators and the staff at Las Campanas Observatory for the help during the FIRE, MagE, and MIKE observations across multiple observing semesters. I would like to thank Mario Mateo for making these observations possible.

Lastly, I would like to thank my wife, family, and friends, both in the department, elsewhere in the US, or abroad, for their generous support during my Ph.D. work.

TABLE OF CONTENTS

CHAPTER

LIST OF FIGURES

FIGURE

LIST OF TABLES

TABLE

LIST OF ABBREVIATIONS

ACS Advanced Camera for Surveys

CPD Circumplanetary Disk

CTIO Cerro Tololo Inter-American Observatory

CTTS Classical T Tauri star

CVSO CIDA Variability Survey in Orion

ESO European Southern Observatory

EW Equivalent Width

FUV Far-Ultraviolet

HST Hubble Space Telescope

IR Infrared

LTE Local Thermodynamic Equilibrium

NIR Near-Infrared

SBC Solar Blind Channel

SOAR Southern Observatory for Astrophysical Research

SUTR Sample-up-the-ramp

TTS T Tauri star

UV Ultraviolet

VLT Very Large Telescope

WTTS Weak T Tauri star

YSO Young Stellar Object

ABSTRACT

Accretion from protoplanetary disks onto the central low-mass pre-main sequence stars (T Tauri Stars) has been extensively studied for several decades. Theoretical, observational, and modeling efforts have shown that accretion from the disk onto the star follows the magnetospheric accretion paradigm, according to which the magnetic field lines truncate the disk, and mass flows along the field lines onto the stellar surface. Studies of a large sample of stars in many star-forming regions have shown that the fraction of accretors decreases as the population ages increase. Nevertheless, it is still unclear how accretion finally ceases and what role the evolution of disks and star properties plays in this process. Understanding the processes shutting off accretion will provide crucial information for studying the properties of disks in which planets are forming and of the stars that host them.

Here, we present a comprehensive study of stars at the last stages of their accretion phase, known as the low accretors, aiming to shed some light on the processes driving accretion to stop. By studying the gas in the inner disk using the H_2 1600 Å bump in the FUV, as well as the dust from near-infrared excess, we found that the disks of low accretors are diverse in dust emission, suggesting that the end of accretion is reached in diverse ways. We also confirmed previous results that stars stop accreting as soon as the inner disk has no gas left.

We showed that the He I λ10830 line is more sensitive at detecting accretion than diagnostics using the Balmer α line of hydrogen. Using this accretion diagnostics, we re-classify 51 stars previously thought to be non-accretors as accretors. We studied a subset of these stars and found that, at low accretion rates, magnetospheric flows accrete mass in the unstable regime, and many stars show complex accreting geometry. Based on the relationship between the inferred disk truncation radius, corotation radius, and mass accretion rate, we proposed that the dipolar fields in low accretors are weak and that the efficiency for the magnetic fields to truncate the disks is low. Moreover, none of the low accretors shows any evidence of accretion near the propeller regime, where mass is removed through centrifugal force, suggesting that the propeller is not the primary process inhibiting accretion at the last stages of disk evolution.

Although the magnetospheric accretion flow model can measure accretion rates as low as $\sim 10^{-11}\,M_\odot\,\mathrm{yr}^{-1}$, none of the low accretors shows accretion rates much below $1 \times 10^{-10}\,M_\odot\,\mathrm{yr}^{-1}$, providing evidence that there is a physical limit of how much mass can be supplied to the star

from its disk. This rate is consistent with the EUV-driven photoevaporative mass loss rate, which suggests that the outer disk cannot supply mass to the inner disks if the mass accretion rate from the outer disk drops below the mass loss rate. Nevertheless, we also showed that for the transitional disk around PDS 70, the mass accretion rate onto the star is too high if the mass transport efficiency is lower than $\alpha \lesssim 10^{-3}$. This suggests that the inner disks of low accretors could harbor an inner disk mass reservoir that is slowly feeding the star.

Lastly, we showed that the magnetospheric accretion model could be applied to the case of accreting giant planets, assuming that they have magnetic field strength on the order of hundreds Gauss. Measuring the mass accretion rates of the planet PDS 70b and c, we found that mass accreting into planets is less than 10% of the mass accreting onto the star, suggesting that giant planet formation, although important in creating gaps in the disk, does not directly starve the star of accreted mass.

Our results provided essential constraints in studying protoplanetary disk evolution, star-disk interactions, and the process of planet formation. Including these constraints in simulations will provide a more complete picture of how young stars, protoplanetary disks, and planets form and evolve.

CHAPTER 1

Introduction

Stars form as a result of the collapse of a molecular cloud core due to their own gravity. Since the primordial cloud possesses some amount of angular momentum, conservation of angular momentum requires that at least some mass collapses onto a disk. These disks consist of gas and dust, and they accrete mass onto the central objects over most of their lifetime. These disks are called protoplanetary disks (or planet-forming disks) as they are thought to be the site of planet formation.

The central objects, later to become stars, form as soon as their disks have formed, and they continue to grow by accreting material from the disks. They are initially called protostars when they are still embedded in their envelopes. They evolve by removing their envelopes, contracting to provide energy, and increasing their central temperature until they reach the main-sequence phase, at which point hydrogen starts burning in the cores. These pre-main sequence stars that have lost their envelopes can be classified based on their masses; intermediate-mass pre-main sequence stars ($\leq 2-3M_{\odot}$) are called Herbig Ae/Be stars whereas the low-mass counterparts are called T Tauri stars (TTS). During the pre-main sequence phase, the spectral type of these TTSs ranges from F to M. Most of the known T Tauri stars are in the K-M spectral type, as expected from the Galaxy's Initial Mass Function.

As the mass in the disk changes due to accretion onto the star or loss through winds, T Tauri stars and their disks evolve with time. The viscous evolution model of protoplanetary disks (Hartmann et al. 1998) predicts that the mass accretion rate from the inner disk onto the star decreases with time, driving disk evolution. As shown in the left panel of Figure 1.1, the measured mass accretion rates generally follow the trend predicted by viscous evolution, albeit with large scatter (Hartmann et al. 2016). In addition to mass accretion, other processes such as dust growth, dust settling, photoevaporation, chemical processes (e.g., ice-line formation), and planet formation are thought to be factors driving evolution in disks. These processes are invoked to explain the diversity of protoplanetary disks observed in panchromatic observations.

From the observational point of view, protoplanetary disks can be classified into two broad categories: primordial disks and debris disks. Primordial disks are gas-rich disks formed with

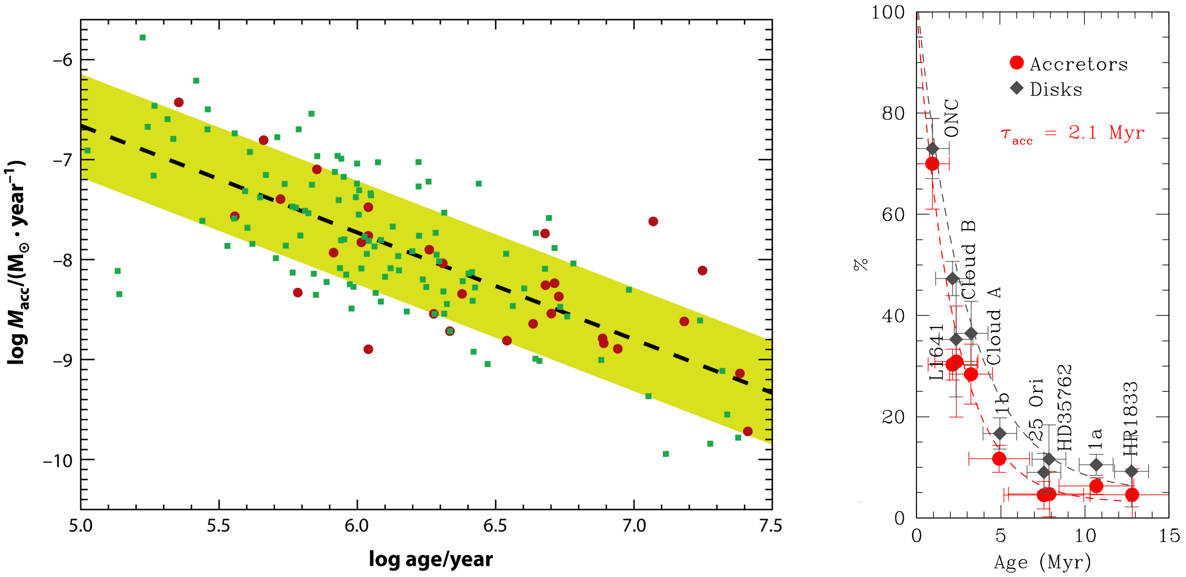

Figure 1.1 The evolution of protoplanetary disk and accretion. *Left:* Stellar mass accretion rates decrease as the age of the population increases, consistent with the prediction of the viscous evolution model of disk accretion. *Right:* The fraction of accretor and the fraction of primordial disk decreases with time. By 10 Myr, most of the stars in a population have stopped accretion. The left panel is from Hartmann et al. (2016), and the right panel is from Briceño et al. (2019).

the host star, whereas gas-poor debris disks result from collisional production of dust after the formation of planets (Wyatt 2008). The primordial disks include full disks, pre-transitional disks, transitional disks, and evolved disks (Espaillat et al. 2014). Full disks are optically thick due to the opacity of the dust, where the inner region reaches the stellar magnetosphere. Pre-transitional disks are disks with optically thick inner regions, an optically thin gap, and optically thick outer regions. Transitional disks have an optically thin cavity between the central star and the edge of the optically thick disks. Evolved disks are similar to full disks, but their fluxes are lower than those of full disks at all wavelengths; the low fluxes may be due to dust settling onto the midplane of the disks. This classification is thought to represent various stages of disk evolution (Williams & Cieza 2011).

T Tauri stars are also classified based on their accretion status. Classical T Tauri stars (CTTS) are those still accreting mass from their protoplanetary disk, and Weak T Tauri stars (WTTS) are those that have stopped accreting (c.f., § 1.3).

1.1 How does accretion stop?

Observations of large samples of young stellar associations have shown that the fraction of CTTS in a given stellar association decreases with the age of the group (Hernández et al. 2007; Fedele et al. 2010; Briceño et al. 2019), and by 10 Myr, less than 10% of TTS are still accreting. These studies are done by gathering a sample of T Tauri stars in a given group and calculating the fraction of stars with disks and fraction of stars that are still accreting using disk and accretion diagnostics, respectively. The right panel of Figure 1.1 shows the fraction of accreting stars and dust disk-bearing stars for kinematically resolved groups in the Orion OB1 association (Briceño et al. 2019). Using the equivalent width of Hα as accretion diagnostic and the near IR color excess as disk indicator, the results shown in Figure 1.1 confirm previous findings that these fractions decrease with age and that the e-folding time of disk and accretion evolution is $\sim 2-3$ Myr. Very few stars are expected to be accreting at 10 Myr.

Despite the wealth of knowledge about accretion in T Tauri stars, as reviewed below, it is still unclear how accretion stops. In this dissertation, I will approach this problem by attempting to answer the following questions:

1. What are the properties of the inner disk in objects with very low accretion rates?
2. What is the structure of the accretion flow for stars accreting at very low rates?
3. What processes are involved in stopping accretion?
4. Is there a physical lower limit for the mass accretion rate – in contrast to an observational low detection limit? If so, do they agree with predictions from disk dissipation studies?

In the following section, I review the relevant background of what is known about accreting T Tauri stars, how we identify them, and how to measure the mass accretion rates and estimate accretion properties.

1.2 Magnetospheric Accretion

Observations and simulations have confirmed the picture of how T Tauri stars accrete mass from their disks – magnetospheric accretion. Magnetospheric accretion was originally proposed to explain accretion in magnetically strong neutron stars accreting mass from their disks (Ghosh et al. 1977; Ghosh & Lamb 1979a,b). Although the magnetic field on T Tauri stars is much weaker than that of neutron stars, it is still sufficient to truncate the inner edge of protoplanetary disks at the disk truncation radius R_t ~few$\times R_\star$ (Hartmann et al. 1994, 2016). Therefore, mass spiraling inward

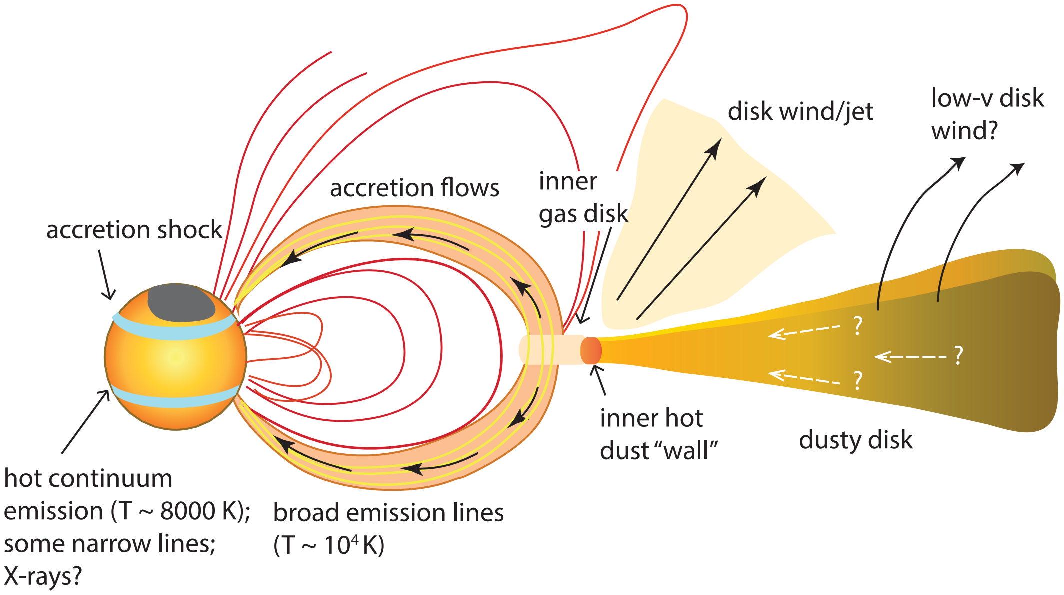

Figure 1.2 An illustration of magnetospheric accretion in T Tauri stars. Mass from the edge of the inner disk flows along the magnetic field lines onto the star, creating accretion shock that releases energy mainly in the UV. Emission lines form in the extended flow and can be observed in the optical/near IR. Figure is from Hartmann et al. (2016).

has to flow along the magnetic field lines threading the disk at that radius. Depending on the location of the truncation radius respective to the stellar corotation radius R_{co}, the point at which the disk Keplerian orbital period equals the stellar rotation period, mass loaded onto the flow can either flow onto the star at ~free-fall velocity if $R_t < R_{co}$, or else ejected onto winds due to centrifugal force (Ghosh et al. 1977; Ghosh & Lamb 1979b; Koenigl 1991). Figure 1.2 shows the schematics of magnetospheric accretion and its connection to the protoplanetary disk.

At the base of the accretion column, the accretion flows, traveling at supersonic speeds, merge with the stellar photosphere through an accretion shock (Calvet & Gullbring 1998). The kinetic energy of the mass flow is released in X-rays, which irradiates the structure above the shock (pre-shock) and the flow below the shock (post-shock), as well as the photosphere. The energy re-processed in the pre-shock, post-shock, and the heated photosphere is released and appears as an excess of optical-UV flux above the photosphere, which is more conspicuous in the UV where the contrast with the cooler stellar photosphere is greatest. Figure 1.3 shows the structure of accretion shock and and its continuum excess over the photosphere of an accreting T Tauri star.

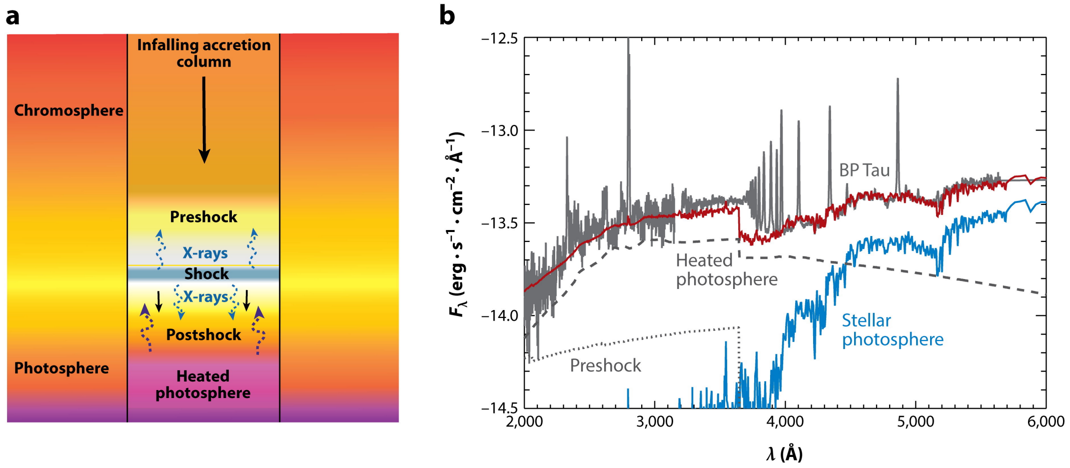

Figure 1.3 The structure of accretion shock and its spectral energy distribution. *Left:* A schematic illustration of accretion shock structure showing the preshock, postshock, and the heated photosphere. *Right:* Accretion shock modeling of a CTTS BP Tau showing components of its spectral energy distribution. Figure is from Hartmann et al. (2016).

1.3 Accretion Diagnostics and their Limitations

Emission from the extended accretion flows in the stellar magnetosphere and from the accretion shock provide tools to identify T Tauri stars that are accreting (CTTS). They also provide ways to learn about the physical properties of the accreting system.

1.3.1 Continuum Excess

The excess flux over the stellar photosphere indicates an additional source of continuum emission from the star. This emission can be observed in two ways: (1) directly measuring the excess, or (2) using veiling of photospheric absorption lines.

If the star's spectral type is known, one can estimate the level of photospheric emission intrinsic to the star. Therefore, any emission in excess of this intrinsic emission indicates that the star is accreting. The excess luminosity can be converted to accretion luminosity using accretion shock models, and from that the mass accretion rate onto the star can be obtained, since

$$L_{acc} = \frac{GM_\star \dot{M}}{R_\star^2}. \tag{1.1}$$

This excess can be measured either using flux-calibrated spectra (c.f., Figure 1.3) or absolute photometry. Due to a greater contrast between the photosphere and the excess flux, measuring the U-band excess has been the traditional method for estimating accretion luminosity (Gullbring et al. 1998). Flux-calibrated spectra are used in place of photometry if available (Calvet & Gullbring

1998). In the optical and near-infrared wavelength, veiling has been used to measure the excess flux (Hartigan et al. 1995); due to excess, photospheric lines in the optical spectra become shallower than those of non-accreting stars. Measurements of the difference in depth of many lines can be used to infer the level of excess. In either method, suitable templates for the photosphere are required. In general, a weak T Tauri star with the same spectral type is used as a template, assuming that the intrinsic photospheric emission of the stars is similar.

One difficulty with this method is that the active magnetic fields that allow magnetospheric accretion also make the star chromospherically active. Unfortunately, this chromospheric emission is more apparent in the UV. For typical mass accretion rates of $\gtrsim 10^{-9}\,M_{\odot}\,\mathrm{yr}^{-1}$, the emission from the accretion shock is much larger than the chromospheric emission, so the U excess provides a reliable indication of accretion. However, for low mass accretion rates, the shock emission is comparable to the chromosphere, making the accretion identification challenging (Ingleby et al. 2011b; Manara et al. 2013).

1.3.2 Neutral Hydrogen Lines

Neutral hydrogen lines in emission have been used to identify T Tauri stars and to determine the accretion luminosities or mass accretion rates. These lines form in the extended accretion flows that are heated to $\sim 10^4$ K, enough to populate the upper excited levels of the atom. In particular, the equivalent width (EW) and the width at the 10% peak (W_{10}) of the hydrogen Balmer Hα line (White & Basri 2003; Jayawardhana et al. 2006; Barrado y Navascués & Martín 2003) are regularly used to classify T Tauri stars into CTTS or WTTS.

The thresholds between the CTTS and WTTS classification based on equivalent width or W_{10} are empirical. Moreover, these thresholds are spectral-type dependent, with a lower threshold for earlier spectral type, reflecting the weaker contrast between the line emission and the continuum for earlier-type stars and the smaller velocity scales in lower mass systems. Two main empirical thresholds were adopted for W_{10}: $270\ \mathrm{km\,s^{-1}}$ for K-M stars (White & Basri 2003) and $200\ \mathrm{km\,s^{-1}}$ for late M stars (Jayawardhana et al. 2006).

These thresholds become less reliable at very low accretion rates since the density, and thus the line width, becomes narrower. In addition, the relative strength of the chromospheric emission becomes more evident (Manara et al. 2017a) making the identification of accreting stars more complicated.

1.3.3 Neutral Helium Lines

Helium is the second most abundant element after hydrogen, and so it is present in a significant amount in the accretion flows. In fact, He I lines have been used as accretion indicators for decades

(Edwards et al. 2003), but their usage has been limited since, in general, Hα is easier to observe. Nonetheless, several He I lines are present in the optical spectra of strong accretors and are used as additional calibrators to measure mass accretion rates (e.g., Alcalá et al. 2017).

One of the strongest He I lines is the line at 10830 Å[1]. The line forms between the $2s^3S$ state and $2p^3P^0$ state in the triplet branch of the neutral helium atom. The configuration of the line provides an advantage for line formation because the lower level of the line is metastable, i.e., the transition between that level to the ground state ($1s^1S$) is radiatively forbidden. Therefore, electrons that are collisionally excited to higher levels, or reach those levels by recombination, will cascade down and accumulate at the $2s^3S$ level. They can then easily absorb light from the star or the accretion shock at 10830 Å. Therefore, the line can be very sensitive even at low density, making it a good indicator of accretion at low rates. Figure 1.4 shows the comparison between Hα and He I λ10830 as accretion diagnostics. The He I line is clearly more sensitive at detecting accretion.

Instead of using line width, as for Hα, the He I λ10830 line indicates accretion status based on the line profile. Thanks to the metastable lower level, absorption features can easily form. In particular, redshifted absorption at ~free-fall velocity indicates that matter moves away from the observer and onto the star. Since the free-fall velocity is large (few$\times 100\ \mathrm{km\,s^{-1}}$), these absorption features can be resolved even with moderate spectral resolution. Due to its sensitivity, I used the He I λ10830 as the primary accretion indicator throughout this dissertation.

1.4 Measuring Mass Accretion Rates: the Magnetospheric Flow Model

As mentioned earlier, the continuum excess is difficult to detect at low accretion rates (Ingleby et al. 2011b), and line equivalent widths or line luminosities may have a significant contribution from chromospheric emission (Manara et al. 2017a). Therefore, at low accretion rates, one of the most reliable ways to measure the mass accretion is through modeling of emission lines formed in the extended accretion flow, once the accretion status of the star has been confirmed through independent methods (e.g., He I line profiles).

Here I described the magnetospheric accretion flow models used throughout this dissertation. The model has been developed in various stages and is described by Hartmann et al. (1994) and Muzerolle et al. (1998b, 2001). The full details of the model are described in the original work, and the summary is given here. The code for the calculation is written in C++, Fortran, and Python, and it is collectively called CV.

---

[1] The wavelength indicated here is the air wavelength of the triplet

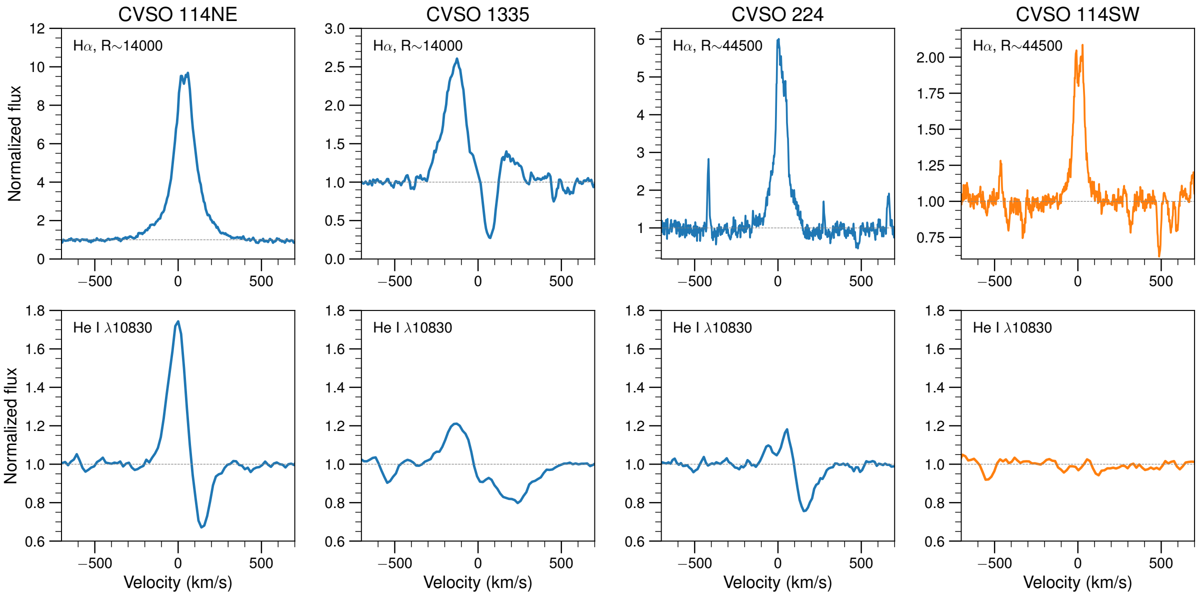

Figure 1.4 A comparison between Hα and He I λ10830 accretion diagnostics. CVSO 114NE, CVSO 1335, and CVSO 224 are accreting, showing redshifted absorption in the He I line observed in moderate spectral resolution. The Hα line of CVSO 224 fails to detect accretion if the traditional methods (EW, W_{10}) are used, even at high spectral resolution. No accretion is detected by both lines for CVSO 114SW.

1.4.1 Basic Assumptions

The magnetospheric model assumes that mass flows along an axisymmetric geometry guided by the stellar dipolar magnetic field, assuming that the magnetic and rotation axes are the same. Mass, confined within the inner and outer field lines, flows from the inner edge of the disk in a steady manner, and their density and velocity are described by analytical expressions derived from that assumption. Figure 1.5 shows the geometry adopted in this model. The temperature structure is calculated analytically from an assumption in the heating, which is nearly steady throughout the flow except at the regions near the disk. It is also assumed that dust that is present in the disk has sublimated in the flow, e.g., the accretion flow is dust-free, and that the flows consist of gas with solar abundances. The radiation fields are calculated assuming the extended Sobolev approximation, and the level populations of the hydrogen atoms are determined by solving the statistical equilibrium equations, assuming a 16-level atom plus continuum.

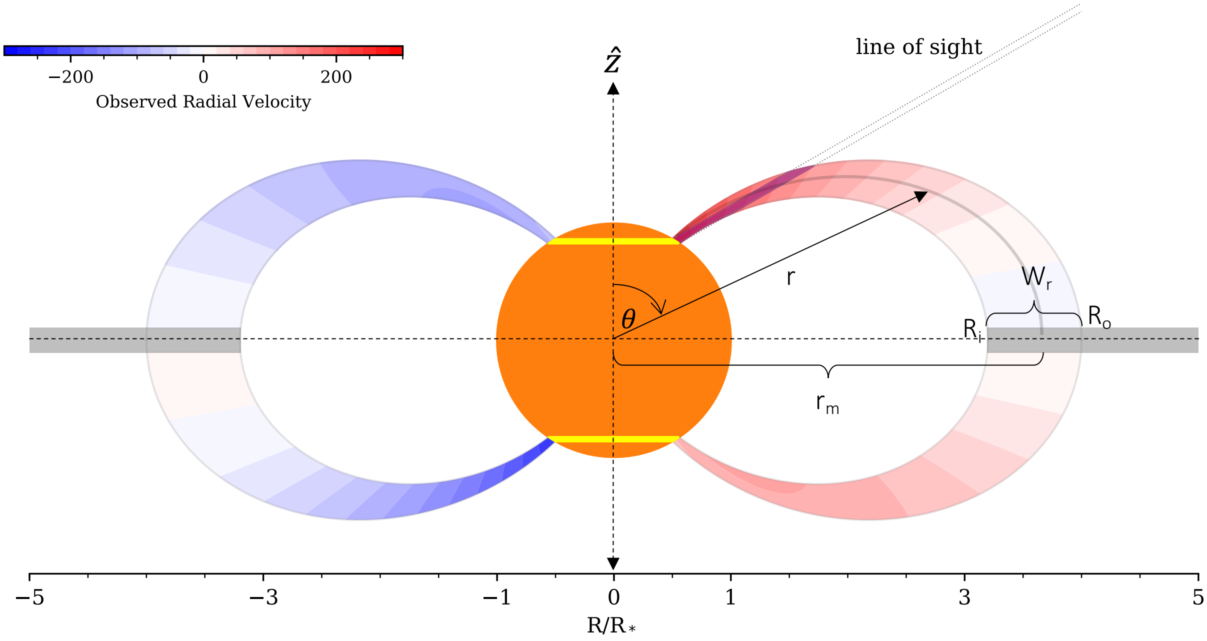

Figure 1.5 The geometry and observed velocity of the magnetospheric accretion model. The parameters in this geometry are $R_i = 3.2R_\star$, $W_r = 0.8R_\star$, and $i = 60°$. The yellow strips on the stars represent the base of the accretion flows, where the accretion shock emits as a hot ring; the horizontal gray bars represent the (opaque) inner disk. Most of the emissions on the red side of the line come from the flow between the star and the observer, whereas the blue side of the line comes from the flow on the backside of the star. Redshifted absorption occurs when high-optical-depth flows absorb light from the shock and/or the stellar photosphere.

1.4.2 The Structure of the Flow

Assuming that the stellar rotation pole and the magnetic pole are pointing at the same direction $\hat{z}$ the magnetic dipole field follow the equation

$$r = r_m \sin^2(\theta), \tag{1.2}$$

where (r, θ) define a position in the spherical coordinate centered at the star, and r_m is the magnetic radius for a given field, measured on the horizontal plane ($z = 0, \theta = \pi/2$) where the field joins the disk. Assuming that the flow has some width W_r at the base and we define R_i as the radius of the innermost field, R_i and W_r completely define the geometry of the the accretion flow.

Assuming a steadyflow, the velocity vector at a given point (r, θ) in the flow is given by

$$\boldsymbol{v_p} = -v_p \cdot \left[\frac{3\alpha^{1/2}(1-\alpha)^{1/2}\hat{R} + (2-3\alpha)\hat{z}}{(4-3\alpha)^{1/2}}\right], \tag{1.3}$$

where $\alpha = r/r_m$, $\hat{R}$ is the unit vector along the horizontal plane, and the poloidal speed along the field v_p is given by

$$v_p = \left[\frac{GM_\star}{R_\star}\left(\frac{R_\star}{r} - \frac{R_\star}{r_m}\right)\right]^{1/2}. \tag{1.4}$$

The model assumes that the magnetosphere is co-rotating with the star, i.e., no rotation is included.

Mass is confined between two field lines specified by R_i and $R_o = R_i + W_r$. The density in the flow is calculated assuming steady flow and is given by

$$\rho = \frac{\dot{M}R_\star}{4\pi(R_\star/R_i - R_\star/R_o)} \frac{r^{-5/2}}{(2GM_\star)^{1/2}} \frac{(4-3\alpha)^{1/2}}{(1-\alpha)^{1/2}}, \tag{1.5}$$

where the mass accretion rate $\dot{M}$ is a parameter (Hartmann et al. 1994).

The temperature structure in the flow is the least understood physical property. Here the model assumes a volumetric heating rate $\sim h_r/r^3$, where h_r is constant throughout the flow. The temperature is calculated using the cooling function of Hartmann (1982). The maximum temperature in the flow $\mathrm{T}_{\mathrm{max}}$ describes each model.

1.4.3 Radiative Transfer Methods and Model Atom

The radiative transfer procedure adopted in this model assumes the extended Sobolev approximation, where only the regions of the same radial velocity can radiatively interact. At a given point $\boldsymbol{r}$ in a direction $\boldsymbol{n}$, the velocity gradient in the flow $\partial \boldsymbol{v_n}(\boldsymbol{r})/\partial r_n$ is large, such that the length scale of the surface of constant velocity $\Delta l_n \sim c_s/(\partial \boldsymbol{v_n}(\boldsymbol{r})/\partial r_n)$ is small, and the local properties (e.g., densities) within it do not change. The optical depth of that surface in the direction $\boldsymbol{n}$ can, therefore, be approximated as

$$\begin{aligned} \tau_v(\boldsymbol{r}, \boldsymbol{n}) &= \int_{\Delta l} d\tau_v = \int_{\Delta l} \chi(\boldsymbol{r}) dl_n \qquad (1.6) \\ &\sim \chi(\boldsymbol{r})\Delta l_n, \qquad (1.7) \end{aligned}$$

where χ is the line absorption coefficient. It depends on the local properties at $\boldsymbol{r}$ and is given by

$$\begin{aligned} \chi(\boldsymbol{r}) &= \frac{\pi e^2}{m_e c} f N_u(\boldsymbol{r}) \left[1 - \frac{g_l N_u(\boldsymbol{r})}{g_u N_l(\boldsymbol{r})}\right] \frac{1}{\sqrt{\pi}\Delta\nu_D}\phi_\nu \qquad (1.8) \\ &= \chi_0(\boldsymbol{r}) \frac{1}{\sqrt{\pi}\Delta\nu_D}\phi_\nu, \qquad (1.9) \end{aligned}$$

where $\Delta\nu_D = \nu_0 c_s/c$ is the Doppler width of the line, ν_0 is the line-center frequency, f is the line oscillator strength, ϕ_v is the Voigt function, N is the number density and g is the statistical weight.

The letters u, l denote upper and lower level, respectively. It follows that

$$\tau(r_0, \boldsymbol{n}) = \chi_0(r_0)\frac{c}{\nu_0}\frac{1}{(\partial v_n/\partial r_n)_{r_0}}. \tag{1.10}$$

The mean intensity at a given point $\boldsymbol{r}$ is given by

$$\bar{J}(\boldsymbol{r}) = [1 - \beta(\boldsymbol{r})]S(\boldsymbol{r}) + \beta_c(\boldsymbol{r})I_c + F(\boldsymbol{r}), \tag{1.11}$$

where β is the escape probability, S is the source function, I is the intensity, F is a non-local term arising from the fact that there could be multiple crossings of constant velocity surfaces, and the subscript c means the continuum. The escape probability can be calculated from the optical depth τ as

$$\beta(\boldsymbol{r}) = \frac{1}{4\pi}\int \frac{1 - e^{-\tau(\boldsymbol{r},\boldsymbol{n})}}{\tau(\boldsymbol{r},\boldsymbol{n})} d\omega(\boldsymbol{n}), \tag{1.12}$$

where ω is the solid angle and the integration is computed over all directions $\boldsymbol{n}$.

The line source function between level i and j can be written as

$$S = \frac{2h\nu^3}{c^2}\left[\left(\frac{N_l g_u}{N_u g_l}\right) - 1\right]^{-1}, \tag{1.13}$$

where h is the Planck constant and ν is the frequency of the transition.

The level populations are calculated in an iterative process. Starting from an initial guess (typically LTE population), the optical depth τ and source functions S are calculated, followed by the mean intensity $\bar{J}$ for each radiative transition using the escape probability (Eqs. 1.11 and 1.12). New populations are then calculated by solving the statistical equilibrium equations using $\bar{J}$ in the radiative rates in each transition. The process is repeated until the populations converge.

1.4.4 Line Profile Calculation

The line profile is calculated using the ray-by-ray method. At an inclination i, the geometry is projected onto the sky, and each point is described by (p, q, z), where (p, q) is the coordinate on the sky and z is now the coordinate along the line of sight (ray). For each frequency ν, the intensity is calculated by

$$I_\nu = I_0 e^{-\tau_{\text{tot}}} + \int_{-\infty}^{z_0} \eta(z) e^{-\tau(z)}\, dz, \tag{1.14}$$

where I_0 is either the photosphere, the hot ring, or 0 if the ray does not cross the star. z_0 is either at the stellar surface or ∞, and η is the line+continuum emissivity calculated from the line-center opacity and the source function (Eq. 1.13) for the line, and hydrogen bound-bound, bound-free, and free-free opacity for the continuum.

The optical depth is calculated by integrating the opacities along the ray. The line opacity is calculated from the population and the Voigt profile, taking into account the radial velocity of each point, and includes radiative, van der Waal, and Stark broadening. The populations, as calculated above, are used for the calculation of the optical depth and the source function at each point along the ray.

The flux is then calculated as

$$F_\nu = \frac{1}{d^2} \int I_\nu dp\, dq, \tag{1.15}$$

where d is the distance.

As an illustration, Figure 1.6 shows an example of a line profile, along with the emergent specific intensity I_ν and the total optical depth $\tau_{\nu,tot}$ at each point in the projected coordinate (p, q) and at five velocities along with the line profile for a typical low accretor. Different regions in the flow contribute to the total emission at different observed velocities. Emission on the blue side of the line (negative velocities) comes from the backside of the flow, as material accreting onto the star is seen moving toward the observer. On the other hand, the red-side emission comes from the flow in front of the star, with redder emission coming from regions closer to the star. The emission near the line center comes from regions further away from the star in the line-of-sight direction and most regions on the side of the star. In this case, redshifted absorption can occur near $\sim 200\ \mathrm{km\,s^{-1}}$ as the flow is occulting the hot ring.

Knowing the stellar parameters ($M_\star$, $R_\star$, T_{eff}), a large grid of models can be created for hydrogen Balmer lines (e.g., Hα, Hβ), resulting in a large numbers of model line profiles. The accretion parameters (R_i, W_r, $\dot{M}$, T_{max}, i) can be inferred from models that best fit the observations.

1.5 Overview of the Dissertation

In this Dissertation, I will address the question of how accretion stops by investigating in detail individual objects that are accreting at very low rates and searching for common properties among low accretors by conducting a survey. Properties that relate to processes that might stop accretion are considered along the way. Chapter 2-4 and Chapter 7 have been published in the Astrophysical Journal (Thanathibodee et al. 2018, 2019b, 2020, 2019a, respectively). Chapter 5 is under review by the Astronomical Journal, and Chapter 6 is in preparation for submission to the Astrophysical Journal.

In Chapter 2, we investigate the inner region of protoplanetary disks surrounding three T Tauri stars that show evidence of very weak to no accretion at 5 Myr, the critical age of disk evolution. The presence of the inner disks is inferred from the 1600 Å bump in the Far-UV spectra of these

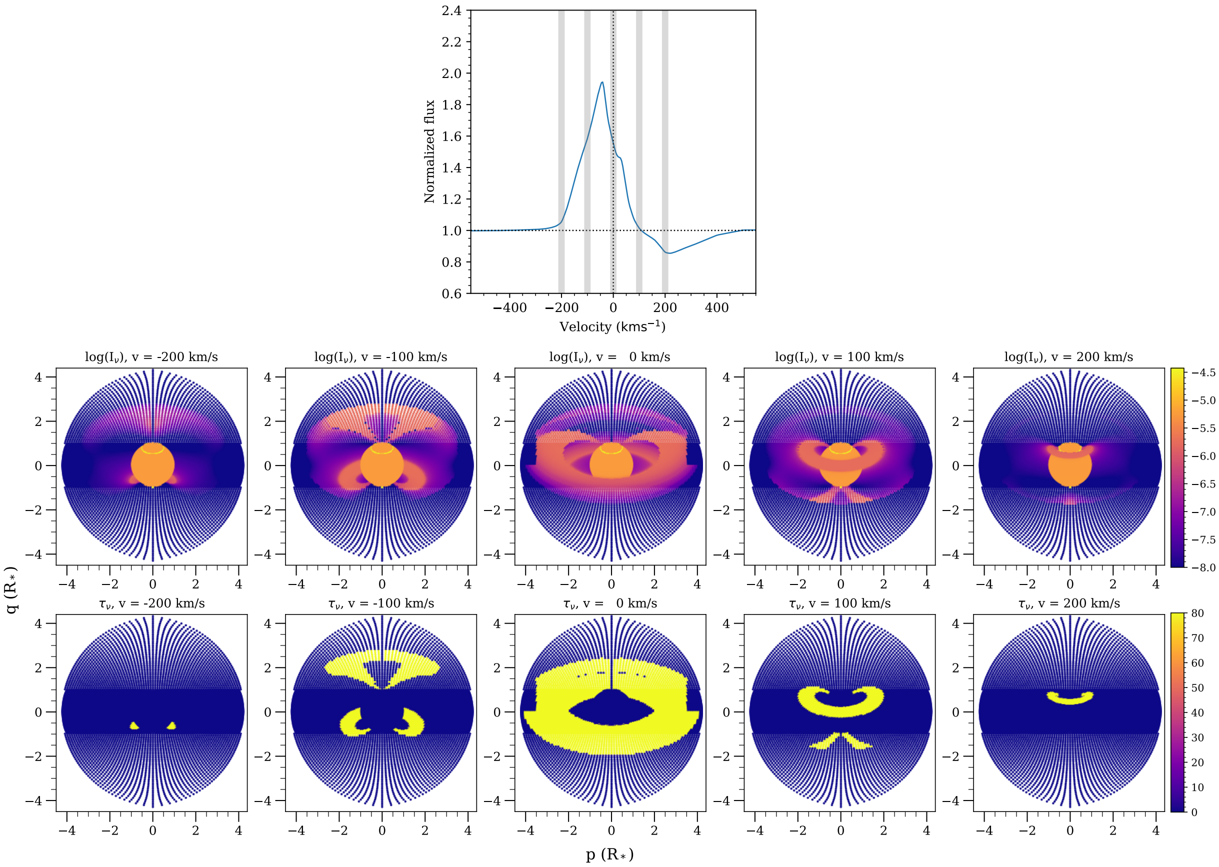

Figure 1.6 The line profile, the emergent specific intensity, and the optical depth of a magnetospheric flow model. Showed here is an example of a K7 star with $\dot{M} = 1 \times 10^{-10}\,M_\odot\,\mathrm{yr}^{-1}$, $R_i = 3.5\,R_\star$, $W_r = 0.7\,R_\star$, $T_{max} = 1.2 \times 10^4\,\mathrm{K}$, and $i = 60°$. The top panel shows the profile with redshifted absorption. The center row shows the intensity, and the bottom row shows the total optical depth along the line of sight. The grey vertical lines in the top panel mark the velocities shown in the lower panels.

stars observed in low resolution with the Hubble Space Telescope. In comparison, we analyze the targets' optical and near IR spectra to infer their accretion properties. In this Chapter, we have confirmed the use of the He I $\lambda 10830$ as a sensitive accretion diagnostic and identified the diverse properties of stars reaching the end of their accretion phase.

The star investigated in Chapter 2, CVSO 1335, shows perplexing emission line profiles not typically seen in spectra of other T Tauri stars. The Hα line of the star shows variable low-velocity sub-continuum redshifted absorption, which makes the determination of mass accretion rate difficult. This type of profile is rare, but it could be related to the fact that this is a low accretor. In Chapter 3, we study this star in detail using magnetospheric accretion models and accretion shock models to determine accretion properties of the star and how the low level of mass accretion plays a role in displaying the observed type of line profile.

The formation of giant planets is thought to be responsible for driving disk evolution by opening gaps in the disk. As these planets form, they will also take mass from the disk that would otherwise accrete onto the host stars. In Chapter 4, we investigate the effect of accreting planets on the stellar mass accretion by modeling the accretion properties of the protoplanet host star PDS 70. The star is the best case of T Tauri stars hosting accreting protoplanets in their disks; in this case, the star hosts two planets observable by optical and near-IR high-resolution observations. Using archival high-resolution spectra and recent data from the TESS mission, we construct phase-resolved magnetospheric accretion models by fitting the line at different rotation epoch; the rotation period is derived from the TESS data. The observations and modeling confirm that PDS 70 is a low accretor. We also introduce here the Hα fitting procedure that takes into account the chromospheric emission of the line found in low accretors. The accretion properties of PDS 70 are compared with previously studied low accretors, as well as the disk properties and accretion properties of its planet, and the expectations from theoretical studies.

Studying individual low accretors provides great insight into the properties of low accretors, but their common properties cannot be determined from only a small sample size. In Chapter 5, we present the results of a survey to search for and characterize low accretors using He I λ10830 as the sensitive probe of accretion. The targets were selected from 11 stellar groups in five star-forming complexes within 500 pc. The stars still show evidence of primordial dust disks, but the traditional accretion indicators (Hα, W_{10}) fail to detect accretion onto the stars. From the observations of 170 objects using the FIRE spectrograph, we classify the He I λ10830 profiles into different types and relate them with the properties of the stars and the disks.

A follow-up study based on a large sample of low accretors is present in Chapter 6, where the objects were selected from the newly identified accretors in Chapter 5. Here, the magnetospheric accretion model is used to model high- and moderate-resolution Hα lines to infer accretion properties (accretion rate, geometry) of the targets. We then search for any correlation between these properties and stellar parameters. Here we improve the accretion modeling procedure from Chapter 4 by directly include a Gaussian component into the fit to represent the chromospheric emission in the Hα line core. Lastly, we determine the limit of mass accretion rate at which the magnetospheric accretion model can be used for the Hα line.

As a window into the future uses of the magnetospheric accretion modeling for low accretors, in Chapter 7 we utilize the model to fit the observation of a special class of low accretors – accreting protoplanets. We calculate the Hα line fluxes for a range of accretion parameters for the protoplanet PDS 70b and c and compare the line fluxes and widths to the observed values. We determine the relationship between the line luminosity and accretion luminosity and compare it to the relationships found in T Tauri stars.

In Chapter 8, I summarize the findings for how different studies of low accretors provide insight into the last stages of accretion and propose future directions to study accretion in different classes of objects and how they could relate to the evolution of stars, planets, and disks around them.

CHAPTER 2

The Evolution of Protoplanetary Disks: Probing the Inner Disk of Very Low Accretors

This chapter was originally published in the Astrophysical Journal, Volume 861, 73 (2018), in collaboration with Nuria Calvet, Gregory Herczeg, César Briceño, Catherine Clark, Megan Reiter, Laura Ingleby, Melissa McClure, Karina Maucó, and Jesús Hernández. It is adapted and reproduced here under the non-exclusive rights of re-publication granted by the American Astronomical Society to the authors.

Abstract

We report FUV, optical, and NIR observations of three T Tauri stars in the Orion OB1b subassociation with Hα equivalent widths consistent with low or absent accretion and various degrees of excess flux in the mid-infrared. We aim to search for evidence of gas in the inner disk in HST ACS/SBC spectra, and to probe the accretion flows onto the star using Hα and He I λ10830 in spectra obtained at the Magellan and SOAR telescopes. At the critical age of 5 Myr, the targets are at different stages of disk evolution. One of our targets is clearly accreting, as shown by redshifted absorption at free-fall velocities in the He I line and wide wings in Hα; however, a marginal detection of FUV H_2 suggests that little gas is present in the inner disk, although the spectral energy distribution indicates that small dust still remains close to the star. Another target is surrounded by a transitional disk, with an inner cavity in which little sub-micron dust remains. Still, the inner disk shows substantial amounts of gas, accreting onto the star at a probably low, but uncertain rate. The third target lacks both a He I line or FUV emission, consistent with no accretion or inner gas disk; its very weak IR excess is consistent with a debris disk. Different processes occurring in targets with ages close to the disk dispersal time suggest that the end of accretion phase is reached in diverse ways.

2.1 Introduction

While the overall view of the evolution of the disks around low mass pre-main sequence stars, or T Tauri stars, is fairly well known, the details of this process are still unclear. At an early stage, T Tauri stars host a disk with dust and gas, from which mass is accreting onto the star. At the dust destruction radius, $\sim$ 10 $R_\star$, the dust in the disk sublimates, creating a dust edge. The gas moves further inward until it reaches the disk truncation radius near the corotation radius, $\sim$ 3-4 $R_\star$. Inside this radius, the stellar magnetic field channels matter from the disk onto the star. Outside of the corotation radius, the magnetic field lifts the gas and pushes it outward, resulting in winds and jets. These processes, along with photoevaporation and planet formation, disperse the dust and gas from the inner disk. At some point, small dust grains are cleared and all the gas dissipates. This process happens rather quickly (Ingleby et al. 2012). By 5 Myr, less than 10% of the stars are still accreting, and a similar fraction keeps an inner dust disk (Fedele et al. 2010). This suggests that there is a link between the presence of the inner dust disk and accretion. However, it is not quite clear if this is also the case for the inner gas disk. For example, it is unclear whether magnetospheric accretion stops because the disk runs out of gas, or by the action of other processes even before the gas is completely depleted. To address this problem, sensitive diagnostics of gas and accretion must be used to probe the lowest accretors, objects which have very little gas left in the inner disks and/or in which very little accretion goes on.

Gas in the inner disk consists of warm atoms, ions, and molecules. The most abundant molecule in the disk is H_2, but its direct observation is difficult because it is a homonuclear molecule lacking a permanent electric dipole component so its rovibrational transitions are very weak. However, the environment in the inner disk, where the temperature is of the order of a few thousand kelvins, allows direct detection of the molecule in the FUV. Two main mechanisms for exciting and dissociating H_2 in the inner disk are Lyα fluorescence (Herczeg et al. 2006) and electron-impact excitation (Bergin et al. 2004). H_2 molecules excited by Lyα photons de-excite back to the electronic ground state, resulting in emission lines in the FUV (1100 - 1700 Å). At the same time, X-rays from the star partially ionize heavy metals in the disk, and the ejected electrons can excite and dissociate H_2. This process results in lines and continuum emission in the FUV, the last mostly around 1600 Å. The transition probabilities associated with these processes are high, so FUV observations of H_2 can be used as a sensitive tool to probe the gas in the inner disk.

We note that a recent study by France et al. (2017) suggests that the 1600 Å feature arises from Lyα-driven H_2O dissociation instead of X-ray-driven, electron-impact H_2 excitation. In this case, the feature still probes the gas in the inner disk, albeit arising from a different mechanism. Even though throughout this Chapter we refer to the FUV 1600 Å feature as H_2 λ1600, we acknowledge that the feature may indeed come from H_2O.

Ingleby et al. (2009) used the H_2 $\lambda1600$ excess feature to probe the inner gas disk of T Tauri stars across an age range of 1-10 Myr; they found that inner disk H_2 is only present in accreting stars, also known as Classical T Tauri Stars (CTTS). Follow-up studies by Ingleby et al. (2012) of non-accreting T Tauri stars, or Weak T Tauri stars (WTTS), confirmed the previous result, namely, that WTTS have cleared the gas from the inner disk as early as 1-3 Myr. Recently, Doppmann et al. (2017) have also explored the link between accretion and the inner gas residue using mid-IR CO emission and found that CO is detected only in accreting sources, identified by M-band veiling. These results seem to suggest that the gas is gone as soon as the accretion stops. To test this assumption further, sensitive tools are needed to probe accretion kinematics and measure the very low accretion rate expected at the transition between accretors and non-accretors.

The traditional diagnostics of accretion are the equivalent width of the Hα line in low resolution spectra, or the width of the line or the presence of redshifted absorption, which require high resolution spectroscopy. However, these diagnostics may fail at very low accretion levels if Hα becomes optically thin.

Being the second most abundant element, Helium is a promising alternative to Hydrogen. In fact, studies of the He I $\lambda10830$ feature in T Tauri stars have shown that the line is a good indicator of accretion and outflows (Edwards et al. 2006; Fischer et al. 2008). Helium atoms in the accretion flow that are ionized by the stellar high energy radiation (e.g., X-ray) recombine and then cascade down the energy levels until they reach the metastable state 1s2s ^{3}S. The emission line at 10830 Å results from the transition 1s2p ^{3}P → 1s2s ^{3}S (Kwan & Fischer 2011). At the same time, He atoms in the flow capture line and continuum photons at their rest wavelength, resulting in absorption at the velocity of the flow. Depending on the observing geometry, outflow or/and infall of material may produce blueshifted or/and redshifted absorption superimposed on the emission line. Thus, redshifted absorption is a definite probe of accretion; velocities of this feature close to the free-fall velocity indicate magnetospheric accretion (Fischer et al. 2008; Kwan & Fischer 2011).

Following the studies of the evolution of the inner gas disk by Ingleby et al. (2009, 2012), we report here observations of three T Tauri stars with flux excess over the photosphere in the near or mid-IR, and with equivalent widths of Hα consistent with low or absent accretion. Our targets belong to the Orion OB1b subassociation, so have ages of ~ 5 Myr (Briceño et al. 2005), a critical age for gas dispersal. We aim to probe for accretion using the Hα and the He I $\lambda10830$ lines, and for the presence of inner gas disk using H_2 $\lambda1600$. The details of the observations and data reduction are given in Section 2.2. Section 2.3 provides the methods of analysis and the results. Finally, the discussion of the findings and the implications of the results are provided in Section 2.4.

Table 2.1 Summary of Observations

CVSO	RA (J2000)	Dec (J2000)	Instrument	Slit/Prism Grating/Filter	Spectral Resolution	Obs. Date UT	Exp. time[a] (sec)
114NE	05 33 01.97	−00 20 59.3	ACS/SBC	PR130L	~70[b]	2016-03-23	2586
			Goodman	2100 l/mm	14000	2014-11-11	3 × 900
			FIRE	0.6″	6000	2014-12-02	201
			FIRE	0.6”	6000	2017-01-05	190
			SAM	g, r, i, z	···	2014-01-23	60, 15, 20, 30
1335	05 32 10.16	−00 37 12.3	ACS/SBC	PR130L	~70[b]	2016-03-22	2586
			Goodman	2100 l/mm	14000	2017-09-18	3 × 600
			MagE	1.0″	4000	2017-11-29	2 × 900
			MagE	1.0″	4000	2017-11-30	600+900
			FIRE	0.6″	6000	2017-01-05	190
114SW	05 33 01.76	−00 21 01.9	ACS/SBC	PR130L	~70[b]	2016-03-23	2586
			Goodman	2100 l/mm	14000	2014-11-11	3 × 900
			M2FS	HiRes	44500	2012-12-10	5 × 1200
			FIRE	0.6″	6000	2014-12-02	402
			SAM	g, r, i, z	···	2014-01-23	60, 15, 20, 30

[a] The listed exposure time for the FIRE observation is for each of the two nods (A/B).

[b] The spectral resolution for PR130L ranges from R~220 @ 1250 Å to R~40 @ 1800 Å. The value shown is at 1600 Å.

2.2 Observations and Data Reduction

2.2.1 Target Selection

The targets for this study, CVSO 1335, CVSO 114NE, and CVSO 114SW, were selected from the CIDA Variability Survey of Orion (Briceño et al. 2005, 2019). This survey characterizes the population of low mass stars in the OB1 association with emphasis on the 1a and 1b subassociations, which span an age range of 5 to 10 Myr, a critical timescale for the evolution of protoplanetary disks (Hernández et al. 2008; Fedele et al. 2010). Our targets are in OB1b with an age of $\sim$ 5 Myr (Briceño et al. 2005) and we use distances calculated from Gaia DR2 parallax measurements (Gaia Collaboration et al. 2018).

The targets were selected as having low Hα equivalent widths (EWs) for their respective spectral type, consistent with low or absent accretion, and excess flux over the photosphere in at least one WISE band, indicative of the presence of a disk. CVSO 114 was not resolved in the original CSVO photometry (Briceño et al. 2005), but it was later found to be a visual pair with an angular separation of 4.9″; we study here each star of the pair. We carried out spectroscopic and photometric observations of the targets. A log of the observations, including instrument specifications and spectral resolutions, is provided in Table 2.1.

2.2.2 FUV Spectroscopy

To investigate the presence of gas in inner disks, we obtained far ultraviolet spectra of CVSO 114 and CVSO 1335 using the Advanced Camera for Surveys/Solar Blind Channel (ACS/SBC) on board the Hubble Space Telescope (Program GO14190). Since the stars were expected to be faint in the FUV, we took advantage of the high throughput PR130L prism at the cost of resolution. The same system was shown to be a reliable setup in our previous studies (Ingleby et al. 2009, 2012). Each target was observed for one orbit with an exposure time of 40 s for target acquisition and 2586 s for science exposure. The CVSO 114 pair was observed on the same field. The spectrograph was able to resolve each component and the spectra were reduced separately.

The ACS/SBC PR130L prism spectra were reduced with custom-written programs in IDL, following similar reductions in Ingleby et al. (2009) and Yang et al. (2012). The counts were extracted from 9-pixel windows centered on the target, with background counts estimated from nearby regions and subtracted from the spectrum. The wavelength solution was obtained from (Larsen et al. 2006) and shifted so that the C IV line occurs at 1549 Å. The counts were then corrected for the extraction aperture and sensitivity, using the detector response function calculated from observations of PG1322+659 in April 2005 by Larsen et al. (2006). Any degradation in the detector sensitivity in the 10 years between those observations and our own observations is unaccounted for and may lead to underestimating the flux.

2.2.3 Optical Spectroscopy

2.2.3.1 SOAR Goodman Observations

We used the Goodman High Throughput Spectrograph (GHTS; Clemens et al. 2004) on the 4.1m SOAR telescope to obtain high-resolution spectroscopy of the CVSO 114 visual pair. In order to obtain spectra for both components we oriented the slit at PA=$42°$.

For determining the velocity width of the Hα line profile, we used 2100 g/mm grating in Littrow mode, centered at 650nm, with the $0.46''$ slit, and the spectroscopic 1×1 region of interest, which provides the native pixel scale of $0.15''$/pixel. This configuration provided a wavelength range of $\sim 630\,\text{Å}$ with a resolution $\mathrm{R} \sim 14000$, equivalent to $\sim 22\,\mathrm{km\,s^{-1}}$. All the basic data reduction was done with the standard routines in the `ccdproc` package in IRAF. The processed individual 2-D spectra in each mode were then median-combined, and finally extracted to 1-D spectra and wavelength calibrated using the `apextract` package in IRAF.

2.2.3.2 MagE Observations

We observed CVSO 1335 using the Magellan Echellette (MagE) instrument (Marshall et al. 2008) on the Magellan Baade Telescope at the Las Campanas Observatory in Chile. The instrument is a medium resolution spectrograph with wavelength coverage of 3200 Å - 1 μm. We used the $1.0''$ slit, providing a spectral resolution of R$\sim$4100. The data were reduced using the MagE Pipeline in the Carnegie Observatories' CarPy package (Kelson 2003; Kelson et al. 2000). We calibrated the flux with spectrophotometric standards observed on the same night at comparable airmass. The flux calibration was performed in IRAF. Here, we present two Hα profiles of CVSO 1335 observed 24h apart. The full MagE spectra of this and other sources are analyzed in Thanathibodee et al. (2019b).

2.2.3.3 M2FS Observations

As part of our program for obtaining Hi-Res observations of a large number of the CVSO stars, we observed CVSO-114SW with the Michigan/Magellan Fiber System (M2FS; Mateo et al. 2012) on the Magellan Clay telescope at Las Campanas Observatory in Chile on the night of 2014 December 10. The instrument was configured in the Hi-Res Echelle mode, with a custom made Hα/Li filter, that isolates orders 53 and 54, covering a wavelength range from 6528 Å to 6791 Å. We used the 75μm slit and 1×2 binning, providing a resolution R$\sim$ $44,500$ (or $\sim$ $7\,\mathrm{km\,s^{-1}}$). Exposures were processed with a combination of custom Python scripts and an IRAF-based pipeline. The processed individual exposures were median-combined into a final frame, on which the spectral extraction and wavelength calibration was performed.

2.2.4 NIR Spectroscopy

To probe for magnetospheric accretion using the He I λ10830 line, we observed the targets with the FIRE spectrograph (Simcoe et al. 2013) on the Magellan Baade telescope at the Las Campanas Observatory in Chile. The CVSO 114 visual pair was first observed on 2014. Subsequent to the HST observation, the instrument was used again to observe CVSO 114NE and CVSO 1335. For both observing runs, the $0.6''$ slit was used. This offers a resolution of R$\sim$6000 in the NIR and can resolve velocities of $\sim$ $50\,\mathrm{km\,s^{-1}}$. We reduced the data using the FIRE reduction pipeline with telluric standard stars and calibration frames taken on the same observing night. Since the wavelength solution of the pipeline is in vacuum wavelength, we converted it to the air wavelength using the equations described in Morton (2000).

Table 2.2. The Magnitudes of CVSO 114 Visual Pair from SOAR Photometry

Band	CVSO 114NE	CVSO 114SW
g	16.68 ± 0.06	14.97 ± 0.03
r	15.65 ± 0.04	13.79 ± 0.04
i	14.41 ± 0.03	12.99 ± 0.03
z	13.70 ± 0.04	12.61 ± 0.04

2.2.5 SOAR Adaptive Optics Imaging

The CVSO 114 visual pair was not resolved in the original CVSO photometry, so we obtained high angular resolution imaging of the pair using the Southern Astrophysical Research telescope (SOAR) Adaptive Optics Module (SAM; Tokovinin et al. 2016). SAM contains a $4K \times 4K$ CCD imager covering a $3' \times 3'$. We used the standard 2×2 binning, yielding a scale of $0.091''$/pixel. We obtained images in the SDSS g, r, i and z filters. The data were reduced with custom Pyraf routines that do the bias subtraction and flat field correction, and we used the 2MASS catalog to derive an astrometric solution for each frame. We calibrated the photometric zero point using photometry for stars in each field from the SDSS DR10. Table 2.2 shows the derived magnitudes.

2.3 Analysis and Results

2.3.1 Stellar Parameters

We took spectral types and reddening corrections for the targets from the CVSO survey (Briceño et al. 2019). All the sources are consistent with $A_V = 0$. We used Table 6 in Pecaut & Mamajek (2013) to get effective temperatures and bolometric corrections, and 2MASS (Skrutskie et al. 2006) J magnitudes to get the stellar luminosities. We determined stellar masses using the Siess et al. (2000) evolutionary tracks. The derived values are shown in Table 2.3.

2.3.2 Spectral Energy Distributions

The spectral energy distribution (SED) gives information about the presence and distribution of dust in the disk. To relate disk properties to the evidence of accretion, we constructed SEDs for the targets, shown in Figure 2.1. The CVSO, and VISTA photometry are taken from Briceño et al. (2019), the Spitzer IRAC and MIPS photometry from Hernández et al. (in preparation), and the Herschel PACS photometry from Maucó et al. (2018). We also include photometry from 2MASS (Skrutskie et al. 2006) and WISE (Wright et al. 2010). We used Pecaut & Mamajek

Table 2.3. Stellar Parameters

CVSO	SpT	A_V (mag)	J (mag)	$L_\star$ ($L_\odot$)	$M_\star$ ($M_\odot$)	$R_\star$ ($R_\odot$)	d (pc)
114NE	M1.5	0.0	12.0	0.24	0.38	1.30	314 ± 11
1335	K5	0.0	11.5	0.66	0.87	1.58	375 ± 6
114SW	K7	0.0	11.2	0.61	0.68	1.65	325 ± 5

(2013) pre-main sequence stellar colors, scaled at the J magnitude, to construct the photosphere for comparison.

The SED of CVSO 114NE shows excess relative to the photosphere in the near-IR and mid-IR, indicating the presence of optically thick dust emission close to the star. In contrast, CVSO 1335 shows no excess in the near-IR. The SED of this star traces the K5 photosphere up to $\lambda \sim 10\ \mu$m, where the emission from the dust starts to appear. The emission is consistent with the median of Taurus at longer wavelengths. This indicates that CVSO 1335 has a transitional disk, in which the inner regions have been mostly cleared of small dust, while still hosting an outer disk (Espaillat et al. 2014). Finally, the SED of CVSO 114SW only shows a small excess over the photosphere at WISE bands 3 and 4.

2.3.3 Accretion Indicators

2.3.3.1 Hα

We assessed the accretion state of the targets using the equivalent widths of the Hα line and the profiles of Hα and the He I λ10830 line. Table 2.4 lists the values of the equivalent widths of the Hα line, EW(Hα), of the targets as well as the width at 10% height of the Hα emission feature (10%-width; W_{10}). The corresponding Hα line profiles are shown in the top row of Figure 2.2. For comparison, we also show in Table 2.4 the Hα equivalent widths from Briceño et al. (2019), estimated from low resolution spectra.

Both the values of the EW(Hα) and the width of the line W_{10} in Table 2.4 indicate that CVSO 114NE and CVSO 114SW can be classified as CTTS and WTTS, respectively, based on the criteria in White & Basri (2003).

The classification is more complicated for CVSO 1335. For its spectral type of K5, the threshold values between CTTS and WTTS in White & Basri (2003) are EW(Hα) $\sim$ 3 Å and $W_{10} \sim 270$ $\mathrm{km\,s^{-1}}$, although these values are very uncertain since they are based on essentially one veiled star. Nonetheless, the values of EW(Hα) (Table 2.4) indicate that the star varies between actively accreting to marginally accreting. However, inspection of the line profiles in Figure 2.2 give a

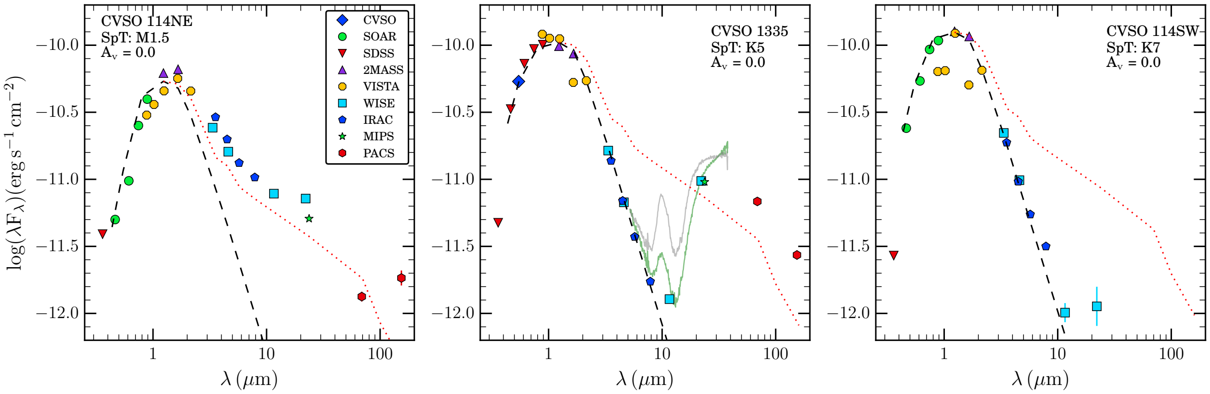

Figure 2.1 Spectral energy distributions of CVSO 114NE, CVSO 1335, and CVSO 114SW. The dashed lines are the photospheric SEDs constructed from Pecaut & Mamajek (2013) colors scaled at the J magnitude of the target. The dotted red line is the median SED of Taurus from Maucó et al. (2016). CVSO 114NE shows excess over the photosphere even in the near-IR, indicating optically thick dust emission close to the star. CVSO 1335 has a transitional disk with no NIR excess but conspicuous excess beyond 10 μm. Plotted in light grey along with CVSO 1335 is the SED of GM Aur scaled to the same WISE band 2 flux. The SED of CVSO 1335 does not have a significant flux around $\sim$ 10 μm, suggesting that it lacks the small grains responsible for the conspicuous silicate feature at $\sim$ 10 μm in GM Aur. Its optically thin gap may be filled with larger, $\sim$2 μm grains such as that of CS Cha; the Mid-IR spectrum of which is scaled and shown here in light green. CVSO 114SW may still have an outer disk as it shows excess in the WISE bands 3 and 4. The SED of CVSO 114NE is also reported by Maucó et al. (2018). The IR spectroscopic data of GM Aur and CS Cha are from NASA/IPAC Infrared Science Archive.

more clear picture of what is happening. The Hα profiles of CVSO 1335 show strong redshifted absorption components, indicating that it was accreting at all the epochs it was observed. The absorption can get to be so strong that it overwhelms the emission, effectively decreasing the equivalent width. The redshifted absorption also complicates the measurement of W_{10}. To better define the emission profile, we subtracted the spectrum of 61 Cyg A, a K5V star, from that of CVSO 1335. The standard star spectrum was taken from the Gaia FGK Benchmark Stars library (Blanco-Cuaresma et al. 2014) and it is shown on the left panel of Figure 2.3, together with the spectra of CVSO 1335. The right panel of Figure 2.3 shows the photosphere-subtracted Hα profiles of CVSO 1335. As shown, the emission beyond the main redshifted absorption is very variable and complex, making the measurement of W_{10} very uncertain. We give two measurements of the W_{10} for CVSO 1335 in Table 2.4. One corresponds to the measurement of the main blue emission; the other includes the red wing, except for the MagE-20171130 profile, in which the red emission is weaker than 10% of the peak flux (Figure 2.3).

2.3.3.2 He I $\lambda10830$

Evidence for magnetospheric accretion is given by a redshifted absorption superimposed on the bright emission of the He I λ10830 line at velocities of the order of the free-fall velocity. For comparison, we calculated the free-fall velocities of each target using the stellar masses and radii, and a truncation radius of R_i = 5 $R_\star$ (Calvet & Gullbring 1998). These velocities are shown in Table 2.4.

For CVSO 114NE, the He I λ10830 profiles show a prominent He I emission at the star's rest velocity as well as conspicuous, redshifted absorption components in both epochs of observations. The maximum velocity of the redshifted absorption, $\sim$ +300 $\mathrm{km\,s^{-1}}$, is consistent with the free-fall velocity of 300 $\mathrm{km\,s^{-1}}$, indicating that magnetospheric accretion is taking place.

The He I λ10830 line profiles of CVSO 114NE shown in Figure 2.2 are remarkably similar, despite being separated by two years. The velocity at the minimum of the redshifted absorption, $v_s \sim 150$ $\mathrm{km\,s^{-1}}$, and the extension of the wing of the redshifted absorption, $v_{max} \sim 300$ $\mathrm{km\,s^{-1}}$, as well as the velocity of the blueshifted absorption, $v_b \sim -240$ $\mathrm{km\,s^{-1}}$, are similar between the two epochs of observation, indicating a fairly steady accretion flow. Nonetheless, although the strength and the width of the emission features are similar in both epochs, the absorption features have slightly different depths and widths. The depth of the redshifted absorption changes by $\sim$ 10% between the two epochs, with a slightly smaller change for the blueshifted absorption. As shown in Figure 2.2, the redshifted absorption is stronger when the blueshifted absorption is weaker. The seesawing behavior seems to preclude stellar continuum changes as the cause of the variability, since if this was the case both lines would change similarly. The varying depth of the absorption features may arise from differences in density or temperature of the flow (Fischer et al. 2008), and/or of mass accretion rate (Costigan et al. 2014).

The He I λ10830 profile of CVSO 1335 shows some emission and an unambiguous redshifted absorption. The absorption component is shallow but broad with a minimum at $v_s \sim 240\,\mathrm{km\,s^{-1}}$ and a wing extending to $v_{max} \sim 490\,\mathrm{km\,s^{-1}}$. This extension is $\sim$20% higher than the free-fall velocity of 410 $\mathrm{km\,s^{-1}}$ (Table 2.4). Fischer et al. (2008) found that the He I λ10830 line did not extend beyond the escape velocity for their sample, except in one case that they attributed to incorrect stellar parameters. The discrepancy for CVSO 1335 may be similarly due to uncertainties in the placement of the continuum or in the stellar parameters. The redshifted absorption component seems to be the superposition of two absorption components, one strongest at $\sim$ +30 $\mathrm{km\,s^{-1}}$ and another at $\sim$ +240 $\mathrm{km\,s^{-1}}$. Following Fischer et al. (2008), this can be interpreted as a combination of redshifted absorption of stellar continuum at low velocities and of the veiling continuum at high velocities by the diluted accretion flow. The presence of the low velocity redshifted absorption component may indicate a high inclination, as it is required for viewing the low-velocity flow against the star. This is also seen in the modeling results in Fischer et al. (2008), in which the strong absorption shifts closer to $v = 0$ as the inclination increases.

CVSO 114SW does not show any detectable He I emission nor redshifted absorption. The presence or absence of the redshifted absorption of the He I $\lambda10830$ line for all the targets are consistent with the accretion classification provided by the profiles of Hα.

2.3.4 Mass Accretion Rates

In addition to the determination of the accretion state, the Hα line can be used to estimate mass accretion rates, using empirical relationships from the literature. We used the relationship between $L_{H\alpha}$ and $\dot{M}$ from Ingleby et al. (2013), estimating $L_{H\alpha}$ from the EW(Hα) and the continuum flux at 6563 Å, which in turn we obtained from the SDSS r magnitude. We also used the relationship between W_{10} and $\dot{M}$ from Natta et al. (2004). The derived values are shown in Table 2.4. The values of $\dot{M}$ determined from the EW(Hα) and W_{10} are consistent for CVSO 114NE. However, they can vary by almost three orders of magnitude in CVSO 1335, depending on the indicator and the value of W_{10} adopted.

2.3.5 H_2 Excess Luminosity

The presence of gas in the inner disk close to the star can be probed using the H_2 features in the FUV. It is difficult to detect these features in the low resolution ACS/SBC spectra; however, Ingleby et al. (2009) found that the excess around 1600 Å, likely due to electron-impact excitation, could be detected in CTTS, even in SBC spectra. Excess in the 1420-1520 Å region, due to Lyα fluorescence, could be detected in some cases.

In order to determine the presence of excess flux at 1600 Å, we first determined a template spectrum for non-accreting stars, the WTTS, to use as reference. We calculated this template using the ACS/SBC FUV spectra of non-accreting WTTSs from Ingleby et al. (2009) and Ingleby et al. (2012). The spectra were corrected for reddening using A_V from the original papers, smoothed, and finally normalized to the same flux in the range of $1700 - 1800$ Å. The median of the normalized WTTS spectra was then calculated and used as template. For each of our three stars, we scaled the template to the minimum flux between 1660-1740 Å to avoid an unidentified emission feature at $\sim$1750 Å. The FUV spectra of the targets and the scaled median WTTS spectrum are shown in the lower row of Figure 2.2. The spectrum of CVSO 114NE shows only a marginal excess over the median WTTS in the $1575 - 1625$ Å and $1420 - 1520$ Å region. CVSO 114SW shows even less excess. CVSO 1335 shows a conspicuous excess over the WTTS in both spectral regions.

To quantify our determinations, we calculated, separately, the stellar flux and the template flux

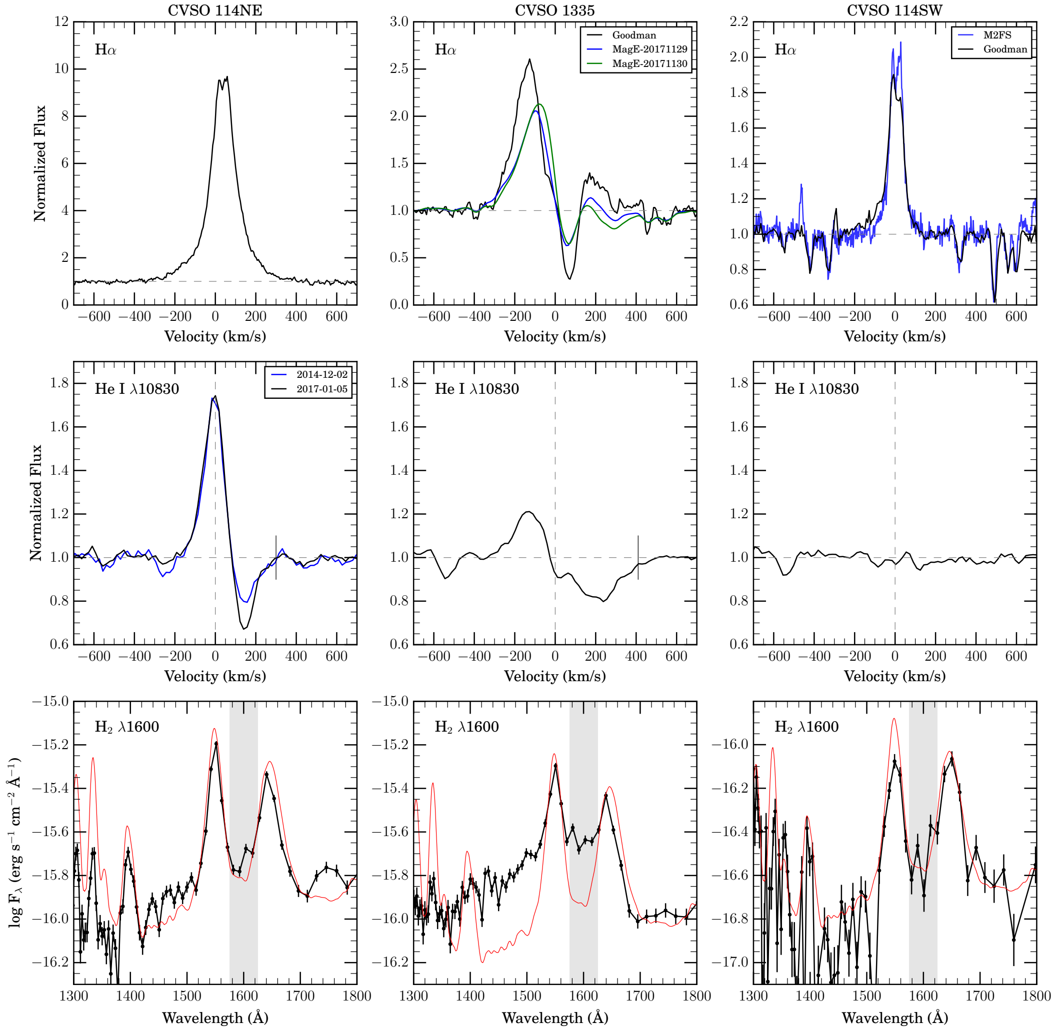

Figure 2.2 Inner disk gas and accretion indicators for CVSO 114NE, CVSO 1335, and CVSO 114SW.
Top: High resolution optical spectra of the Hα feature. CVSO 1335 shows weak, but very broad emission, superimposed by a strong redshifted absorption component. CVSO 114NE shows strong emission and wide wings. CVSO 114SW exhibits weaker emission profile with narrow wings. The profile seems to change between the Goodman observation (black) and M2FS observation (blue). *Middle:* ACS/SBC FUV spectra in the 1600 Å region. The median spectrum of non-accreting WTTS from Ingleby et al. (2009, 2012) is also shown (red line). The H_2 excesses are calculated over the $1575 - 1625$ Å region (gray shade). CVSO 1335 shows clear excess over the median WTTS in the shaded region and 1420-1520 Å region, whereas CVSO 114NE and CVSO 114SW show only marginal excess. *Bottom:* FIRE spectra showing the He I λ10830 line. The black vertical bar in the left and middle panels shows the free-fall velocity of the star. While CVSO 114SW does not exhibit any significant He I feature, CVSO 114NE and CVSO 1335 show conspicuous emission and redshifted absorption. CVSO 114NE shows variability in the redshifted absorption features from two epochs of observations, as well as weak blueshifted absorption.

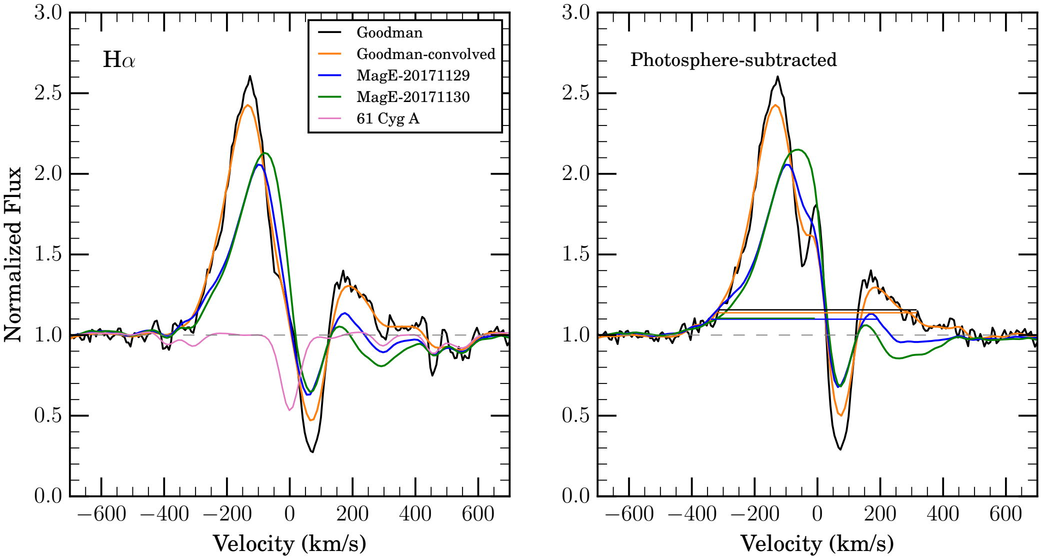

Figure 2.3 Hα profiles of CVSO 1335. The left panel shows all medium resolution spectra of CVSO 1335. For comparison, the orange line shows the Goodman spectrum convolved to the resolution of the MagE spectra. In pink, the spectrum of 61 Cyg A, a K5 main sequence star, is shown. The spectrum is convolved from R∼65000 to R∼4100, comparable to the resolution of MagE. The right panels show the Hα features after photospheric subtraction. The horizontal lines show the 10% level of the peak of the profiles.

from their respective monochromatic fluxes f_λ as

$$F = \int_{1575\text{Å}}^{1625\text{Å}} f_\lambda \mathrm{d}\lambda. \tag{2.1}$$

We then calculated the H_2 excess luminosity as

$$\mathrm{L}_{\mathrm{H}_2} = 4\pi d^2 \left(F_{\text{star}} - F_{\text{wtts}}\right), \tag{2.2}$$

where F_{wtts} is the scaled template and d is the distance to the star.

The uncertainties in this calculation arise from the placement of the template spectrum relative to the stellar spectrum and from the uncertainty in each data point from the reduction process. To estimate this uncertainty, we assumed that the flux f_λ for each data point is an independent random variable with a normal distribution N(x, σ), where x and σ are the measured flux and the uncertainty from the reduction pipeline, respectively. For each of the 10000 realizations, the flux for each data point was randomized from the normal distribution, resulting in the spectrum over the FUV range. We then calculated the integrated flux using eq.(2.1). The mean and the standard deviation of the mean (SDOM) of the stellar flux and the template flux were then used to calculate

Table 2.4 Measured & Derived Properties

CVSO	EW_{H_α}	W_{10}[a]	$\dot{M}$-EW	$\dot{M}$-W_{10}	L_{H_2}	Σ_{H_2}	v_{ff}[b]	v_s[c]	v_{max}[d]
	(Å)	($km\,s^{-1}$)	(10^{-10} $M_\odot\,yr^{-1}$)		(10^{-6} $L_\odot$)	(10^{-6} $g\,cm^{-2}$)	($km\,s^{-1}$)		
114NE					$\lesssim 3.79 \pm 0.02$	$\lesssim 7.4$	300	150	300
LowRes	37.5	···	2.4	···					
Goodman	35.2	350	2.3	3.2					
1335					23.00 ± 0.02	> 18.2	410	238	490
LowRes	9.1	···	7.0	···					
Goodman	5.6	277/626	4.1	0.63/1500					
MagE[e]	3.8	310/531	2.7	1.30/180					
MagE[f]	4.3	310	3.0	1.30					
114SW					$\lesssim 0.72 \pm 0.01$	$\lesssim 3.2$	354	···	···
LowRes	2.5	···	< 0.9	···					
M2FS	1.6	158	< 0.5	< 0.04					
Goodman	1.8	187	< 0.6	< 0.08					

[a] Two measurements show the ambiguity of the placement of the profile's red wings.
[b] Free-fall velocity.
[c] Velocity at which the He I λ10830 absorption is strongest.
[d] Maximum velocity of the He I λ10830 redshifted absorption.
[e] UT2017-11-29.
[f] UT2017-11-30.

the H_2 luminosity using eq.(2.2).

To evaluate the significance of the measurements, we compared the mean stellar flux F_{star} with the standard deviation of the calculated template flux SD(F_{wtts}). We found that only the H_2 luminosity measurement of CVSO 1335 is significant at the 3σ level. We report the H_2 luminosity for the targets in Table 2.4, with the measurements for the CVSO 114 visual pair as upper limits.

Following Ingleby et al. (2009), we calculated the disk H_2 surface density from the H_2 luminosity, assuming that the 1600 Å feature is due to electron-impact excitation. This is given by

$$\Sigma_{H_2} = \frac{2m_H}{R}\left(\frac{z L_{H_2}}{\pi h\nu\sigma_{1600}\Delta\lambda v \chi_e}\right)^{1/2}, \tag{2.3}$$

where m_H is hydrogen mass, R and z are the radius and height of H_2 emitting region, respectively, $h\nu$ is the photon energy at 1600 Å, σ_{1600} is the H_2 cross section to electron impact at this wavelength, $\Delta\lambda$ is an assumed width of the 1600 Å feature, v is the impacting electron velocity, and χ_e is the electron fraction. As in Ingleby et al. (2009), we adopt R = 1 AU, z = 0.1 AU, $\sigma_{1600} = 10^{-20}$ cm^2 Å^{-1}, $\chi_e = 5 \times 10^{-3}$, and electron kinetic energy of 12 eV. We take $\Delta\lambda$ = 1625 Å − 1575 Å = 50 Å. The results are shown in Table 2.4. Following the discussion in Ingleby et al. (2009), we report the calculated Σ_{H_2} as a lower limit. Since the L_{H_2} detections of the CVSO 114 pair are not significant, we report their Σ_{H_2} as upper limits.

2.4 Discussion

We report observations of three $\sim$5 Myr old T Tauri stars obtained in ground- and space-based observatories to characterize and evaluate their accretion state. The stars seem to be in different stages of protoplanetary disk evolution at the same age, and we discuss them in detail here.

2.4.1 CVSO 114NE

Detailed modeling of the SED of CVSO 114NE indicates that the star is surrounded by an accretion disk, with dust as close to the star as 0.07 AU (Maucó et al. 2018). Inside this radius, dust sublimates but gas continues moving in until it reaches the magnetospheric radius, from which it falls onto the star along the accretion streams that give rise to the clear signatures of accretion seen in this star. Given the kinematic evidence for accretion, one would reasonably assume that there is still gaseous material in the inner disk feeding the accretion streams. However, the FUV spectrum of CVSO 114NE shows essentially no excess over the WTTS median either around 1600 Å or shortward of the 1548 Å C IV line. The accretion luminosity of CVSO 114NE, $L_\star = GM_\star\dot{M}/R_\star \sim 3 \times 10^{-3} M_\odot\,\mathrm{yr}^{-1}$, is lower than that of most of the CTTS observed previously with the ACS (Ingleby et al. 2009), so the H_2 emission maybe below the detection limit. However, for FP Tau, a star only slightly cooler than CVSO 114NE, with an accretion luminosity of $\sim 1 \times 10^{-3} M_\odot\,\mathrm{yr}^{-1}$, clearly shows excess over the WTTS even at ACS/SBC resolution (Ingleby et al. 2009).

The weakness of the H_2 FUV emission may arise from occultation effects. Marginal detection due to occultation could be possible if the gas is distributed asymmetrically. Axial asymmetries have been observed on larger scales ($>\sim 15$ AU) in AB Aur by ALMA using ^{12}CO J = $2-1$ (Tang et al. 2017), where the disk has spiral arms. However, it is unclear if this is the case on a small scale in this star. In any event, stellar occultation of the H_2 emitting region necessitates high inclination. For example, an inclination of 75° is needed to hide the region within $\sim 4R_\star$. Highly inclined disks can also absorb FUV radiation. For instance, Schneider et al. (2015) find that the flux at around 1600 Å can change by a factor of 5 during several epochs in the case of AA Tau ($i \sim 75°$). However, the He I emission line profiles seem to suggest low inclinations. The peak of the emission is at the stellar rest velocity, suggesting a geometry such that the He I emission region in accretion flows has low radial velocity. The line profile modeling of Fischer et al. (2008) indicates that the He I λ10830 emission peak moves blueward and the absorption minimum moves closer to the stellar rest velocity as inclination to the line of sight increases. This suggests that CVSO 114NE, in which the He I λ10830 minimum is at $\sim$0.5 v_{ff}, is unlikely to be at high inclination.

Finally, we consider the possibility that CVSO 114NE is a spectroscopic binary. If this is the case then it could resemble the AK Sco system, in which a reduction of 10% in the Lyα excited H_2 at periastron was interpreted in terms of increased Lyα optical depth in the accretion stream (Gómez de Castro et al. 2016).

To shed some light on the perplexing properties of CVSO 114NE, multi-epoch, higher resolution FUV spectroscopy is needed to examine the Lyα and X-ray variability via H_2 line emission, as well as near-IR spectroscopy to follow the accretion variability. In addition, optical spectroscopy monitoring is required to explore the possibility of the star being a spectroscopic binary.

2.4.2 CVSO 1335

Both the H_2 FUV spectrum and the Hα and He I λ10830 lines indicate that CVSO 1335 is actively accreting gas from the inner disk onto the star. The main issue with this object is the value of the mass accretion rate. As discussed in §2.3.4, there is a large discrepancy between values of $\dot{M}$ determined from the luminosity and from the 10%-width of the Hα line. The later estimator is generally considered more accurate (White & Basri 2003), but in this case, the actual value of W_{10} is difficult to determine. Nonetheless, analysis of the line profiles shows that the line is very broad at all epochs of observation, despite the variability of the red emission wing of the line (Figure 2.3), and the 10%-width is of the order of $\sim 600\,\mathrm{km\,s^{-1}}$, which would correspond to an accretion rate of $\sim 10^{-7} M_\odot\,\mathrm{yr}^{-1}$ according to the Natta et al. (2004) calibration. However, if this was the case, the accretion luminosity of CVSO 1335 would be of the order of 2.5 $L_\odot$, about 4 times the stellar luminosity (Table 2.4), resulting in a heavily veiled spectrum. In contrast, the agreement of the optical and near-IR fluxes of CVSO 1335 with the photospheric fluxes (Figure 2.1) and the presence of absorption lines consistent with the standard (Figure 2.3) indicate a very low veiling in CVSO 1335. Moreover, the accretion luminosity expected from the H_2 luminosity of CVSO 1335 would be $\sim 0.05 L_\odot$ from the data of Ingleby et al. (2009), which would correspond to $\dot{M} \sim 3 \times 10^{-9} M_\odot\,\mathrm{yr}^{-1}$. This conflicting evidence is more likely due to the unreliability of the calibration of empirical indicators such as the 10%-width, which is based on higher accretors in which Hα profiles are more symmetric and redshifted absorptions are not typically seen. Detailed modeling of the line profiles and the accretion shock emission are required to obtain a more accurate estimate of the mass accretion rate in this object.

In contrast to CVSO 114NE, CVSO 1335 shows no near-IR excess over the photosphere (Figure 2.1.) As discussed in §2.3.2, CVSO 1335 is surrounded by a transitional disk, that is, an optically thick disk truncated at some radius from the star, with a small amount of optically thin dust coexisting with the gas inside the cavity (Espaillat et al. 2014). This is the second transitional disk analyzed in the CVSO survey, after the 10 Myr CVSO 224 in Ori Ob1a (Espaillat et al. 2008). Determining the physical properties of the disk is beyond the scope of this Chapter, but we can get some insight by comparing the SED of CVSO 1335 to that of other transitional disks. For reference, in Figure 2.1 we have added the IRS spectra of two other stars surrounded by transitional disks, GM Aur and CS Cha, scaled to the same photospheric flux as CVSO 1335. These stars have masses comparable to CVSO 1335, and therefore are expected to have comparable disk dissipation timescales (Hernández et al. 2005; Carpenter et al. 2006; Kennedy & Kenyon 2009; Ribas et al. 2015). GM Aur is located in the 1-2 Myr Taurus association and has a spectral type of K3 and a mass of 1.2 $M_{\odot}$ (Calvet et al. 2005). CS Cha is in the 2.5 Myr old Cha I association, with a spectral type of K6 and a mass of 0.9 $M_{\odot}$ (Espaillat et al. 2007). In both stars, the outer disk is truncated at tens of AU and the silicate emission arises from dust in an optically thin region inside the cavity (Calvet et al. 2005; Espaillat et al. 2007). Although we lack mid-IR spectroscopy for CVSO 1335, we can compare its fluxes in WISE bands 3 and 4 to those of GM Aur and CS Cha; WISE band 3, which is wide enough to encompass the silicate feature, is particularly informative. We find that the mid-IR fluxes of CVSO 1335 are consistent with the IRS spectrum of CS Cha, and about a factor of 10 lower than GM Aur. This is interesting because grains in the optically thin region of CS Cha have grown to a size of $\sim 2\mu$m without smaller grains (Espaillat et al. 2007), while in GM Aur the size distribution is similar to the ISM, with grain sizes between 0.005 μm and 0.25 μm. The maximum size is also larger than the ISM in CVSO 224, the other transitional disks analyzed in the CVSO survey (Espaillat et al. 2008), leading to the speculation that dust evolution has already taken place in these 5-10 Myr populations. Nevertheless, the absence of sub-μm dust grains in CVSO 1335, similarly to CS Cha, may suggest a more rapid dust evolution in its mass range, since the smallest grains are still present in older, but lower stellar mass, transitional disks with substantial grain growth such as TW Hya (Calvet et al. 2002) and CVSO 224 (Espaillat et al. 2008).

2.4.3 CVSO 114SW

CVSO 114SW is a WTTS as it has a weak and narrow Hα profile. The absence of emission or redshifted absorption of He I λ10830 profile strengthens the classification of the star as non-accreting. Although the SED of the star is essentially photospheric in the near-IR, there seems to be some excess in WISE bands 3 and 4 (Figure 2.1), which would indicate that the star hosts a debris disk. Using the Cieza et al. (2013) criterion, the star can be classified as a warm debris disk since it has mid-IR excess and is not accreting.

2.5 Summary & Conclusions

We probe the inner gas disk and accretion properties of three, 5 Myr, T Tauri stars from the CVSO survey at various stages of the dust evolution. We summarize our conclusions as follow:

1. At 5 Myr, diverse states of accretion are found, and they seem to be independent of the state of dust evolution or the stellar mass. This implies that this evolution may be slightly stochastic and proceed in diverse ways.

2. CVSO 114NE shows a very low level of H_2 in the inner disk, and yet its Hα and He I λ10830 profiles indicate that it is still actively accreting. A non axially symmetric geometry for the inner disk and/or a highly inhomogeneous accretion flows leading to variability could potentially explain this perplexing situation. Future observation using multi-phase higher resolution spectroscopy, and more detailed modelings may shed some light into this peculiar finding.

3. CVSO 1335 has significant amount of gas in the inner disk, as indicated by the H_2 $\lambda1600$ flux. Similarly, the Hα and He I λ10830 profiles clearly show that it is accreting, although the accretion indicators give inconclusive values for $\dot{M}$. It hosts a transitional disk, which has cleared the small dust from the inner disk, as shown by weak emission in the NIR. The similarity of the flux in the WISE 3 band between CVSO 1335 and the transitional disk around CS Cha, a star of comparable mass and thus similar disk dissipation time scale, suggests that as in CS Cha, grains in the inner disk have grown to a single $\sim$ μm size. Comparison with transitional disks of different stellar masses and ages suggests a trend of lack of sub-μm grains for higher stellar masses, but larger samples need to be studied to confirm this suggestion.

4. CVSO 114SW has no excess of H_2 $\lambda1600$ over median WTTS, suggesting that there is essentially no gas left in the inner disk. This agrees with Hα and He I λ10830 diagnostic showing that the star is not accreting. The evidence of some IR excess suggests that the star may have a debris disk.

5. Among three accretion indicators discussed in this Chapter, EW(Hα) is the least sensitive, unable to diagnose a star conclusively as an accretor. While the presence of the redshifted absorption feature of the line conclusively suggests that a star is accreting, it complicates the measurement of $\dot{M}$ using traditional metrics such as EW and W_{10}. Detailed modeling of the origin of the redshifted absorption of Hα is needed to solve this problem.

6. The redshifted absorption in the He I λ10830 line proves to be a very sensitive probe of accretion. It is a promising accretion indicator to study the low accretors, since veiling

and/or filling by emission is less problematic than the profiles in CTTS with high $\dot{M}$ (Fischer et al. 2008). However, the link between the profile morphology and quantitative estimates of accretion is still incomplete. In many cases, the line profile is also time-dependent (e.g., Fischer et al. 2008). In future studies, a more exhaustive exploration of parameter space, as well as physical modeling (e.g., Kurosawa et al. 2011), are needed.

CHAPTER 3

Complex Magnetospheric Accretion Flows in the Low Accretor CVSO 1335

This chapter was originally published in the Astrophysical Journal, Volume 884, 86 (2019), in collaboration with Nuria Calvet, James Muzerolle, César Briceño, Ramiro Franco Hernández, and Karina Maucó. It is adapted and reproduced here under the non-exclusive rights of re-publication granted by the American Astronomical Society to the authors.

Abstract

Although the magnetospheric accretion model has been extensively applied to T Tauri Stars with typical mass accretion rates, the very low accretion regime is still not fully explored. Here we report multi-epoch observations and modeling of CVSO 1335, a 5 Myr old solar mass star which is accreting mass from the disk, as evidenced by redshifted absorption in the Hα profile, but with very uncertain estimates of mass accretion rate using traditional calibrators. We use the accretion shock model to constraint the mass accretion rate from the Balmer jump excess measured with respect to a non-accreting template, and we model the Hα profile, observed simultaneously, using magnetospheric accretion models. Using data taken on consecutive nights, we found that the accretion rate of the star is low, $4 - 9 \times 10^{-10}$ M$_\odot$ yr^{-1}, suggesting a variability on a timescale of days. The observed Hα profiles point to two geometrically isolated accretion flows, suggesting a complex infall geometry. The systems of redshifted absorptions observed are consistent with the star being a dipper, although multi-band photometric monitoring is needed to confirm this hypothesis.

3.1 Introduction

Low-mass pre-main sequence stars, or T Tauri stars (TTS), are formed surrounded by disks and evolve accreting mass from these disks. The accretion of the material from the inner region of protoplanetary disk onto the star follows the magnetospheric accretion paradigm (Hartmann et al. 2016). Under this framework, gaseous material, heated by the stellar radiation field and other processes, flows along the magnetic field lines onto the star, creating an accretion shock at the base of the flow. The emission from the accretion shock is observed as an excess over the stellar photosphere (Calvet & Gullbring 1998). Emission lines form in the magnetospheric accretion flows, so that the kinematics of the flow can be inferred from the line profiles. Numerical simulations of magnetized stars (e.g., Romanova et al. 2003) as well as magnetospheric accretion models (Hartmann et al. 1994; Muzerolle et al. 1998a, 2001; Kurosawa et al. 2011) have confirmed this picture for accreting T Tauri stars(Classical T Tauri star; CTTS) and have provided insight into the physical properties of accretion, including the geometry of the flows.

One of the most important properties of accretion is the mass accretion rate $\dot{M}$. This can be estimated by either directly measuring the excess over the photosphere and inferring the accretion luminosity, $\mathrm{L_{acc}} = \mathrm{GM_\star \dot{M}/R_\star}$, or by using emission lines. Specifically, the excess flux over the photosphere can be extracted from the optical flux by measuring the veiling of photospheric absorption lines and measured directly in the UV (e.g., Ingleby et al. 2013). The accretion luminosity can then be measured using accretion shock models (Calvet & Gullbring 1998; Robinson & Espaillat 2019), or slab models (e.g., Gullbring et al. 1998; Herczeg & Hillenbrand 2008; Manara et al. 2016; Alcalá et al. 2017), to fit the excess and account for the flux outside the wavelength regions where the excess is observed. Emission lines have been used to infer the mass accretion rate via empirical relationships between the line luminosity or line width and the accretion luminosity (Muzerolle et al. 1998b; Natta et al. 2004; Calvet et al. 2004; Ingleby et al. 2013; Alcalá et al. 2014). These relationships have been calibrated with direct measurements of accretion luminosity from the excess over the photosphere, obtained simultaneously in many cases. A more direct method to measure accretion rates from emission lines is by modeling the line profiles with magnetospheric accretion models. This has been done for hydrogen Balmer lines (Muzerolle et al. 2001; Natta et al. 2004; Espaillat et al. 2008), Na D line (Muzerolle et al. 2001), and He I λ10830 line (Fischer et al. 2008; Kurosawa et al. 2011). Modeling emission lines also provides information about accretion geometry.

Finding the method that best estimates the mass accretion rates is especially relevant for the stars with the lowest accretion rates, the *low accretors*. Population studies show that the mass accretion rate scales with stellar mass (e.g., Muzerolle et al. 2003; Herczeg & Hillenbrand 2008; Alcalá et al. 2014; Manara et al. 2015), suggesting that a mass range is implied when a star is designated as a low accretor. For example, the current detection limit of mass accretion for solar-mass star is $\sim 10^{-10}\, M_\odot\, \mathrm{yr}^{-1}$ (Ingleby et al. 2013; Manara et al. 2013), whereas this accretion rate is not unusual for mid-M type stars (e.g., Alcalá et al. 2017).

As expected from viscous evolution of protoplanetary disks, the mass accretion rate onto the star decreases with time (Hartmann et al. 1998). Studies of many star-forming regions also show that the frequency of accretors, as well as the frequency of disk-bearing T Tauri stars, in a given population decreases as the age of the population increases (Fedele et al. 2010; Hernández et al. 2008; Briceño et al. 2019). However, it is unclear how accretion proceeds at very low accretion rates and how it finally stops. To understand processes occurring at the last stages of accretion it is necessary to carry out systematic studies of T Tauri stars accreting at very low accretion rates. This is the main motivation for our ongoing observational and modeling program to search and characterize low accretors.

As the initial result of our study of low accretors, we presented the characterization of the inner disk of three 5 Myr T Tauri stars in Thanathibodee et al. (2018). One target, CVSO 1335, was particularly interesting. The star is a pre-main sequence solar analog with $\mathrm{M}_\star = 0.87\,M_\odot$, $\mathrm{R}_\star = 1.58\,R_\odot$, and spectral type of K5. The star, located in the 5 Myr old Ori OB1b subassociation (Briceño et al. 2019), is a CTTS, based on the presence of redshifted absorption in the He I λ10830 line. Thanathibodee et al. (2018) (Chapter 2) showed that the protoplanetary disk surrounding the star is gas-rich, as indicated by fuorescent FUV H_2 emission, while the spectral energy distribution indicates that it is a transitional disk with a gap depleted of small dust. That work also showed that the star had complex Hα line profiles in several epochs, which complicated the measurement of its mass accretion rate. The accretion rates determined with different indicators differed by more than 3 orders of magnitude. The lower range of the measured mass accretion rate at $\sim 10^{-10}\,M_\odot\,\mathrm{yr}^{-1}$ would suggest that the star is a low accretor for its mass. The disagreement between the accretion diagnostics and the complex features in Hα, especially the persistent low-velocity redshifted absorption which is found in AA Tau-like stars (e.g., Bouvier et al. 2007; Fonseca et al. 2014) and other dippers (e.g., Alencar et al. 2018), makes this star an ideal target for a detailed study of accretion properties in low accretors.

Here we report the observations and the characterization of the accretion rate and the accretion geometry in the low accretor CVSO 1335. Optical spectra of the star are presented in Section 3.2, with the analysis and modeling in Section 3.3. The implication of the model results are presented in Section 3.4 with a summary in Section 3.5.

3.2 Observations

The analysis of the Hα line in Thanathibodee et al. (2018) was based on observations with the moderate-resolution (R$\sim$4100, 73 $\mathrm{km\,s^{-1}}$) MagE Spectrograph on the 6.4m Magellan Baade telescope at the Las Campanas Observatory in Chile, as well as the high-resolution (R$\sim$14000, 22 $\mathrm{km\,s^{-1}}$) Goodman Spectrograph on the CTIO SOAR Telescope. The MagE spectrograph covers the full optical range from 3200-8200Å, giving access to the Balmer jump.

Table 3.1. Summary of Observations

Instrument	Start Date (UT)	Exp. time (sec)	Airmass	SNR[a]
Goodman	2017 Sep 18[b]	3×600	1.22	35
MagE	2017 Nov 27	3×600	1.75	290
	2017 Nov 28	3×600	1.14	260
	2017 Nov 29[b]	2×900	1.14	280
	2017 Nov 30[b]	600+900	1.14	260

[a] Signal-to-noise at 6560 Å.

[b] Reported in Thanathibodee et al. (2018) and Chapter 2.

We report here additional spectra observed on 2017 November 27 and 28, which we reduced similarly to the MagE spectra reported in Thanathibodee et al. (2018). In total, we have four MagE spectra observed in consecutive nights, and one Goodman spectra observed about two months earlier. Table 3.1 shows the details of all observations of CVSO 1335.

The top panel of Figure 3.1 shows the optical spectra of CVSO 1335 observed with the MagE spectrograph. Several emission lines are presented in the spectra, including the hydrogen Balmer lines and the Ca H & K doublet. We do not detect the O I $\lambda6300$ in the MagE spectra, suggesting that the stellar or disk wind is very weak in the system, and the contrast between the line and the continuum could be low for a K5 star. The lower panel in Figure 3.1 shows the corresponding Hα profiles from the MagE and Goodman spectra, as well as other emission lines. To remove the photospheric contribution from the O I lines and the chromospheric and photospheric contributions from the H I lines, which are generally found in active young stars (Manara et al. 2013, 2017a), we subtracted the line profile of RECX 1, a standard non-accretor (Weak T Tauri star; WTTS), from the CVSO 1335 profiles. The standard star has similar stellar parameters as those of CVSO 1335 (SpT=K5-6, M$_\star = 0.9\,M_\odot$, R$_\star = 1.8\,R_\odot$, age~5-9 Myr), so its spectrum can be used to represent the underlining photospheric and chromospheric emission of the target (Ingleby et al. 2011b). The spectrum of RECX 1 was obtained by the UVES spectrograph and was retrieved from the ESO archive. We convolved the UVES spectrum down to the resolution of the MagE and Goodman spectrographs before subtraction.

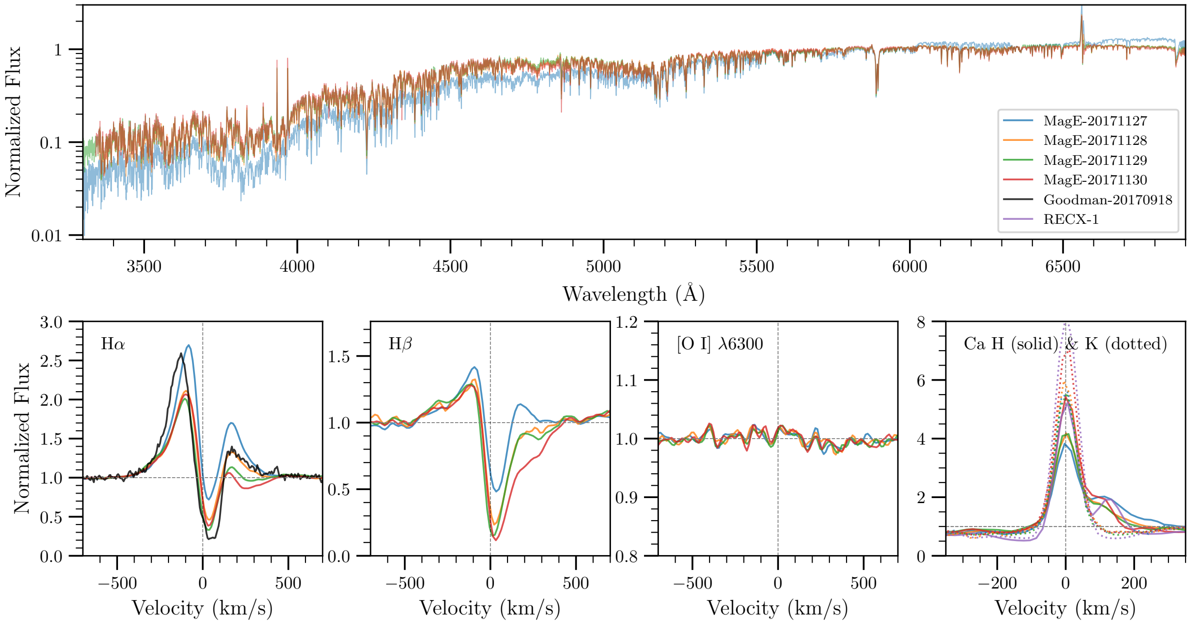

Figure 3.1 Spectra and emission line profiles of CVSO 1335. *Top:* Optical spectra of CVSO 1335 observed with the MagE spectrograph (R∼4100). The spectra are normalized to unity at ∼6000Å. *Bottom:* Profiles of the Hα, Hβ, O I lines, and the Ca II HK doublet. We also include a high resolution Hα profile observed by the Goodman spectrograph (R∼14000). For the hydrogen lines, the chromospheric contribution have been subtracted by the convolved spectrum of RECX 1, a non-accretor observed by UVES. The hydrogen Balmer lines shows complex and variable features, in particular a low-velocity redshifted absorption. This absorption is especially strong for the Hβ line observed on the last 3 epochs. The O I λ6300 lines show no detection. The Ca II lines are symmetric, showing minimal variation in epochs separated by 1 day, and increases in strength on 20171130. The emission to the right of the Ca II H line is from Hϵ. The Ca II lines of RECX 1 are comparable to those of CVSO 1335 observed on 20171130.

3.3 Analysis and Results

Using the data in §3.2, we carry out detailed modeling to determine mass accretion rates in CVSO 1335 at the different epochs of observations, and estimate its accretion geometry.

3.3.1 Accretion Shock Model

We use accretion shock models from Calvet & Gullbring (1998) to measure the mass accretion rate. This model is based on an assumption that the accretion flow is a cylindrical column in which the material flows vertically onto the stellar surface. At the height where the ram pressure of the flow and the thermodynamic pressure of the stellar photosphere are equal, an accretion shock occurs in which the kinetic energy of the flow is released. Approximately half of the X-rays emitted from the shock are absorbed by the material in the incoming flow, the *pre-shock*, and the rest by the *post-shock* region and the stellar photosphere below the shock. Energy reprocessed by these regions emerges as the shock emission. The input parameters of the model are the stellar mass, radius, and effective temperature, the energy flux of the accretion column, and the filling factor (Calvet & Gullbring 1998). In general, the energy flux F determines the spectral slope around the Balmer jump, while the filling factor f, the fraction of the stellar surface area covered in the accretion flow, influences the strength of the Balmer jump.

To compare the predictions of the model with the observations, we need to add the shock emission to a photospheric+chromospheric template for the star's spectral type. Since TTS are magnetically active, their chromospheric emission may be significant in the UV region for the low accretors (Ingleby et al. 2013). We use the spectrum of the non-accreting T Tauri star RECX 1 (Ingleby et al. 2013) as the template for the stellar photosphere+chromosphere. We used the low-resolution X-shooter spectra of the star, taken from the ESO Archive, for this analysis. Finally, the model spectra are generated by adding the spectral template, the pre-shock, the post-shock, and the heated photosphere.

We created a grid of models varying the energy flux F between $1.0 \times 10^{10} - 9.0 \times 10^{11}\,\mathrm{ergs\,cm^{-2}\,s^{-1}}$ and the filling factor f between 0.05 and 2.05$\%$ to find the best fit to the observed spectra. Since the seeing during the observation was higher than the size of the slit, we expected some uncertainty in the absolute flux level. Without simultaneous photometric measurement during the MagE observation, we assumed that the optical spectra were approximately constant as we did not observe an evidence of optical veiling nor did we expect any such veiling in such a low accretor. Therefore, we adjusted the flux level of all spectra to correspond to the star's SDSS r' magnitude. With this uncertainty, we assumed a conservative estimate of the flux calibration in the UV part at the 10$\%$ level.

To determine if there is a detection of the Balmer jump due to the accretion shock, in addition to that from the chromosphere, we calculated the integrated flux in the spectral range $3300 - 5000\,\text{Å}$ of the observed spectra and compared the measurements with the integrated fluxes of spectra in our grid of shock models. We found that the predicted fluxes were higher than the observed fluxes in all models, but the excess was within the 10$\%$ uncertainty of the flux measurement for a set of models with low accretion rates. Nevertheless, these results suggest that there is no detection of the accretion shock contribution to the Balmer jump in all of our observations and that the jump is mainly chromospheric as is the case in the template WTTS. Therefore, we estimate an upper limit of the mass accretion rate by adopting the highest accretion rate among the models with predicted flux within 10$\%$ of the observed one. Figure 3.2 shows the models with the highest accretion rates of which the fluxes are still consistent with the measurement. Table 3.2 shows the upper limits to the mass accretion rates for each epoch. These limits allow for the possibility of accretion

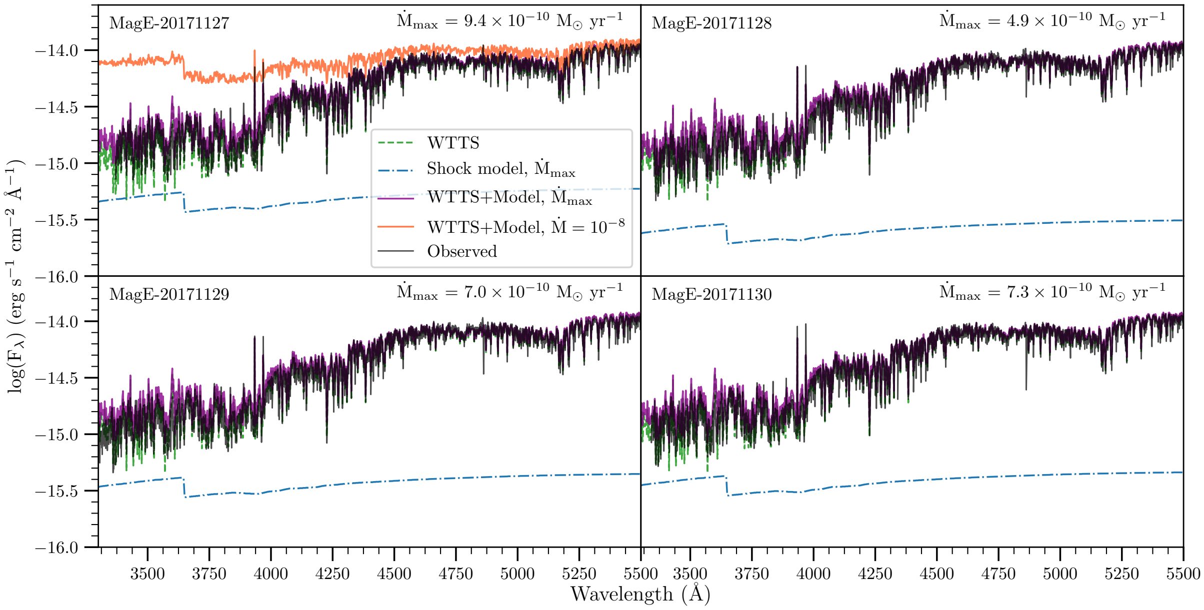

Figure 3.2 The results from the accretion shock model of four MagE spectra of CVSO 1335. The observed spectra are normalized to the star's SDSS i' magnitude. No significant excess over the non-accretor standard is detected in all of the spectra. Upper limits are calculated assuming 10% uncertainty in the flux and photometric calibration. For comparison, the orange line shows the model of the star at the mass accretion rate of $1.0 \times 10^{-8}\, M_\odot\, \mathrm{yr}^{-1}$, a typical accretion rate for T Tauri stars.

variability on a daily timescale.

3.3.2 Magnetospheric Accretion Model

To estimate the mass accretion rates and the geometry and properties of the accretion flows we modeled the profiles of Hα with magnetospheric accretion models from Muzerolle et al. (2001). The model is described in Hartmann et al. (1994); Muzerolle et al. (1998a, 2001), and here we summarize the main assumptions. The model assumes that the geometry of the magnetospheric accretion flows is axisymmetric, following the dipole magnetic field, with the magnetic pole aligned to the stellar and Keplerian disk rotation poles, assumed to be the same. Material flows toward the star inside the boundary controlled by the magnetic dipole geometry and specified by the innermost radius of the disk R_i and the width at the base of the flow W. The mass flow is steady and set by the total mass accretion rate $\dot{M}$. The temperature at each point in the flow is a free parameter, and each model is specified by the maximum temperature in the flow $T_{\max}$. The models use the extended Sobolev approximation to calculate mean intensities, which in turn are used to calculate radiative rates in the statistical equilibrium for the level populations of a 16-level hydrogen atom

Table 3.2. Results of Accretion Shock Models

Obs. Date UT	$\dot{M}_{\text{shock}}$ ($10^{-10}\,M_{\odot}\,\text{yr}^{-1}$)	$\log(\text{L}_{\text{acc}}/\text{L}_{\odot})$	$\log(\text{L}_{\text{acc}}/\text{L}_{\star})$
20171127	$\lesssim 9.39$	$\lesssim -1.37$	$\lesssim -1.19$
20171128	$\lesssim 4.93$	$\lesssim -1.65$	$\lesssim -1.47$
20171129	$\lesssim 7.04$	$\lesssim -1.49$	$\lesssim -1.31$
20171130	$\lesssim 7.27$	$\lesssim -1.48$	$\lesssim -1.30$

(Muzerolle et al. 2001). The line flux is determined by using a ray-by-ray method, in which the specific intensity and the total optical depth at each ray are calculated at a given inclination i. The final Hα line profile is calculated from the spatially integrated specific intensity.

We calculated a large grid of models with parameters covering ranges shown in Table 3.3. The ranges of parameters are chosen to cover all possible values based on previous parametric exploration of Muzerolle et al. (2001). In particular, they found that as $\dot{M}$ decreases, T_{max} needed to be increased in order to reproduce the observation; T_{max} between 10k and 12k is required for $\dot{M}$= $10^{-9}\,M_{\odot}\,\text{yr}^{-1}$. We adopted this range for our modeling since the expected mass accretion rate is lower than this value, based on the accretion shock model. To compare the line profile results with the observations, we convolved the model profiles with the instrumental profile of the spectrograph and use the χ^2 statistics to determine the best fit for each observation.

We show examples of fitting line profiles using the standard model in Figure 3.3. First, we attempted to fit the Hα profile for night 20171130 using the entire velocity range of the line. The best fit, shown on the left panel, could not reproduce the the multiple emission and absorption components in the line profiles. Therefore, we attempted to fit each component in the line profile separately.

To fit the low-velocity redshifted absorption component of the line, we selected the model that gave the best fit to observations in the velocity range of 0-150 $\text{km}\,\text{s}^{-1}$. Qualitatively, we found that models with low mass accretion rates, large magnetospheres, high inclinations, and high temperatures could reproduce the narrow absorption component at $\sim$ 75 $\text{km}\,\text{s}^{-1}$. We then created a grid of models with parameters suitable for exploring these ranges of parameter space. The ranges and the value of the parameters are shown in Table 3.3, and an example of the best fit model for these parameters are shown in the center panel of Figure 3.3.

For the rest of the line profile with the standard model, excluding the 0-150 $\text{km}\,\text{s}^{-1}$ region, we found that the best fit models tended to favor higher accretion rates, small magnetospheres, high inclinations, and high temperatures. We therefore created another set of models to explore these

Table 3.3. Range of Model Parameters

Parameters	Min.	Max.	Step
Standard Model			
$\dot{M}$ ($10^{-9}\,M_\odot\,\mathrm{yr}^{-1}$)	0.1	9.0	0.1, 1.0
R_i ($\mathrm{R}_\star$)	2.2	5.4	0.4
W ($\mathrm{R}_\star$)	0.8	2.0	0.4
T_max (K)	10000	12000	250
i (deg)	10	85	5
Small Magnetosphere			
$\dot{M}_\mathrm{in}$ ($10^{-10}\,M_\odot\,\mathrm{yr}^{-1}$)	1.0	9.5	0.5
$R_\mathrm{i,in}$ ($\mathrm{R}_\star$)	1.4	3.8	0.4
W_in ($\mathrm{R}_\star$)	0.2	0.6	0.2
$T_\mathrm{max,in}$ (K)	11000	12000	200
i_in (deg)	55	85	5
Large Magnetosphere			
$\dot{M}_\mathrm{out}$ ($10^{-10}\,M_\odot\,\mathrm{yr}^{-1}$)	1.0	9.5	0.5
$R_\mathrm{i,out}$ ($\mathrm{R}_\star$)	5.5	8.0	0.5
W_out ($\mathrm{R}_\star$)		0.3, 0.5, 1.0, 1.5	
$T_\mathrm{max,out}$ (K)	11000	12000	200
i_out (deg)	65	85	5

parameters, shown in Table 3.3. By excluding the low-velocity redshifted absorption from the fit, the model could fit the wings of the line, including the redshifted absorption component near the free-fall velocity ($\sim 200\ \mathrm{km\,s^{-1}}$). Shown in the right panel of Figure 3.3 is an example of the best fit for the small magnetosphere.

The general trend from these fits is that the components of the Hα line profile could be reproduced using low mass accretion rate, high temperature, and high inclination.

3.3.3 Modified Magnetospheric Accretion Model

3.3.3.1 Computations with the new geometry

To fit the entire line profile, we modified the magnetospheric accretion model to include two magnetospheric flows in concentric shells; the *inner flow* resembles a small magnetosphere, and the *outer flow* corresponds to a larger magnetosphere covering the entire accretion structure. A schematic drawing of the new geometry is shown in Figure 3.4. We also slightly modify the calculation of the line profile. For a given inclination, the standard model calculates the emerging

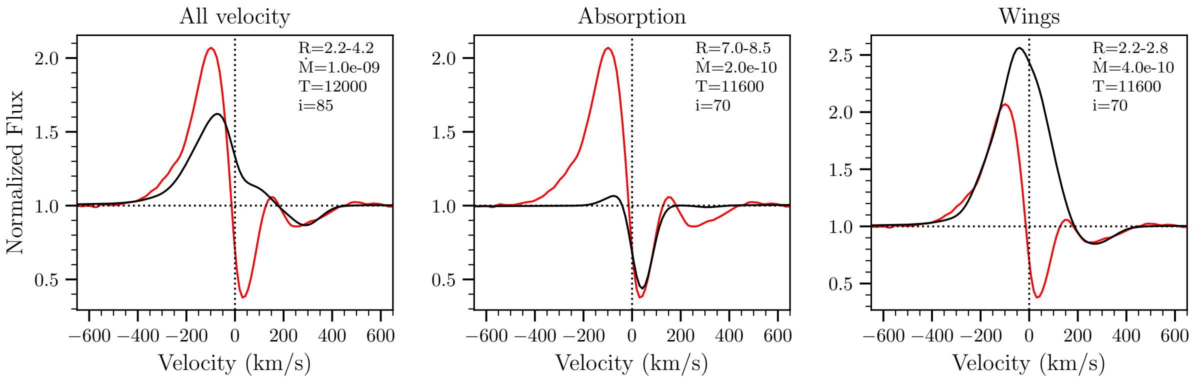

Figure 3.3 Best fits for the Hα line using the standard magnetospheric accretion model. The convolved model line profiles are shown in black, while the observations, taken from 20171130, are shown in red. *Left:* The best fit for the entire velocity range range. The model could not reproduce the observation. *Center:* The best fit model for the low-velocity redshifted absorption using a large magnetosphere and a low accretion rate. *Right:* The best fit model for the entire line profile, excluding the low-velocity redshifted absorption. The profile can be reproduced with a small magnetosphere and a slight increase in the mass accretion rate.

specific intensity $I_{\nu,p,q}$ and the total optical depth $\tau_{\nu,p,q}$ at each location in the projected coordinate system (p,q) on the sky. To calculate the composite profile with both magnetospheric flows, we assume that the flows are geometrically separated and the source function and level populations of each flows are independent. For the inner flow, the specific intensity includes the emission from the stellar photosphere and the accretion shock, which is absorbed by the accreting material, and the emission from the flow itself. The emission from the outer flow includes only that from the accretion flow. The total emission map of the entire geometry is then given by

$$\mathcal{I}_{\nu,total} = \exp(-\mathcal{T}_{\nu,outer}) \cdot \mathcal{I}_{\nu,inner} + \mathcal{I}_{\nu,outer}, \tag{3.1}$$

where $\mathcal{I}$, $\mathcal{T}$ are 2D maps of the specific intensity and optical depth, respectively. Finally, the model line flux is calculated as

$$F_\nu = \iint \mathcal{I}_{\nu,total}\, dp\, dq. \tag{3.2}$$

It is computationally impractical to compute the profile from all possible combinations of all small flows and large flows. For each observed profile, we selected 100 best fits for the small and large magnetosphere models, as outlined above. Even though the large magnetosphere could physically be similar in all epochs, the 100 best-fit model profiles of the magnetosphere could be different from epoch to epoch. This is because the depth and shape of the low-velocity redshifted absorption, to which the large magnetosphere models are fitted, still depend on the strength of the emission from the small magnetosphere, especially when that emission is strong. Assuming

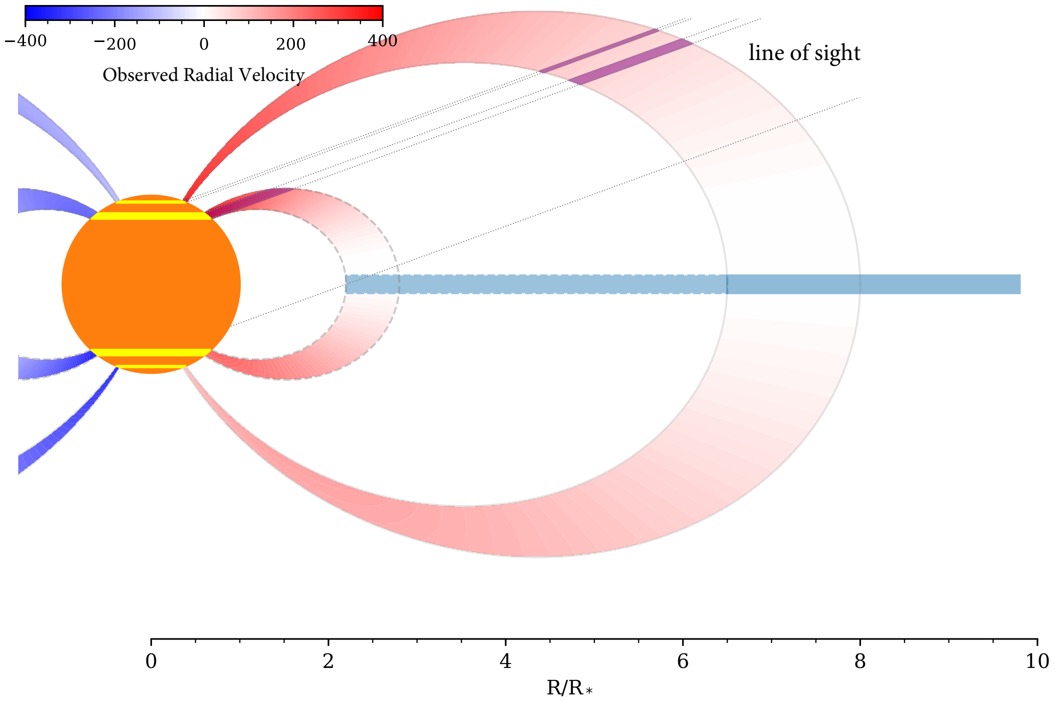

Figure 3.4 The side view schematic of the geometry of the modified magnetospheric accretion model. The material flows from the gas disk onto the star along two geometrically separated, axisymmetric flows. The inner flows originates from $\sim$ 2.5 R$_\star$ and the outer flow, covering the entire geometry, originates at $\sim$ 7 R$_\star$. The color at each point in the flow represents the relative velocity of the emission from that point as view from an observer at the inclination of 70°.

that the large magnetospheres are similar, which is supported by the persistent nature of the low-velocity component, we produced a global best fit of the large magnetosphere by combining the 100 best fits from each observed model. The final model line profiles for each observed profiles are then calculated by the combination of the 100 best fits of the small magnetosphere and the global best fits of the large magnetosphere.

We selected the best fits in each step using the minimization of χ^2, given by

$$\chi^2 = \sum_i \frac{(F_{\mathrm{obs},i} - F_{\mathrm{model},i})^2}{F_{\mathrm{obs},i}}, \tag{3.3}$$

where i indexes over the pixels in the observed spectra in relevant velocity ranges. In addition, we have experimented with other fitting methods including Root Mean Square Error (RMSE), the Mean Absolute Deviation (MAD), and the Mean Absolute Percentage Error (MAPE) of each models. The mean and the standard deviation of the first 100 best fits of these statistics are very similar to those using the χ^2 fit, suggesting that the choice of statistical tools does not affect the general results.

3.3.3.2 General Results for Hα

Figure 3.5 shows the χ^2 best fit model for each of the five Hα observations. Our two-shell models are able to qualitatively reproduce the observed profiles in all epochs. Table 3.4 shows the mean and standard deviation of model parameters from the first 1000 χ^2 best fits for each observed profile. These model profiles are qualitatively similar.

For both inner and outer flows the models requires high temperatures, with $T_{\max} \sim 11000\,\mathrm{K}$. The inclination for the outer flow is fairly constant at $\sim 70°$, while that of the inner flows vary slightly. Similarly, the mass accretion rates for the outer flow are quite steady at $\sim 2 \times 10^{-10}\, M_{\odot}\,\mathrm{yr}^{-1}$, while the accretion rates for the inner flow are somewhat more variable. These results suggest that the inner flow and the outer flow are slightly misaligned, and the outer flows are more stable than the inner flows.

The corotation radius R_c, outside which mass cannot accrete onto the star, is an absolute upper limit of the size of the magnetosphere. As a consistency check, we calculate R_c of the star, assuming that the disk plane is aligned with the equatorial plane of the stellar rotation. Since the rotation period of the star is still undetermined, we use the measured projected rotational velocity $v\sin(i)$ of the star as a proxy. In this case, the corotation radius is given by

$$R_c = (GM)^{1/3} \left(\frac{R_\star \sin(i)}{v \sin(i)} \right)^{2/3}, \tag{3.4}$$

where i is the inclination of the system. With $v\sin(i) = 11.5\ \mathrm{km\,s^{-1}}$ based on APOGEE results (J. Hernandez, private communication), we found that $R_c \sim 8.9\,R_\star$ for $i = 70°$. This is consistent with the model results for the outer flows (Table 3.4) and suggests that the infall originates close to the stellar corotation radius.

We calculated the residual of the model from the observation (Figure 3.5, lower panel), and found that the model systematically over-predicts some emission on the red side of the profile at $\sim 100\ \mathrm{km\,s^{-1}}$. This may indicate that the absorption component of the model is not extended enough, suggesting that there is additional absorbing material that is not accounted for.

3.3.3.3 Testing the Model with Hβ

To test the consistency of the two-shell model, we applied the modeling set up to the Hβ lines observed simultaneously with Hα. We found that, similarly to the case of Hα, the one-flow geometry could not reproduce the Hβ observations. We therefore followed the procedure outlined in §3.3.3.1 to model the Hβ lines.

Figure 3.6 shows the best fits of the four Hβ profiles. The models are able to qualitatively reproduce the observation in all epochs. However, the models cannot entirely fit the strong low-

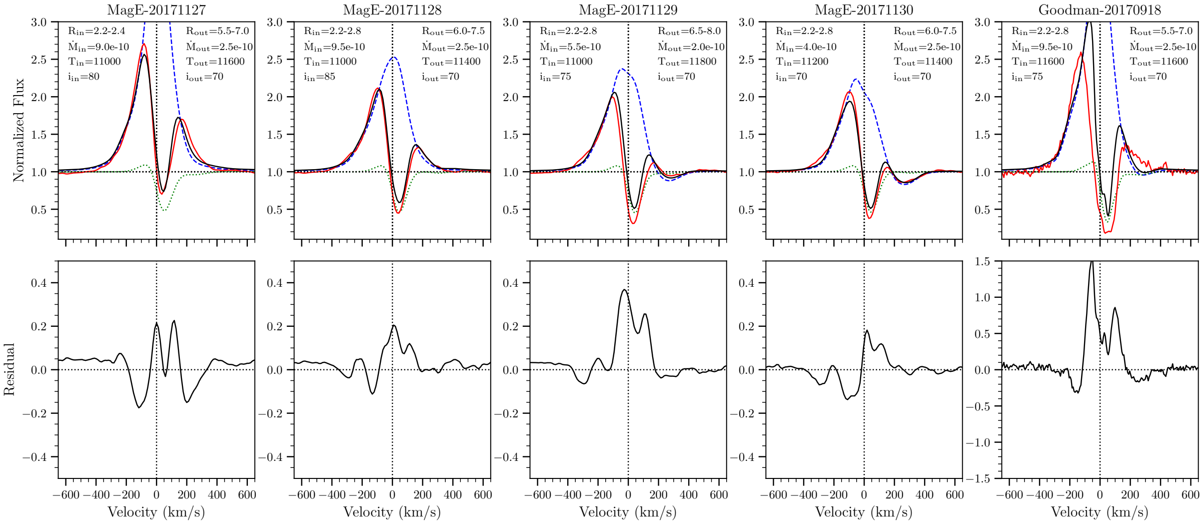

Figure 3.5 The best fits from the modified magnetospheric accretion model for Hα. The top row shows the comparisons between the observed profiles (red) and the convolved model profiles (black). The green dotted lines and the blue dashed lines are the flux from the outer and inner flows, respectively. The bottom row shows the residual between the observed and the model profile ($F_{\rm model} - F_{\rm obs}$). Our model with two accretion flows can qualitatively reproduce the observed line profiles in all epochs, spanning several months. The model has some difficulty fitting the Goodman spectra, possibly due to its higher resolution that the model could not account for. However, the general results are clear that multiple flows are required to fit the profile. Evidently, the model is missing some absorption component at $\sim 100\ \rm km\,s^{-1}$, which may indicate even more complex geometry.

velocity redshifted absorption in three epochs, suggesting that extra absorbing material is needed. As shown in Table 3.4, the geometries, temperatures, and inclinations of both the inner flows and the outer flows for Hβ are consistent with those of Hα. In fact, Hβ profiles calculated using the parameters that produce the best fits for Hα show two redshifted absorption components as seen in the observed Hβ profiles and the best fit profiles. This seems to indicate that the global properties of the flows derived from both lines are similar. However, in the best-fit models for Hβ the mass accretion rates in the outer flows for Hβ are slightly higher than those for Hα, and the opposite is found for the inner flow. In addition, the discrepancy between the accretion rates in the inner flows and outer flows become smaller for Hβ. This could indicate that Hα and Hβ are formed in a slightly different region in the accretion flows with different filling factors, or it could indicate deviations in the temperature distribution assumed in our model.

3.3.3.4 Model Limitation

Stellar winds and disk winds may be present in accreting stars surrounded by protoplanetary disks. In fact, high-sensitivity and high spatial resolution observation have shown the presence of neutral

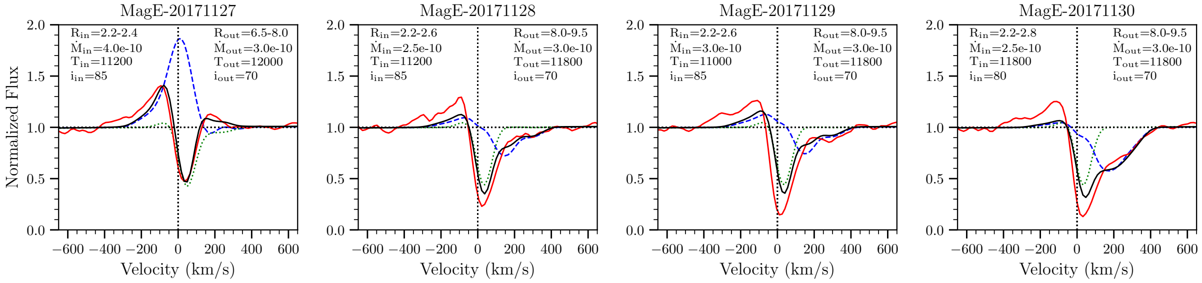

Figure 3.6 The best fits from the modified magnetospheric accretion model for Hβ. The legends are the same as in Figure 3.5. The modified geometry qualitatively reproduced the observation in all epoch, especially the emission and the high-velocity redshifted absorption. The deviation between the model and the observation at the low-velocity redshifted absorption is more prominent for this line compared to the Hα line models.

hydrogen emission component from an extended region close to the central accreting stars, which is likely to be from winds (Gravity Collaboration et al. 2017; Koutoulaki et al. 2018). Our magnetospheric accretion model does not include a wind component, but we do not expect a significant contribution of the line emission from winds, since the mass accretion rate is low (Muzerolle et al. 2001).

Another limitation of the model is based on the axisymmetric assumption. Simulations (Romanova et al. 2003, 2004) have shown that the accretion flow is generally not axisymmetric and the magnetic pole is likely not aligned to the rotation axis. However, without a measurement of the magnetic properties of CVSO 1335, a parametric study using MHD simulations would be prohibitively expensive. Our model allows a parametric study with a significantly smaller resources requirement.

Lastly, the model assumes only a strictly dipolar geometry, which is likely not the case for more evolved T Tauri stars such as CVSO 1335. However, adding a complex flow prescription would add more parameters to the study and the model would lose its generality. By keeping the geometry simple, we can make simple inferences about the relationship between the parameters in the model.

Table 3.4 Results of the Modified Magnetospheric Accretion Model

Spectrum	$\dot{M}_{\rm in}$ ($10^{-10}\,M_{\odot}\,{\rm yr}^{-1}$)	$R_{\rm i,in}$ ($\rm R_{\star}$)	$W_{\rm in}$ ($\rm R_{\star}$)	$T_{\rm max,in}$ (10^4 K)	$i_{\rm in}$ (deg)	$\dot{M}_{\rm out}$ ($10^{-10}\,M_{\odot}\,{\rm yr}^{-1}$)	$R_{\rm i,out}$ ($\rm R_{\star}$)	$W_{\rm out}$ ($\rm R_{\star}$)	$T_{\rm max,out}$ (10^4 K)	$i_{\rm out}$ (deg)
Hα										
Goodman-20170918	8.2±1.4	2.2±0.0	0.4±0.1	1.15±0.03	72±3	2.4±0.4	5.8±0.5	1.5±0.1	1.14±0.03	70±0
MagE-20171127	7.9±1.7	2.2±0.1	0.2±0.0	1.15±0.04	75±8	2.4±0.4	5.9±0.5	1.5±0.1	1.14±0.03	70±0
MagE-20171128	8.8±0.6	2.2±0.0	0.6±0.1	1.15±0.03	85±1	2.3±0.6	6.4±0.9	1.5±0.1	1.14±0.03	71±2
MagE-20171129	5.3±1.0	2.2±0.0	0.6±0.1	1.14±0.03	77±3	2.4±0.5	6.6±0.9	1.5±0.1	1.14±0.03	70±1
MagE-20171130	5.2±1.9	2.1±0.2	0.6±0.0	1.14±0.03	69±4	2.3±0.4	6.3±0.8	1.5±0.1	1.15±0.03	70±0
Hβ										
MagE-20171127	3.1±1.5	2.2±0.0	0.2±0.0	1.13±0.03	72±14	3.5±0.7	6.8±0.8	1.5±0.1	1.15±0.03	70±0
MagE-20171128	3.6±1.2	2.2±0.0	0.5±0.1	1.14±0.03	85±0	3.5±0.7	7.1±0.8	1.5±0.1	1.15±0.03	71±2
MagE-20171129	3.9±1.1	2.2±0.0	0.5±0.1	1.14±0.03	85±0	3.5±0.8	7.0±0.9	1.5±0.1	1.15±0.03	71±2
MagE-20171130	3.9±1.0	2.0±0.2	0.6±0.0	1.15±0.04	82±2	3.5±0.8	7.1±0.9	1.5±0.1	1.15±0.03	71±2

3.3.4 Effects of Inclination and Mass Accretion Rate

Given that there are some similarities of the Hα and Hβ line profiles of CVSO 1335 to those of dipper stars such as AA Tau (Bouvier et al. 2007, see §3.4.2), it is insightful to explore the effects that could change the observed line profiles while keeping the two-flow geometry, especially in assessing the frequency of a type of profile. In Figure 3.7, we show Hα profiles using the two-flow geometry with parameters similar to the average results in Table 3.4 but changing the inclination and the total mass accretion rate. Specifically, we selected $\mathrm{R_{i,in}} = 2.2\,\mathrm{R_\star}$, $\mathrm{W_{in}} = 0.6\,\mathrm{R_\star}$, with constant ratio of mass accretion rate between the inner and outer flow $\dot{M}_{\rm in}/\dot{M}_{\rm out}$=3. For the model with high $\dot{M}$, we also calculated the profiles with a slightly lower temperature ($T_{\rm max,in}$=10000 K and $T_{\rm max,out}$=11000 K, compared to 11400 K and 11600 K for the fiducial model). We found that the low-velocity redshifted absorption (v$\lesssim$ $100\,\mathrm{km\,s^{-1}}$) only appears in models with low total accretion rates in moderate to high inclination, $i \gtrsim 65°$, in agreement with our findings in §3.3.2. The velocity of the deepest absorption moves closer to the line center as the inclination increases. On the other hand, the high velocity redshifted absorption (v$\gtrsim$ $200\ \mathrm{km\,s^{-1}}$) appears in almost all inclinations at low accretion rates, and the velocities of such absorptions are fairly constant. There is some degree of degeneracy between the mass accretion rate and temperature, as models with lower temperature and higher accretion rate are similar to those with higher temperature and lower accretion rate (e.g., green dashed line and black solid line in Figure 3.7).

Figure 3.8 shows the Hα line profiles with the same parameters as those in Figure 3.7, but with a constant $\dot{M}_{\rm out} = 2\times10^{-10}\,M_\odot\,\mathrm{yr^{-1}}$ while varying the $\dot{M}_{\rm in}$ from 3×10^{-10} to $3\times10^{-9}\,M_\odot\,\mathrm{yr^{-1}}$. Interestingly, the low-velocity redshifted absorption appears conspicuously regardless of the mass accretion rate of the inner flow. This suggests that the outer flow could be responsible for a significant amount of emission if the accretion rate is high enough, as in Figure 3.7. The outer flow acts as an absorber only in a very low accretion regime ($\sim 2-4\times10^{-10}\,M_\odot\,\mathrm{yr^{-1}}$).

3.4 Discussion

3.4.1 Measuring Mass Accretion Rates in Low Accretors

As we have shown in §3.3.1, the mass accretion rate of CVSO 1335 could be variable, with an upper limit of the order of $\sim 4-9\times10^{-10}\,M_\odot\,\mathrm{yr^{-1}}$. These estimates disagree with the mass accretion rate measurements using traditional methods such as the full width at the 10% height ($\mathrm{W_{10}}$; Natta et al. 2004). In a previous study (Thanathibodee et al. 2018), we calculated the accretion rate of CVSO 1335 using the $\mathrm{W_{10}}$ method and found that the accretion rates should be of the order of $10^{-8}-10^{-7}\,M_\odot\,\mathrm{yr^{-1}}$ to account for the width of the Hα line. To account for the presence of the redshifted absorption, we estimated $\mathrm{W_{10}}$ by measuring the half-width on the blue side, in which no

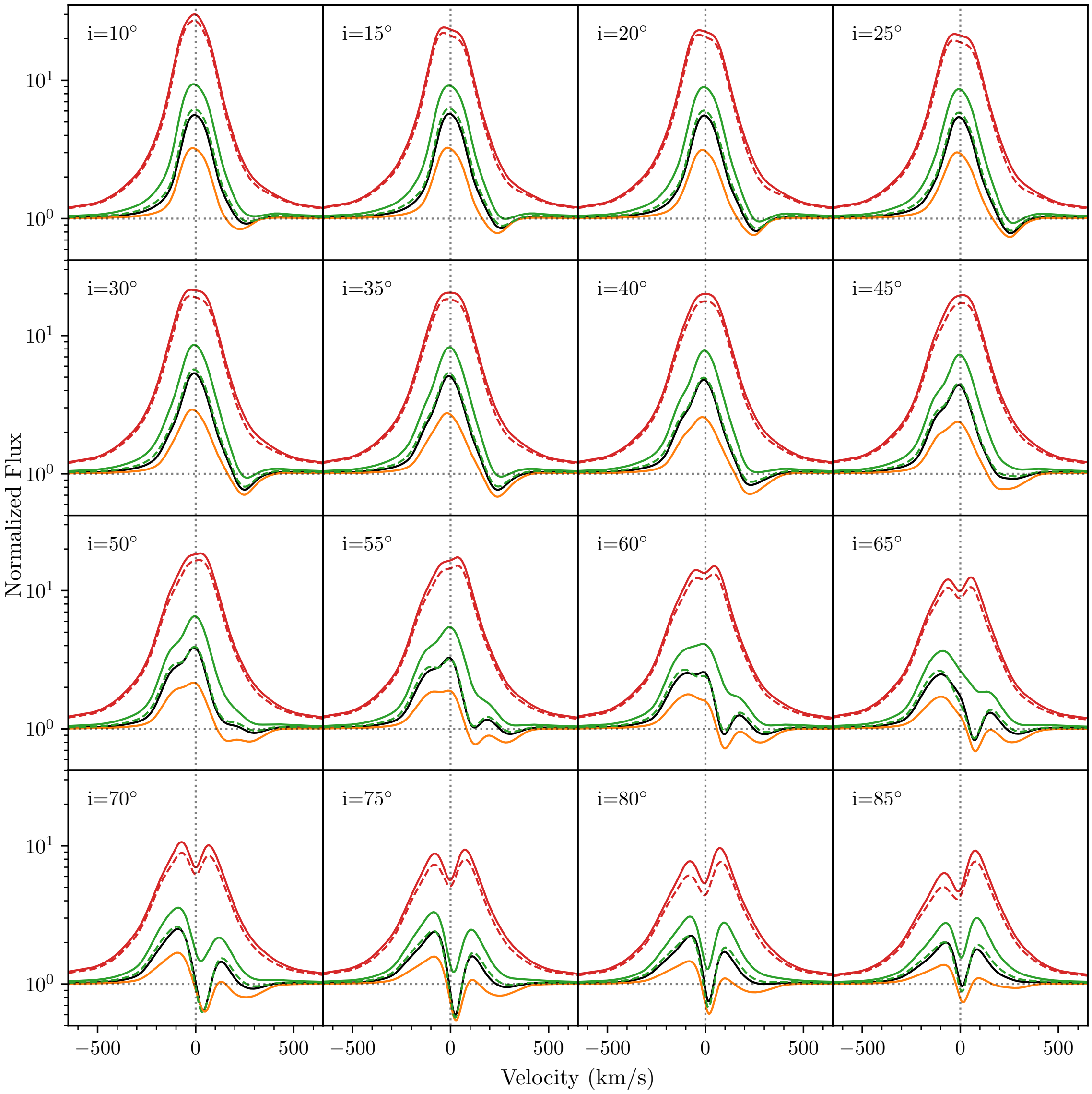

Figure 3.7 Hα line profiles for the two-shell accretion geometry with varying inclinations, mass accretion rates, and temperatures. Note that the y-axis is in the log scale. The black lines show the Hα profiles with parameters similar to those in Table 3.4, with $\dot{M}_{\text{in}} = 6 \times 10^{-10}\, M_\odot\,\text{yr}^{-1}$ and $\dot{M}_{\text{out}} = 2 \times 10^{-10}\, M_\odot\,\text{yr}^{-1}$. The orange, green, and red lines show the profiles at 0.5, 2.0, and 5.0 times the total mass accretion rate of the black line, respectively. For each $\dot{M}$ the dashed lines show the profiles with a slightly lower T_{max} (see text.) The low-velocity redshifted absorption starts appearing at $i \geq 65°$, shifting closer to the line center as the inclination increases. The line profiles at low inclinations are similar to those typically observed.

absorption is present. The resulting full width of $\sim 600\ \text{km}\,\text{s}^{-1}$ still gives $\dot{M} \sim 8 \times 10^{-8}\, M_\odot\,\text{yr}^{-1}$. As shown in Figure 3.2, such an accretion rate would produce a significant excess in the blue part of the optical spectrum of the star, in disagreement with the observation. Our results show that

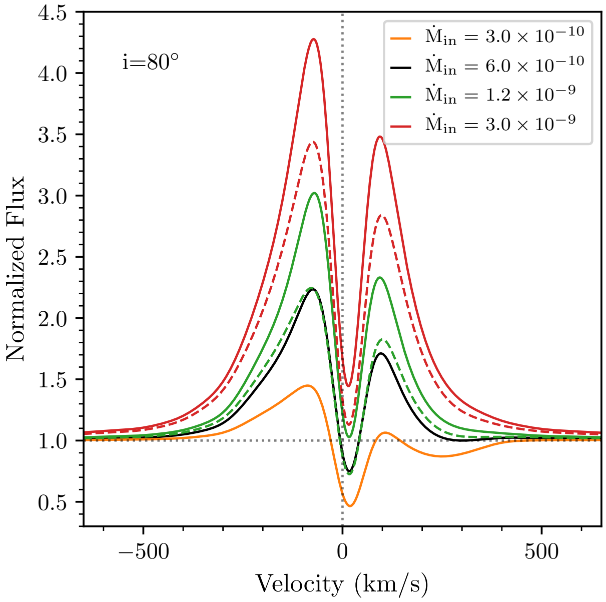

Figure 3.8 Model of Hα line in the same two-shell accretion geometry at different mass accretion rates and temperatures. The legends are the same as in Figure 3.7, but the accretion rate of the outer flow $\dot{M}_{\rm out}$ is fixed at $2 \times 10^{-10}\, M_\odot\, {\rm yr}^{-1}$.

in low accretors such as CVSO 1335, the width at the 10% height of the Hα line is not a reliable method for measuring the mass accretion rate. The absorption near the line center complicates the measurement of the W_{10} as the actual height cannot be reliably measured.

On the other hand, the mass accretion rates of CVSO 1335 determined in this study by using the magnetospheric accretion model and accretion shock model to fit Balmer line profiles and the Balmer jump are consistent with the accretion rates determined from the Hα luminosity in Thanathibodee et al. (2018), suggesting that Hα line luminosity is a reliable mass accretion rate estimator. Nevertheless, there is a limit to the estimates of mass accretion rates using line luminosities imposed by the chromospheric contribution to the emission lines (Manara et al. 2013). The chromospheric contribution is significant in low accretors, since the accretion-originated line emission is weak, and the resulting mass accretion rate would have a high relative uncertainty. On the other hand, line profile modeling can disentangle between the narrow chromospheric core emission and the broad line wings from the accretion flow (Espaillat et al. 2008). Therefore, direct modeling of the Hα lines, with chromospheric emission taken into account, is required for an accurate measurement of accretion rates in the low accretion regime and/or with a presence of low-velocity redshifted absorption.

As shown by Ingleby et al. (2011b) emission at the Balmer jump is difficult to detect in low accretors, including the case of CVSO 1335 as shown here. This is because the accretion shock emission is weak compared to the photospheric and chromospheric emission in the UV. Nevertheless, the non-detection of the Balmer jump sets a useful upper limit on the mass accretion rate for objects in which other accretion indicators, such as redshifted absorption, are present.

3.4.2 The Origin of the Low-Velocity Redshifted Absorption

The Hα profiles of CVSO 1335 show two systems of redshifted absorption. One is a persistent low-velocity ($v \sim 75\ \mathrm{km\,s^{-1}}$) redshifted absorption seen in all epochs; another is very variable complex system, located at velocities consistent with free-fall velocities (c.f. Fig. 3.1.)

Stars classified as dippers, such as AA Tau (Bouvier et al. 1999, 2003, 2007) and LkCa 15 (Alencar et al. 2018), show comparable redshifted absorptions. Using line profile decomposition, these studies indicate the presence of low-velocity blueshifted and redshifted absorption components, attributed to a hot wind and to the magnetospheric accretion flow, respectively, in a system viewed at high inclination. The velocities of the blue and redshifted absorption components are correlated and vary in absolute value between $\sim$ 10 and 60 $\mathrm{km\,s^{-1}}$, such that the highest redshifted velocity corresponds to the lowest blueshifted velocity. The low velocity absorption components do not seem to be correlated with the stellar rotation period, unlike the system at nearly free-fall velocities, which is highly variable and tends to appear near the photometric minimum in the dippers; these absorption are also attributed to magnetospheric infall (Bouvier et al. 1999, 2003, 2007; Alencar et al. 2018).

The observed low- and high-velocity redshifted absorptions in the Hα profiles of CVSO 1335 could in principle correspond to those observed in dippers. The star does not seem to exhibit any blueshifted absorption in any of its emission lines, possibly due to its low mass accretion rate, and consequently low mass loss rate. The spectral resolution of our MagE data could not significantly detect temporal variations in the location of the low velocity absorption of the order of those seen in dippers, although the comparison between the MagE and Goodman spectra, spanning over two months, seems to suggest that the absorption are fairly stable within the low velocity range.

Another characteristic of dippers are episodes of dust obscuration observed via reddening of the stellar spectra. In CVSO 1335, the spectrum observed on 2017-11-27 is redder than in other epochs (cf. Figure 3.1), which could be due to a similar reddening process. In support of this possibility, we found that we could reproduce the mean of the spectra in other epochs, adopted as template, by correcting the 2017-11-27 spectrum for extinction using the opacity of silicate dust grains with a size distribution $n(a) \propto a^{-3.5}$ between $a_{min} = 0.005\mu$m and $a_{max} = 0.25\mu$m, and a dust-to-gas mass ratio of 0.004, comparable to ISM grains (D'Alessio et al. 2001). We estimate that a low column density of $\mathrm{N_{gas+dust}} \sim 9 \times 10^{-3}\,\mathrm{g\,cm^{-2}}$ is required to produce the observed obscuration. A more detailed analysis using time-series optical spectra is required to confirm the existence of dust obscuration events in this star.

The high velocity redshifted absorption in CVSO 1335 is highly variable, as it is in dippers, but our limited number of observations does not allow us to determine if it correlates with the stellar period, which we expect to be ~ 6.5 days based on a $v \sin(i)$ measurement (§3.3.3.2). We require multi-band photometric monitoring of the star to test the hypothesis that the star is a dipper and observations are under way. Contemporaneous optical-NIR spectroscopic observations are also needed to link the light-curve variation in the photometry to the structure of accretion. Finally, HST observation using high-resolution FUV spectrographs would give insights into the connection between all components in the inner disk and the accretion in this low accretor. These properties will be followed up in future studies.

3.4.3 Magnetospheric Accretion in Two-Shell Geometry

The presence of accretion-originated low-velocity redshifted absorption *in addition* to redshifted absorption near free-fall velocity and broad wings suggests that there are two distinct accreting components, which we called two accretion flows in a two-shell geometry (c.f. Fig. 3.5, Table 3.4). This structure is an idealization of the real geometry that must be much more complicated. Depending on the actual structure of the accretion geometry, the difference in mass accretion rate between the inner and outer flows could be explained in different ways. If the inner and outer flow are physically disconnected, the mass accretion rate of the flows would naturally be different. On the other hand, if the two flows represent one complex, but physically connected, accretion flow, the actual mass accretion rate should be the same. The difference in $\dot{M}$ we find could be due to different azimuthal coverage of the inner and outer flows. We note that since the low-velocity redshifted absorption component is stable, the azimuthal coverage of the outer flow must be fairly uniform. In this case, if the inner flow is concentrated in a smaller azimuthal region, the density in the flow would be higher than that in the outer flow which covers a larger volume. Since the model assumes axisymmetric flows, the mass accretion rate inferred from the concentrated rate in the inner flow would be higher than the actual rate.

Although our model could not determine the actual geometry in the accretion flow, the agreement between our simple models and the observations suggests that the two-flow structure must be representing conspicuous features in the real situation that give rise to the observed features. Here we explore the implication of such structure.

3.4.3.1 Complex Stellar Magnetic Field Structure

The two-shell geometry could be reminiscent of a complex structure of the stellar magnetic field that gives rise to complex accretion flows. For example, it could be that the accreting material is the combination of magnetic dipolar and multipolar fields (Long et al. 2007, 2012). Spectropolarimetric observations of accreting T Tauri stars have shown evidences of higher order magnetic fields in stellar magnetosphere; for example Donati et al. (2007, 2011) showed that both the dipole and octupole components are present in the (K5) T Tauri star V2129 Oph. Based on these results, Romanova et al. (2011) used 3D MHD simulations to show that some material could be channelled onto the star via octupole fields at lower latitude in addition to the dipole accretion at higher latitude. CVSO 1335 could exhibit a similar magnetic field structure, and due to its high inclination the dipole flow could occult the higher-order flows at lower latitude. Alencar et al. (2012) calculated Hα line profiles based on the results of the simulations, and the low-velocity redshifted absorption was not present in the profiles, while it is conspicous in CVSO 1335. However, this could be due to the combined effect of a lower inclination and higher mass accretion rate in V2129 Oph compared to CVSO 1335 (see §3.3.4).

Another explanation for the two flow geometry is that the accretion in CVSO 1335 is at the interface between stable and unstable accretion in a strictly dipolar magnetic field. Results from 3D MHD simulation show that in this transition region, matter flows along two large funnels and through several small accretion tongues that deposite matter near the stellar surface (Romanova et al. 2008; Kulkarni & Romanova 2009). If this is the case for CVSO 1335, the outer flows could be the larger funnels that occult the several small tongues, which are the inner flows. To test either of these hypotheses, spectropolarimetric observations and MHD simulations with the exact stellar parameters of CVSO 1335 are required.

Lastly, the process responsible for the low-velocity redshifted absorption in this star could be similar to that proposed by Bouvier et al. (2003), based on results of numerical simulations (Romanova et al. 2012; Miller & Stone 1997), namely an "inflated" magnetosphere, resulting from differential rotation between the star and the disk. No radiative transfer model of such geometry has been applied to the Balmer lines in AA Tau yet, although some progress has been made for modeling the low-velocity blueshifted absorption (Esau et al. 2014).

3.4.3.2 Complex Inner Disk Structure due to a Planetary Companion

Another possibility that gives rise to geometrically separated accretion flows is that the inner disk that provides the material is not radially uniform. One example of such condition is that the inner disk, inside the corotation radius, may exhibit a gap structure at $\sim 5\,\mathrm{R}_{\star}$. In this case, very little material at that radius is flowing into the star along the magnetic field lines, thus leaving a gap between two shells of material flowing from the inner ring and from the ring at corotation. Rings and gaps in protoplanetary disks have been observed in larger scales in sub-mm (e.g., ALMA Partnership et al. 2015; Long et al. 2018a) and infrared scattered light (e.g., Avenhaus et al. 2018). Hydrodynamic simulations of protoplanetary disks have shown that these rings and gaps could be the consequences of a planet forming in the disk (Bae et al. 2017). However, it is unclear that similar process could happen in the inner disk. Nevertheless, if the gap is produced by a planet, it is unlikely that the planet's orbit is stable inside an actively accreting magnetosphere. Bae et al. (2017) have shown that a planet could open a secondary gap at $\sim 0.5r_p$, where r_p is the orbital radius of the planet, which implies that the planet could be at $\sim 10\,\mathrm{R}_\star$ (a$\sim$0.087 au, P$\sim$10 d). Since the Shakura-Sunyaev α parameter could be high in the MRI-driven innermost region of the disk (Mohanty et al. 2018), and the mass of the gap-opening planet increases with α (Bae et al. 2017), the planet, if it exists, should be massive (several $\mathrm{M_{Jup}}$).

Planets have been found to orbit the central stars with orbits of a few days, i.e., hot Jupiters. Many studies have indicated the presence of close-in planets around (non-accreting) weak TTS (e.g., van Eyken et al. 2012; Mann et al. 2016; David et al. 2017), but evidence of such planets around an actively accreting pre-main sequence stars are still sparse. So far, the only proposed planets in such category are a $11.3\,\mathrm{M_{Jup}}$ planet with $\sim$9 days period orbiting the 2 Myr star CI Tau (Johns-Krull et al. 2016), and a $\mathrm{M}_p \sin i \sim 19.3\,\mathrm{M_{Jup}}$ planet with a 24.8 day period around the 0.5 Myr star AS 205A (Almeida et al. 2017), based on the radial velocity method. With the parameters of CVSO 1335, a comparable planet would cause an RV signature of $\sim 1\ \mathrm{km\,s^{-1}}$; spectroscopic monitoring of the star is required to test this hypothesis.

3.4.3.3 Observability of Low-Velocity Redshifted Component

We have shown that the modified magnetospheric accretion model with a two-flow geometry is able to reproduce the observed Hα and Hβ profiles of CVSO 1335. Therefore, it is insightful to consider this model for other T Tauri stars. As shown in Figure 3.7, producing two redshifted absorption components requires low accretion rates and high inclinations; for high accretion rates, the two-flow model produces similar profiles to the standard model since Hα has become optically thick. Nevertheless, the model could be used for other lines that are more optically thin even with high accretion rate, but this remains to be calculated.

For low mass accretion rates the presence of the low velocity component still depends on the inclination of the system (c.f. Figure 3.7). Assuming that all stars orient randomly, one would expect that a significant portion of the low accretors exhibit a similar type of profiles. Several studies have shown that complex Hα line profiles are not uncommon (e.g., Reipurth et al. 1996; Antoniucci et al. 2017), but Hα profiles with two redshifted absorption components, as seen in CVSO 1335, are rare even in CTTS with low accretion rates. This suggests that other factors contribute to the formation of such geometry. The two scenarios discussed in this section could explain the rarity of multiple redshifted absorption profile.

In order to have complex magnetic fields, required for scenario discussed in §3.4.3.1, pre-main sequence stars need to have solar or higher mass and/or old age (e.g., Villebrun et al. 2019). In this regard, solar mass low accretors are rare since stars in this mass range account for only $\lesssim 10\%$ of a young population (e.g., Briceño et al. 2019), and the number of accretors decreases sharply with age. The frequency of low accretors are not yet available, but the number should be less than the frequency of all CTTS at 5 Myr, $\sim$ 15% (Briceño et al. 2019; Fedele et al. 2010). Therefore, the upper limit of the frequency of solar-mass low accretor is $\sim$1.5% of all T Tauri stars in a given population, and $\sim$0.75% would have a high inclination. This fraction means that only a few stars in a given population could show line profiles similar to those of CVSO 1335, since the number of T Tauri stars in a given population is on the order of a few hundreds (e.g., Luhman et al. 2018; Luhman 2018) to thousands (e.g., Sung et al. 2009; Briceño et al. 2019). It is therefore conceivable that many solar mass stars could have a magnetosphere in the two-flow geometry at some point in their life, but the frequency of observing them is low and only CVSO 1335 has been identified as such so far.

In the gap opened by a planet scenario, the required mass of the planet is several Jupiter mass. If the planet exist, it would be classified as a hot Jupiter due to its close orbit. Since, only $\sim$ 1% of solar mass stars, and even less in M-type stars, host such planets (Dawson & Johnson 2018), the expected number of CTTS with CVSO 1335-type profiles is as equally small as in the case of complex magnetic fields.

3.5 Summary

We applied accretion shock models and magnetospheric accretion models to MagE and Goodman optical spectra of the 5 Myr old, $\sim$ solar mass star CVSO 1335 to characterize the accretion properties of this low accretor. Here we summarize our findings:

1. The Balmer jump of CVSO 1335 does not show any significant excess over the WTTS used as template, confirming that CVSO 1335 is a low accretor. Using accretion shock models, we find variable upper limits of the mass accretion rates $\sim 4-9\times10^{-10}\,M_\odot\,\mathrm{yr}^{-1}$. These limits are in agreement with estimates based on Hα line luminosity. However, they contradict the measurements based on the line width, which would indicate rates as high as $10^{-8}\,M_\odot\,\mathrm{yr}^{-1}$.

2. The excess at the Balmer jump does not provide an estimate of the mass accretion rate in CVSO 1335, or in general in low accretors. On the other hand, line profile fitting provides a measurement of the accretion rate, as well as the geometry of the accretion flows. Therefore, modeling line profiles is the only reliable method to accurately measure mass accretion rate in low accretors.

3. Redshifted absorption components superimposed on the Hα and Hβ emission lines are conspicuous in CVSO 1335 and are found in all epochs. The line profiles are variable with

clear multiple components, which cannot be explained using the standard magnetospheric accretion model. A modified magnetospheric accretion model, with two separated accretion flows, can explain the low-velocity redshifted absorption simultaneously with broad wings and high-velocity redshifted absorption in the Hα and Hβ lines. The inner flows have higher and more variable $\dot{M}$ compared to the outer flows. High inclination ($i \sim 70°$) and high accretion flow temperature (T$_{\rm max} \gtrsim 11000$) are required to reproduce the profiles.

4. The required high inclination, in addition to the presence of a persistent low velocity component and a highly variable high velocity component, with velocities comparable to free-fall velocities, may indicate that CVSO 1335 is a dipper. Multi-band photometric monitoring is required to test this hypothesis.

5. Our simple two-flow geometry represents a more complex accretion geometry. This could suggests a complex magnetic field structure including higher-order fields, unstable accretion, or an inflated magnetosphere. Alternatively, a ringed structure in the inner disk resulting from the presence of a companion, could be responsible for this geometry. The rarity of Hα profiles with multiple redshifted absorption components is compatible with both scenarios.

CHAPTER 4

Variable Accretion onto Protoplanet Host Star PDS 70

This chapter was originally published in the Astrophysical Journal, Volume 892, 81 (2020), in collaboration with Brandon Molina, Nuria Calvet, Javier Serna, Jaehan Bae, Mark Reynolds, Jesús Hernández, James Muzerolle, and Ramiro Franco Hernández. It is adapted and reproduced here under the non-exclusive rights of re-publication granted by the American Astronomical Society to the authors.

Abstract

The PDS 70 system has been subject to many studies in the past year following the discovery of two accreting planets in the gap of its circumstellar disk. Nevertheless, the mass accretion rate onto the star is still not well known. Here we determined the stellar mass accretion rate and its variability based on TESS and HARPS observations. The stellar light curve shows a strong signal with a 3.03 ± 0.06 days period, which we attribute to stellar rotation. Our analysis of the HARPS spectra shows a rotational velocity of $v \sin\, i \;=\; 16.0 \pm 0.5$ $\mathrm{km\,s^{-1}}$, indicating that the inclination of the rotation axis is 50 ± 8 degrees. This implies that the rotation axes of the star and its circumstellar disk are parallel within the measurement error. We apply magnetospheric accretion models to fit the profiles of the Hα line and derive mass accretion rates onto the star in the range of $0.6 - 2.2 \times 10^{-10}\, M_{\odot}\,\mathrm{yr}^{-1}$, varying over the rotation phase. The measured accretion rates are in agreement with those estimated from NUV fluxes using accretion shock models. The derived accretion rates are higher than expected from the disk mass and planets properties for the low values of the viscous parameter α suggested by recent studies, potentially pointing to an additional mass reservoir in the inner disk to feed the accretion, such as a dead zone. We find that the He I λ10830 line shows a blueshifted absorption feature, indicative of a wind. The mass-loss rate estimated from the line depth is consistent with an accretion-driven inner disk MHD wind.

4.1 Introduction

The pre-main sequence star PDS 70 has attracted much recent attention because it hosts the most unambiguous example of planets in the process of formation, namely two giant planets inside the gap of the circumstellar disk (Keppler et al. 2018; Haffert et al. 2019). Indicators that the planets are still forming include the submillimeter emission detected around them, interpreted as arising in circumplanetary disks (CPDs, Isella et al. 2019), and by the Hα emission coincident with the location of the protoplanets in NIR images (Wagner et al. 2018; Haffert et al. 2019), interpreted as forming in accretion flows from the circumstellar disks into the planet-CPD systems (Thanathibodee et al. 2019a; Aoyama & Ikoma 2019).

PDS 70 is a K7 star (Riaud et al. 2006; Pecaut & Mamajek 2016) located in the 5-10 Myr old Upper Sco association (Gregorio-Hetem & Hetem 2002). Its circumstellar disk has been classified as a pre-transitional disk (Espaillat et al. 2008), based on the large size ($\sim 65\,\mathrm{au}$) of the cavity in the disk inferred from the spectral energy distribution (SED) of the system and consistent with NIR imaging (Dong et al. 2012). Gregorio-Hetem & Hetem (2002) classified the star as a Weak T Tauri star (WTTS) based on an Hα equivalent width of 2 Å, and thus identified it as a non-accretor (White & Basri 2003; Barrado y Navascués & Martín 2003). More recently, Long et al. (2018b) classified the star as a non accretor, based on the lack of emission in Paβ. Similarly, Joyce et al. (2019) found essentially no excess over the photosphere in the Swift U band flux of PDS 70, from which they infer that the star is accreting at a extremely low level, $\dot{M} \sim 6 \times 10^{-12} M_{\odot}\,\mathrm{yr}^{-1}$, consistent with no accretion. On the other hand, Haffert et al. (2019) reported a redshifted absorption component in the Hα profile of the star and concluded that the star is accreting.

Thanathibodee et al. (2018, 2019b) are carrying out a program searching for the lowest accretors; preliminary results of this program find that around 20-30 % of stars previously classified as WTTS are still accreting, presumably at very low levels (Chapter 5 of this Dissertation). The new accretors in this program have been identified using the He I λ10830 line. Redshifted absorption components at velocities consistent with free-fall, which are formed in magnetospheric accretion flows, may appear in this line even at low densities, due to the metastable nature of its lower level. Therefore, the He I λ10830 line can detect very low levels of accretion, even in cases when traditional accretion tracers, such as Hα, exhibit no sign of stellar accretion. (Thanathibodee et al. 2019b).

Given the different assessments in the literature, in this Chapter, we revisit the accretion status of PDS 70. In agreement with Haffert et al. (2019), we find that it is accreting mass from the disk. We also obtain a reliable estimate of the mass accretion rate and its variability. The mass accretion onto the star is important because it is a key constraint on models of planet formation. For instance, Zhu et al. (2011) found that multiple planets were needed to create cavities of the order of tens of au, but in this case, mass coming from the outer disk would be partitioned between the planets and little would reach the star; however, this was at odds with the relatively high mass accretion rates onto the star measured in transitional disks (cf. Espaillat et al. 2014). The constraints imposed by the mass accretion rate can be particularly useful for a case so well characterized as PDS 70. In this case, we have a well studied circumstellar disk (Dong et al. 2012; Keppler et al. 2019), we have clear detection of planets with approximate mass and radius (Keppler et al. 2018; Müller et al. 2018), and we also have estimates of the mass of the circumplanetary disks (Isella et al. 2019) and the mass accretion rates onto the planets (Thanathibodee et al. 2019a; Haffert et al. 2019; Aoyama & Ikoma 2019). With a good estimate of the mass accretion rate onto the star, the system will be ideal for testing models of planet formation and planet-disk interaction.

This Chapter is organized as follows. In Section 4.2 we describe the observations and data sources. In Section 4.3 we derive stellar properties and apply magnetospheric models to fit Hα profiles and derive the mass accretion rate onto the star and its variability. In Section 4.4, we discuss the implications of our results. Finally, in Section 4.5 we give our conclusions.

4.2 Observations and Data Sources

4.2.1 NIR Spectroscopy

We obtained a near-infrared spectrum of PDS 70 using the FIRE spectrograph on the Magellan Baade Telescope at the Las Campanas Observatory in Chile. With the $0\farcs6$ slit, the spectrograph achieved a resolution of $\sim$6000 for simultaneous spectral coverage in the range 0.9 - 2.4μm. We observed the star in two nodding positions (A/B), each with an exposure time of 126.8 s in the Sample-Up-The-Ramp (SUTR) mode. A telluric standard star was observed immediately afterward. The average airmass and seeing of the observation were 1.1 and $1\farcs0$, respectively. The spectral extraction, wavelength calibration, and telluric correction were performed using the IDL-based FIRE data reduction pipeline (Simcoe et al. 2013).

4.2.2 TESS

PDS 70 was observed with TESS (TIC179413040) with 2 minutes cadence for 24 days, and the photometry was reduced by the TESS pipeline. We downloaded the extracted light curve from the Mikulski Archive for Space Telescopes (MAST). The Simple Aperture Photometry (SAP) flux and the Pre-search Data Conditioning SAP flux (PDCSAP) from the pipeline appear to be the same for the star, and we choose to use the PDCSAP flux. We use the `Lightkurve` software (Lightkurve Collaboration et al. 2018) to extract and normalize the light curve. Figure 4.1 shows the 24-day

Table 4.1 Summary of Observations and Data Sources

Instrument	Obs. Date (UT)	Exp. time (sec)	No. of Obs.	SNR[a]
FIRE	2019 Apr 26	253.6	1	260
TESS	2019 Apr 26 to 2019 May 20	2×60	13,887	570
HARPS	2018 Mar 29	900	6	15
	2018 Mar 30	900	6	11
	2018 Mar 31	900	6	18
	2018 Apr 18	1800	1	21
	2018 Apr 19	900	2	8
	2018 Apr 20	1800	2	22
	2018 Apr 21	1800	1	22
	2018 Apr 22	1800	1	22
	2018 Apr 23	1800	1	22
	2018 May 01	1800	2	14
	2018 May 06	1800	2	26
	2018 May 13	1800	2	17

[a] Signal-to-noise at 10830 Å for FIRE, median SNR for HARPS.

light curve of PDS 70.

4.2.3 Optical Spectroscopy

We downloaded spectra of PDS 70, obtained with the HARPS instrument (Mayor et al. 2003) on the European Southern Observatory (ESO) 3.6m telescope (Program ID 098.C-0739, PI: Lagrange), from the ESO Archive Science Portal. HARPS provided 32 high-resolution (R$\sim$115,000) spectra of the star observed across $\sim$2 months in 2018. We used the data automatically reduced and calibrated by the HARPS pipeline for our analysis. Table 1 shows the details of the observations.

4.3 Analysis and Results

4.3.1 Stellar Properties

4.3.1.1 Rotation Period

To determine the rotation period of PDS 70, we constructed a periodogram from the TESS light curve, using the `Psearch` code (Saha & Vivas 2017), which combines the Lomb-Scargle and Lafler–Kinman methods. As shown in the bottom left panel of Figure 4.1, the periodogram shows

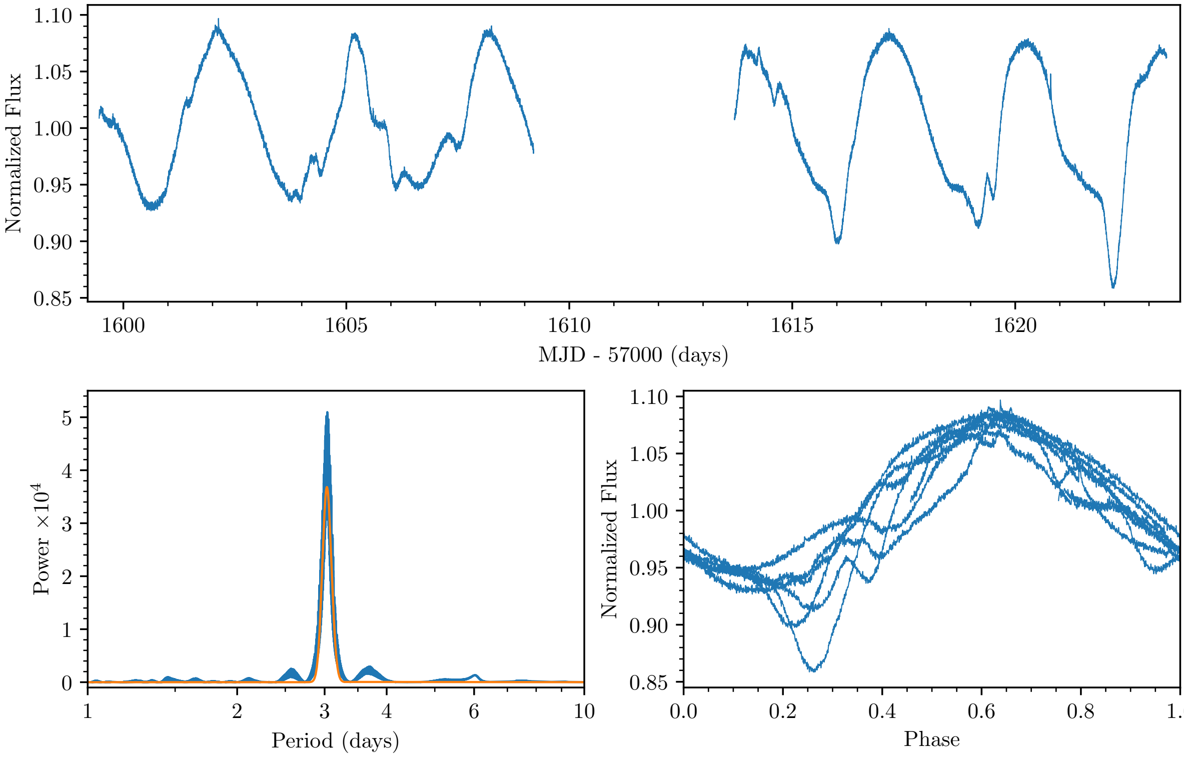

Figure 4.1 TESS light curve, periodogram, and phase-folded light curve of PDS70. *Top*: TESS light curve of PDS 70. The flux has been normalized to the median flux. *Bottom left*: Lomb-Scargle periodogram of the light curve (blue). The periodogram shows a strong peak at 3.03 d. The orange line shows the Gaussian fit to the power spectrum. *Bottom right*: The phase-folded light curve using the period $P = 3.03\,\mathrm{d}$.

a strong power at the period of 3.03 days. To estimate the uncertainty of the period, we fit a Gaussian to the strongest peak in the periodogram (Venuti et al. 2017). The corresponding period from the fit is 3.03 ± 0.06 days, where the uncertainty is the 1σ propagation of the fitted Gaussian width in frequency space.

We visually inspect the period by folding the light curve with the calculated period of 3.03 d. As shown in the bottom right panel of Figure 4.1, the period is consistent with the light curve. The amplitude of the light curve is on the order of 10%, consistent with variation due to starspots phasing in and out of the line of sight (Herbst et al. 1994; Venuti et al. 2017). Smaller dips can be seen at phase $\sim 0.3 - 0.4$, suggesting that there could be other factors that modulate the light curve, such as obscuration of the inner disk warp (Bouvier et al. 2003). The 3.03 d period is also consistent with a typical rotation period of T Tauri stars (e.g., Karim et al. 2016). Therefore we conclude that the period of the light curve is the rotation period of the star since other types of variations would modulate the light curve in different timescales (e.g., Siwak et al. 2018).

We calculate the corotation radius, at which the Keplerian orbital period is equal to the stellar rotation period, and outside of which accretion cannot occur (Hartmann et al. 2016). Using the stellar mass $\mathrm{M}_\star = 0.76 \pm 0.02\,\mathrm{M}_\odot$ and radius $\mathrm{R}_\star = 1.26 \pm 0.15\,\mathrm{R}_\odot$ (Müller et al. 2018), we obtain the corotation radius as

$$R_{co} = \left(\frac{GM_\star P^2}{4\pi^2}\right)^{1/3} = 6.4 \pm 0.8\,R_\star, \tag{4.1}$$

where the uncertainty is calculated with the standard error propagation.

4.3.1.2 Rotational Velocity

We used the Fourier method (Carroll 1933) to calculate the projected rotational velocity ($v \sin i$) of the star. The method requires isolated photospheric lines at sufficient SNR at a high spectral resolution to have a reliable line shape (Simón-Díaz & Herrero 2007). Since none of the HARPS spectra has enough SNR for the analysis, co-adding the spectra is required. We first calculated the radial velocity (RV) by cross-correlating each spectrum with a PHOENIX photospheric template (Husser et al. 2013) and fitting a Gaussian to the cross-correlation function. The median and the standard deviation of the RV is $+6.0 \pm 1.5\ \mathrm{km\,s^{-1}}$. We corrected all 32 spectra with RV=$6.0\ \mathrm{km\,s^{-1}}$, and combined them by averaging the spectra weighted by the median SNR (c.f. Table 4.1). The resulting spectrum has a median SNR of ~ 46. We then selected 20 photospheric lines that are clearly isolated, including the Li I $\lambda6708$ line, and calculated a Fourier power spectrum for each line. From the first zero in the Fourier spectrum, we calculated the $v \sin i$, adopting a limb darkening coefficient $\epsilon = 0.6$, which is appropriate for spectra in the optical range (Claret 2000). Based on the median and the standard deviation of $v \sin i$ measured from these 20 lines, the rotational velocity of the star is $v \sin(i) = 16.0 \pm 0.5\ \mathrm{km\,s^{-1}}$.

We combined our measurement of $v\,\mathrm{sin}i$ with the rotation period P from Section 4.3.1.1 and $\mathrm{R}_\star = 1.26 \pm 0.15\,\mathrm{R}_\odot$ (Müller et al. 2018), to obtain the inclination of the star as

$$i = \sin^{-1}\left(\frac{P\,v\sin(i)}{2\pi R_\star}\right) = 50 \pm 8^\circ\ (1\sigma). \tag{4.2}$$

Keppler et al. (2019) found $i = 51.7 \pm 0.1^\circ$ and $i = 52.1 \pm 0.1^\circ$ for the inclination of the protoplanetary disk in two different ALMA observations. Therefore, our results suggest that the stellar and disk rotation axes are parallel to each other within the measurement errors.

4.3.2 Accretion Status of PDS 70 from FIRE Observations

Optical hydrogen lines such as Hα have been used to determine if a T Tauri star is still accreting. However, Hα may fail at very low accretion rates due to a comparatively significant contribution from chromospheric emission (Manara et al. 2017a), especially when observed in low or moderate

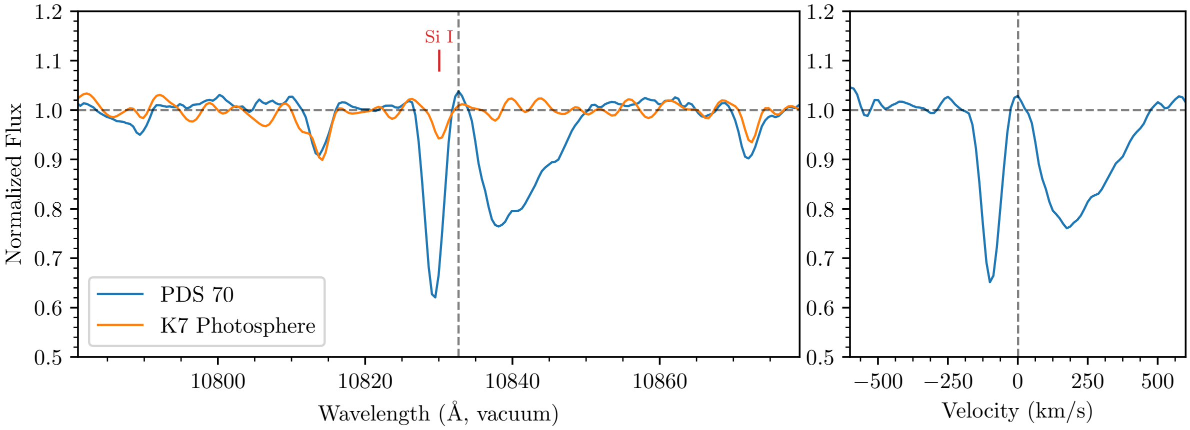

Figure 4.2 He I λ10830 line profile of PDS 70. Left: The line before subtraction of the photosphere. The Si I line is indicated. The nominal line center, calculated by averaging the frequency of the He I λ10830 triplet weighted by the gf values, is shown as the vertical dashed line. Right: The line after photospheric subtraction. The line shows both blueshifted and redshifted absorption components.

spectral resolution. On the other hand, the He I λ10830 line has been found to be very sensitive to accretion and thus to be a good tracer for low-accretors (Thanathibodee et al. 2018). In particular, the presence of a redshifted absorption component in the line profile is a direct indicator of accretion. Here we use this line to probe the state of accretion of PDS 70.

The He I λ10830 line is shown in Figure 4.2. [1] In general, the He I λ10830 line is conspicuous in accreting stars. However, for low accretors observed at a medium or low spectral resolution, the Si I at 10830 Å(vacuum) could contaminate the He I line at 10833 Å. Therefore, we constructed a photospheric template of the star from interpolating in a PHOENIX model spectrum (Husser et al. 2013) with the same effective temperature and gravity as PDS 70, and convolved it first to the rotational velocity of the star and then to the resolution of the FIRE spectrograph. As shown in the left panel of Figure 4.2, the contribution from the Si I to the overall absorption of the He I line is negligible. The right panel of Figure 4.2 shows the line after subtracting the photospheric template. The line shows strong and conspicuous redshifted and blueshifted absorption features. The presence of the redshifted absorption feature is a definitive indication that the star is accreting. As with many low accretors with this type of profile, the He I emission is weak or undetectable (Chapter 5).

---

[1] The analysis of the FIRE data is performed in the vacuum wavelength, and the vacuum line center of the He I λ10830 is at 10833 Å. Nevertheless, we will refer to the line using the air wavelength following the standard convention.

Table 4.2. Range of Model Parameters

Parameters	Min.	Max.	Step
$\dot{M}$ ($10^{-10} M_{\odot}$ yr^{-1})	0.2	4.5	0.1, 0.5
$T_{\rm max}$ (K)	10000	12000	250
$R_{\rm i}$ ($R_{\star}$)	2.0	6.0	0.4
$W_{\rm r}$ ($R_{\star}$)	0.2	2.0	0.4
i	30	75	5

4.3.3 Measurement of the Mass Accretion Rate

At very low levels of accretion, the most reliable way to measure the mass accretion rate is to model the resolved profile of emission lines (Thanathibodee et al. 2019b). High resolution is needed to distinguish the chromospheric feature of the line, which appears as a narrow and mostly symmetric feature at the line center, and magnetospheric features that extend out to the star's free-fall velocity. Here we use the magnetospheric accretion model of Muzerolle et al. (2001) to model the Hα line profiles from the HARPS spectra.

4.3.3.1 Magnetospheric Accretion Model

The physics of the magnetospheric accretion models is given in detail in Hartmann et al. (1994) and Muzerolle et al. (1998a, 2001). Here we describe the basic assumptions. The model assumes that the accreting material flows along the magnetic field of the star, taken as dipolar. It assumes that the stellar rotation axis, the dipolar magnetic axis, and the disk Keplerian rotation axis are aligned. As a result, the accretion flow is axisymmetric. The free parameters of the model are the disk truncation radius ($R_{\rm i}$), the radial width of the accretion flow on the equatorial plane ($W_{\rm r}$), and the maximum temperature of the gas in the flow ($T_{\rm max}$). The density in the flow is set by the mass accretion rate, $\dot{M}$, and the geometry. We solve a 16-level hydrogen atom, in which the mean intensities for the radiative rates are calculated with the extended Sobolev approximation, to obtain level populations and source functions. The line profile is calculated using a ray-by-ray method for a given inclination (i) between the magnetic axis and the line of sight.

We calculate a large grid of models varying the model parameters, as shown in Table 4.2. Although we have a measurement of the inclination of the rotation axis (see Section 4.3.1.2), we probe a larger range of inclinations to verify the axisymmetric assumption of the model; differences between the model inclination and the rotational inclination would suggest a possible misalignment between the rotation axis and the magnetic axis. We only calculate models in which the outer

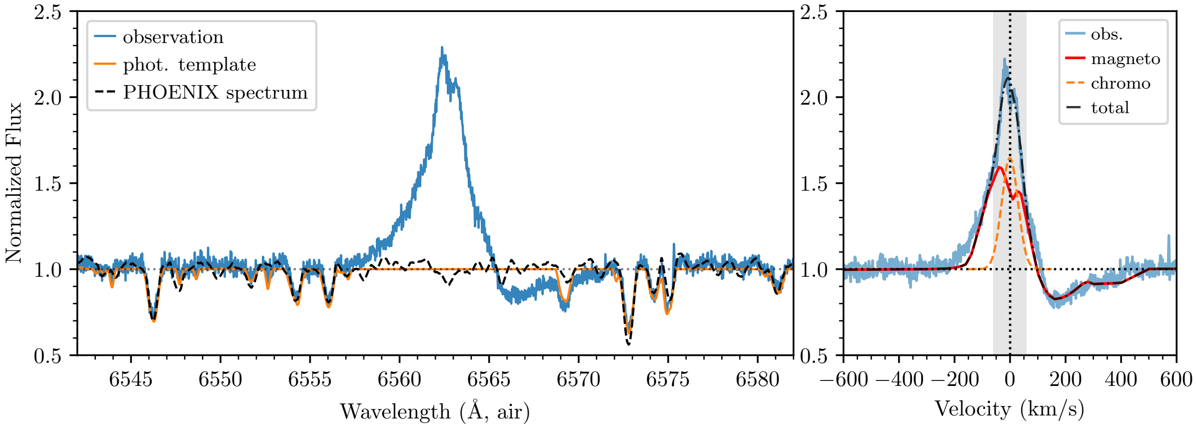

Figure 4.3 A representative Hα line profile of PDS 70. Left: The line before subtraction of the photosphere. An adopted photospheric template, constructed from the star's spectrum during quiescence, is shown in orange. The emission feature is excluded in the construction of the photospheric template. In comparison, the black line shows a K7 template from the PHOENIX model. Right: The photospheric-subtracted line profile (blue) and the best fit model (red). The line center ($\pm 60\ \mathrm{km\,s^{-1}}$, shaded) is excluded from the magnetospheric model fit. The dashed orange line shows the best fit for the chromospheric profile, and the dash-dotted line shows the total model line profile. For this observation, the best fit parameters are $\mathrm{R_i} = 4.0\,\mathrm{R_\star}$, $\mathrm{W_r} = 0.6\,\mathrm{R_\star}$, $\dot{M}$=1.0 × $10^{-10}\,M_\odot\,\mathrm{yr}^{-1}$, $\mathrm{T_{max}}$=11,500 K, and $i = 45°$.

radius of the flow, $\mathrm{R_i}$+$\mathrm{W_r}$, is inside the corotation radius of the star $\mathrm{R_{co}} = 6.4\,\mathrm{R_\star}$. The range of $\dot{M}$ is selected to cover a typical range at which Hα starts to fail as an accretion diagnostics (few $\times 10^{-10}\,M_\odot\,\mathrm{yr}^{-1}$; Thanathibodee et al. 2018). The lower end of the $\dot{M}$ range is chosen from our pre-grid calculations, in which the Hα profiles can still be in emission. The range of the flow temperatures is selected to be consistent with the expected $\mathrm{T_{max}}$ at low $\dot{M}$ (Muzerolle et al. 2001; Thanathibodee et al. 2019b). In total, we calculate 64,800 models.

4.3.3.2 Fitting Hα Line Profiles

The chromospheric contribution to the hydrogen lines becomes significant in low accretors. In addition, photospheric absorption lines can affect the shape of the redshifted absorption features in the line. Therefore, the photospheric and chromospheric contributions to the line need to be taken into account before modeling the line profile.

We constructed a photospheric template of the star using its normalized spectrum at the most quiescent state, during which the Hα line is symmetric and purely in emission. We replaced the Hα emission feature and any small features within 30% of the standard deviation of the flux with $\mathrm{F_\lambda} = \mathrm{F_{\lambda,norm}} = 1$. We then used a box filter to smooth the spectrum, resulting in a photospheric template. The left panel of Figure 4.3 shows a spectrum of the star and the photospheric template derived from the stellar spectra. In comparison, we plot a photospheric template interpolated from the PHOENIX model spectra (Husser et al. 2013), in the same spectral resolution and rotational velocity. The template is similar to the PHOENIX spectra, and it better reproduces the Fe I absorption line at 6569.2 Å.

We fit each observation by calculating the root-mean-square error (RMSE) for all profiles in the grid of models. The RMSE is given by

$$\mathrm{RMSE} = \sqrt{\frac{\sum_{i=1}^{N} \left(F_{\mathrm{obs},i} - F_{\mathrm{model},i}\right)^2}{N}}, \tag{4.3}$$

where F_is are normalized fluxes at any given pixel and N is the total numbers of pixels in the relevant velocity range. This statistic avoids giving weight to any particular feature of the observed profile, unlike the χ^2 statistics, which is biased toward emission features if the deviation is normalized by the observed flux at a given pixel. We only consider the velocity range of -250 to $+400\ \mathrm{km\,s^{-1}}$, comparable to the star's free-fall velocity, and exclude the region $\pm 60\ \mathrm{km\,s^{-1}}$ to avoid fitting the chromospheric feature of the line. The best fit models are the models with the smallest RMSE, and the mass accretion rate and the accretion geometry is inferred from the weighted mean parameters of the model with RMSE ≤ 0.1. To verify that the line center is Gaussian, indicating that it arises in the chromosphere, we fit a Gaussian profile to the residual of the best fit, and then add the Gaussian profile to the photospheric profile. The right panel of Figure 4.3 shows an example of the best fit for one of the observed profiles. The observed line profile is reproduced by adding the best fit magnetospheric profile with a Gaussian profile. [2] The mass accretion rate of the star based on this observation is $1.0 \times 10^{-10}\, M_\odot\,\mathrm{yr}^{-1}$.

4.3.3.3 Accretion Variability

To explore the variability of the mass accretion rate and accretion geometry, we grouped the 32 HARPS spectroscopic observations by rotation phases, calculated from the period in Section 4.3.1.1, and stacked them, resulting in 8 spectra representing observations in different phases. The phase ϕ is defined such that $\phi = 0$ at Modified Julian Date (MJD) 0.0. The grouping was done such that observations on the same night fell on one group, and the profiles were similar. As shown in Figure 4.4, the star shows rotational variability in the line profiles. From phase 0.00, the redshifted absorption component becomes stronger and is strongest at phase 0.49. On the other hand, the magnetospheric component of the line from phase 0.57 to 0.90 is mostly in emission, with weak to no redshifted absorption.

---

[2] Since determining the properties of the chromosphere is beyond the scope of this Chapter, we do not attempt to fit the line center with a double-Gaussian model typically employed to fit chromospheric lines (e.g., Rauscher & Marcy 2006).

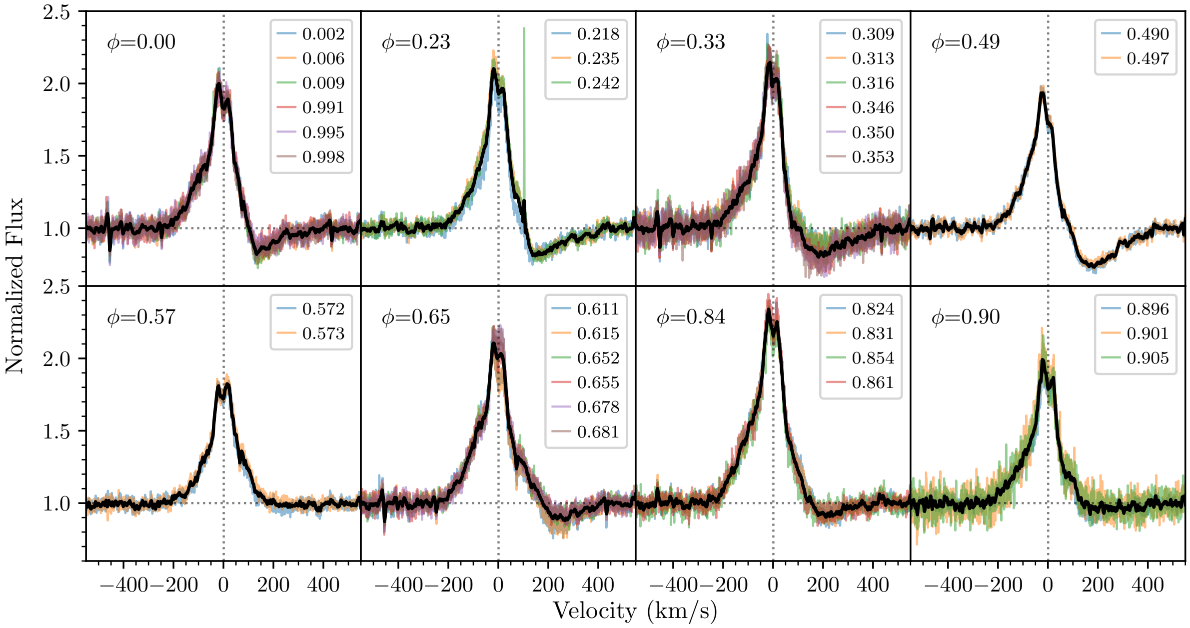

Figure 4.4 The Hα line profiles of PDS 70 grouped and stacked in eight phases in the rotation period. Most of the spectra in the same group are from the same night, but spectra observed ~ 1 rotation period apart shows remarkable similarity. The stacked spectra are smoothed with the Savitzky-Golay filter 21 pixels in size for clarity.

To quantify the phase-variation of properties of the accretion flow, we fitted the stacked spectra at each phase with the grid of models, as described in 4.3.3.2. The results are shown in Table 4.3, in which the last column shows the number of models within the RMSE≤ 0.1 criterion. The last row of the Table shows the phase-averaged values for each model parameters calculated by weighting each observation with a phase duration $\Delta\phi$, where

$$\Delta\phi_i = \frac{\phi_{i+1} - \phi_i}{2} + \frac{\phi_i - \phi_{i-1}}{2}. \tag{4.4}$$

Except for the flow temperature T$_{\mathrm{max}}$, the model parameters show various degrees of variability. In particular, the observed $\dot{M}$ can vary by more than a factor of three during the rotation phase.

Figure 4.5 shows a representative best fit for each of the observed profiles. As shown in the figure, our best fit models show good agreement with the observed line profiles. The chromospheric fits to the residual (dashed orange lines) are centered at $v \sim 0\ \mathrm{km\,s^{-1}}$, as expected, except at $\phi = 0.57$. In this case, the magnetospheric model could not well reproduce the symmetric feature of the observed profile and tends to under-predict the emission on the red wing, causing the residual (from which the chromosphere is fitted) to be redshifted. Since redshifted absorption suggests material flowing along the line of sight, the symmetric line profile suggests that there is a region of the magnetosphere with little to no flow, which is passing in front of the star at the given phase. The modifications to the current model required to test this hypothesis are beyond the scope of this chapter.

We compare the best-fit parameter values and the properties of the observed line profiles as a function of phase in Figure 4.6. The top two rows of the Figure show the velocity at the lowest flux and the equivalent width (EW) of the redshifted absorption feature of the Hα line, respectively. While the flow temperature is constant, general trends can be seen for other model parameters. When the absorption is weak with the smallest EW, the mass accretion rate is low, the truncation radius (R_i) is small, and the magnetosphere is thin. Thicker and larger magnetospheres correspond to stronger absorption features and higher mass accretion rates. The model inclination i, which probe the inclination of the magnetic axis, seems to vary slightly with a similar trend seen in the redshifted velocity. The slight variation in the redshifted velocity, and to some extent the inclination, seems to suggest that there could be a small misalignment between the magnetic axis and the rotation axis, resulting in a non-axisymmetric accretion flow. Numerical simulation of accreting magnetized star with misaligned axis (Romanova et al. 2003) suggests that even a small misalignment ($\Delta i \sim 5^\circ$) results in non-axisymmetric flow, with mass preferentially flow along a particular path. We note, however, that the uncertainty in the inclination is large compared to the model variation. Therefore, this alone, without the variability of other observed and model parameters, would not suggest the misalignment.

The variation of the model parameters suggests that we may be probing different portions of this asymmetric flow. However, as our current model does not allow misalignment between the stellar rotation axis and the magnetic axis, we caution that such effects have to be further investigated in the future. Nevertheless, our model still provides an estimate of the mass accretion rate and its possible variation. Future spectropolarimetric observations would provide insight into the geometry of the magnetosphere (Donati et al. 2007, 2011).

We also note that in Figure 4.5, the chromospheric components is varying slightly between phases, especially the strength of the line, while the width and the line center are constant. We defer a discussion about chromospheric component to future studies.

4.4 Discussion

4.4.1 Accretion Shock Emission

Our variability analysis indicates that the mass accretion rate onto PDS 70 is in the range $0.6 - 2.2 \times 10^{-10} M_\odot\,\mathrm{yr}^{-1}$ (Table 4.3). Material accreting at this rate is slowed down through an accretion shock at the stellar surface before merging with stellar material. Emission from this shock shows

Table 4.3. Results of the Magnetospheric Accretion Model

Phase	$\dot{M}$ ($10^{-10}\,M_\odot\,\mathrm{yr}^{-1}$)	$\mathrm{R_i}$ ($\mathrm{R}_\star$)	$\mathrm{W_r}$ ($\mathrm{R}_\star$)	$\mathrm{T_{max}}$ (10^4 K)	i (deg)	Numbers of models
0.00	1.3±1.1	3.6±1.0	0.5±0.4	1.09±0.07	47±14	1229
0.23	1.7±1.3	3.7±1.0	0.7±0.5	1.09±0.07	42±12	1548
0.33	1.8±1.3	3.5±0.9	0.7±0.4	1.09±0.07	50±13	1441
0.49	2.2±1.3	3.9±0.9	0.8±0.4	1.10±0.07	48±12	1333
0.57	0.6±0.2	3.1±1.3	0.2±0.0	1.09±0.06	48±17	259
0.65	0.9±0.7	2.7±0.9	0.3±0.2	1.10±0.06	55±15	432
0.84	1.0±0.8	3.0±0.9	0.3±0.2	1.09±0.06	58±14	483
0.90	0.8±0.7	3.0±1.0	0.3±0.2	1.09±0.06	56±15	571
Average	1.3±0.5	3.4±0.4	0.5±0.2	1.09±0.00	50±6	

more conspicuously in the UV (Calvet & Gullbring 1998; Hartmann et al. 2016).

We show in Figure 4.7 optical fluxes for PDS 70 from Gregorio-Hetem & Hetem (2002) and fluxes in the Swift/UVOT U, uvw1, and uvw2 bands (Joyce et al. 2019). Except for one case, observations at uvw1 and uvw2 were obtained at different epochs. The V-I colors are similar to those of a K7 star from Pecaut & Mamajek (2013), indicating no extinction.

We also show in Figure 4.7 the total flux expected for PDS 70 when the emission from accretion shocks with $\dot{M}$ between $0.8\times10^{-10}\,M_\odot\,\mathrm{yr}^{-1}$ and $2.2\times10^{-10}\,M_\odot\,\mathrm{yr}^{-1}$ are added to the stellar flux. The accretion shock emission is calculated using the methods of Calvet & Gullbring (1998) for the PSD 70 mass and radius, and for one characteristic value of the energy flux in the accretion column $\mathcal{F} = 10^{12}\,\mathrm{erg\,cm^{-2}\,s^{-1}}$ (Ingleby et al. 2013). The intrinsic stellar spectrum is taken from the Weak T Tauri star HBC 427 (Ingleby et al. 2013), scaled to the stellar radius and distance. The WTTS spectrum includes emission from the stellar chromosphere, which is strong in young stars (Ingleby et al. 2011a). As shown in Figure 4.7, the observed Swift fluxes are consistent with the accretion rates estimated from the magnetospheric modeling of Hα (Table 4.3).

Joyce et al. (2019) obtained an accretion rate $\dot{M} \sim 6\times10^{-12}\,M_\odot\,\mathrm{yr}^{-1}$ using the correlation of the flux excess in the U band and the accretion luminosity from Venuti et al. (2014). As can be seen in Figure 4.7, the flux at the U band is dominated by stellar photospheric and chromospheric emission, as expected for low accretors Ingleby et al. (2011a), so we argue that this band is not optimal to obtain accretion shock emission in this star. In general, relationships between the U excess and the accretion luminosity cannot be calibrated at low levels of accretion and should not be used.

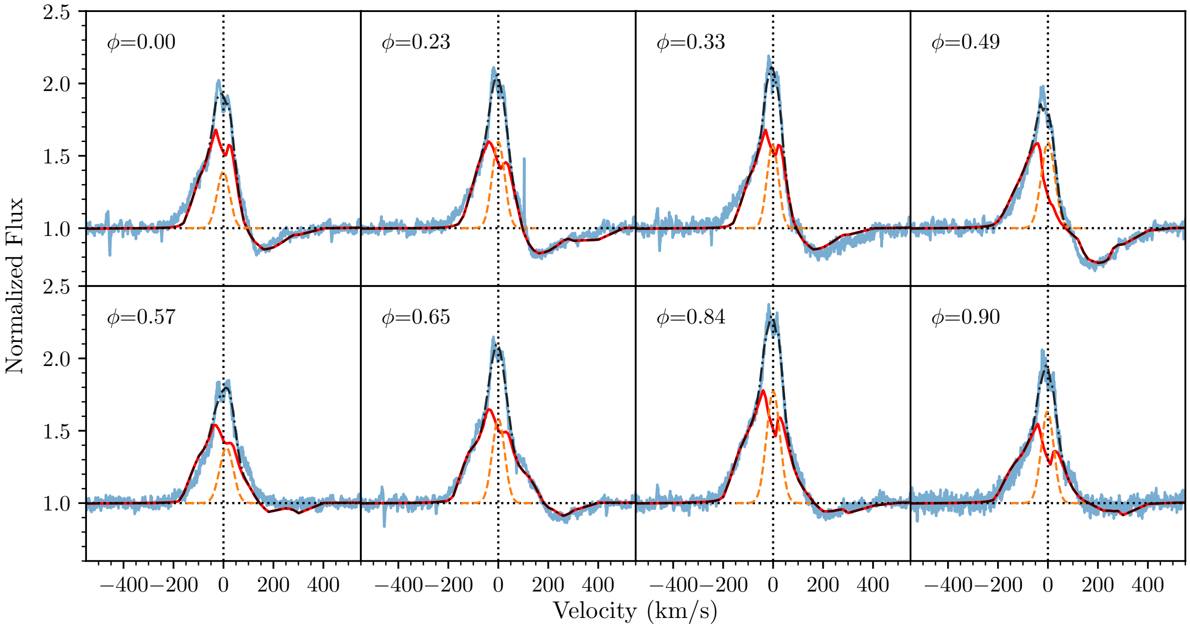

Figure 4.5 Line profiles of the representative best fits for each of the observed phases. The observation is shown in blue, and the magnetospheric model is shown in red. The dashed orange lines are the chromospheric contributions, with the total model profile shown in dashed-dot black lines.

4.4.2 The Stellar Mass Accretion Rate as a Potential Diagnostic of Disk Accretion Processes

Our analysis suggests that PDS 70 is accreting at a moderate rate of $\sim 10^{-10}\ M_{\odot}\mathrm{yr}^{-1}$. Where does this mass come from? Does the outer disk gas flow across the cavity, or is there a mass reservoir to sustain the stellar accretion in the inner disk?

Numerical simulations have shown that the outer disk gas, beyond the gap opened by planets, can flow into the inner regions of the disk. The mass flow rate depends upon various factors, including the number of planets responsible for the gap, planets' masses, planets' accretion efficiency, and protoplanetary disk thermodynamics (Lubow & D'Angelo 2006; Zhu et al. 2011; Müller & Kley 2013). In general, these numerical studies show that the mass flow rate across the gap is $1 - 100\ \%$ of the mass accretion rate beyond the gap (Lubow & D'Angelo 2006; Zhu et al. 2011; Müller & Kley 2013).

In order to examine if the outer disk gas can explain PDS 70's accretion rate, we first calculate the accretion rate of an unperturbed viscous accretion disk. We adopt the disk surface density and temperature profiles used in Bae et al. (2019):

$$\Sigma(R) = 2.7\ \mathrm{g\ cm^{-2}} \left(\frac{R}{40\ \mathrm{au}}\right)^{-1} \exp\left(-\frac{R}{40\ \mathrm{au}}\right) \tag{4.5}$$

and

$$T(R) = 38\,\mathrm{K}\left(\frac{R}{40\,\mathrm{au}}\right)^{-0.24}. \tag{4.6}$$

In Figure 4.8, we present the disk accretion rate, calculated as $\dot{M}_d = 3\pi\nu\Sigma$ where ν is the disk kinematic viscosity defined as $\nu = \alpha c_s^2/\Omega$. Here, α is the Shakura-Sunyaev viscosity parameter characterizing the mass transport efficiency (Shakura & Sunyaev 1973), c_s is the disk sound speed, and Ω is the angular frequency. At 70 au, beyond the common gap opened by PDS 70b and c, the accretion rate is

$$\dot{M}_d = 1.5 \times 10^{-10} M_\odot \mathrm{yr}^{-1}\left(\frac{\alpha}{10^{-3}}\right). \tag{4.7}$$

If the disk accretion is efficient (i.e., $\alpha \gtrsim 10^{-3}$) so the outer disk supplies gas at $\gtrsim 10^{-10}\ M_\odot\ \mathrm{yr}^{-1}$, it is thus possible that the stellar accretion is sustained by the mass reservoir in the outer disk, as the two planets within the gap are known to take only a small fraction of the supply ($\sim 10^{-11}\,M_\odot\,\mathrm{yr}^{-1}$; Wagner et al. 2018; Haffert et al. 2019; Thanathibodee et al. 2019b; Aoyama & Ikoma 2019). However, when the mass flow rate across the gap is significantly reduced and/or the disk has a low mass transport efficiency (i.e., $\alpha \ll 10^{-3}$), the stellar accretion rate of $\sim 10^{-10}\,M_\odot\,\mathrm{yr}^{-1}$ is difficult to explain with the outer disk mass reservoir. In this case, we may need to invoke an inner disk mass reservoir (e.g., dead zone) that can feed the star for a prolonged period of time with a low efficiency (Hartmann & Bae 2018). The presence of compact sub-millimeter continuum emission shown in ALMA observations (Long et al. 2018b; Keppler et al. 2019) may support this inner reservoir scenario.

Manara et al. (2019) used the planet population synthesis models of Mordasini et al. (2009, 2012) to make predictions for stellar mass accretion rates and disk masses and compare them with observations of the Lupus and Chamaeleon star-forming regions. Their disk models assume a viscosity parameter of $\alpha = 2 \times 10^{-3}$, and planets accrete the disk gas at a fraction of the disk viscous accretion rate. With the assumed viscosity parameter, the stellar accretion could be sustained by the outer disk reservoir, subject to a decrease in the presence of planets.

Their models, however, produce a larger fraction of weak accretors than observed in transition disks. As they already pointed out, one possible explanation to this conflict is that their prescription of gas accretion onto planets over-predicts the real accretion rate, and thus reduces the mass flow rate across the gaps more than it actually would. Instead, as we suggested above, this could be reconciled with an inner disk reservoir with a small α, as the stellar accretion in this case would be less sensitive to the formation of giant planets in the outer disk. It will be interesting to run low-viscosity counterparts of planet population synthesis models to explore this possibility.

In summary, since our current understanding of protoplanetary disk accretion physics is incomplete, we cannot conclude whether PDS 70's accretion rate is sustained by an inner or an outer disk reservoir. We note that our calculations here are based on an assumption that the disk has a uniform

α; other possibilities will be explored in future work. Future observations that can characterize the inner disk properties and search for potential inner disk winds, together with those that can constrain the level of turbulence in the outer disk, will help better understand the origin of PDS 70 accretion. In addition, observational searches of low accretors and accurate determination of $\dot{M}$ (Thanathibodee et al. 2018, 2019a) will help find the observational low limit of $\dot{M}$ to compare with expectations of exoplanets population models.

4.4.3 Origin of the Blueshifted Absorption in He I λ10830

The presence of a sub-continuum blueshifted absorption feature in the He I λ10830 line has been attributed to winds (Edwards et al. 2003, 2006). In particular, the narrow blueshifted absorption is interpreted as a wind coming from the inner disk. The co-existence of blueshifted and redshifted absorption with very weak emission in the line center has been observed for a few stars in the high-resolution survey of He I λ10830 line (Edwards et al. 2006). However, most of the stars in the surveys, and all of the stars with blue+red absorption, have high levels of accretion, $\dot{M} \geq 10^{-8}\,M_{\odot}\,\mathrm{yr}^{-1}$. Interestingly, PDS 70, with its very low accretion level, also shows a similar type of profile. In fact, in our ongoing survey of very low accretors, more than $\sim$10% of disk-bearing K-M TTS with weak Hα show blue+redshifted absorption. The velocity of the blueshifted absorption ($\sim -85\ \mathrm{km\,s^{-1}}$) is consistent with the wind coming from the inner disk.

We can estimate the mass loss rate from the wind by adopting the procedure outlined in Calvet (1997). For a line formed in the wind, the optical depth at a given velocity v is given by

$$\tau = \frac{\pi e^2}{m_e c}\frac{fc}{\nu_0}\frac{n_l(v)}{dv/dz}, \tag{4.8}$$

where f is the oscillator strength, ν_0 is the line frequency, n_l is the population of the lower level, and dv/dz is the velocity gradient. The mass loss rate is given by

$$\dot{M}_w \sim \Delta A v \mu m_H n_H(v) \sim \Delta A v \mu m_H \eta n_l(v), \tag{4.9}$$

where ΔA is the cross-section area of the wind at v, μ is the mean molecular weight, n_H is the number density of hydrogen, and $\eta \equiv n_H/n_l$. To the first approximation, $dv/dz \sim v/R_\star$ and $\Delta A \sim \pi(2R_\star)^2$ (Calvet 1997). We estimate the parameter η by calculating a typical fraction between the number density of the lower level of He I λ10830 to the total hydrogen number density. We use the C17.01 release of the software Cloudy (Ferland et al. 2017) to calculate the level populations in a slab of gas assuming that the ionization radiation is an X-ray with a blackbody temperature of 5×10^6 K and $L_X = 5 \times 10^{29}\,\mathrm{erg\,s^{-1}}$ consistent with the luminosity measured by

Swift (Joyce et al. 2019).[3] Assuming that the wind is $\sim 10\,R_\star$ from the star with a thickness of $1\,R_\star$, we find that $\eta \sim 10^7$ for a relevant range of n_H across the slab. With $\tau \sim 0.5$, estimated from the depth of the feature, and $\mu = 2.4$, we find that $n_l(v = 85\ \mathrm{km\,s^{-1}}) \sim 55\,\mathrm{cm^{-3}}$ and $\dot{M}_w \sim 10^{-11}\,M_\odot\,\mathrm{yr}^{-1}$. This mass loss rate is consistent with that expected from a MHD inner disk wind in which $\dot{M}_w \sim 0.1\dot{M}_{acc}$, suggesting that the blueshifted absorption in He I λ10830 forms by a similar mechanism as in high accretors (Calvet 1997; Edwards et al. 2006; Kwan et al. 2007). Since the blueshifted velocity is high, it is unlikely that the feature is formed in photoevaporative winds (c.f. Alexander et al. 2014). The features in the He I λ10830 lines of low accretors are described in detail in Chapter 5.

Our detection of wind and accretion signatures confirms the existence of gas in the inner disk around PDS 70. Long et al. (2018b) searched for first overtone CO lines in low resolution near-IR spectra and could not find them, from which they inferred that the inner disk of PDS 70 was gas poor. However, the lack of detection could be due to the difficulty of separating the disk emission from the intrinsic photospheric CO absorption lines (Calvet et al. 1991). Observations of ground state CO lines or of fluorescent H_2 lines can help confirm the presence of gas in the inner disk of PDS70.

4.5 Summary and Conclusions

We have analyzed TESS photometry, archival HARPS spectra, and a FIRE near-IR spectrum of PDS 70, a $\sim 5\,$Myr star with two confirmed giant planets forming in its circumstellar disk. The TESS variability is consistent with rotational modulation of spots on the stellar surface, indicating magnetic activity as found in other young stars. The period derived from TESS observations and the measured $v \sin i$ yield an inclination to the line of sight consistent with the disk inclination derived from submillimeter data, indicating that the rotational axes of the star and the disk are parallel to each other within uncertainties. We find redshifted absorption features in the He I λ10830 line and in Hα, confirming that the star is accreting. We model the Hα profiles assuming magnetospheric accretion and find mass accretion rates in the range $0.6 - 2.2 \times 10^{-10}\,M_\odot\,\mathrm{yr}^{-1}$. These values of $\dot{M}$ predict a UV flux from the surface accretion shocks consistent with the flux observed in Swift UV bands. We analyze changes in the geometry of the magnetospheric flows with rotation phase and find that it could be non-axisymmetric, consistent with a small tilt between the stellar rotation axis and the magnetic axis. The relatively high values of the mass accretion rate may indicate the need for an additional mass reservoir in the disk to feed the flows onto the star. We estimate the mass loss rate from the blueshifted absorption feature in the He I λ10830 line and find

---

[3] Joyce et al. (2019) model the X-ray spectra with two temperatures. Here we adopted a temperature inside the range of those temperatures.

that the rate and the velocity of the line are consistent with the wind being driven by accretion. The detection of accretion and winds confirms the existence of gas in the inner disk.

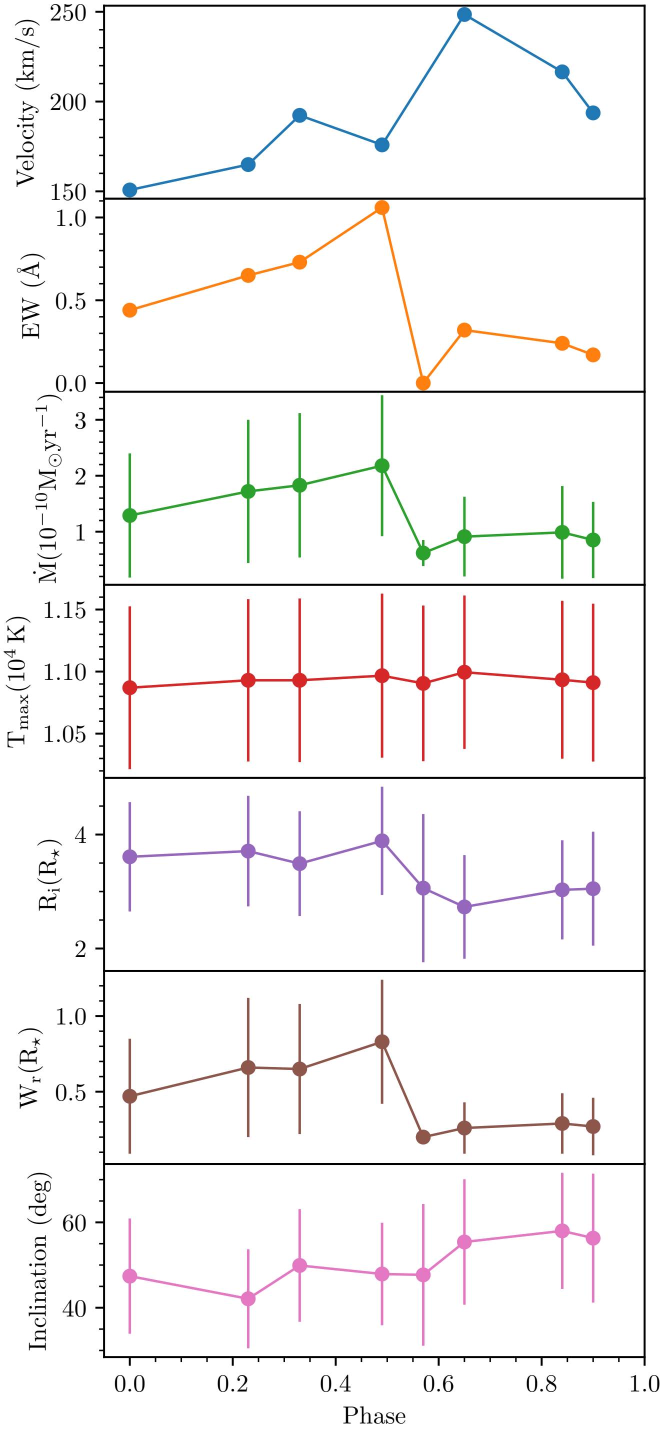

Figure 4.6 Variability of line profile and accretion properties. The properties of the redshifted absorption component in the observed line profile (top two rows) and that of the magnetospheric accretion model fit parameters are plotted as a function of rotation phases. The velocity of the redshifted absorption is excluded for phase 0.57 since the feature is undetected.

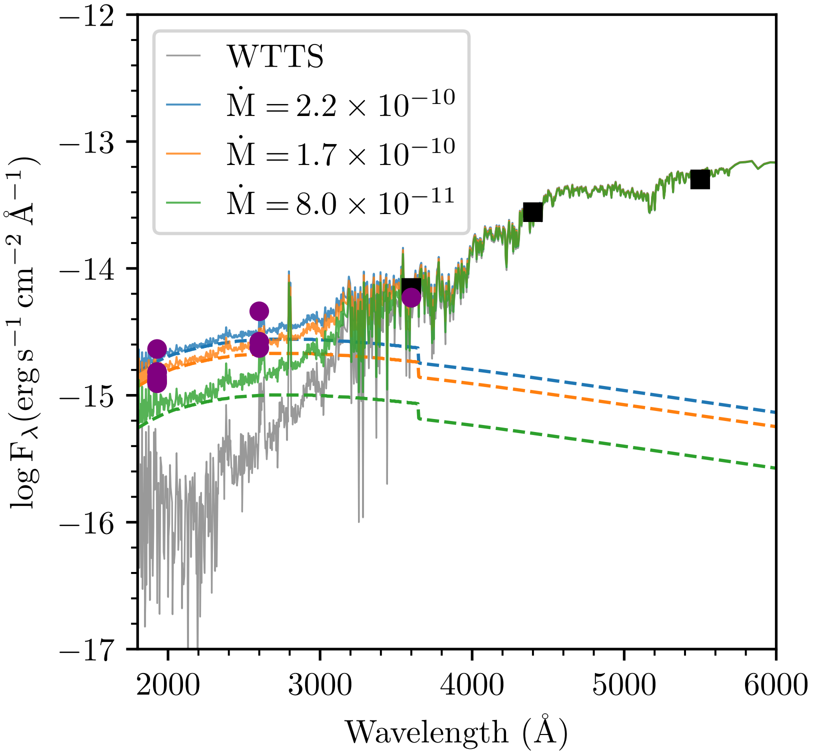

Figure 4.7 Optical and UV fluxes of PDS 70 and model spectra, including emission from the accretion shock. The optical fluxes (black squares) are taken from Gregorio-Hetem & Hetem (2002) and the Swift U, uvw1, and uvw2 fluxes (purple) from Joyce et al. (2019). The gray line is the spectrum of the weak T Tauri star HBC 427 with the same spectral type as that of PDS 70; we added the expected emission from the accretion shock to this spectrum. The solid lines show the total emission for different mass accretion rates and the dashed line of the same color showing only the shock emission.

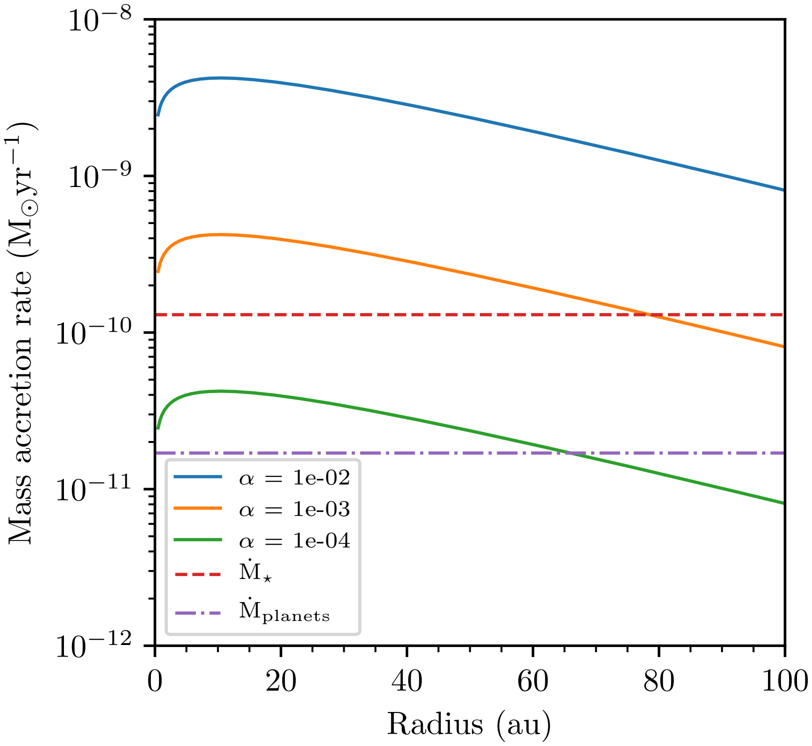

Figure 4.8 The accretion rates of a viscous disk as a model for PDS 70. We adopt disk surface density and temperature profiles described in Equations (4.5) and (4.6). Three different viscosity parameter values are assumed: $\alpha = 10^{-2}, 10^{-3}$, and 10^{-4}. The horizontal lines show the mass accretion rate of the star (red dashed line) and the total mass accretion rates of the planets (purple dash-dotted line).

CHAPTER 5

A Census of the Low Accretors. I. The Catalog

This chapter has been submitted to, and is under review by, the Astronomical Journal, in collaboration with Nuria Calvet, Jesús Hernández, Karina Maucó, and César Briceño. It is adapted and reproduced here.

Abstract

Observations have shown that the disk frequency and the fraction of accreting pre-main sequence stars decrease with the age of the population and that some stars appear to have disks while their accretion has stopped. Still, it is unclear how disk-bearing stars stop their accretion. To provide insight into the last stages of accretion in low-mass young stars, we conducted a survey of disk-bearing stars that are thought to be non-accretors to identify stars still accreting at very low rates. Here we present a catalog of the survey of disk-bearing non-accreting stars in Chamaeleon I, Orion OB1, Upper Scorpius, γ Velorum, and Upper Centaurus Lupus, using He I λ10830 as a sensitive probe of accretion. We classify the line profiles into six types and argue that those showing redshifted and/or blueshifted absorption are still accreting. Using these classifications, we found that, among disk-bearing stars previously classified as non-accretors, at least 20-30% are still accreting, with a larger fraction of those at younger population ages. While the difference between the outer disk signature and accretion status is unclear, we find a difference between the inner disk excess and accretion status. There is no preference in the spectral type of the newly identified accretors, suggesting that the processes inhibiting accretion do not directly depend on mass in the typical mass range of T Tauri stars. Lastly, we found that at a low accretion level, the Hα width at the 10% height criteria mischaracterizes a larger fraction of accretors than the line's equivalent width.

5.1 Introduction

Born in molecular clouds, systems of stars and their protoplanetary disks are left to evolve independently after their birthplace has dispersed. After a few million years, these young disks appear in diverse ways, showing different types of gaps, rings, and substructures in panchromatic observations (e.g., Andrews 2020). Several physical and chemical processes are known to be drivers of disk evolution, including, for example, mass accretion, mass loss through photoevaporation or winds, dust growth and settling, and planet formation (e.g., Alexander et al. 2014; Williams & Cieza 2011). Each of these processes occurs in different timescales and affects the disks and their stars in different ways.

One of the key processes occurring during the disk lifetime is mass accretion. While the processes that drive accretion and the momentum transport in the disks (disk accretion) are still unclear, much is known about the mass accretion from the disk onto the star (stellar accretion) that effectively reduces the amount of mass in the disk. For low-mass stars (T Tauri Stars; TTS), their strong magnetic fields give rise to magnetospherically-controlled accretion, by which mass from the inner edge of the disk flows along the field lines onto the central star (Hartmann et al. 2016). Accretion signatures such as emission lines form in these flows, and they are used to identify accreting stars and to measure the mass accretion rates in a given population (e.g., Muzerolle et al. 1998b; White & Basri 2003; Natta et al. 2004).

The presence of dust in the disk results in flux excess above the stellar photosphere in the infrared. Infrared colors are used to show the diversity and evolutionary stages of the disk and to identify disk-bearing stars in a population (e.g., Meyer et al. 1997; Luhman 2004; Hernández et al. 2007; Esplin et al. 2014). Studies of a large number of star-forming regions, such as those by Fedele et al. (2010) and Briceño et al. (2019), used accretion and disk diagnostics to calculate the frequencies of accreting stars and disk-bearing stars as a function of the population age and found that these frequencies decrease with time. However, the observed frequency of accretors is lower than that of disks at any given age, suggesting that the evolutionary timescale of dust in disks is longer than that of accretion and that some disk-bearing stars are no longer accreting. Nevertheless, it is unclear what processes are responsible for stopping accretion.

One of the processes proposed to stop accretion is photoevaporation. In this model, gas in the upper regions of the disk is heated by stellar high-energy photons and gradually escapes from the system (Alexander et al. 2014). At some point, the mass accretion rate through the disk decreases to the level of the mass-loss rate from photoevaporation, and no mass is left to feed the inner regions of the disk. As a result, accretion stops in a short timescale ($\sim 10^5$ yr). Still, the level of photoevaporative mass loss rate is unclear. For example, Manzo-Martínez et al. (2020) found that the mass loss rate of $\sim 1 - 3 \times 10^{-9}\, M_\odot\, \mathrm{yr}^{-1}$ is consistent with the observed disk fraction in a wide age range. Nevertheless, mass accretion rates much lower than these limits are still observed in many sources (Thanathibodee et al. 2018, 2020; Manara et al. 2016; Hartmann et al. 2016).

Planets are a natural outcome of the star-formation process, and indeed the Kepler mission has shown that a significant fraction of stars hosts at least one planet (e.g., Winn & Fabrycky 2015).

The formation of giant planets in disks could be a catalyst for stopping disk and stellar accretion since some mass accreting through the disk needs to go into the forming planets. Models of accreting disks with giant planets (Zhu et al. 2011) as well as planet-population synthesis model (Manara et al. 2019) have shown that the presence of giant planets can significantly decrease the mass accretion rate of the host stars, even though they still host disks with a reasonably high mass. However, the effect of giant planets on stellar mass accretion rate could be over-predicted, as in the case for PDS 70 (Thanathibodee et al. 2020), in which the mass accretion rate of the star is still much higher than the combined mass accretion rates of the two giant planets (Thanathibodee et al. 2019a).

The properties of the star itself could also stop accretion onto the star. For accretion to occur, the disk truncation radius needs to be inside the corotation radius, defined as the radius at which the Keplerian orbital period equals the stellar rotation period (Ghosh et al. 1977; Ghosh & Lamb 1979b; Koenigl 1991). The star enters the "propeller" regime when the corotation radius is comparable to the magnetic radius (i.e., the truncation radius, Romanova et al. 2009; Lii et al. 2014; Romanova et al. 2018). These radii depend on the strength of the magnetic field, the rotation period of the star, and the mass accretion rate, all of which evolve with time. In the propeller regime, the mass that reaches the disk-magnetospheric boundary is ejected through winds and either leaves the system or falls back onto the disk. A small amount of matter may diffuse inward and accrete onto the star. Due to the dynamic nature of the system, the accretion may occur sporadically as matter accumulated at the boundary pushes the disk inward (Romanova et al. 2018).

The propeller regime can be achieved by a decrease in the mass accretion rate (Romanova et al. 2018) since the truncation radius increases as the accretion rate decreases. On the other hand, the disk-locking mechanism ensures that the corotation radius stays the same as long as the star is accreting (e.g., Vasconcelos & Bouvier 2015). The effect of this scenario is that the star would evolve toward the propeller regime over time, reaching the episodic accretion/outflow as a strong propeller. Although T Tauri stars in the propeller regime have been observed (e.g., Petrov et al. 2021; Potravnov et al. 2017), it is unclear if this effect alone would be responsible for stopping accretion, or the processes that deplete the disks, e.g., photoevaporation or planet formation, would be much more significant.

To answer the question of how accretion stops, we need to assemble and study in detail systems in the final stages of accretion. These are star-disk systems accreting at a very low, nearly undetectable accretion rate – the low accretors.

One of the challenges in identifying stars accreting at very low rates is the activity of the stellar chromosphere. In low-mass young stars, the same magnetic fields that allow magnetospheric accretion to occur also induce strong chromospheric activity, resulting in emission in the UV continuum and optical spectroscopic lines in excess of photospheric fluxes. At low accretion levels, chromospheric emission could dominate the continuum and affect lines typically used as accretion indicators. Therefore, the measurement of accretion is hindered and limited by the chromosphere, as shown by Ingleby et al. (2011b) and Manara et al. (2013, 2017a). An accretion indicator that can mitigate the contamination from the chromosphere is needed to search for low accretors.

Unlike traditional accretion indicators such as the U-band excess and Hα fluxes and widths, the He I λ10830 identifies accretion using only the morphology of the line (Edwards et al. 2006). Specifically, redshifted absorption at a velocity comparable to that of the star's free-fall velocity implies that material absorbing photons is moving away from the observer, i.e., accreting onto the star. Since the lower level of the He I λ10830 line is metastable, electrons accumulate on it, so absorption features can easily appear. A blueshifted feature can also be used to probe stellar/MHD winds, (Edwards et al. 2003) which correlate with accretion (Hartigan et al. 1995). Since the redshifted or blueshifted features appear at high velocities, they can be distinguished from the chromospheric feature at the line center, making the He I λ10830 line a very sensitive probe of accretion.

Here, we report the results of a survey to search for low accretors using the He I λ10830 line as the probe for accretion. We describe the selection criteria, the properties of the targets, and the observations in Section 5.2. In Section 5.3, we show the main results. We discuss the implications of the results in Section 5.4 and conclude our study in Section 5.5.

5.2 Targets and Observations

As discussed earlier, the fractions of disk-bearing stars are systematically larger than the fractions of accretors (Classical TTS; CTTS). Fedele et al. (2010) found that the e-folding time of disks with IR excess and accretion are 3 Myr and 2.3 Myr, respectively. Briceño et al. (2019) arrives at a similar result of 2.1 Myr for the decay of accretion, based on a self-consistent study of stars in the same star-forming complex. From these values, we estimate that $\sim 5-15\%$ of a given population are non-accreting TTS (Weak TTS; WTTS) that still have disks, depending on the age. We aim to observe a sample of these stars to look for the low accretors.

5.2.1 Target Selection

We focus our survey in the nearby star-forming regions within 500 pc, including Chamaeleon I, Orion OB1 (including cloud A/B, OB1a/b and their sub-groups, such as the 25 Ori cluster and the σ Orionis cluster), Upper Scorpius, γ Velorum, and Upper Centaurus Lupus. For comparison and analysis regarding age, we group the stars into two age bins. Table 5.1 shows the properties of each group and the number of stars included in our sample.

Table 5.1 Stellar Group Properties

Group	Age (Myr)	No. of members	No. of known accretors	References Age/members/Acc	No. observed
Chamaeloen I	2	229	67	(1)/(1)/(2)	12
Ori Cloud B	2.5	68	20	(3)/(3)/(3)	4
σ Ori	3	297	65	(4)/(5)/(5)	12
Ori Cloud A	3.3	222	61	(3)/(3)/(3)	27
Ori OB1b	5.0	556	65	(3)/(3)/(3)	45
Upper Sco	5-11	1631	31	(6)/(6)/(7)	43
γ Vel	7.5	208	8	(8)/(9)/(10)	3
25 Ori	7.6	223	10	(3)/(3)/(3)	2
HD 35762	8.0	86	4	(3)/(3)/(3)	3
Ori OB1a	10.8	844	51	(3)/(3)/(3)	16
Upper Cen Lupus	16±2	154	5	(11)	3

References. — (1) Luhman et al. (2008); (2) Manara et al. (2017b); (3) Briceño et al. (2019); (4) Hernández et al. (2007); (5) Hernández et al. (2014); (6) Luhman et al. (2018); (7) Manara et al. (2020); (8) Hernández et al. (2008); (9) Jeffries et al. (2014); (10) Frasca et al. (2015); (11) Pecaut & Mamajek (2016)

To select candidates with a low level of accretion, we assembled a census of the stellar population in each group, taking those members for which either high- or low-resolution optical spectra were available. For stars with only low-resolution spectra (e.g., those in Orion OB1 and Upper Sco), we selected stars for which the equivalent width of the Hα line was at or below the traditional threshold for accretion at their spectral type (White & Basri 2003). For stars with high-resolution Hα profiles for which the width at the 10% peak of the line (W_{10}) were available, we selected those with W_{10} at or below $\sim 270\ \mathrm{km\,s^{-1}}$ (within the uncertainty), the threshold set by White & Basri (2003). By construction, these included some accretors if the empirical threshold for very low mass stars (M5-M8) by Jayawardhana et al. (2003) at $200\ \mathrm{km\,s^{-1}}$ is used. In Table A.1, we marked stars with W_{10} greater than $200\ \mathrm{km\,s^{-1}}$ that are included in our sample.

The final selection was completed by including only stars for which the spectral energy distribution (SED) showed evidence of having a primordial disk, either full, evolved, or transitional (Espaillat et al. 2014). This was done primarily by selecting the stars identified as having disks in the original population studies for each group, using either Spitzer or WISE photometry. When disk identifications were not available, we combined the 2MASS (Skrutskie et al. 2006) and WISE catalogs (including ALLWISE and unWISE, Wright et al. 2010; Schlafly et al. 2019) to derive near-IR and mid-IR colors and probe for dust emission from disks. Figure 5.1 shows our targets in the accretion-indicator (EW(Hα) or W_{10}) and infrared color space. Some stars evidently show

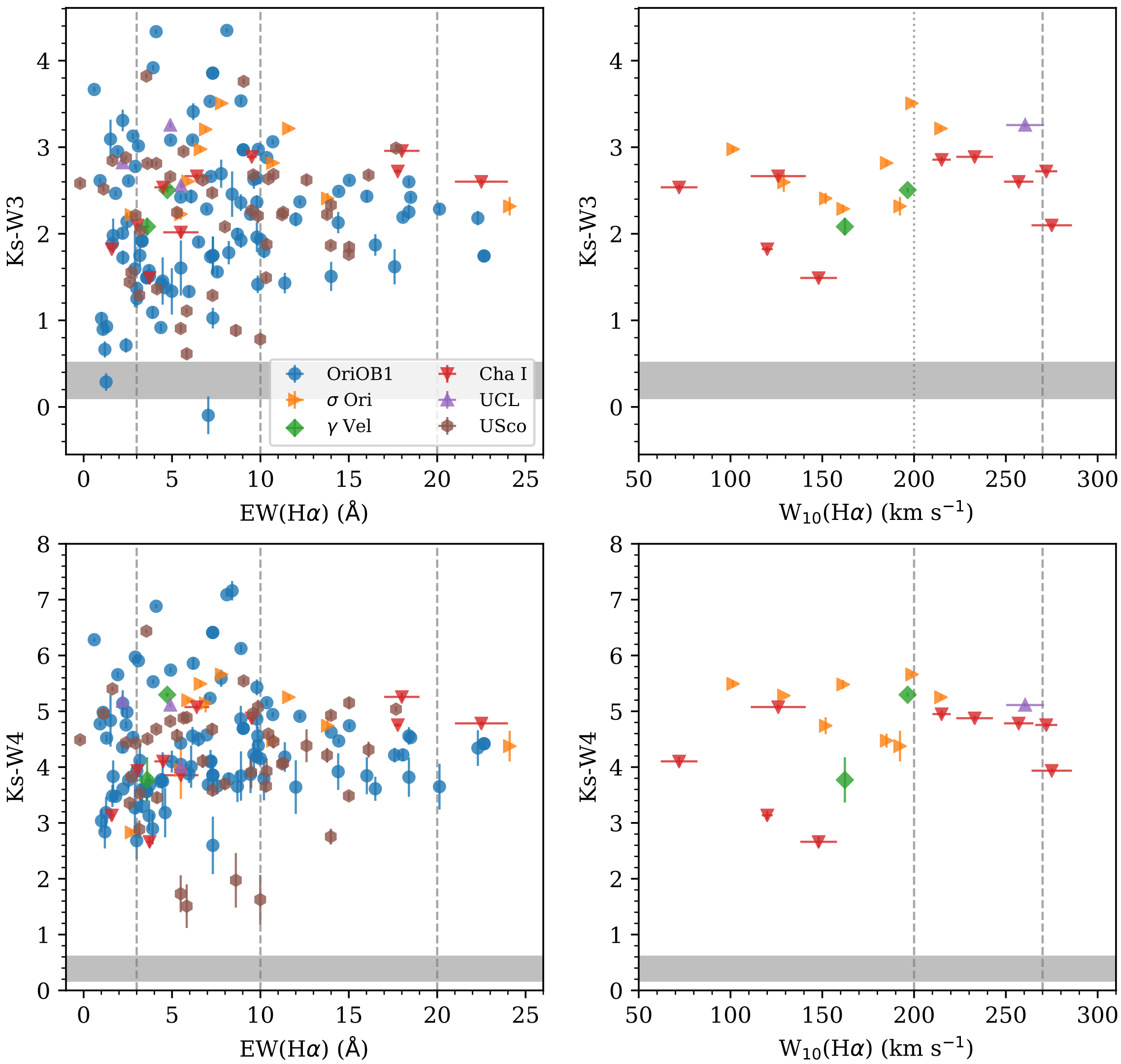

Figure 5.1 Survey targets plotted in the accretion indicator-disk indicator space. The vertical lines on the left column are White & Basri (2003)'s thresholds of accretors for spectral types K5 (3 Å), M2.5 (10 Å), and M5.5 (20 Å). On the right column, the vertical lines are the thresholds of accretors adopted by White & Basri (2003) (270 $\mathrm{km\,s^{-1}}$) and Jayawardhana et al. (2006) (200 $\mathrm{km\,s^{-1}}$). The shaded regions correspond to the photospheric colors for stars of spectral types K0-M5 from Pecaut & Mamajek (2013). See § 5.2.1 for the selection criteria applied in each stellar association.

a low level of excess in one of the colors, but they are included in the sample as they still show excesses in another color.

For consistency in further analysis, we re-determined the stellar parameters for all of the targets using only the spectral type and extinction value from the literature. We first estimate the effective temperature by adopting the SpT-Teff scale of Pecaut & Mamajek (2013) for spectral types M3 and earlier. For later type stars, we adopted the scaling of Herczeg & Hillenbrand (2015) since they included much later spectral types than Pecaut & Mamajek (2013). We then calculated the apparent bolometric magnitude using the extinction-corrected J band magnitude and J-band bolometric correction from Pecaut & Mamajek (2013) and Herczeg & Hillenbrand (2015). For stars for which the extinction is reported in other bands, we converted A_λ to A_J using the Cardelli et al. (1989) extinction law with R_v=3.1. The stellar bolometric luminosity was then calculated from the bolometric apparent magnitude and Gaia EDR3 geometric distances from Bailer-Jones et al. (2021). We adopted the mean population distances for stars without Gaia EDR3 parallaxes.

Using the luminosity and effective temperature, we then calculated stellar radii $R_\star$ using the Stefan-Boltzmann law. We determined the masses of the stars $M_\star$ using the MassAge code (Hernández, et al. in prep.), which uses the pre-main sequence isochrone of MIST (Choi et al. 2016; Dotter 2016). Finally, we calculated the free-fall velocity by

$$v_{ff} = \sqrt{\frac{2GM_\star}{R_\star}\left(1 - \frac{R_\star}{R_i}\right)}, \tag{5.1}$$

where R_i is the infall radius, assumed to be $5\,R_\star$ (Calvet & Gullbring 1998).

In the following sub-sections, we describe the source catalog for each region, including the adopted selection criteria and the relative completeness. We compiled the stellar properties of our targets in Table A.1.

5.2.1.1 Orion OB1

The targets in the Orion OB1 association were selected from the CIDA Variability Survey of Orion OB1 (CVSO, Briceño et al. 2019). These targets included stars in the Orion A and B clouds, the Orion OB1a and OB1b sub-associations, and the 25 Ori and HD 35762 stellar groups. We first selected stars classified by Briceño et al. (2019) as type W (non-accretor) and type CW (borderline accretor-non accretor), based on equivalent widths of the Hα line (White & Basri 2003) in low resolution spectra. The CW type was introduced based on the possibility that the Hα line was variable, and so a star near the threshold could either be CTTS or WTTS, depending on the time of the observation. Among these stars, we selected those with Ks$-$W3 and/or Ks$-$W4 color larger than 1.5 magnitudes, adopted from the color threshold of disks studied by Luhman & Mamajek (2012); Esplin et al. (2014). Our sample includes all W and C/W type stars in the CVSO with Ks$-$W3 $\geq$ 1.5 that are brighter than a 2MASS J magnitude of 13.5. We also included eight stars with J$>$ 13.5. Since later-type stars are generally fainter in the J band, our sample is biased toward the brighter, earlier spectral types.

5.2.1.2 σ Orionis

The sample from σ Ori was selected from all of the weak accretor candidates identified by Hernández et al. (2014). These stars have high-resolution Hα observations that show W_{10} $< 270\ \mathrm{km\,s^{-1}}$, so they would be classified as non-accretors according to White & Basri (2003). However, their IRAC colors are consistent with having primordial disks.

5.2.1.3 γ Velorum

We selected the γ Vel sample from the Gaia-ESO survey (Frasca et al. 2015). With high-resolution spectrographs on ESO telescopes, Frasca et al. (2015) measured W_{10} for a large number of stars in the group and also determined their spectral type. We cross-matched the Frasca et al. (2015) catalog with the ALLWISE catalog and used the Ks$-$W3 color to establish the presence of disks. Our targets were those with W_{10} less than $270\ \mathrm{km\,s^{-1}}$ and Ks$-$W3 $\geq$ 1.5. We also included 2MASS J08094701-4744297, a K0 member of γVel (Hernández et al. 2008), which was not included in the Frasca et al. (2015) study. The IR colors are consistent with a disk-bearing star, but its Hα is in absorption with a slight central reversal.

5.2.1.4 Chamaeleon I

Seven candidates in this group were selected from the Gaia-ESO survey of Sacco et al. (2017) using the same criteria as for the γVel targets, i.e., stars having $W_{10} \leq 270\ \mathrm{km\,s^{-1}}$. One target, 2MASS J11004022-7619280 (Sz 8), was removed from the candidate list since Luhman (2004) found that its EW(Hα) is 67 Å, which is significantly larger than the accretor threshold of EW=20 Å for its spectral type of M3.75. Five additional targets were selected from the Esplin et al. (2017) compilation of members in Cha I; two of these targets were classified as WTTS using W_{10} (Nguyen et al. 2012), and another three were selected using the Hα equivalent width reported by Luhman (2004). Ks$-$W3 $\geq$ 1.5 criterion was used to select targets with disks.

5.2.1.5 Upper Centaurus Lupus

The three targets in this group were selected by cross-matching the Sco-Cen member list published by Pecaut & Mamajek (2016) with the ALLWISE catalog. The equivalent widths of Hα measured by Pecaut & Mamajek (2016) were used as a selection criterion, in addition to the IR colors. The well-known star PDS 70 is among these targets. We included this disk-bearing star in our analysis since it could have been classified as a non-accretor using either W_{10} or EW, without a detailed analysis of the line profile (Thanathibodee et al. 2020).

Table 5.2. Log of Observations

Name	RA	Dec	Obs. Date	Airmass	Exp. Time	SNR
CVSO 267	05:02:17.48	−04:08:25.6	2018-11-24	1.12	317.0	166.9
CVSO 288	05:06:49.89	−03:54:33.1	2020-01-09	1.32	422.8	120.2
CVSO 298	05:08:57.73	−01:29:16.1	2020-01-11	1.33	422.8	89.8
CVSO 378	05:17:37.15	+05:59:48.3	2020-01-11	1.35	422.8	79.4
CVSO 415	05:18:43.99	+00:53:45.4	2020-01-11	1.32	443.8	66.8

Note. — The exposure times are the combined values from two nodding positions. Table 5.2 is shown in its entirety as Table A.2 in Appendix A. A portion is shown here for guidance regarding its form and content.

5.2.1.6 Upper Scorpius

The targets in this group were selected from the compiled census of Upper Sco by Luhman et al. (2018) and Esplin et al. (2018). First, we selected stars that were classified as having disks with types “full”, “evolved”, or “transition”, using magnitude excess in W2, W3, W4, and/or IRAC. We downloaded the low-resolution optical spectra published by Luhman et al. (2018) and calculated the EW(Hα) for each candidate using IRAF. The final targets included in our survey are those with EW lower than the White & Basri (2003) thresholds.

5.2.2 Observations

We observed the targets during the 2018A, 2019A/B, and 2020A/B semester using the FIRE spectrograph (Simcoe et al. 2013) at the Magellan Baade Telescope at the Las Campanas Observatory in Chile. We used the 0.6” slit in the echelle mode, which provided a spectral resolution of R$\sim$6000 ($\sim 50\,\mathrm{km\,s^{-1}}$) for the wavelength range $0.9 - 2.4$ μm simultaneously. The sampling of the spectrograph is 4 pixels per resolution element (i.e., $12.5\ \mathrm{km\,s^{-1}}$/px). For each target, we obtained the spectra in two nodding positions. A nearby telluric standard star was observed within ~ 1 hr of the science targets at the same airmass. We used the IDL-based FIREHOSE data reduction pipeline (Simcoe et al. 2013) to reduce the raw data, providing telluric-corrected and (vacuum) wavelength-calibrated spectra. Table 5.2 shows the log of observations. Since some stars were observed more than once, we have 183 observations in total.

5.2.3 Companions in the Sample

We cross-matched our targets with multiplicity studies in the regions that we observed (Kounkel et al. 2019; Tokovinin & Briceño 2020; Tokovinin et al. 2020; Caballero et al. 2019; Barenfeld et al. 2019). We found that six of our targets are close binaries that were not resolved by the FIRE spectrograph. These include four photometrically resolved binaries CVSO 1842 (0.624"), CVSO 952 (0.68"), J16123916 (0.12"), and J16253849 (0.88"), as well as two spectroscopic binaries CVSO 1695 and CVSO 1745. For this survey, we treated them as single stars.

We also found resolved binaries during our survey that were not resolved by the CVSO but were resolved by Gaia EDR3 or were previously identified pairs. These pairs include CVSO 2071, CVSO 1567, CVSO 1600, and the known binary CVSO 1415 (V716 Ori) and CVSO 1747 (V861 Ori). We denoted the newly identified pairs with their relative direction (e.g., E/W, NE/SW), while we referred to the known pairs using their A/B designation. We analyzed their accretion properties separately.

5.3 Analysis and Results

5.3.1 Spectra Normalization and Subtraction

In order to detect the He I $\lambda10830$ line in the spectra of the targets, it is crucial to separate the line profiles from the underlying photospheric spectra of the stars. We used the PHOENIX model spectra (Husser et al. 2013) for the photosphere. To compare the observed spectra and the corresponding model spectra, we interpolated in the grid of PHOENIX spectra using the stellar effective temperature and gravity. Comparing the template spectra, we found a weak dependence on the value of $\log g = 4.0$, so we adopted a representative value of $\log g = 4.0$ for all template spectra. Since we are only interested in the He I $\lambda10830$ line profile and its features, we normalized the continuum of both the observed and template spectra to unity, removing the large-scale shape. We limited the observed spectra to the range $\lambda \sim 9900 - 11100\,\text{Å}$ (e.g., order 24-27 of the spectrograph) to avoid strong atmospheric absorption features just outside this wavelength range. We determined the continuum by smoothing the spectra using a Savitzky-Golay filter with large box size. The filter smoothed out typical photospheric absorption lines and chromospheric and magnetospheric emission lines so that the resulting spectra were that of the pseudo-continuum. The observed normalized spectra were then obtained by dividing the reduced spectra by the continuum.

The high resolution allows for better identification of the continuum in the template spectra since most photospheric lines are resolved. To detect the continuum, we fitted the spectra using low-order polynomials, divided the spectra by the result and identified the points below 1σ and above 3σ from the median. The final continuum was determined by fitting the spectra exclud-

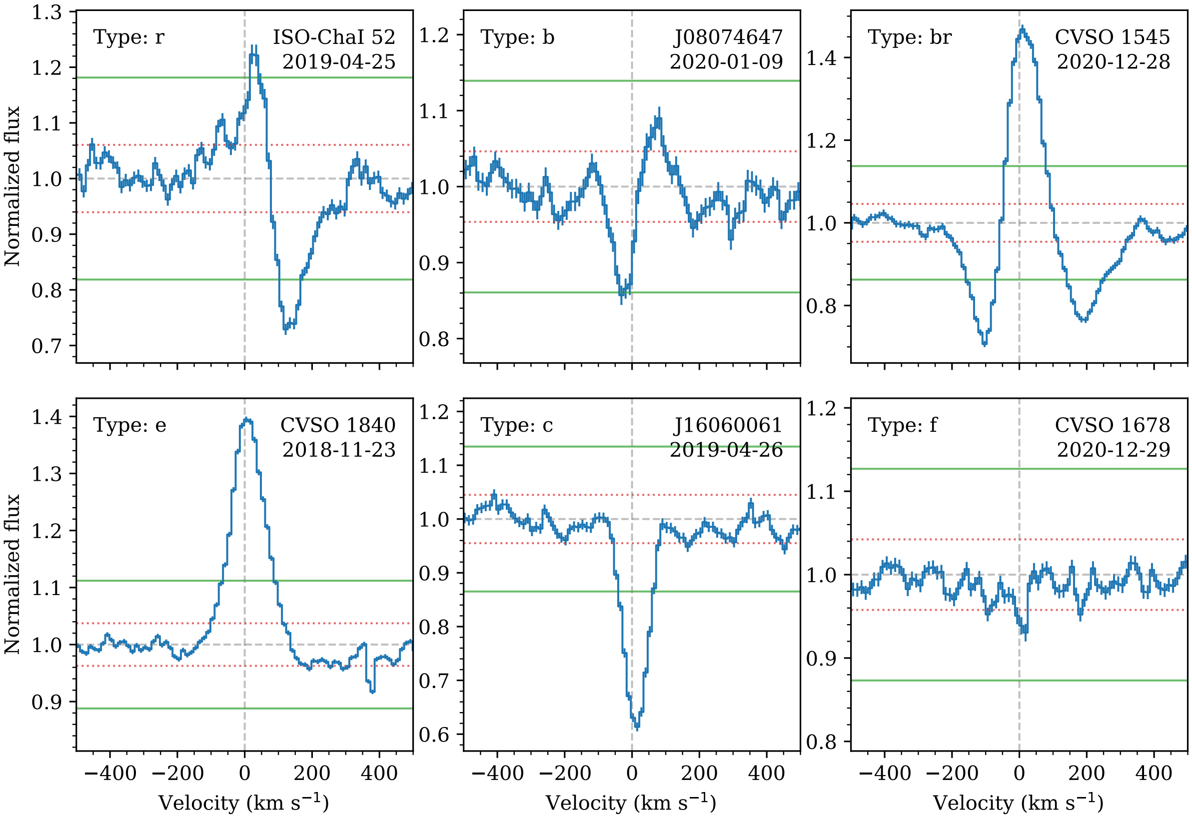

Figure 5.2 Examples of the different types of He I λ10830 line profiles found in this survey. We identify stars with profiles with types as in the upper row with accreting stars, whereas those in the lower row we describe as non-accretors. The horizontal lines show the level of uncertainty from the continuum. The red dashed lines specify the flux at $1\sigma_t$ from the continuum, and the solid green lines are at $3\sigma_t$. Only (absorption/emission) features where their extrema are greater than $3\sigma_t$ away from the continuum are considered detection.

ing the points identified earlier; the normalized template spectra were obtained by dividing the initial spectra by the continuum. We then convolved the spectra to R=6000 to be used for cross-correlations and spectral subtractions.

We obtained the apparent radial velocity (RV) of the stars by calculating the cross-correlation function (CCF) between the normalized template and the normalized observed spectra and fitting the peak of the CCF using a Gaussian model. We then applied the RV shift to the observed spectra. The residual spectra were obtained by

$$F_{\lambda,res} = F_{\lambda,obs} - F_{\lambda,templ} + 1.0. \tag{5.2}$$

We considered two sources of uncertainty in this analysis, both derived from the empirical data. First, the uncertainty associated with the observation within $\pm 450\ \mathrm{km\,s^{-1}}$ from line center ($\sigma_l =$

$1/SNR$), which was calculated directly from the resulting spectra from the reduction pipeline. Second, the uncertainty in determining the continuum level (σ_{con}) arises from uncertainties in spectral type, radial velocity, and rotational velocity of the star. Here we adopt a very conservative σ_{con}, such that 95% of the points in the normalized spectrum, excluding the region of the He I line, are within 1σ from unity. Since the SNR of the observation is generally greater than 20 and much higher in most cases, σ_{con} is the dominant source of uncertainty. The sum of these uncertainties is then

$$\sigma_t = \sqrt{\sigma_l^2 + \sigma_{con}^2}. \tag{5.3}$$

We considered a feature in the line profile as detected if its extrema are at least $3\sigma_t$ from the continuum, taking into account the uncertainty at that pixel.

The discrepancy between the photospheric features of the observations and the templates can be seen by features in the residual spectra (e.g., Fig. 5.2, A.1). Such discrepancy may be introduced by effects discussed above. Our conservative adoption of the uncertainty of the continuum helps cover the uncertain properties of the stars that results in the incomplete subtraction of the continuum by the adopted template.

5.3.2 Morphological Classification of the He I λ10830 Line Profile

To try to infer accretion properties via the He I $\lambda10830$ line, we classify the line profiles into six types, based on the detection of blue/redshifted features. Here we list the properties of each type, and Figure 5.2 shows examples of the profile types.

Type *r* – redshifted absorption. The line profile shows redshifted absorption below the continuum, covering a range of velocities comparable to free-fall velocities, significantly greater than $25\,\mathrm{km\,s^{-1}}$ (0.5 resolution element/2 pixels) from the line center. The type includes profiles with or without emission at the line center or the blue wings. They also include stars with distinctive central absorption that have broad red wings.

Type *b* – blueshifted absorption. The lines show detectable blueshifted absorption with absolute values of the velocity equal or greater than $25\,\mathrm{km\,s^{-1}}$. The type includes profiles with or without emission, either at the line center or in the red.

Type *br* – blue+redshifted absorption. These profiles show both redshifted and blueshifted absorption, regardless of the feature at the line center.

Type *e* – emission. These profiles show detectable emissions without any detectable absorption feature. These emission features could formally be on the red or blue side, i.e., with velocity $\geq 25\ \mathrm{km\,s^{-1}}$ from the line center.

Type *c* – central absorption. These profiles show detectable sub-continuum absorption at or near the line center.

Type *f* – featureless. These are profiles without any detectable feature.

Table A.3 and Figure A.1 give the profile type for all the targets, and Table 5.3 indicates the number of stars showing profiles of each type. Note that the sum of the frequencies in each column may not add to 100%, due to type change in multiple observations (c.f., § 5.3.4).

5.3.3 Quantifying the He I λ10830 Feature

For the He I λ10830 line with detectable features (all except type *f*), we measured the equivalent widths and the velocity ranges of the features by integrating the normalized flux above or below the continuum. We classify the features into three velocity ranges: blue, central, and red, regardless of the overall type of profiles in §5.3.2. For example, a profile with type *br* may show three features: blueshifted absorption, central emission, and redshifted absorption. In this Chapter, a positive equivalent width refers to an emission feature, whereas a negative one refers to absorption. Table A.3 shows the equivalent width EW_x and the edges and the extrema of the feature in velocity space, $v_{b,x}$, $v_{r,x}$, and $v_{0,x}$, where x refers to blue (b), red (r), and central (c) features. Figure 5.3 shows an example of feature identification and measurements. Figure 5.4 shows the distribution of the equivalent widths for the three types of features, and Figure 5.5 shows the velocity at minimum of the redshifted and blueshifted absorption as a function of the free-fall velocity from infinity, $v_{ff,\infty} = (2GM/R)^{1/2}$. The velocities in the Figure have been normalized to $v_{ff,\infty}$.

5.3.4 Multiple Observations

Among 170 stars in our survey, 12 stars were observed more than once. We primarily re-observed stars that show peculiar absorption features, including those with type *br*, those with broad redshifted absorption without an emission component, or those with central absorption accompanied by hints of emission at the line wings. We also randomly selected some representative stars of each type for a second epoch observation.

As shown in Figure 5.6, the type of the He I λ10830 line profile changed by more than 3σ in the second observation for 8 out of the 12 stars. As exemplified by PDS 70, for which we secured three epochs of observations, and by J08075546, the most conspicuous changes seem to occur in the blueshifted component, which can disappear entirely in timescales of even days. The depth and velocity of the central velocity component are also very variable, with the most significant change seen in CVSO 1295, in which the component disappears, replaced by a broad redshifted component. Most of the other examples show changes in depth of the components but not changes in type. In any event, in calculating the frequency of each of the profile types in Table 5.3, we count the number of stars exhibiting each type of profile in one or more observations. As a result, the sum of frequencies for all profile types will not be equal to 100%.

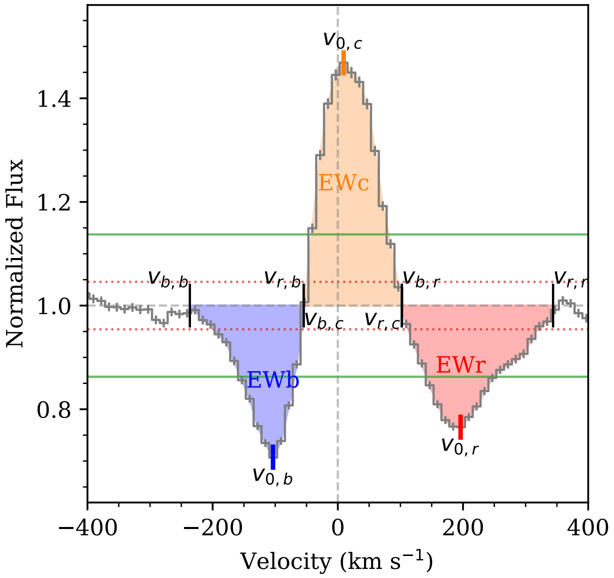

Figure 5.3 Profile of He I λ10830 in CVSO 1545 as an example showing different features in the line. Black vertical lines show the velocities of the edges of each feature, and the colored vertical lines show their extrema. The shaded regions show the area of which the equivalent widths are calculated. Horizontal lines have the same meaning as in Fig. 5.2.

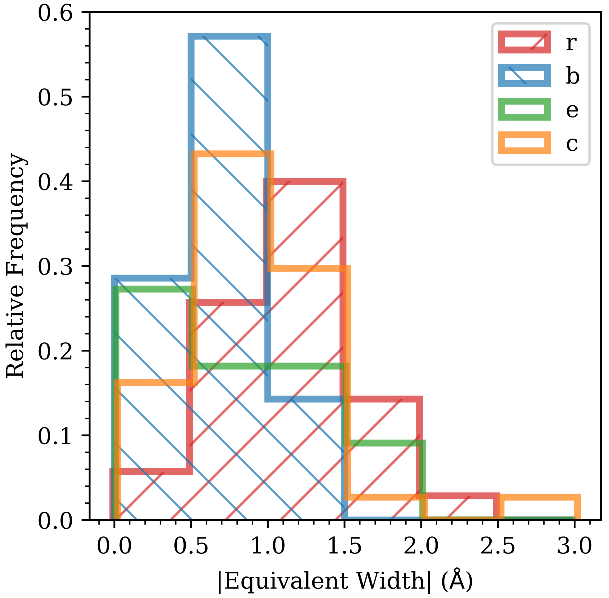

Figure 5.4 Distribution of the absolute equivalent widths of each component in the line profiles. Included in the plot are equivalent widths of the redshifted, blueshifted, and central absorption, and the emission components (Table A.3).

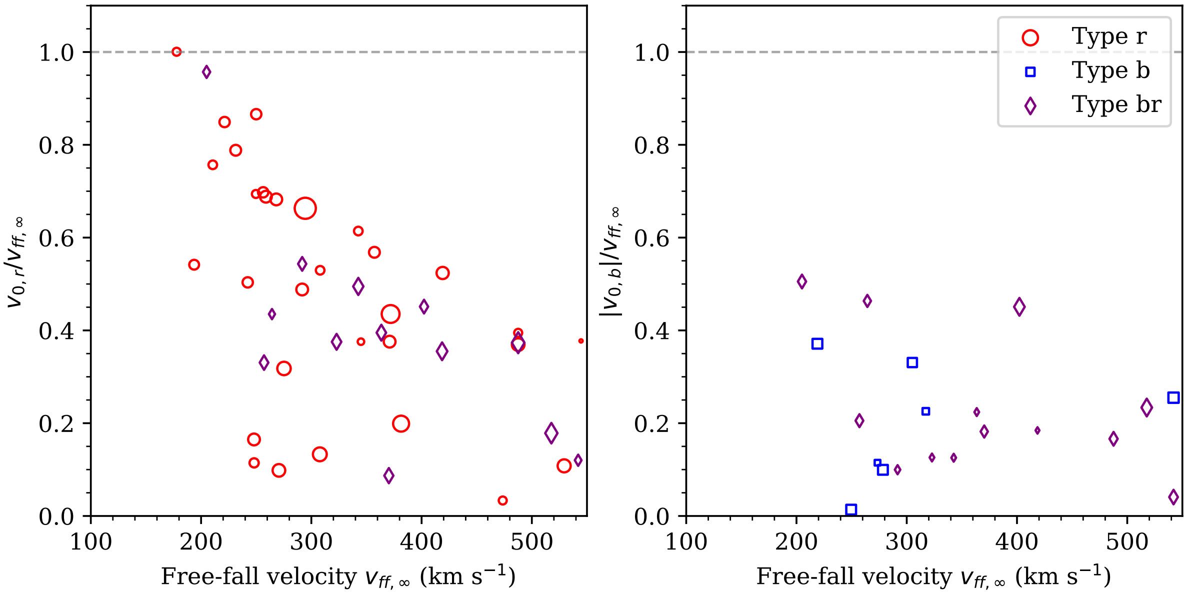

Figure 5.5 The velocities at feature minima compared to free-fall velocities $v_{ff,\infty}$ for observations showing type *r*, *b*, and *br*. The marker sizes scale with the equivalent width of the feature.

5.3.5 Nature of Line Profiles and their Relationship to Accretion

The He I λ10830 line profiles are known to be a probe of accretion and wind in T Tauri stars (Edwards et al. 2003, 2006). Here we discuss the physical properties of the stars exhibiting each type of the line profiles.

Redshifted absorption is a telltale of accretion, as the material absorbing the light moves away from the observer along the line of sight. The presence of redshifted absorption superimposed on emission profiles is predicted in magnetospheric accretion, with absorption features below the continuum that may extend to the free-fall velocity depending on mass accretion rate and inclination (Hartmann et al. 1994; Muzerolle et al. 2001; Edwards et al. 2006; Fischer et al. 2008). The velocities at the minimum of the redshifted components in stars with profiles of type *r* and *br* are a fraction of the free-fall velocity (Figure 5.5), as expected in magnetospheric accretion, and therefore we considered them to be accretors.

Blueshifted absorption in line profiles has been interpreted as indicating the presence of a wind, and Edwards et al. (2006) found that this component was only present in the accreting stars in their study. According to Figure 5.5, the velocities at the minimum of the blueshifted components in type *b* objects have velocities $\leq 150 \text{ km s}^{-1}$, and the depth of the features are > 0.5, with corresponding equivalent widths ≤ 1 Å (Table A.3, Figure 5.4). These characteristics preclude stellar winds and point towards disk winds (Edwards et al. 2006). Accretion-powered MHD winds are expected in disk regions inside ~ 1 au in young stars (c.f., Alexander et al. 2014). The terminal velocity of

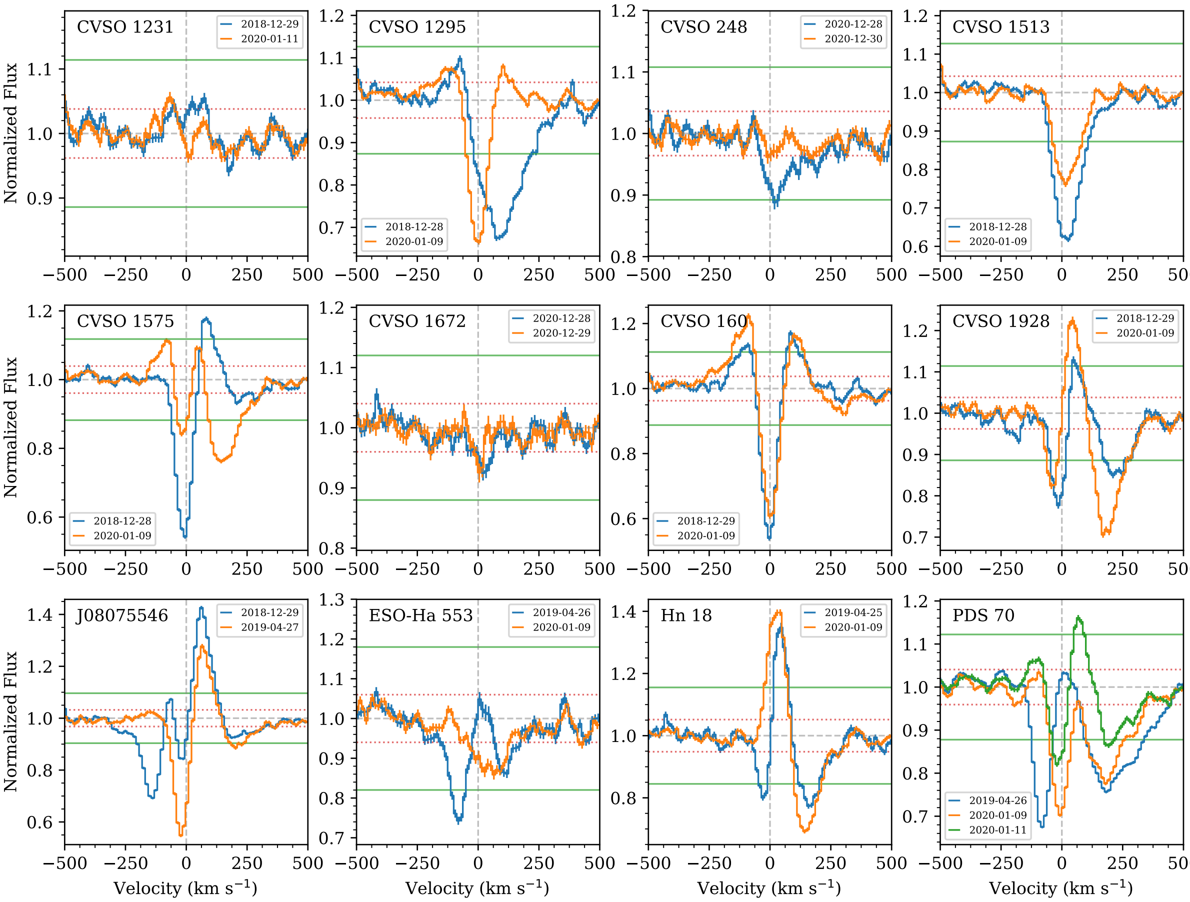

Figure 5.6 Profiles of the He I λ10830 line for stars with more than one observations. The epoch of the observations is indicated. Lines show uncertainties in the continuum, as in Fig. 5.2.

these winds is comparable to the Keplerian velocity at the launching radius in the disk (Blandford & Payne 1982), so their maximum velocity would be $\sim 112\ \mathrm{km\,s^{-1}}\ (\mathrm{M}/0.4\mathrm{M}_{\odot})^{1/2}(\mathrm{R}/1.2\mathrm{R}_{\odot})^{-1/2}$ for ejection at $\sim 5\ \mathrm{R}_{\star}$, consistent with the velocities observed in type *b* objects. Therefore in this study, we classify a star in which the He I λ10830 line shows profiles with types *r*, *b*, or *br* in at least one observation as an *unambiguous accretor*.

The nature of the stars of type *e*, showing only an emission feature in the He I λ10830 line, is unclear. The distribution of emission equivalent widths in type *e* stars is shown in Figure 5.4. Most of the accreting stars in the Edwards et al. (2006) sample had equivalent widths of the emission component significantly larger than 1 Å; however, the emission equivalent width of some of the stars with the lowest veiling – and therefore the lowest degree of accretion – in the Edwards et al. (2006) sample were consistent with those of stars with type *e* in our sample, indicating that some of these targets may still be accreting. Therefore, we classify the stars with He I λ10830 profile type *e* as *possible accretors*.

In main sequence and post-main sequence stars, the absorption at the line center (i.e., type *c*) is usually associated with chromospheric absorption. Sanz-Forcada & Dupree (2008), using high-resolution spectra, found that the absorption equivalent widths of the He I λ10830 of active giants are on the order of $\sim$ 1 Å, whereas those of dwarfs and sub-giants generally have absorption EW(He I) $\lesssim$0.4 Å regardless of activity (Zarro & Zirin 1986). Most of our targets with type *c* have absorption EW of $\sim$1.5 Å and lower, consistent with active giants. Nevertheless, a small fraction of the targets show EWs that are larger than active giants, and it is possible that given the right geometry, low-velocity redshifted absorption could be seen as central absorption. This is supported by the multiple observations of CVSO 1295 (§5.3.4), for which the profile changed from type *c* to *r*. This suggests that some stars with type *c* could still be accreting, and therefore, we classify these stars as *possible accretors*, pending future observations.

We classify stars showing the profile type *f* as non-accretors since there is no evidence for any significant amount of material reaching the magnetosphere of the star, which would cause some absorption or emission in the He I line. However, due to our very conservative uncertainty estimation and moderate spectral resolution, many stars could be classified as type *f* when in fact, some emission/absorption is still present. For example, ESO-Hα 553 (§5.3.4) shows a profile type *b* in 2018, but a later observation in 2020 showed no detection since the weak central absorption in the profile is not strong enough to be "detected" by our criteria.

5.3.6 Observed Frequencies of He I λ10830 Line Type

In Table 5.3, we show the number and frequency of stars in our sample that exhibit each type of He I λ10830 line profile. These numbers are based on the number of stars showing the type of profile in one or more observations (c.f., § 5.3.4). We divide the sample into two groups based on the age of the population and set the boundary at 5 Myr. At this age, only 10% of the accretors remain (Fedele et al. 2010; Briceño et al. 2019), with an e-folding timescale for accretion of 2.1 Myr. Therefore, objects with ages $\leq$ 5 Myr can be perceived as those with typical evolving disks. On the other hand, disks at the older age bin represent those that somehow survive to an old age beyond the typical disk lifetime.

Edwards et al. (2006) classified the He I λ10830 profile in types according to the nature of the absorption component: redshifted, blueshifted, or redshifted and blueshifted subcontinuum absorption, similar to our *r*, *b*, and *br* types; they found that the profiles did not change category with multiple observations, from which they inferred that the type of profile was intrinsic to the star. Unlike their case, we found that about 33% of the stars (4/12) changed their profile type and, more importantly, their accretion classification between the two epochs of observations (c.f., §5.3.4). These stars were CVSO 1295 (r→c), CVSO 248 (r→f), CVSO 1575 (c→br), and ESO-Hα 553

Table 5.3 Line Profile Frequencies

Profile type	Frequency		
	Age $<$ 5 Myr (55)	Age $\geq$ 5 Myr (115)	All Ages (170)
r	15/55 = 27.3%	19/115 = 16.5%	34/170 = 20.0%
b	2/55 = 3.6%	5/115 = 4.3%	7/170 = 4.1%
br	5/55 = 9.1%	9/115 = 7.8%	14/170 = 8.2%
e	2/55 = 3.6%	9/115 = 7.8%	11/170 = 6.5%
c	13/55 = 23.6%	22/115 = 19.1%	35/170 = 20.6%
f	23/55 = 41.8%	54/115 = 47.0%	77/170 = 45.3%
r+b+br	20/55 = 36.4%	31/115 = 27.0%	51/170 = 30.0%
r+b+br+e+c	33/55 = 60.0%	62/115 = 53.9%	95/170 = 55.9%

Note. — The frequencies in each age bin are calculated per the total number of stars in that bin. The frequencies in the last column are calculated per 170 stars. The sum of the frequencies in each column may not equal 100% due to some stars having different profile types in repeated observations (c.f., § 5.3.4).

(b→f). Therefore, we classify these stars as episodic accretors. In general, we classify a star as an accretor when one or more observations show evidence of accretion (He I type *r*, *b*, *br*). It is possible that some absorption features may be associated with stellar flares (Hill et al. 2017), but observations of flares show absorption features at high velocity that are weaker than observed here (Fuhrmeister et al. 2020).

Following these considerations, an inspection of Table 5.3 indicates that between 30% and ∼50% of the WTTS with IR excess are still accreting, with a higher fraction at early ages.

5.4 Discussion

Since accretion is the process connecting the disks and the host stars, it is conceivable that the different processes that give rise to different types of accretion-probing lines were related to the properties of the disks and/or the stars. In this section, we aim to search for the connections between the characteristics of the He I λ10830 line, which probes accretion, and the properties of the stars and their disks.

5.4.1 Line profiles and disks properties

Near and mid-infrared color-color diagrams have been used to probe the evolutionary stages of protoplanetary disks. Here we use the 2MASS and (ALL/un)WISE magnitudes of the stars to assess their disk properties. Among the 170 stars in our survey, 131 stars have clean photometry (ccf and photometric flag = 0, A/B, respectively) in the W3 and W4 bands. Only these stars were included in the analysis in this section for consistency. We have verified that this sub-sample is representative of the overall sample by comparing the distributions of spectral type and mass using a two-sided Kolmogorov-Smirnov test and finding that they are not statistically different (p-value = 1.0 for both spectral type and mass).

Figure 5.7 shows the Ks−W3 and Ks−W4 color excesses over photospheric colors for the disk-analysis targets. The intrinsic photospheric color is interpolated from Table 6 of Pecaut & Mamajek (2013). We also draw the regions corresponding to the location of full disks, evolved disks, transitional disks, debris disks, and diskless WTTS as defined by Luhman & Mamajek (2012) and Esplin et al. (2014), and used to characterize the disk populations in Upper Sco and Taurus, respectively. The region of full disks in Figure 5.7 encompasses objects with the reddest colors in Taurus, including Class I sources (Esplin et al. 2014).

The different regions refer to the evolutionary status of the dust in the disk. Full disks are those that can be explained by optically thick disks that extend all the way to the truncation radius of the inner disk at a few stellar radii, and the range of colors can be understood in terms of different degree of dust settling in the disk (D'Alessio et al. 2006). Evolved disks are those with weak excesses over the photosphere at all bands due to the high degree of dust settling in the disk (Manzo-Martínez et al. 2020). In contrast, transitional disks have near-IR colors consistent with those of evolved disks but mid-IR colors similar to those of full disks. These disks have large cavities or gaps, with corresponding decreased emission at short wavelengths (c.f., Espaillat et al. 2014). Debris disks are gas-poor disks in which the weak emission is due to secondary dust created by collisions between larger bodies (c.f., Wyatt 2008).

The accretors and possible accretors are shown in the top two panels of Figure 5.7, while the featureless objects are shown in the lower panel. The disks of the accretors and possible accretors occupy the evolved disk region and the bluest end of the full disk region, with E(Ks−W4) ≤ 4 for most of the objects (Figure 5.8). This distribution of colors is more consistent with the disk population of Upper Sco (Luhman & Mamajek 2012) than with that of the younger Taurus (Esplin et al. 2014) indicating a more advanced degree of dust evolution. However, essentially none of the accretors and possible accretors are located in the debris disk regions, while a significant fraction of the type *f* objects occupy this region. The distributions of the E(Ks−W4) shown in Figure 5.8 are not statistically different, except when comparing between accretors (*r*, *b*, *br*) and the other two groups. But what seems evident is that the median of the excess decreases, starting with the accretors, to the possible accretors, to the non-accretors, with a larger fraction of accretors retaining their disks.

The left panel of Figure 5.8 shows the excess in the H−Ks color of the sample as a function of

E(Ks−W4), while the right panel shows the distribution of E(H−Ks) for the different types. The H−Ks color is a probe of the innermost dust disk, and for the low accretors, it depends on the height of the disk at the dust destruction radius (Manzo-Martínez et al. 2020). There is a clear difference between the accretors (type *r*, *b*, *br*) and the other types. Most of the objects with excesses in H−Ks above the photosphere are accreting, with E(H−Ks) of the order of 0.1 - 0.2, comparable to stars on the blue end of the CTTS locus (Meyer et al. 1997). The medians of E(H−Ks) are shown as dashed vertical lines in Figure 5.8. Half of the accretors retain their inner dust disk, as the median is comparable to the upper limit of the photospheric color. On the other hand, the medians for possible accretors and non-accretors are well consistent with the photosphere, suggesting that they have essentially lost their inner dust disks.

Half of the accretors and the three stars that changed accretion status do not show micron-sized dust emission in the inner disks. This suggests that the accretors with little inner disk left are at the very end of the accretion phase. It may be possible that the processes removing small dust from the inner disk, such as dust growth and planet-induced dust gap opening, may be related to stellar accretion. Future monitoring of the targets will help clarify the relationship between their accretion flows and inner disks.

5.4.2 Accretion and Spectral Type

Two effects are at play in considering the spectral type distribution of the low accretors. On the one hand, it is well known that the mass accretion rate and disk lifetime depend on stellar mass. In particular, disks around lower-mass stars tend to live longer (Hernández et al. 2005; Carpenter et al. 2006), with the Peter Pan Disks – disk-bearing T Tauri stars accreting at very old ages– being extreme cases (Silverberg et al. 2020). One would then expect to find more accretors at later spectral types since they have more chance to survive. On the other hand, accretion luminosity and/or accretion-induced line emissions are easier to detect in late-type TTS compared to early-type TTS due to contrast effects (Manara et al. 2017b). Therefore, one could expect that the distribution of spectral types for the newly discovered accretors (i.e., those previously identified as non-accretors) would favor earlier spectral types since those at later spectral types would have already been identified. We perform several Kolmogorov-Smirnov (K-S) tests to compare the distribution of spectral types to test these predictions.

The comparison set for these tests is drawn from T Tauri stars in the CVSO survey (Briceño et al. 2019). The CVSO, with a total of 2062 K and M-type T Tauri stars, comprises some of the most populous star-forming groups with ages range from $\sim$2 Myr to $\sim$12 Myr, and therefore it can be considered a representative set of low-mass pre-main sequence stars. For the typical distribution of accreting TTS (CTTS), we selected all stars identified as accreting using the EW criteria. For

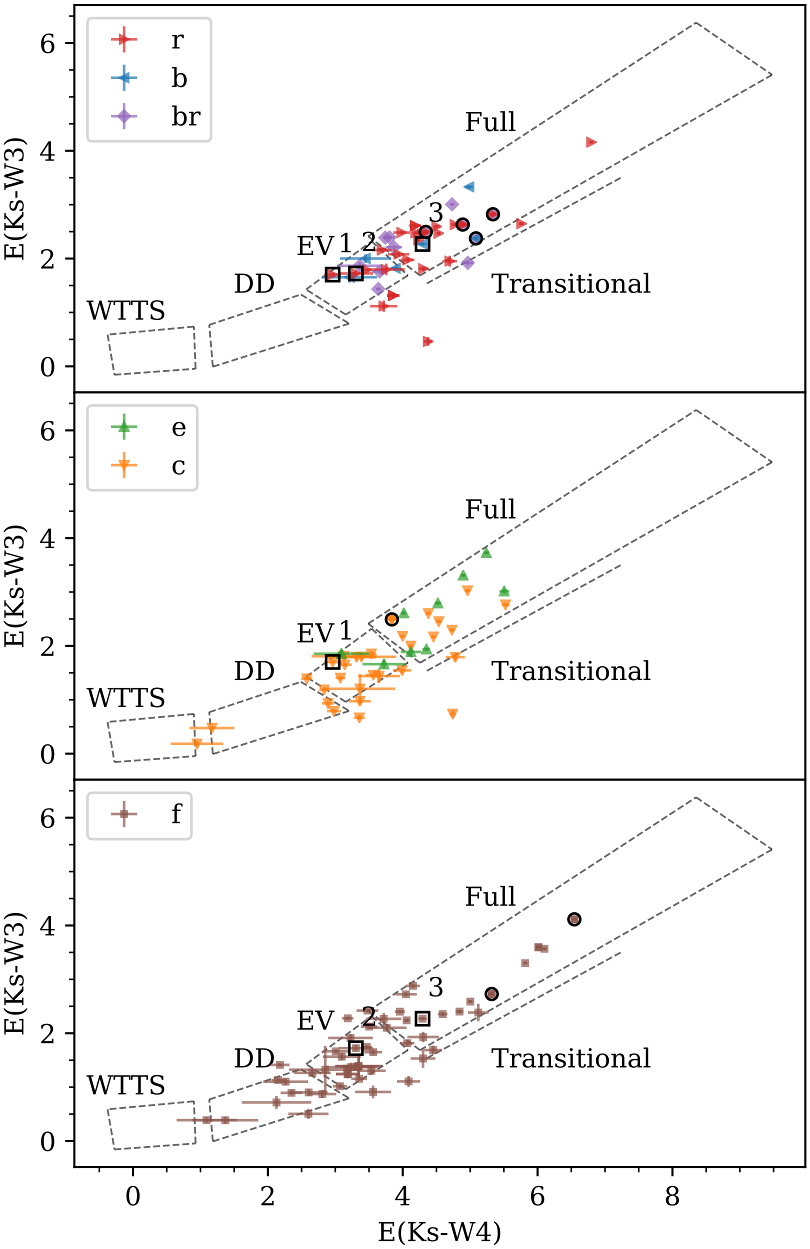

Figure 5.7 The W3 and W4 color excess for stars showing different type of line profiles and accretion properties. Stars marked in circles are those with the same accretion status in their multiple observations. The three stars marked in squares and numbered are stars that change accretion status in different observations. The stars marked with numbers 1, 2, and 3 are CVSO 1295, CVSO 248, and ESO-Hα 553, respectively.

the typical non-accretors, we selected stars from CVSO identified as WTTS with Ks$-$W3 color consistent with no or very weak primordial disk (Ks$-$W3 $\leq$1).

Figure 5.9 shows the distribution of spectral types, as a proxy for mass, for our sample, known

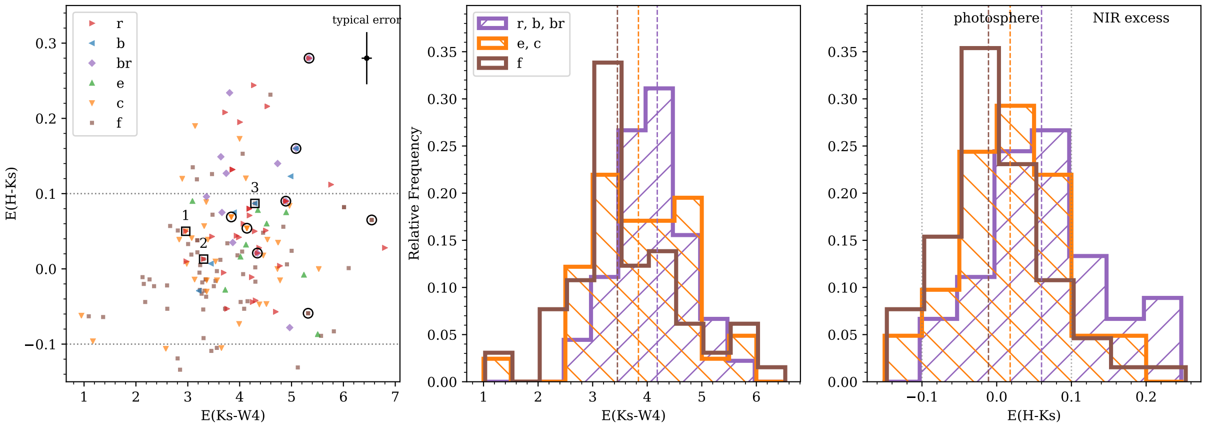

Figure 5.8 The H−Ks and Ks−W4 color excess for stars showing different types of line profiles and accretion properties and their distribution. Stars marked in circles are those with the same accretion status in their multiple observations. The three stars marked in squares and numbered are stars that change accretion status in different observations. The dotted gray lines in the left and right panels indicate an area within which the H−Ks colors are consistent with the photosphere. In the center and the right panel, dashed lines indicate the median of each group.

CTTS, and disk-less WTTS from Orion OB1 (Briceño et al. 2019). The left panel shows that our sample is different from the set of all TTS in Orion OB1, where we over-sample the later spectral types (K-S test, p-value=0.01). However, our sample is not statistically different from the disk-bearing stars in CVSO (p-value=0.67). These results confirm previous studies showing that disks last longer at lower stellar mass (e.g., Carpenter et al. 2006). The similarity of the distribution between our sample (“WTTS with disks”) and the disk-bearing TTS also suggests that a similar fraction of TTS at different masses could be classified as “WTTS with disks”. This has been seen in studies comparing fractions of accreting stars and disk-bearing stars across many star-forming regions (Hernández et al. 2008; Fedele et al. 2010; Briceño et al. 2019), and in all cases, the fraction of accretors are systematically lower than fractions of disk-bearing stars. This suggests a slightly longer timescale for the (dust) disk dispersal than the lifetime of accretion-feeding inner disks.

For the newly identified low accretors in this survey, their SpT distribution is similar to that of the disk-less stars (CVSO WTTS; p-value=0.20 and a similar median SpT), but it is quite different from that of known accretors (CVSO CTTS; p-value=0.003). The median SpT=M0 for known accretors in CVSO, compared to M2.5 for new accretors and M2 for disk-less stars, suggests that the original CVSO accretor classification seems to miss the lower mass targets. This could be because of the known result that the mass accretion rate scales with mass for TTSs with roughly the same age (e.g., Manara et al. 2016) and, therefore, the mass accretion rates for late-type TTSs are much smaller than the earlier-type counterparts.

Another possibility for the differences in the distribution between CVSO CTTS and CVSO

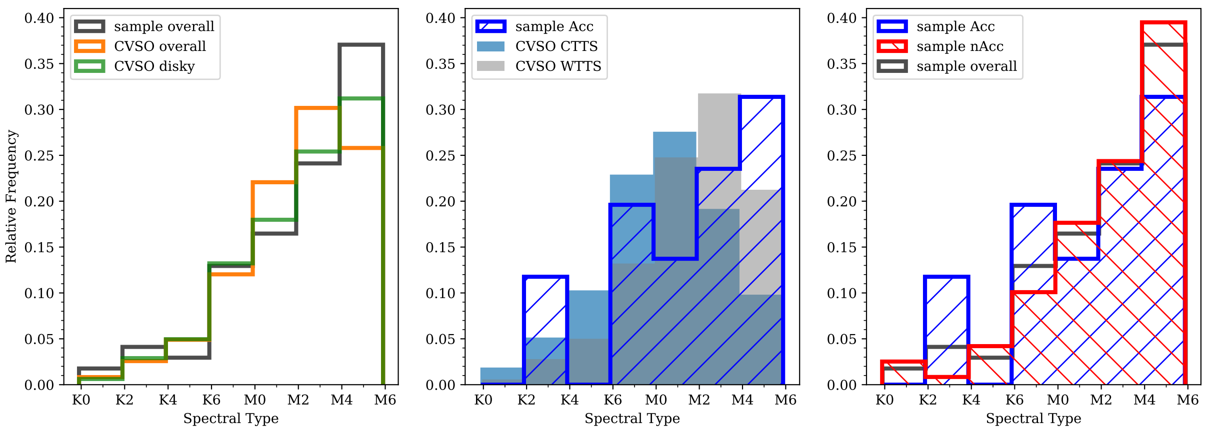

Figure 5.9 The distribution of spectral types for objects with different classifications. For all panels, Acc and nAcc are our samples classified using He I profiles. CVSO CTTS/WTTS are from Briceño et al. (2019). The WTTS samples are selected with Ks−W3<1.0, which could include some debris disks.

WTTS/our new accretors is that this is simply an observational bias. Later spectral type TTSs are also the fainter ones. Though the photometric selection of the CVSO went down to V∼19.5-20, which is fainter than the expected magnitude of unreddened M6 stars at a few Myr age, the spectroscopic follow-up was much shallower, typically down to V∼18. Therefore, the incompleteness at spectral types M4-6 is significant. Figure 14 of Briceño et al. (2019) shows that the survey is complete in spectral type only down to M3. In addition, most of the stars in Orion OB1 are WTTS (85%) and even more so in the Orion OB1a population (95%). It is conceivable that the distribution of spectral types is more complete for the WTTS than it is for the CTTS at the faint (M4-M6) end, as only a small number of late-type CTTS would have been observed.

We compare the SpT distribution within our targets in the right panel of Figure 5.9. We find no statistical difference between any of the distribution from accretors, non-accretors, or overall sample, suggesting that the processes that are masking the detection of accretion do not depend on mass. We speculate that geometrical effects, such as the inclination of the system, could play a role in making the detection difficult, as they have significant effects on the Hα line profile in very low accretion rates (Thanathibodee et al. 2019b). Modeling of accretion-related lines of these newly identified low accretors will test this scenario.

5.4.3 Sensitivity of Hα as an Accretion Diagnostic

In Figure 5.10, we show the distribution of EW(Hα) and W_{10}(Hα) for accretors, non-accretors, and the overall sample. Generally, the equivalent width of accretors does not show any preference toward either low or high values, compared to non-accretors and the overall sample. Nevertheless, we can identify two peaks in the distribution: one at ∼3 Å and another at ∼9 Å. This is because these bins are immediately below the EW threshold for accretors determined in White & Basri (2003) and adopted by Briceño et al. (2019) for Orion targets and our survey. Specifically, the cutoff is at 3 Å for spectral type earlier than K5 and 10 Å for spectral type earlier than M2.5. These results also suggest that a more significant fraction of missing accretors are those that are just below the threshold, as expected.

The W_{10} distribution shows a significant difference between accretors and non-accretors; most accretors have large W_{10}. This is also expected since large wings in the Hα profiles are a typical indicator of magnetospheric accretion. Our results also reflect the uncertainty in defining the cut-off between non-accretors and accretors, since at low accretion rates, the geometry of accretion plays a strong role in shaping the line profiles (Thanathibodee et al. 2019b). For example, redshifted absorption in Hα is ubiquitous at low accretion rate (Muzerolle et al. 2001), and could complicate the measurements of the Hα equivalent width (Thanathibodee et al. 2018).

The fact that we can still find accretors among the supposedly non-accreting stars suggests that surveys of accreting stars using Hα line width are not complete. Here, we can quantify the fraction of missing accretors based on the selection criterion and compare their effectiveness. There are 49 newly identified accretors among 166 stars classified as non-accretors using EW(Hα). This translates to $\sim 30\%$. On the other hand, there are 12 accretors recovered from 20 stars classified as non-accretors using W_{10} – a fraction of $\sim 60\%$. The fraction decreases very slightly to $7/13 = 54\%$ for stars with $W_{10} < 200\ \mathrm{km\,s^{-1}}$ if the criterion of Jayawardhana et al. (2006) is used.

The 60% recovery fraction for W_{10}=270 $\mathrm{km\,s^{-1}}$ is statistically higher than the 30% fraction for EW (Fischer's exact test p-value=0.01). This higher "recovered" fraction for the W_{10} compared to the EW of the line could be because it is more susceptible to geometry, as discussed earlier. Given the non-uniformity of our sample, as well as the low number of stars being observed, we can estimate that at least 20-30% of disk-bearing stars classified as non-accretors are in fact still accreting, depending on the age.

One implication of these results is that if the fraction of accretors is purely based on low-resolution spectroscopic or photometric EW(Hα) measurements, the fraction needs to be modified. With spectral types and disk properties derived from photometry, the total fraction of accreting stars in a given population can be calculated as

$$f_{acc} = f_{acc,H\alpha} + \alpha \times \left(f_{disk} - f_{acc,H\alpha}\right), \tag{5.4}$$

where $f_{acc,H\alpha}$ is the fraction of accreting stars calculated from Hα emission in spectra, f_{disk} is the fraction of disk-bearing systems derived from infrared photometry, and α is the fraction of disk-bearing WTTS that are still accreting $\sim 20 - 30\%$.

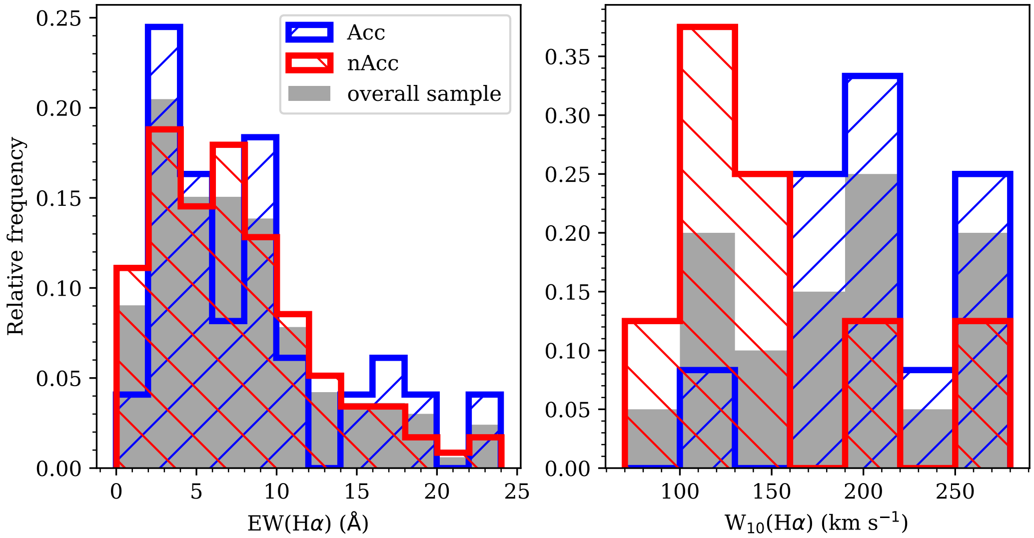

Figure 5.10 The distribution of EW(Hα) and W_{10} for objects with different classification. For all panels, Acc and nAcc are our samples classified using He I profiles.

We estimate the changes in the fraction of accretors by adopting an e-folding timescale for disks of 3 Myr (Fedele et al. 2010), and a timescale for accretion of 2.1 Myr (Briceño et al. 2019). Assuming an exponential decay, the fractions of disk-bearing non-accretors are 13%, 10%, and 3% for 3, 5, and 10 Myr, respectively. With the recovery fraction of 30% at $\leq$5, and 20% at a later age, these fractions decrease to 9%, 7%, and 2%, consistent with the increase of the accretion timescale by $\sim$0.2 Myr from the original value. This result is consistent within the spread of the many values of the accretion e-folding time presented in previous works (e.g., Fedele et al. 2010; Briceño et al. 2019)

5.5 Summary and Conclusions

To shed some light on the processes occurring at the last stages of accretion, we conducted a survey to search for and characterize stars that are still accreting at very low accretion rates, the so-called low accretors. Using the He I λ10830 as a sensitive probe of accretion, we observed 170 T Tauri stars previously classified as non-accretors based on their EW(Hα) and W_{10}(Hα), but still showing evidence of disks in the infrared. Based on 183 observations of these stars, we summarize our findings and conclusions as follows:

1. We found that the He I λ10830 profiles can be classified into six types: redshifted absorption, blueshifted absorption, blue+redshifted absorption, central absorption, emission, and featureless. The first three types are consistent with accretion and/or disk winds. Central ab-

sorption and emission profiles are uncertain, and they could be due to active chromospheres or accretion. The featureless profiles are consistent with no accretion.

2. We identified 51 stars as low accretors that had previously avoided accretion detection in Hα. This number accounts for 30% of our sample, with a slightly larger fraction in the younger ($< 5\,$Myr) populations. Among 12 low accretors with multiple observations, four stars show evidence for episodic accretion. These episodic accretors could be in the propeller regime of accretion, and detailed modeling of emission lines is needed to determine the geometry of the infall region.

3. Based on the analysis of IR excess emission from dusty disks, we found evidence of disk evolution among all types of accretors, as probed by the excess in the (Ks$-$W4) and (Ks$-$W3) colors. Stars identified as unambiguous accretors show evidence of a stronger disk emission signature compared to possible accretors and non-accretors, as shown by their median (Ks$-$W4).

4. Most objects with excess emission in the H$-$Ks colors, indicative of the presence of an inner disk, are found to be accreting; however, half of the accretors have near-IR colors consistent with the photosphere. This suggests that very little dust remains in the inner disk in the last stages of accretion.

5. A similar fraction of stars can be classified as low accretors independent of spectral type in our sample (mid-K to mid-M), suggesting that the processes stopping accretion do not depend strongly (if at all) on mass.

6. A large fraction of the missing accretors is found just below the EW(Hα) threshold between accretors and non-accretors (White & Basri 2003). We found that the recovery fraction for accretors is $\sim 30\%$ using the EW(Hα) criterion, and $\sim 60\%$ using the width at 10% of the Hα peak, W$_{10}$, criterion. This suggests that the W$_{10}$ diagnostic may be susceptible to other effects (e.g., geometry) in low accretors.

7. The 20-30% unambiguous accretors fraction among disk-bearing WTTS decreases the discrepancy between the disk timescale and accretion timescale by $\sim 0.2\,$Myr, but does not alter the interpretation of previous studies.

CHAPTER 6

A Census of the Low Accretors. II. Accretion Properties

This chapter is in preparation for submission to the Astrophysical Journal, in collaboration with Brandon Molina, Javier Serna, Nuria Calvet, Jesús Hernández, James Muzerolle, and Ramiro Franco Hernández. It is adapted and reproduced here.

Abstract

Much is known about the processes driving accretion from protoplanetary disk onto low-mass pre-main sequence stars (T Tauri stars). Nevertheless, it is unclear how accretion stops. To determine the accretion properties and their relation to stellar properties and to gain insight into the last stages of accretion, we present here a detailed analysis of 24 low and possible accretors, identified as such using the He I λ10830 line in a previous study. We model moderate-resolution Hα profiles of these stars using magnetospheric accretion flow models that take into account the chromospheric contribution at the line center. Based on parameters derived from 20 stars with the Hα profiles that can be well reproduced with magnetospheric+chromospheric models, we find a power-law relation between the disk truncation radius and the mass accretion rate that is steeper than that predicted by theory or simulations. Comparing the corotation and truncation radii, we find that most of our targets are accreting in the unstable regime and rule out the propeller as the main process stopping accretion. For the truncation radius to be the same as the magnetic radius, the dipole magnetic field and/or the efficiency parameter ξ need to be smaller than previously determined, suggesting that higher-order fields dominate in low accretion rates. Lastly, we determine that the lowest accretion rates that can be detected by Hα line modeling is $1-3\times10^{-11}\,M_\odot\,\mathrm{yr}^{-1}$ for M3 stars and $3-5\times10^{-11}\,M_\odot\,\mathrm{yr}^{-1}$ for K5 stars. These limits are lower than the observed accretion rates in our sample, suggesting that we have reached a physical lower limit. This limit, $\dot{M}\sim10^{-10}\,M_\odot\,\mathrm{yr}^{-1}$, is consistent with EUV-dominated photoevaporation.

6.1 Introduction

Detailed modeling of emission line profiles of accreting T Tauri stars (TTS) provides valuable information on accretion properties such as mass accretion rate and accretion geometry. Comparing the stellar properties with the accretion properties of stars and disks provides insight into the star and disk connection, as well as their evolution.

In an effort to understand the last stages of evolution of stellar accretion, we have conducted a survey to search for T Tauri stars near the end of their accretion phase – the low accretors. These stars still host primordial dust disks at different stages of evolution, but their signatures of mass accretion onto the stars are very weak, indicating that the mass accretion onto these stars has nearly stopped. Using a sensitive probe of accretion – the He I λ10830 line – we identified 51 stars accreting at very low, but unknown rate (Chapter 5). We found correlations between accretion properties derived from the He I line and properties of the disk, and in particular, we found that accreting stars, albeit at very low rates, still have dust in the inner disk. We also found evidence that the processes stopping accretion may not be directly related to the stellar mass, suggesting that common processes ending accretion may occur in a wide range of masses.

Although qualitative comparisons between the He I λ10830 accretion signature and properties of the disks and the stars have provided us with some insight into the last stages of accretion, a more quantitative analysis is needed to get the complete picture. In particular, the He I line, although sensitive to accretion, does not provide the measurement of the mass accretion rates or the geometry of accretion. However, this information can be obtained by detailed modeling of emission lines formed in the accretion flows using the magnetospheric accretion model.

Here we report observations and magnetospheric accretion flows modeling of 22 newly identified low accretors and two possible accretors to search for correlations between accretion properties and properties of stars and the disks. By quantitatively analyzing the mass accretion rates and geometry, we aim to gain insight into the last stages of stellar accretion.

This Chapter is organized as follows. In § 6.2 we describe the observations and data sources. In § 6.3 we derive stellar properties and apply magnetospheric models to fit Hα profiles and derive the mass accretion rate onto the star and its geometry. In § 6.4, we discuss the implications of our results. Finally, in § 6.5 we give our conclusions.

6.2 Targets, Observations, and Data Sources

In this Chapter, we work with a subset of the newly identified accretors and possible accretors from Chapter 5. In general, we included most stars in the Orion OB1 association and stars from other star-forming regions with available archival spectra. Our targets include stars from Chamaeleon

Table 6.1 Adopted and Derived Stellar Parameters of the Targets

Target Name/ 2MASS ID	Loc	SpT	$M_\star$ ($M_\odot$)	$R_\star$ ($R_\odot$)	He I[a] λ10830	$v \sin i$ ($\mathrm{km\,s^{-1}}$)	Ref.[b]
J08074647-4711495	γVel	M4	0.16	0.84	b	12.9 ± 1.6	(1)
J08075546-4707460	γVel	K3	1.15	1.50	b,br	20.5 ± 4.1	(1)
ISO-ChaI 52	Cha I	M4	0.18	1.17	r	10.46 ± 1.31	(2)
CHSM 13620	Cha I	M2	0.34	1.72	r	18.9 ± 3.5	(1)
SO682	σOri	M0.5	0.46	1.83	r	16.58 ± 0.79	(2)
CVSO 40	OriOB1a	M0	0.53	1.47	r	15.23 ± 0.84	(2)
CVSO 156	OriOB1b	M2	0.34	1.96	r	8.71 ± 1.31	(2)
CVSO 298	OriOB1a	M0	0.56	1.33	br	14.56 ± 0.49	(2)
CVSO 1295	Ori Cloud A	K7.5	0.59	1.54	c,r	17.43 ± 1.65	(2)
CVSO 1545	OriOB1b	M4	0.17	1.58	br	9.08 ± 1.35	(2)
CVSO 1575	Ori Cloud A	K7.5	0.57	1.65	c,r	12.60 ± 1.02	(2)
CVSO 1600E	OriOB1b	M3	0.27	1.65	r	15.65 ± 0.54	(2)
CVSO 1600W	OriOB1b	M3	0.27	1.54	r	7.45 ± 3.52	(2)
CVSO 1711	Ori Cloud A	M0	0.52	1.57	r	7.18 ± 2.77	(2)
CVSO 1739	OriOB1b	M5	0.1	1.21	r	14.65 ± 1.62	(2)
CVSO 1763	Ori Cloud A	K3.5	1.09	1.49	r	9.21 ± 2.05	(2)
CVSO 1772[c]	OriOB1b	M3	0.29	1.04	e	11.79 ± 1.19	(2)
CVSO 1842[c]	OriOB1b	M2.5	0.32	1.03	e	11.72 ± 2.13	(2)
CVSO 1886	OriOB1b	M3	0.28	1.02	br	17.48 ± 1.07	(2)
CVSO 1928	Ori Cloud A	M0.5	0.47	1.54	r	14.20 ± 0.42	(2)
CVSO 1942	Ori Cloud B	K6	0.72	1.57	r	7.99 ± 2.55	(2)
J16020757-2257467	USco	M2.5	0.32	1.03	r	14.35	(3)
J16042165-2130284	USco	K2	1.39	1.98	br	17.30 ± 0.40	(4)
J16253849-2613540	USco	K7	0.56	2.46	r	17	(5)

[a] Type of He I λ10830 line profile from Chapter 5: r=redshifted absorption, b=blueshifted absorption, br=blue+redshifted absorption, c=central absorption, and e=emission

[b] References for $v \sin i$: (1) Frasca et al. (2015); (2) This study, see § 6.3.2 for details.; (3) Jönsson et al. 2020; (4) Dahm et al. (2012); (5) James et al. (2006)

[c] Possible accretors according to the He I λ10830 lines

I, γ Velorum, σOri, Orion OB1, and Upper Scorpius, and they cover a wide range of stellar parameters. We also include two possible accretors, CVSO 1772 and CVSO 1842, in which the He I λ10830 lines are in emission without a detectable absorption. Two of our targets, CVSO 1295 and CVSO 1575, are episodic accretors, as their profiles show definite accretion signatures only at some epochs.

6.2.1 Stellar Parameters

In Table 6.1, we list the stars included in our survey, their stellar parameters, the type of their He I λ10830 profiles, and their rotational properties. We adopted the spectral type, mass, and radius from Chapter 5. We also gathered the projected rotational velocities $v \sin i$ from the literature. For some of the stars in which these data are not available, we determined the $v \sin i$ from their spectra (c.f., § 6.3.2).

6.2.2 Optical Spectroscopy

We obtained optical spectra of 18 stars out of the 51 new accretors identified in Chapter 5, using the MIKE spectrograph on the Magellan Clay telescope at the Las Campanas Observatory in Chile. We use the 0.7” slit and the red camera, resulting in the spectral resolution of R$\sim$32500 for a wavelength range 4900-9500 Å. We reduced the data using the CarPy package.

In addition to the MIKE data, many stars in the Southern Star-forming region were observed using instruments on the ESO/VLT. We downloaded spectra of these stars from the ESO Archive Science Portal. These data had been reduced and calibrated by their instruments’ pipeline. Table 6.2 shows the details of the observations and data sources.

6.3 Analysis and Results

6.3.1 Mass Accretion Rates and Accretion Geometry

After independently determining that the stars are accreting using the He I λ10830 line, we can be certain that the Hα emission will have some contribution from the accreting material in the magnetosphere at least in some epoch. Given that the procedure and precedence for modeling the Hα are well established, and the line modeling is well developed, we use the magnetospheric accretion model to fit the Hα lines of the newly identified low accretors to infer accretion properties of the star.

6.3.1.1 Magnetospheric Accretion Model

We use the magnetospheric accretion models of Hartmann et al. (1994) and Muzerolle et al. (1998a, 2001), the details of which are described in the original papers. In essence, the model assumes an axisymmetric accretion flow following a dipolar magnetic field. The flow is characterized by the disk truncation radius R_i and the width W_r on the disk. The density in the flow is parameterized by the mass accretion rate $\dot{M}$, whereas the temperature is described by the maximum flow temperature T_{max}. The line profile calculation is done using the ray-by-ray method for a given inclination i.

Table 6.2 Summary of Observations and Data Sources

Target	Instrument	Spectral Resolution	Obs. Date (UT)	Exp. time (sec)	SNR[a]	ESO Program ID
New Observations						
ISO-ChaI 52	MIKE	32500	2020-11-23	2311	30	···
SO682	MIKE	32500	2020-11-23	600	30	···
CVSO 40	MIKE	32500	2020-11-23	803	39	···
CVSO 156	MIKE	32500	2020-11-23	1440	38	···
CVSO 298	MIKE	32500	2020-11-23	1419	40	···
CVSO 1295	MIKE	32500	2020-11-23	900	39	···
CVSO 1545	MIKE	32500	2021-01-17	1200	24	···
CVSO 1575	MIKE	32500	2020-11-23	900	39	···
CVSO 1600E	MIKE	32500	2021-01-17	1200	23	···
CVSO 1600W	MIKE	32500	2021-01-17	600	9	···
CVSO 1711	MIKE	32500	2021-01-17	420	26	···
CVSO 1739	MIKE	32500	2021-01-17	2250	19	···
CVSO 1763	MIKE	32500	2020-11-23	630	36	···
CVSO 1772	MIKE	32500	2021-01-17	1976	12	···
CVSO 1842	MIKE	32500	2021-01-17	1500	16	···
CVSO 1886	MIKE	32500	2021-01-17	1440	16	···
CVSO 1928	MIKE	32500	2020-11-23	720	23	···
CVSO 1942	MIKE	32500	2020-11-23	835	39	···
Archival Data						
2MASS J08074647-4711495	GIRAFFE	19200	2020-10-04	6000	34	188.B-3002(A)
2MASS J08075546-4707460	GIRAFFE	19200	2020-10-04	2400	147	MULTI
CHSM 13620	GIRAFFE	19200	2020-10-04	1200	67	188.B-3002(E)
2MASS J16020757-2257467	XSHOOTER	18340	2019-06-07	1400	95	0103.C-0887(B)
2MASS J16042165-2130284	XSHOOTER	18340	2019-06-19	520	187	0103.C-0887(B)
2MASS J16253849-2613540	UVES	42310	2005-04-16	780	101	075.C-0272(A)

[a] Median Signal-to-noise between 6555-6570 Å.

We create a large grid of models for each star, varying the accretion parameters within ranges appropriate for the observed profile. We started with a large and coarsely spaced grid to search for the approximate location of the reasonably fit model. For a few representative stars, we started the coarse grid with the range of accretion rates from $10^{-10}i\,M_\odot\,\mathrm{yr}^{-1}$ to $10^{-9}\,M_\odot\,\mathrm{yr}^{-1}$ and $\mathrm{T}_{\mathrm{max}}$ from 10,000 K to 14,000 K, and inclinations of 10°to 80°. After identifying that the mass accretion rates for the stars were of the order of $1 \times 10^{-10}\,M_\odot\,\mathrm{yr}^{-1}$ and $\mathrm{T}_{\mathrm{max}}$~12,000 K, we focused our parameter space around these values. After defining a new grid and finding the best fits (c.f., § 6.3.1.2), we verified that most of the best fits were not at the edge of the parameter space; otherwise, we expanded the parameter space accordingly. Once the the approximate parameters were identified, we created the final grid where the parameters are more finely spaced. We adopted the $\mathrm{T}_{\mathrm{eff}}$=6,000 K for the accretion shock component on the stellar surface in all cases. This value is less than 8,000 K used for modeling of stars at higher accretion rates, as we expected that there is no veiling from the accretion shock in the continuum. We had verified that removing this shock component (i.e., set the value to the stellar $\mathrm{T_{eff}}$) had no effect in the overall fitting of the models. Table 6.3 shows the range of parameters used in the final grid of models for each star. From these grids, we determine the best fit models and infer accretion parameters from them.

Applying the results and their implications discussed the in following sections should be mindful of the limitations of the model. In particular, the model assumes no magnetic obliquity and strictly dipolar geometry. Moreover, the temperature distribution in the flow is uncertain. The model that include magnetic obliquity and non-dipolar fields has not been developed, but simulations with such features exist (Romanova et al. 2003, 2004; Long et al. 2007). However, running such simulations for a large number of stars would be very computationally expensive.

Some developments have been made to resolve the uncertainty of the temperature distribution in the flow. Using all hydrogen lines observable with the X-shooter spectrograph, Colmenares et al. (in prep.) found that the temperature distribution assumed in our model is consistent with a large number of stars in the Lupus and Chamaeleon I region. Therefore, we argue that the uncertain nature of the temperature distribution would not be a major effect in our analysis.

6.3.1.2 Fitting the Line Profiles

To fit the model to observation, we first remove the photospheric absorption lines from the observed spectrum using a PHOENIX model spectrum (Husser et al. 2013) with an appropriate effective temperature and gravity for the star. That is

$$F_{obs} = F_{obs,0} - F_{phoenix}(T_{eff}, \log g) + 1, \tag{6.1}$$

where $F_{phoenix}$ has already been convolved to the spectral resolution of the observation, and all the spectra involved are normalized.

As seen in previous studies, the chromospheric contribution to the Hα line can be significant in low accretors (Manara et al. 2017a), and line profile modeling has to take the chromospheric emission into account. In our previous study (Thanathibodee et al. 2020), we approached this problem by fitting the residual between the best fit model profiles and the observation with a Gaussian to verify that it is consistent with what is expected from chromospheric emission. In this Chapter, we improved upon that idea by directly incorporating the Gaussian into the fitting procedure.

Table 6.3 Range of Model Parameters

Target	$\dot{M}$ ($10^{-10}\,M_\odot\,\mathrm{yr}^{-1}$)	i (deg)	$\mathrm{T}_{\mathrm{max}}$ (10^4 K)	R_{i} ($\mathrm{R}_\star$)	W_{r} ($\mathrm{R}_\star$)	a_c	σ_c ($\mathrm{km\,s^{-1}}$)	No. of Models
CVSO 40	1.0/2.0/0.1	10/80/10	1.15/1.25/0.025	2.6/5.0/0.4	0.4/1.6/0.4	0/3.1	0/35	9240
CVSO 156	0.5/1.5/0.1	10/80/10	1.15/1.25/0.025	2.6/5.0/0.4	0.4/1.2/0.4	0/3.1	0/35	9240
CVSO 298	0.4/2.0/0.2	10/80/10	1.00/1.25/0.05	3.4/5.8/0.4	0.4/1.6/0.4	0/2.3	0/35	9072
CVSO 1295	0.5/1.5/0.1	10/80/10	1.15/1.25/0.025	2.6/5.0/0.4	0.4/1.2/0.4	0/0.7	0/35	9240
CVSO 1545	0.5/1.5/0.1	10/80/10	1.00/1.25/0.05	2.6/5.0/0.4	0.6/1.4/0.4	0/7.3	0/35	11088
CVSO 1575	0.5/1.5/0.1	10/80/10	1.15/1.25/0.025	2.6/5.0/0.4	0.4/1.2/0.4	0/1.9	0/35	9240
CVSO 1600E	0.5/1.5/0.1	10/80/10	1.15/1.25/0.025	2.6/5.0/0.4	0.4/1.2/0.4	0/4.2	0/35	9240
CVSO 1600W	0.5/1.5/0.1	10/80/10	1.15/1.25/0.025	2.6/5.0/0.4	0.4/1.2/0.4	0/16.0	0/35	9240
CVSO 1711	0.5/1.5/0.1	10/80/10	1.15/1.25/0.025	2.6/5.0/0.4	0.4/1.2/0.4	0/2.5	0/35	9240
CVSO 1739	0.5/1.5/0.1	10/80/10	1.15/1.25/0.025	1.4/5.0/0.6	0.5/1.5/0.5	0/7.0	0/35	9240
CVSO 1763	0.6/5.0/0.5	10/80/10	1.125/1.25/0.025	2.6/5.0/0.4	0.8/1.6/0.4	0/0.8	0/35	11592
CVSO 1772	0.5/1.5/0.1	10/80/10	1.15/1.25/0.025	2.6/5.0/0.4	0.4/1.2/0.4	0/2.4	0/35	9240
CVSO 1842	0.1/1.0/0.1	10/80/10	1.00/1.20/0.05	3.0/5.4/0.4	0.6/1.8/0.4	0/3.4	0/35	8400
CVSO 1886	1.0/3.0/0.2	10/80/10	1.15/1.25/0.025	1.2/3.6/0.4	0.6/1.8/0.4	0/2.2	0/35	12320
CVSO 1928	0.2/2.0/0.2	10/80/10	1.10/1.30/0.05	1.8/4.2/0.4	0.8/1.6/0.4	0/1.8	0/35	5600
CVSO 1942	0.2/1.5/0.1	10/80/10	1.10/1.225/0.025	2.2/5.0/0.4	0.8/1.6/0.4	0/1.7	0/35	16128
ISO ChaI 52	0.1/1.0/0.1	10/80/10	1.15/1.25/0.025	2.2/5.0/0.4	0.8/1.6/0.4	0/3.2	0/35	17280
CHSM 13620	0.2/3.0/0.2	10/80/10	1.12/1.21/0.01	3.3/3.7/0.1	0.7/0.85/0.05	0/1.2	0/35	18000
J16020757	0.5/1.5/0.1	10/80/10	1.15/1.25/0.025	2.6/5.0/0.4	0.4/1.6/0.4	0/2.2	0/35	12320
J16253849	0.5/1.5/0.1	10/80/10	1.15/1.25/0.025	2.6/5.0/0.4	0.4/1.6/0.4	0/1.0	0/35	12320
J08074647	0.5/1.5/0.1	10/80/10	1.15/1.25/0.025	2.6/5.0/0.4	0.4/1.6/0.4	0/2.4	0/35	12320
J08075546	0.5/1.5/0.1	10/80/10	1.15/1.25/0.025	2.6/5.0/0.4	0.4/1.6/0.4	0/1.3	0/35	12320
J16042165	0.5/1.5/0.1	10/80/10	1.15/1.25/0.025	2.6/5.0/0.4	0.4/1.6/0.4	0/1.2	0/35	12320
SO682	0.5/1.5/0.1	10/80/10	1.15/1.25/0.025	2.6/5.0/0.4	0.4/1.2/0.4	0/1.0	0/35	9240

Note. — The range in each column has the format Min/Max/Step, except for a_c and σ_c with the format Min/Max.

For each model line flux in the velocity space $F_v(\dot{M}, R_i, W_r, T_{max}, i)$, the total model profile is given by

$$F_{v,total} = F_v(\dot{M}, R_i, W_r, T_{max}, i) + a_c e^{-v^2/(2\sigma_c^2)}, \tag{6.2}$$

where a_c and σ_c are the are the amplitude and the width of the Gaussian function representing the chromosphere, in the unit of the continuum and $\mathrm{km\,s^{-1}}$, respectively. Here we fix the center of the Gaussian at the stellar rest velocity. We then calculate the fit statistics by varying a_c and σ_c to minimize the χ^2,

$$\chi^2 = \sum_j \frac{\left(F_{j,total}(a_c, \sigma_c) - F_{j,obs}\right)^2}{F_{j,obs}}, \tag{6.3}$$

where j indexes over the pixels within $\pm v_{ff,\infty} = \sqrt{2GM_\star/R_\star}$, the free-fall velocity from infinity, and F_{obs} is the normalized observed flux in the native spectral pixels.

To determine the best fit model in a given grid, we calculate the likelihood,

$$L = Ne^{-\chi^2/2}, \tag{6.4}$$

for each combination of model parameters. N is a normalization chosen so that the highest likelihood in the grid is unity.

Figure 6.1 shows the example of the best fit for two stars employing our fitting procedures. The line profile of CVSO 1928, shown on the left panel of the figure, shows a redshifted absorption component and a slightly broader blue wing compared to the red. In this case, the chromosphere contributes significantly to the line profile, accounting for most of the emission at the line center, whereas the magnetosphere contributes primarily at the wing. On the other hand, the magnetospheric contribution can account for most of the line profile of CVSO 1295, shown on the right panel of Figure 6.1. The magnetospheric model can fit the low-velocity redshifted absorption and the wide blue and red wings simultaneously. Some residual can be seen near the peak, where the model slightly under-predict the emission. This region could be where the chromospheric emission can contribute. However, in our approach, we assume that the model components are additive, which may not be the case for lines where the magnetospheric flow absorbs lines from both the photosphere and the chromosphere. A possible approach to account for such radiative transfer effect is to add a Gaussian component, in addition to the continuum from the star, in the profile calculations. However, such approach is much more computationally expensive than what we have adopted here, especially when a large number of stars are involved. Another approach is to fix the chromospheric line *a priori* from independent measurements; this requires knowledge of the formation of chromospheric emission lines. These approaches will be explored in future studies.

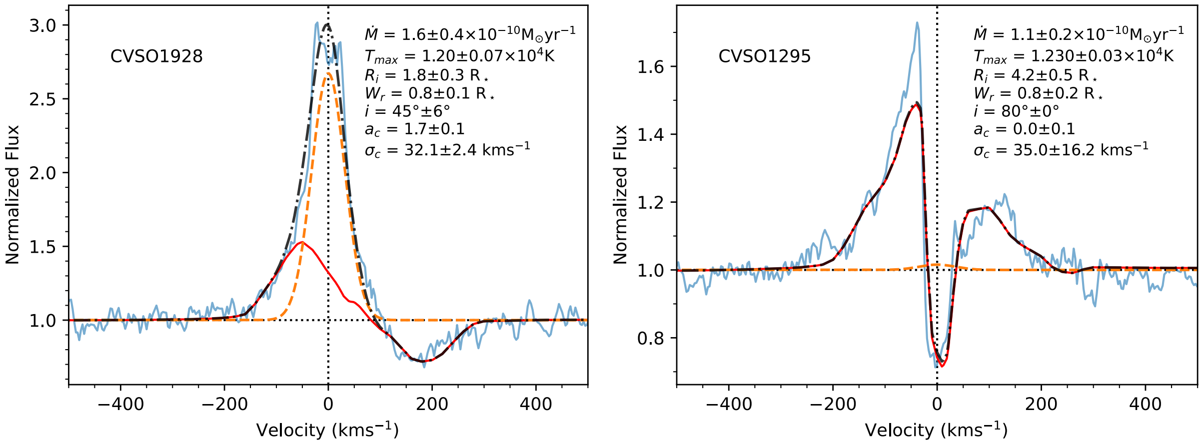

Figure 6.1 Examples of the fitting procedure incorporating the chromospheric emission. The dotted horizontal and vertical lines show the continuum level and the line center, respectively. The solid blue lines are the observation. The solid red lines are the contribution from the magnetospheric model. The dashed orange lines are the best fits for the chromospheric components of the line. The dash-dotted black lines are the best fit total model.

6.3.1.3 Inferring the Accretion Parameters

We determine the accretion parameters for each star by calculating the weighted mean and standard deviation of each parameter from models with a normalized likelihood of more than 0.5, where we use the likelihood L as the weight. Table 6.4 shows the accretion parameters retrieved from the magnetospheric accretion modeling and Figure 6.2 shows the Hα profiles where the accretion models can fit the observation very well. We plot the distribution of the parameters for all the samples selected for analysis in Figure 6.4.

6.3.2 Rotational Velocity

We measure the projected rotational velocity ($v \sin i$) of the stars using the Fourier method, following the procedure of Thanathibodee et al. (2020). We refer the reader to Serna et al. (2021, submitted) for a more detailed description of the method employed here. In summary, we corrected the spectra by shifting them with the measured apparent radial velocity calculated using the cross-correlation method with template spectra. We then calculated the Fourier power spectra of 3 to 15 photospheric lines. The number of photospheric lines used for each star depend on the signal-to-noise ratio of its spectrum and the strength of the absorption lines. The $v \sin i$ are then calculated from the location of the first zero in the power spectra. We include the $v \sin i$ measurement in Table 6.1, along with the stellar parameters.

Table 6.4 Results of the Magnetospheric Accretion Model

Star	$\dot{M}$ ($10^{-10}\,M_{\odot}\,\mathrm{yr}^{-1}$)	$\mathrm{R_i}$ ($\mathrm{R_\star}$)	$\mathrm{W_r}$ ($\mathrm{R_\star}$)	$\mathrm{T_{max}}$ (10^4 K)	i (deg)	a_c [a]	σ_c ($\mathrm{km\,s^{-1}}$)	Good
CVSO 40[b]	2.0±0.0	4.2±0	1.2±0	1.23±0.0	80±0	0.0±0	35.0±0	N
CVSO 156	1.1±0.3	3.4±0.7	0.7±0.2	1.21±0.04	80±0	2.8±0.2	25.3±2.5	Y
CVSO 298	1.5±0.4	4.2±0.6	0.8±0.4	1.14±0.08	79±0	2.3±0.1	27.8±3.7	Y
CVSO 1295	1.1±0.3	4.2±0.6	0.8±0.3	1.21±0.04	80±0	0.1±0.1	23.1±15.9	Y
CVSO 1545	0.9±0.3	3.3±0.7	0.8±0.2	1.18±0.06	79±2	5.2±1.4	34.2±2.5	Y
CVSO 1575	0.9±0.3	4.3±0.8	0.5±0.2	1.18±0.03	79±0	1.2±0.1	17.8±5.6	Y
CVSO 1600E	1.2±0.2	3.3±0.5	0.9±0.3	1.2±0.03	80±0	3.6±0.3	24.6±1.7	Y
CVSO 1600W	1.4±0.1	3.3±0.3	0.9±0.2	1.21±0.04	50±0	3.9±0.9	22.8±4.9	Y
CVSO 1711	1.0±0.3	4.0±0.8	0.6±0.2	1.2±0.04	80±0	2.4±0.1	30.8±3.6	Y
CVSO 1739	1.3±0.2	2.6±0.0	1.5±0.0	1.18±0.04	80±0	1.0±0.3	14.9±0.8	Y
CVSO 1763	3.8±0.6	3.6±0.5	1.2±0.0	1.21±0.03	79±0	0.0±0.0	4.4±11.6	N
CVSO 1772	0.7±0.2	4.5±0.5	1.0±0.2	1.18±0.03	79±0	2.4±0.0	26.4±2.9	Y
CVSO 1842	0.8±0.1	4.1±0.5	0.6±0.0	1.07±0.03	80±0	3.4±0.0	21.8±1.6	Y
CVSO 1886	2.4±0.4	2.1±0.2	1.8±0.1	1.23±0.03	79±0	1.5±0.1	23.2±1.9	Y
CVSO 1928	1.4±0.4	2.9±0.8	1.0±0.2	1.2±0.07	40±17	1.6±0.2	31.8±4.1	Y
CVSO 1942	1.3±0.1	4.4±0.6	0.8±0.1	1.2±0.03	23±11	1.4±0.2	32.8±4.2	Y
ISO-ChaI 52	0.9±0.1	2.6±0.3	0.8±0.0	1.14±0.03	41±5	1.8±0.2	21.4±2.7	Y
CHSM 13620	1.6±0.6	2.6±0.4	1.0±0.4	1.19±0.05	79±1	0.7±0.2	23.8±4.7	Y
J16020757	0.8±0.3	3.7±0.8	1.3±0.3	1.19±0.03	40±25	2.0±0.3	28.9±5.1	Y
J16253849	1.1±0.2	2.7±0.2	0.4±0.0	1.21±0.05	79±0	0.0±0.0	0.2±0.3	N
J08074647	0.6±0.1	3.7±0.6	1.5±0.2	1.17±0.03	47±29	2.3±0.1	27.0±3.1	Y
J08075546	1.2±0.2	3.4±0.7	0.4±0.0	1.2±0.04	43±6	0.4±0.1	26.2±8.2	Y
J16042165	1.4±0.1	4.5±0.5	0.4±0.0	1.23±0.02	65±4	0.5±0.3	23.2±12.6	Y
SO682	1.3±0.2	3.6±0.5	0.9±0.2	1.22±0.03	80±0	0.0±0.0	3.7±5.0	N

[a] a_c is in units of the continuum level as the profiles are fitted to the normalized flux.
[b] Too few models to determine uncertainty.

6.3.2.1 Stars Excluded from Further Analysis

As shown in Figure 6.3, the magnetospheric accretion model has difficulty reproducing observations of four stars. All of these stars show low-velocity redshifted absorption features in the line profile, but the magnetospheric model cannot reproduce the absorption feature while producing enough emission to fit the emission component of the line. This is unlike the case of CVSO 1295 (Fig. 6.1), in which the emission component is weak, ~ 1.5 times the continuum, while in these stars, the line peaks at $\sim 2.5 - 5$ times the continuum. We speculate that these stars have a flow structure similar to the low accretor CVSO 1335, with its conspicuous low-velocity redshifted absorption in the Hα line in multi-epoch observations (Thanathibodee et al. 2019b). Modeling these lines would likely require the two-flow models, as for CVSO 1335. In the interest of comparing parameters for large numbers of low accretors, as opposed to performing a detailed study of individual objects, we exclude these four stars from further analysis.

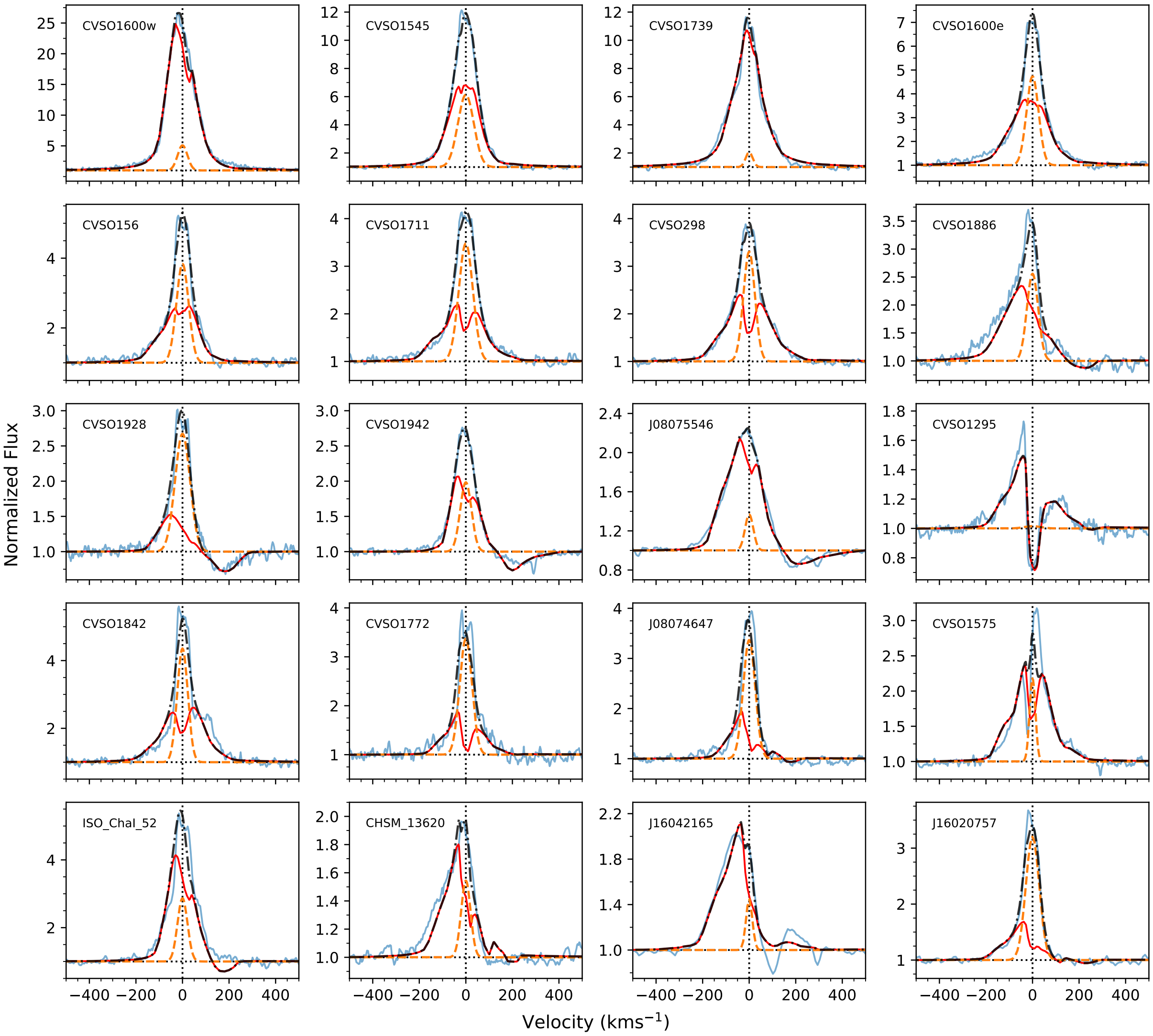

Figure 6.2 The best fits Hα line modeling for stars with good fits. Line types and colors as in Figure 6.1

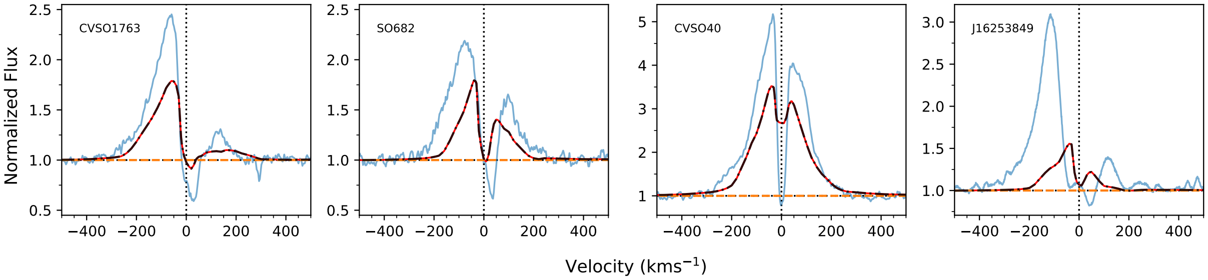

Figure 6.3 Same as Fig. 6.2, but for stars where the accretion flow model has difficulties reproducing the observations.

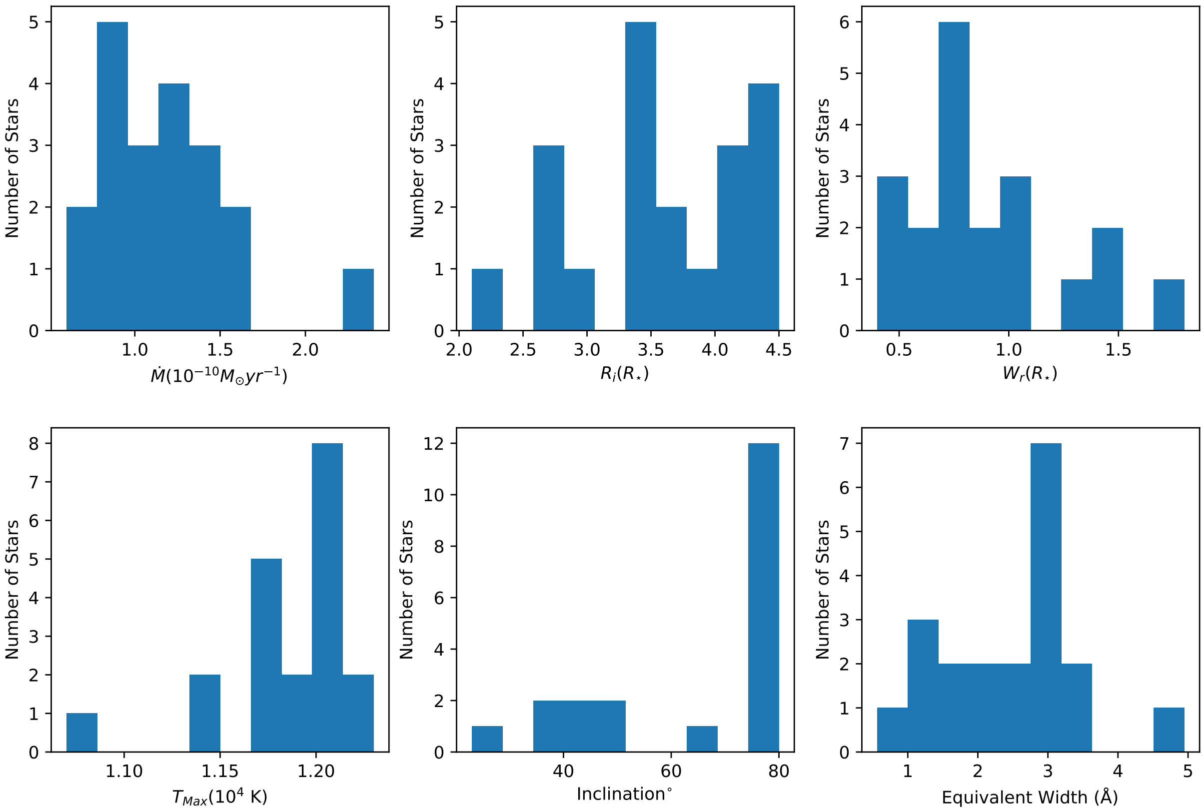

Figure 6.4 The distribution of model parameters for the 20 stars included in the analysis.

6.4 Discussion

In this section, we discuss inferences drawn from the accretion rates and flow geometries determined for the sample of low accretors. As explained above, we exclude four stars that seem to require more complex geometries to fit their Hα profiles (Thanathibodee et al. 2019b). Therefore, the discussion in this section will be based on 20 stars, indicated as 'Y' in Table 6.4. In the calculations that follow, we assume a minimum uncertainty of $0.1\,\mathrm{R}_\star$ for $\mathrm{R_i}$ and adopt a 10% uncertainty for $v \sin i$ in stars without the estimate.

6.4.1 Accretion Rates and Stellar Properties

Simulations of accreting magnetized stars have shown that accretion occurs differently depending on the geometry of the magnetic field. Analytical arguments, assuming a dipolar magnetic field, relate the accretion properties and those of the star with the expression

$$R_M = \xi \left(\frac{\mu^4}{4G\mathrm{M}_\star \dot{\mathrm{M}}^2} \right)^{1/7} \approx 18\xi \frac{B_3^{4/7} R_2^{12/7}}{M_{0.5}^{1/7} \dot{M}_{-8}^{2/7}}, \tag{6.5}$$

where R_M is the magnetic radius, at which the field truncates the disk, μ is the magnetic moment, B_3 is the strength of the surface dipolar magnetic field in kG, $R_2 = \mathrm{R}_\star/2\mathrm{R}_\odot$, $M_{0.5} = \mathrm{M}_\star/0.5\mathrm{M}_\odot$, $\dot{M}_{-8}$ is the mass accretion rate in the unit of $10^{-8}\,M_\odot\,\mathrm{yr}^{-1}$, and ξ encapsulates the details of the disk-magnetosphere interaction (Hartmann et al. 2016). From this equation, we expect that the geometry of the accretion flow, represented by the magnetic radius, will depend on the mass accretion rates for similar stellar parameters.

Mass accretion depends on the rotational velocity of the star. One metric used to determine if the system is in the accreting regime or in the propeller regime, when accretion does not occur, is the fastness parameter, defined as a ratio between the angular velocity of the star and the angular Keplerian velocity at the magnetic radius. It can be written as (e.g., Ghosh & Lamb 1979a; Romanova et al. 2018)

$$\omega_s = \frac{\Omega_\star}{\Omega_K(r_M)} = \left(\frac{R_M}{R_{co}}\right)^{3/2}, \tag{6.6}$$

where $\Omega_\star$ is the angular rotational velocity, $\Omega_K(R_M)$ is the angular Keplerian velocity at R_M, and R_{co} is the corotation radius.

In this sub-section, we investigate these relationships to determine the properties of the low accretors.

6.4.1.1 Accretion Rates and Accretion Geometry

In the left panel of Figure 6.5, we plot the truncation radius $\mathrm{R_i}$ versus the mass accretion rates. Due to the relatively large uncertainty in both parameters, we adopted the orthogonal distance regression to determine the trend between the parameters instead of the simple linear regression. The black dashed line shows the fit for the overall sample, and it suggests that the truncation radius increases as the mass accretion rate decreases.

The characteristics of the magnetic fields in T Tauri stars depend on the properties of the stars on their evolutionary tracks (e.g., Villebrun et al. 2019); the magnetic field strength becomes weaker as stars evolve from being fully convective to having radiative cores, for example. This evolution depends on the stellar mass and the age, which are reflected in the spectral type. In general, earlier spectral type (K-type) T Tauri stars are more massive and/or older than later-type T Tauri stars. On the left panel of Figure 6.5 we separate the K-type stars from the M-type stars. For the K-type stars, the truncation radius tends to be high, $\sim 4\,\mathrm{R}_\star$, regardless of the mass accretion rate. On the other hand, there is a stronger relationship between the two parameters for the M-type stars than for the whole sample. One star not following the trend is CVSO-298, with $\log \dot{M}$ = -9.82 and $\log \mathrm{R_i}$= 0.61. It is an M0 star in the Orion OB1a sub-association, with an age of $\sim$ 10 Myr (Briceño et al. 2019), and therefore it is the oldest star in the sample.

The trend for the M-type stars is expected from the relationship presented in Eq. 6.5, suggesting that dipolar magnetic fields still dominate the accretion processes in low-mass low accretors. The same cannot be said for higher mass or older stars, as no apparent trend emerges. It is possible that as the star gets older, the dipolar magnetic fields become weaker, as expected in studies directly measuring magnetic field properties of T Tauri stars (Villebrun et al. 2019; Lavail et al. 2017), making the relationship between $\mathrm{R_i}$ and $\dot{M}$ less meaningful as it is derived from an assumption of dipolar field.

Fitting a linear relationship to the M-type stars, we found that the mass accretion rates and the truncation radius can be related by a power law given by

$$R_i \propto 1/\dot{M}^{0.56\pm0.13}. \tag{6.7}$$

This result is robust against the star with the highest accretion rates in our sample (CVSO 1886, log $\dot{M}$ = -9.62), without which we have the exponent of 0.57 ± 0.19. The exponent (0.56 ± 0.13) is much larger than that found by simulations (0.19-0.22, Blinova et al. 2016; 0.2, Kulkarni & Romanova 2013; 0.34, Ireland et al. 2021), or that derived from equating the disk ram pressure and the magnetic pressure, as in Eq. 6.5, $2/7 = 0.29$. This suggests that there could be some other type of pressure terms in the disk balancing the magnetic pressure. Kulkarni & Romanova (2013) propose that as the magnetosphere is compressed by the disk, the truncation radius becomes less dependent on the mass accretion rate, and therefore the relationship between $\mathrm{R_i}$ and $\dot{M}$ will become weaker. Following the idea, the steep relationship between the two parameters could imply that the magnetospheres of low accretors are barely compressed, consistent with their low mass accretion rate as the disks would not have much ram pressure. Given that these simulations were run for accretion rates higher than $\sim 10^{-9}\, M_{\odot}\, \mathrm{yr}^{-1}$ for a typical set of stellar parameters, expanding the simulations to much lower rates is needed to test these possibilities.

6.4.1.2 Accretion Geometry and Rotation Properties

It is known from theoretical studies and simulations that accretion can be in different regimes depending on the relationship between the corotation radius and the disk truncation radius. The fastness parameter ω_s, relating the truncation radius and the corotation radius (Eq. 6.6), can be used to distinguish accreting into different regimes. The system is in the propeller regime if $\omega_s > 1$ ($\mathrm{R_i}$ $>$ $\mathrm{R}_{c}o$), and steady accretion cannot occur. Instead, some mass will get ejected from the system through winds, while some mass accumulates at the transition region between the two radii and gets periodically loaded onto the star (e.g., Romanova et al. 2018). For non-propellers, accretion may be in the stable or in the unstable regime. In the stable regime, accretion occurs in large funnels, and the light curve of the star, modulated by accretion hot spots, will be periodic (Romanova et al. 2008). Our axisymmetric accretion flow models most resemble this type of flows. The unstable regime, in turn, can be classified into two types based on how the mass is loaded onto the star. In the chaotic unstable regime, mass is loaded in several tongues that could be short-lived, whereas the ordered unstable regime is characterized by tongues merging to form one to two funnels (Blinova et al. 2016).

The boundaries between these regimes also depend on the magnetic obliquity, i.e., the misalignment between the rotation axis and the magnetic axis. Accretion is in the ordered unstable regime for $\omega_s \lesssim 0.45$ for a wide range of the values of obliquity, and the boundary between the stable and unstable regime is $\omega_s \sim 0.54 - 0.6$ for a misalignment between 5° and 20° (Blinova et al. 2016).

The corotation radius is typically calculated from the star's rotation period and the known mass and radius. Since the rotation periods of most of the stars in our sample are not available, we have to infer the period from the projected rotational velocity $v \sin i$. Assuming that the inclination of the stellar rotation is the same as the inclination found from the line modeling (Table 6.4), we calculate the corotation radius as

$$R_{co} = \left[\frac{G M_\star R_\star^2 \sin^2 i}{(v \sin i)^2} \right]^{1/3} . \tag{6.8}$$

Since the assumption of axial symmetry is not necessarily correct, we adopt a minimum uncertainty of 15° for the inclination, unless the modeling results suggest a larger value. The uncertainties in the final values are calculated using standard error propagation methods.

The right panel of Figure 6.5 shows the correlation between the truncation radius and the corotation radius. Four solid lines show the boundary between accretion regimes based on the value of the fastness parameter. None of our targets is in the propeller regime, including the possible accretors (CVSO 1772, CVSO 1842) and episodic accretors (CVSO 1295, CVSO 1575) in our sample. A likely explanation is that these stars are accreting most of the time, but the accretion detection using He I λ10830 in Chapter 5 has some limitations, as discussed therein.

Most of the targets are in the unstable regime, with about half of them in the ordered unstable regime. Given that the gap between the ordered unstable regime and the stable regime is small, it is likely that most of our targets are in the regime in which large funnel flows are present, and applying the magnetospheric model to these cases is appropriate.

These results suggest that low accretors, except for having large truncation radii, are accreting "normally" and are not close to the propeller regime. As noted above, this interpretation is dependent on the assumption that there is no magnetic obliquity. In reality, corotation radii calculated from Eq. 6.8 are likely to be upper limits, as the mean inclination should be $\sim 60°$. Nevertheless, the R_{co} depends on $\sin^{2/3}(i)$, so the effect of inclination is small at a moderate to high inclination. Therefore, there could be more stars in the stable regime, but it is unlikely that any stars would be in the propeller regime. In this case, we can infer that accretion stops not because the

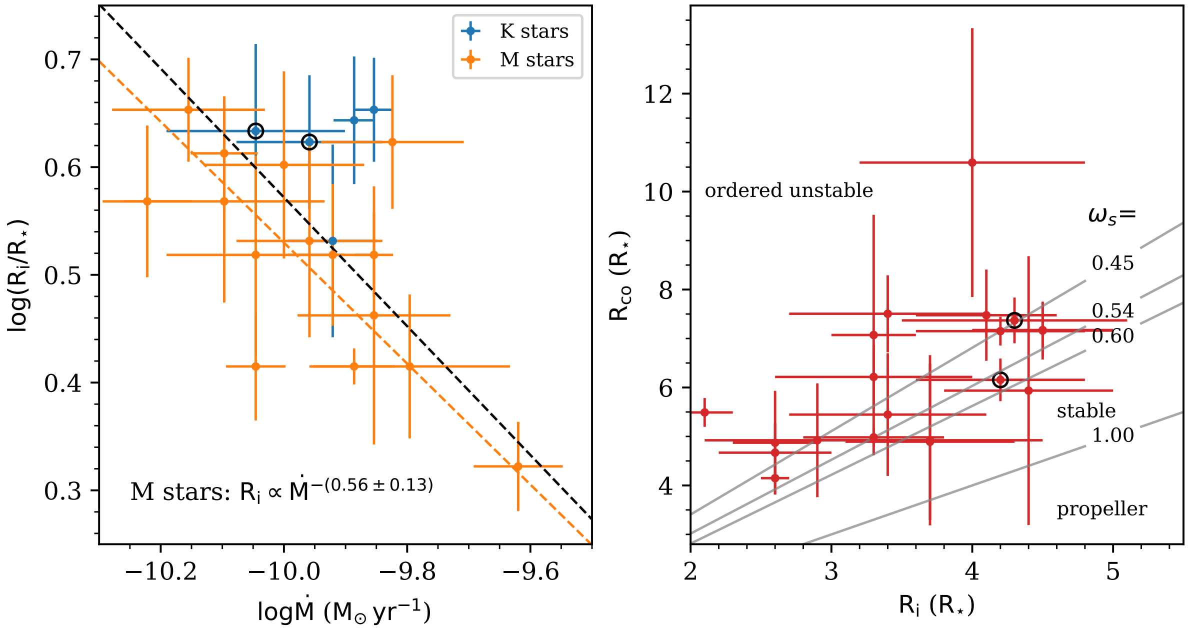

Figure 6.5 Relationships between the truncation radius R_i and the mass accretion rate and the corotation radius in low accretors. *Left:* The truncation radius as a function of $\dot{M}$, plotted in log scale. K-type stars are plotted in blue and M-type stars are plotted in orange. The black line is the best fit calculated from linear orthogonal distance regression for the whole sample. The orange line is the fit for M-type stars. *Right:* The corotation radius as a function of the truncation radius. The gray lines correspond to different radius ratios for different values of fastness parameters ω_s, shown on the plot. The lower right region of the plot is the propeller regime, and the upper left region is the ordered unstable regime. The boundary between the stable and unstable regime is $\omega_s \sim 0.54 - 0.6$, depending on the obliquity of the magnetic axis (Romanova et al. 2008, 2018). Stars marked in black are episodic accretors.

system reaches the propeller regime but from other processes. However, another possibility is that our sample does not include stars nearing the propeller regime because they were not identified as accretors even with the He I λ10830 line. To test this hypothesis would require observing stars identified as possible accretors in multi-epoch observations.

6.4.1.3 The Disk-Magnetosphere Interaction of Low Accretors

Equation 6.5 provides an explicit relationship between accretion rates and accretion and stellar properties, as discussed above. Given that $R_M = R_i$, the truncation radius, we can use the measurements from our sample to determine the average values of the magnetic field B and the parameter ξ.

Figure 6.6 shows the relationship between the truncation radius R_i inferred from the magnetospheric accretion flow model fitted to observations and the magnetic radius R_M calculated from

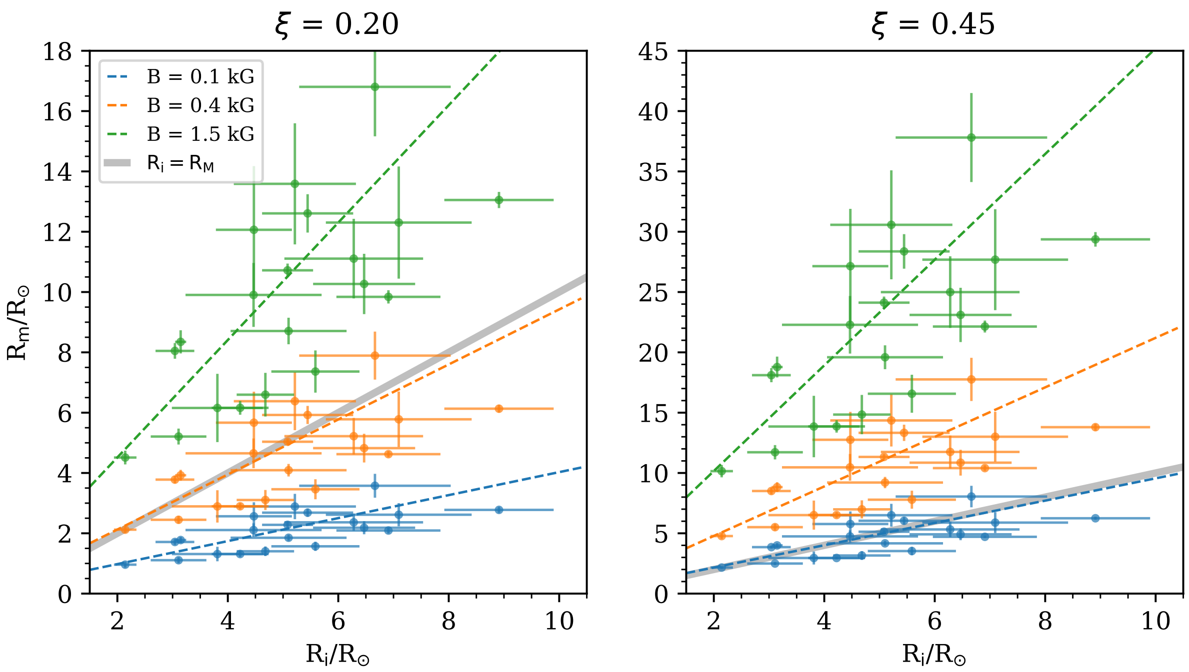

Figure 6.6 The magnetic radii calculated from mass accretion rates and the inferred truncation radii from the model, varying ξ and the surface magnetic field strength B. Different colors refer to different magnetic field strengths. The dashed lines are the linear regressions of the two radii. The solid gray lines are the one-to-one relationship between the two measurements.

Eq. 6.5 using the inferred $\dot{M}$. Different colors in the plot refer to different strengths of the surface dipolar magnetic field.

The dashed lines are the best linear fits calculated using the orthogonal distance regression, as in Figure 6.5, and the solid gray lines are the one-to-one relationship. From these fits, it is evident that for the magnetic radius to be the same as the truncation radius, the stars generally require a low value of ξ or a low value of the magnetic field B.

We can compare these values to theoretical expectation ($\xi \sim 1$) and numerical simulations. For example, Kulkarni & Romanova (2013) and Blinova et al. (2016), using the large suite of models of their numerical simulations, investigated the relationship between the magnetic radius calculated from the models and that calculated from theoretical prediction such as that presented in Eq. 6.5. Their models are for truncation radii between $\sim 2-6\,\mathrm{R}_\star$, which are appropriate for comparison with our data. Blinova et al. (2016) found that the parameter ξ ranges from $0.5 \lesssim \xi \lesssim 0.9$ for stable accretion and $0.8 \lesssim \xi \lesssim 0.93$ for unstable accretion; a similar range is found by Kulkarni & Romanova (2013).

For our estimates to be consistent with the high values of ξ obtained in the simulations, the magnetic field strength needs to be as low as 0.1 kG or even lower, as the analysis in Figure 6.5

indicates. Given that the total magnetic field strength in T Tauri stars is on the order of a few kG (e.g., Lavail et al. 2019), this suggests that the magnetic field that is responsible for accreting mass, i.e., the dipolar field, is very weak compared to other topologies (e.g., quadrupole and octupole). Weaker dipole components compared to higher-order fields are found in observations (e.g., Gregory et al. 2008; Donati et al. 2011; Chen & Johns-Krull 2013), but not as much as that of our results. It is possible that as the star evolves, most of the magnetic field lines are in the higher-order configuration, but we can still see accretion as if the dipolar field dominated because the mass accretion rate is so low such that even a weak field is able to truncate the disk. Measurements of the components of the magnetic fields in very low accretors would be required to test this hypothesis.

We also note that the simulations suggesting high values of ξ are run for stars accreting at relatively high accretion rates, $\sim\ 10^{-7}\,M_{\odot}\,\mathrm{yr}^{-1}$. It is possible that at low accretion rates, the efficiency for the magnetic fields to truncate the disk decrease significantly. Whether the two parameters are directly related, or they result from a common cause (e.g., evolution of stars/disks) is unclear. Simulations of accreting stars at very low rates are needed to explore this scenario.

6.4.2 The Distribution of Accretion Parameters

To search for common properties among the low accretors, we plot the distributions of the best fit model parameters for the 20 stars in Figure 6.4. The mass accretion rates and the truncation radius are discussed separately in §6.4.1 and §6.4.4. Here, we discuss the findings and implications for other parameters.

6.4.2.1 Inclination

Perhaps the most surprising finding in these distributions is that the inclination of low accretors are very high. It is possible that this is in part due to the assumption that there is no magnetic obliquity, and the inclinations of the stellar rotation axes are somewhat smaller than $\sim 80^{\circ}$. Tilted magnetospheres should produce light curves that are different from aligned magnetospheres (e.g., Romanova et al. 2004). Photometric monitoring of these stars will help to test this hypothesis.

Another possibility for the high inclinations is that it is an observational bias in the survey to search for low accretors (Chapter 5), which used the equivalent width and the width at 10% peak (W_{10}) as criteria for selecting low accretor candidates.

We illustrate this bias in Figure 6.7, in which we show Hα profiles calculated for an M2 low accretor observed at different inclinations. The spectral type of the star is the median spectral type of the newly identified accretors in Chapter 5. We assumed that the chromospheric contribution to the line, modeled as a Gaussian, stays constant at EW=4.1 Å, i.e., more than 50% lower than White

& Basri (2003)'s threshold of accretion for an M2 star. As shown by panel (a) of the Figure, the line profiles change both in strength and shape as the viewing inclination changes. In particular, at a low inclination, the total line profile (shown in blue) is dominated by the emission from the magnetosphere. The line is also brighter since few regions of the flow are occulted by the star, the flows in front, or the disk. However, the line is narrow at a low inclination, as the line of sight is closer to normal with the poloidal velocity field of the accretion flow. The line becomes weaker and broader at high inclinations due to the same effects discussed above. In this limit, the chromosphere dominates the emission line.

When observations are made to determine accretion status, no chromospheric contribution is removed, as it is unknown. Therefore, the measurement of EW and W_{10} will intrinsically include the effect of the chromosphere. Panel (b) of Figure 6.7 shows the measurement of EW and W_{10} for the profiles in panel (a) with and without the chromospheric contribution. For reference, the thresholds for accretion classification, EW ≥ 10 Å and $\mathrm{W}_{10} \geq 270\ \mathrm{km\,s^{-1}}$ (White & Basri 2003), are indicated in the Figure. Without the chromospheric contribution, the star would have been classified as an accretor if the EW criterion had been used and if it had an inclination of 45° or less; at higher inclinations, the EW would be below, or at least barely above, the threshold. On the other hand, it would be classified as an accretor at high inclination if the W_{10} criterion had been used.

When taking into account the chromosphere, a similar trend is found for equivalent widths, except that it would need to have a high inclination, > 60 °, to be classified as non-accretor. For W_{10}, it would always be classified as non-accretor, regardless of inclination. This is because, at a high inclination, the peak is raised by the chromospheric contribution, so the measurement at the 10% peak is at the narrower part of the line profile.

In Chapter 5, stars selected as low accretors candidates are those classified as non-accretors using either W_{10} or EW. Since most of the targets were selected based on the equivalent width of Hα, the survey preferentially included stars at higher inclinations as those were stars with the highest chance of being (mis-)classified as non-accretors. Therefore, it is not surprising that most of our targets show high inclination in the magnetospheric modeling.

6.4.2.2 The Equivalent Width of the Chromospheric Emission

For the parameters related to the Gaussian chromospheric contribution, we plot instead in the equivalent width of the chromospheric line, calculated as

$$EW_c = \sqrt{2\pi} a_c \sigma_{c,\lambda}, \tag{6.9}$$

where $\sigma_{c,\lambda}$ is the Gaussian width converted to wavelength scale.

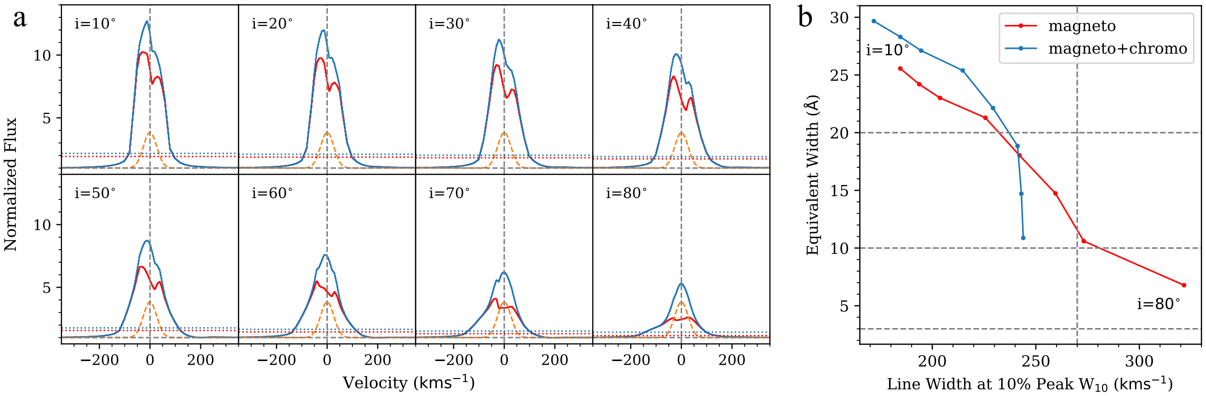

Figure 6.7 Changes in line strength and morphology due to inclination. We adopted the stellar parameters of the M2 star CVSO 156 with model parameters R$_i$=2.6 R$_\star$, W$_r$=0.4 R$_\star$, $\dot{M}$=9 $\times$ 10^{-11} $M_\odot\,\mathrm{yr}^{-1}$, and T$_{\mathrm{max}}$=1.15 $\times$ 10^4 K.
(a) The line profiles at different inclinations from $i = 10°$ to $i = 80°$. The red lines are the profiles of the magnetospheric model. The orange lines are the chromospheric contribution, assumed to be constant for all inclinations. The blue lines are the sum of the two components. The dotted horizontal lines show the level at 10% of the peak flux.
(b) The equivalent width and the width at the 10% flux (W$_{10}$) corresponding to the profiles in (a). The same color scheme is used. The points at the upper left of the plot are those with low inclinations, and the points at the lower right are high at inclinations. The horizontal lines are the accretor EW threshold of White & Basri (2003) for spectral type K5, M2.5, and M5.5, and the vertical line is the W$_{10}$ threshold of 270 $\mathrm{km\,s^{-1}}$ (White & Basri 2003).

Most of the stars have the EW of the chromospheric component less than 5 Å, and a portion of them require very small or almost no chromospheric contribution. Given that most of the newly identified low accretors have the equivalent width of Hα of less than 10 Å (Figure 5.10 of Chapter 5), these results confirm previous findings that the chromospheric contribution can be very significant in the line (e.g., Manara et al. 2013).

6.4.3 The Lowest Measurable Mass Accretion Rates

The distribution of mass accretion rates of our sample, shown in Figure 6.4, suggests that most of the stars accrete at $\sim 10^{-10}\,M_\odot\,\mathrm{yr}^{-1}$, with the lowest at $\sim 5 \times 10^{-11}\,M_\odot\,\mathrm{yr}^{-1}$. Is this a physical limit, or is it the lowest rate that can be measured using line modeling?

To address this question, we run two grids of models for two 5 Myr stars, a K5 star and an M3 star accreting at very low accretion rates, from $10^{-12}\,M_\odot\,\mathrm{yr}^{-1}$ to $10^{-10}\,M_\odot\,\mathrm{yr}^{-1}$. The two spectral types are representative of the targets in our sample. As the line profiles also depend on the geometry and temperature, we also varied R$_i$, W$_r$, and T$_{\mathrm{max}}$ within the ranges found in Figure 6.4. We fixed the inclination at 60°. In all cases, we assume no contribution from the accretion shock. Chromospheric emission is also not included.

We show the results of the two small grids in Figure 6.8. In both stars, the emission component is stronger for large and narrow magnetospheres, as in Muzerolle et al. (2001). The redshifted absorption component of the line can be seen in all geometries for a wide range of accretion rates. Assuming that we can detect a feature in the line that has $\sim 30\%$ deviation from the continuum (i.e., signal-to-noise ~ 3, see also CVSO 1928 in Fig. 6.2), we can estimate the lowest mass accretion rates detectable with each model by determining if the emission feature is greater than ~ 1.3 and the absorption feature is deeper than ~ 0.7, both in the normalized unit of the continuum. For the K5 stars, we can see that the features would still be detectable at $\sim 3 - 5 \times 10^{-11}\, M_{\odot}\, \mathrm{yr}^{-1}$ (green and orange lines) in all geometries considered. For the M3 stars, the lowest detectable mass accretion rate is $\sim 1 - 3 \times 10^{-11}\, M_{\odot}\, \mathrm{yr}^{-1}$ (i.e., red and green lines).

The situation is more complicated in the actual observations since chromospheric emission will be presented in the line. However, if the accretion rates are truly low (but higher than $\sim 10^{-12}\, M_{\odot}\, \mathrm{yr}^{-1}$), the redshifted absorption will be very evident, as seen in all cases in Figure 6.8. These absorption features are much broader than the typical width of the chromospheric lines (Table 6.4), and therefore accretion will still be detectable as long as the spectra are obtained at a sufficiently high resolution (we used R=32500, i.e., that of MIKE, in Figure 6.8).

The results from the two stars can also be approximately extrapolated; that is, the limit would be slightly lower than $3 \times 10^{-11}\, M_{\odot}\, \mathrm{yr}^{-1}$ for a spectral type later than M3, and somewhat higher than $5 \times 10^{-11}\, M_{\odot}\, \mathrm{yr}^{-1}$ for a spectral type earlier than K5.

6.4.4 How Does Accretion Stop?

The analysis and discussion in previous sub-sections have provided some evidence of how accretion stops. In § 6.4.1, we can see that essentially all low accretors are accreting in the unstable regime, but none is close to the propeller regime. Therefore, we can infer that accretion does not stop by the stellar rotation reaching the propeller regime, or at least this process is not the main driver stopping accretion. Instead, other processes must be at play.

As discussed by Thanathibodee et al. (2020) in the study of the PDS 70 system, the formation of giant planets may, in some way, contribute to decrease accretion onto the star. However, as shown in that work, the mass accretion rates of the two planets are very low compared to that of the host star, and therefore mass accretion onto planets is unlikely to be the primary source stopping accretion. Nevertheless, the formation of giant planets creates large gaps in the protoplanetary disk; this could make disk dispersal processes such as photoevaporation more pronounced (Alexander et al. 2014).

The fact that most of the stars in our sample are accreting at $\sim 10^{-10}\, M_{\odot}\, \mathrm{yr}^{-1}$ even though the model can essentially detect accretion a factor of magnitude lower than that suggests that we have obtained a physical lower limit to the mass accretion rate in the mass range covered by the stars in our sample. Two possibilities may be able to explain this observational result.

First, it is possible that this is a selection bias, such that we only selected stars classified as accretors using the He I $\lambda10830$ line, and that the line is not sensitive below $10^{-10}\,M_{\odot}\,\mathrm{yr}^{-1}$. Therefore, we have missed stars accreting at $\sim 10^{-11}\,M_{\odot}\,\mathrm{yr}^{-1}$. Continuous monitoring of possible accretors (c.f., Chapter 5) could be used to explore this possibility.

One implication of the sensitivity problem is that we cannot rule out a possibility that the inner disk could host a gas reservoir with low viscosity (Hartmann & Bae 2018). In this case, the inner disk is first separated from the outer disk due to processes that deplete the outer disk (e.g., photoevaporation). Due to low viscosity, the inner disk will drain slowly and will last long. The mass accretion rate onto the star will decrease with time, and with a sufficiently sensitive probe, accretion could be detected at the level well below $10^{-10}\,M_{\odot}\,\mathrm{yr}^{-1}$. If $\sim 10^{-10}\,M_{\odot}\,\mathrm{yr}^{-1}$ is the physical limit, the inner disk mass reservoir scenario can be reconciled with other processes removing gas from the disk, such as inner disk winds (Hartmann & Bae 2018).

Second, it is also possible that $10^{-10}\,M_{\odot}\,\mathrm{yr}^{-1}$ is the actual limit to the rate at which a star can accrete mass from its inner disk. If the inner disk depletion timescale is short (due to, e.g., high viscosity), the mass accreted onto the star is then essentially controlled by the supply of mass from the outer disk. In this scenario, photoevaporation could play a crucial role, since photoevaporation models suggest that mass accretion onto the stars ceases in a very short time scale ($\sim 10^{5}\,\mathrm{yr}$) once the mass accretion rates equal the photoevaporative mass loss rates. With the steady supply of mass from the outer disk, controlled by the photoevaporative rate, our results suggest that the photoevaporative mass loss rates should not be higher than $1 \times 10^{-10}\,M_{\odot}\,\mathrm{yr}^{-1}$ for the mass range considered in this study ($0.1 - 1.2\,M_{\odot}$) at the last stages of disk evolution.

Models of photoevaporation as well as observational constraints suggest a wide range of photoevaporative mass loss rates from $\sim 10^{-10}\,M_{\odot}\,\mathrm{yr}^{-1}$ to $10^{-8}\,M_{\odot}\,\mathrm{yr}^{-1}$, depending on which energy range irradiates the disk (EUV, X-ray, or FUV; Clarke et al. 2001, Owen et al. 2011, Gorti & Hollenbach 2009). Our results agree with the low rates of mass accretion predicted by EUV-dominated photoevaporation, suggesting that it is likely the main mechanism depleting disks at their last stages of evolution. It is possible that the higher mass loss rates from other mechanism are needed at earlier stages of disk evolution, as the disk lifetime would be longer than observed if the EUV-dominated photoevaporation operates alone at all timescales (Alexander et al. 2014).

Regardless of the mechanism removing mass from the disk, it is now quite clear that mass accretion onto the star stops due to the properties of the disk as opposed to those directly related to the stars, as previously suggested in Chapter 5. It is possible that accretion stops because the disk runs out of gas, but how the processes that remove mass from the disk essentially stops accretion remains unclear. Detailed studies of disk properties (e.g., density, mass, gap sizes, dust settling) and their related radiation fields (FUV, X-ray) are needed to pinpoint the most probable processes stopping accretion. This is a subject for a follow-up study.

6.5 Summary and Conclusions

In this Chapter, we conducted a study of 22 accretors and two possible accretors identified as such using the profiles of He I λ10830 line. We applied the magnetospheric accretion model (Hartmann et al. 1994; Muzerolle et al. 1998a, 2001) to fit the Hα lines of the stars observed with moderate resolution spectrograph, and inferred the accretion properties from the best fitting models. We summarize our findings as followed:

1. Most of the Hα lines have a significant contribution from the narrow chromospheric emission component of the line. Representing the chromospheric emission with a Gaussian, we find that 20 stars can be fitted very well with the combined magnetospheric+chromospheric model. These stars are used for further analysis.

2. A fraction of stars shows low-velocity redshifted absorption on top of bright emission in the Hα line profile. We speculate that the magnetospheres of these stars are similar to that of CVSO 1335 (Thanathibodee et al. 2019b), where accretion occurs in complex, multi-flows geometry.

3. We find an anti-correlation between the disk truncation radius and the mass accretion rates in the M-type stars of the sample. However, the power-law relation is much steeper than that expected from theory and simulations, suggesting that the pressure balance between the magnetosphere and the inner disk is much more complicated than that assumed in the derivation of magnetic radii, at least in low accretion rates.

4. The disk truncation radius and the mass accretion rates are not correlated in the K-type stars of the sample, which may be due to departures of the magnetic field from dipolar geometry in these stars.

5. We calculated corotation radii from the projected rotational velocity of the stars and found them to be always larger than the truncation radii, which implies that the magnetic propeller is not the primary agent stopping accretion. We also find that essentially all low accretors accrete in the unstable regime.

6. We compared the magnetic radius calculated from mass accretion rates and stellar parameters with the truncation radius inferred from the model and found that either the efficiency

parameter ξ or the dipolar magnetic field B need to be weak for the two radii to be the same. For the efficiency parameters to be comparable to other studies, the dipole magnetic field must be much smaller than the total magnetic fields, assumed to be at a few kG. This suggests that, as stars evolve, most of the magnetic fields are in higher-order configurations, but the dipole component can still truncate the disk due to the low accretion rates.

7. The inferred high inclinations of the majority of our targets suggest a possible observational bias introduced by adopting the equivalent width of Hα as a selection criterion to identify low accretor candidates. This is because the equivalent width of the line depends strongly on inclination for low accretors, such that it will often go below the threshold at a high inclination. Therefore, more low accretor candidates get selected at high inclinations.

8. Mass accretion rates of low accretors are not much lower than $1 \times 10^{-10}\, M_{\odot}\, \mathrm{yr}^{-1}$, regardless of the mass of the star, even though we could detect rates 5 to 10 times lower. This suggests that photoevaporative mass loss rates are of the same order since otherwise, these low rates would not have been detected. This value for the photoevaporative rate is consistent with the low end of EUV-driven photoevaporation. As we ruled out the propeller as the main driver stopping accretion, the same mass accretion rates across the mass range suggest that the processes that stop mass accretion onto the star actually occur in the disk. Accretion may stop simply because the disk runs out of gas.

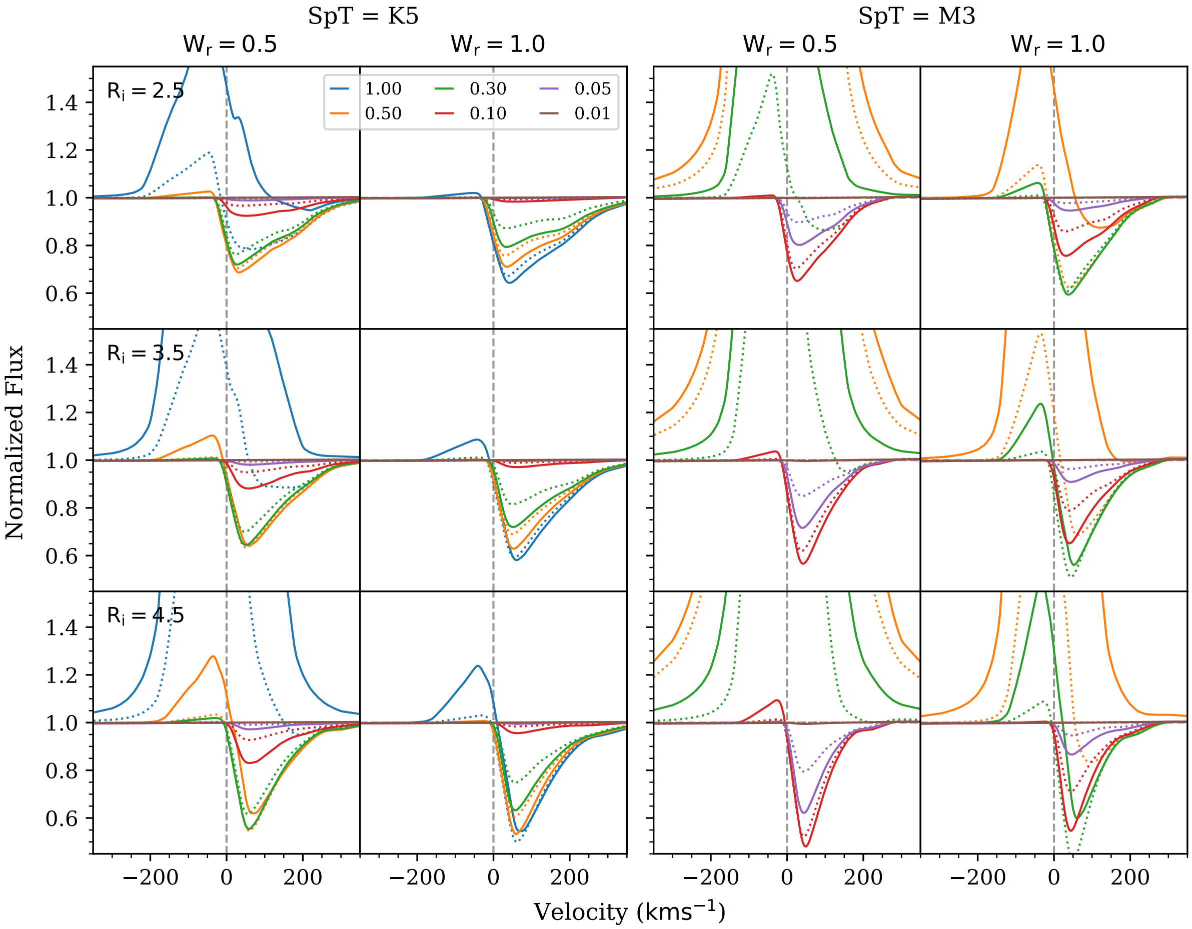

Figure 6.8 The variation of line profiles at the lowest limit of accretion for stars with spectral types K5 and M3. The two columns for each spectral type are for W_r=0.5 and W_r=1.0, respectively. Each row refers to a fixed truncation radius R_i. Different colors are for different mass accretion rates; the legend shows the mass accretion rates in units of $10^{-10}\,M_\odot\,\mathrm{yr}^{-1}$. The solid lines are the profiles calculated for $T_{\max}$=13,000 K and the dotted lines are for $T_{\max}$=12,000 K. The range of the y-axis is fixed at low values to focus on the feature of the line near the continuum. The model at $\dot{M} = 10^{-12}\,M_\odot\,\mathrm{yr}^{-1}$, shown in brown, can barely be seen apart from the continuum.

CHAPTER 7

Magnetospheric Accretion as a Source of Hα Emission from Proto-planets around PDS 70

This chapter was originally published in the Astrophysical Journal, Volume 885, 94 (2019), in collaboration with Nuria Calvet, Jaehan Bae, James Muzerolle, and Ramiro Franco Hernández. It is adapted and reproduced here under the non-exclusive rights of re-publication granted by the American Astronomical Society to the authors.

Abstract

Advances in high-resolution imaging have revealed Hα emission separated from the host star. It is generally believed that the emission is associated with forming planets in protoplanetary disks. However, the nature of this emission is still not fully understood. Here we report a modeling effort of Hα emission from the planets around the young star PDS 70. Using standard magnetospheric accretion models previously applied to accreting young stars, we find that the observed line fluxes can be reproduced using a range of parameters relevant to PDS 70b and c, with the mean mass accretion rate of log($\dot{M}$) = -8.0 ± 0.6 $\mathrm{M_{Jup}\,yr^{-1}}$ and -8.1 ± 0.6 $\mathrm{M_{Jup}\,yr^{-1}}$ for PDS 70b and PDS 70c, respectively. Our results suggest that Hα emission from young planets can originate in the magnetospheric accretion of mass from the circumplanetary disk. We find that empirical relationships between mass accretion rate and Hα line properties frequently used in T Tauri stars are not applicable in the planetary mass regime. In particular, the correlations between line flux and mass accretion rate underpredict the accretion rate by about an order of magnitude, and the width at the 10% height of the line is insensitive to the accretion rate at $\dot{M} < 10^{-8}$ $\mathrm{M_{Jup}\,yr^{-1}}$.

7.1 Introduction

One of the thrilling new frontiers in exoplanet research is the unraveling of the earliest stages of planet formation. The advances of high-contrast, high-spatial-resolution technology have produced direct and indirect evidence of planets forming in circumstellar disks since very early ages. The regions cleared of small dust in the transitional disks (c.f. Espaillat et al. 2014) were the first structures identified in protoplanetary disks, and they were attributed to the interaction of forming planets with the disk. Submillimeter interferometry has now shown that structures are present in probably most disks, and in particular, ringed structures are ubiquitous in disks around stars of all spectral types (Andrews et al. 2018). Again, these structures are thought to be due to planets forming in disks (e.g., Bae et al. 2017; Zhu et al. 2011), although alternative hypotheses such as dust accumulation in condensation fronts of different molecular species (Zhang et al. 2015) have also been discussed. The best evidence of young planets comes from direct imaging, and so far detections have been claimed for a handful of systems with different degrees of reliability. For example, features in Hα image around LkCa 15 are thought to be from planets (Kraus & Ireland 2012; Sallum et al. 2015), but later studies have shown that such features could come from the circumstellar disk (Mendigutía et al. 2018; Currie et al. 2019). Reggiani et al. (2018) reported a detection of a planet candidate interior of the spiral arm of the disk around MWC 758; however, Wagner et al. (2019) could not confirm this detection and instead found another candidate exterior of the spiral arm. Other claims of planets around young stars include HD 100546 (Quanz et al. 2013a, 2015; Brittain et al. 2014; Currie et al. 2015; Follette et al. 2017), HD 169142 (Quanz et al. 2013b; Biller et al. 2014; Reggiani et al. 2014), HD 163296 (Pinte et al. 2018; Teague et al. 2018).

Robust planet detections have been reported around the star PDS 70, a K7 star in the $\sim$ 5-10 Myr old Upper Sco association. PDS 70 is surrounded by a disk with an $\sim 80\,$au cavity (Riaud et al. 2006; Hashimoto et al. 2012, 2015; Keppler et al. 2018); it is also a pre-transitional disk (Espaillat et al. 2007), that is, a disk with a large cavity but with another optically thick disk in the innermost au from the star. This configuration was first identified by SED fitting (Hashimoto et al. 2012; Dong et al. 2012), and later confirmed by observations in the NIR with SPHERE (Keppler et al. 2018) and in the submillimeter with ALMA (Long et al. 2018a; Keppler et al. 2019). Keppler et al. (2018) reported the discovery of a companion at $\sim$ 22 au from the star in the gap between these two disks, confirmed by the 4-σ detection of Hα emission at the location of the companion using MagAO narrow filters (Wagner et al. 2018). The companion, PDS 70b, has a mass between 5 and 14 Jupiter masses, as indicated by a comparison of magnitudes and colors with different model predictions. However, hydrodynamic simulations including PDS 70b on a circular orbit failed to reproduce the large width of the cavity, and an additional companion beyond the orbit of PDS 70b was suggested (Keppler et al. 2019). Indeed, using adaptive-optics-assisted integral-field spectroscopy with VLT/MUSE, Haffert et al. (2019) detected Hα emission from PDS 70b and reported additional Hα emission from a second planet, PDS 70c.

High angular resolution observations by ALMA revealed the presence of 855 μm dust emission from a circumplanetary disk (CPD) at the position of PDS 70c, with an estimate of dust mass between $2 - 4.2 \times 10^{-3}\,\mathrm{M}_{\oplus}$ (Isella et al. 2019). CPD detection around PDS 70b is still unclear since ALMA observation (Isella et al. 2019) shows a slight offset between the position of the planet and that of the 855 μm emission. Nevertheless, an estimated dust mass of $1.8 - 3.2 \times 10^{-3}\,\mathrm{M}_{\oplus}$ could be attributed to CPD of PDS 70b if it is present.

Mass accretion rates have been estimated for both PDS 70b and c. Wagner et al. (2018) detection of Hα emission at the location of PDS 70b led them to conclude that the planet is actively accreting mass from its disk. They used the Hα flux to estimate a mass accretion rate onto the planet of $\dot{M} \sim 10^{-8} M_{\mathrm{Jup}}\,\mathrm{yr}^{-1}$, which is consistent with the upper limit estimated by Christiaens et al. (2019) from the lack of detection in Brγ. Haffert et al. (2019) also inferred values of the mass accretion rate, but they used the width at the 10% height (W_{10}) of the Hα line estimates for PDS 70b and c, applying the correlation from Natta et al. (2004). The mass accretion rates for PDS 70b determined by Haffert et al. (2019) is similar to that by Wagner et al. (2018), even though the Hα flux is an order of magnitude lower. This is due to uncertainties in the diagnostics used to estimate mass accretion rates.

The correlations used to estimate mass accretion rates from emission line properties are determined from line luminosities and accretion luminosities calculated for T Tauri stars (e.g., Natta et al. 2004; Rigliaco et al. 2012; Ingleby et al. 2013). Since accretion in that type of stars occurs through a magnetosphere, the assumption that the T Tauri star $\mathrm{L}_{\mathrm{line}}$ vs. $\mathrm{L}_{\mathrm{acc}}$ calibrations are valid for planets would imply that mass is loaded from the CPD onto the planet through magnetospheric accretion as well. However, this has not yet been proven.

The relationship between Hα line luminosity and accretion properties have also been explored to some extent in other types of models. It has been suggested that Hα emission arises in regions of the order of a few hundred planet radii heated to $8000 - 10000\,\mathrm{K}$ by the shock on the CPD surface due to infalling gas from the circumstellar disk (Szulágyi & Mordasini 2017). Using 1D radiative transfer model, Aoyama et al. (2018) calculated the properties of the CPD shock and predicted the Hα fluxes for different densities and planetary masses for an application to the suggested planet around LkCa 15. Nevertheless, given the low surface density of the circumstellar disk around PDS 70 at the locations of both planets ($\sim 10^{-2}\mathrm{g\,cm}^{-2}$; Keppler et al. 2019), the model of Aoyama et al. (2018) would imply a weak Hα emission, more than an order of magnitude lower than observed in PDS 70b and c.

In this Chapter, we explore the possibility that the Hα flux associated with the young planets in PDS 70 system arises in magnetospheric flows akin to those present in young stars surrounded by accretion disks. According to the magnetospheric model for accretion, the stellar magnetic field truncates the disk and matter falls towards the star at nearly free-fall velocities, merging with the photosphere through a shock at the stellar surface (Hartmann et al. 2016). For typical magnetic field strengths and mass accretion rates, the truncation radius is of the order of a few stellar radii. The line profiles and strength of the emission lines seen in the optical and near-IR spectra of young, low mass stars, i.e., T Tauri stars, can be explained by formation on the magnetospheric accretion flows (Muzerolle et al. 1998a, 2001; Thanathibodee et al. 2019b). For this model to be valid for planets, a planetary magnetic field with sufficient strength to truncate the disk at several planetary radii is needed, as well as densities and temperatures in the magnetospheric flows capable of producing an Hα line comparable with observations.

The core accretion mechanism postulates three main phases in the formation process of giant planets: accumulation of planetesimals and/or pebbles into a core, slow gas accretion in an envelope, and runaway growth of the gas envelope, when the mass of the envelope reaches the mass of the core (Pollack et al. 1996). At or near the last stages of the runaway phase, mass is transferred from the circumstellar disk to the CPD and from it to the planet (Papaloizou & Nelson 2005; Ginzburg & Chiang 2019). Detailed Hydrodynamic (HD) and Magnetohydrodynamic (MHD) numerical simulations of the flows inside the Hill radius show that mass flows onto the CPD from high latitudes, almost vertically, and that some material on the CPD midplane actually flows back into the circumstellar disk, away from the system (Machida et al. 2008; Tanigawa et al. 2012; Gressel et al. 2013; Szulágyi et al. 2016, 2019). The mass flows are not axially symmetric and are mostly directed toward the planet only well inside a few percents of the Hill radius, as the high-resolution simulations of Tanigawa et al. (2012) show. For parameters corresponding to Jupiter, the Hill radius is $R_H \sim$ 0.34 au $\sim$ 730 Jupiter radii. Since these simulations mainly focus on the disks, their resolutions do not reach regions much closer to the planet, and they do not show how mass actually transfers onto the planetary core.

The region of interaction between a planet and its CPD has been explored by Batygin (2018). This author proposes that the interior of the forming planet becomes convective because of its high luminosity, and a magnetic field of the order of 0.5 - 1 kG is generated as a result. This field truncates the disk at a few, 4 - 5, planet radii, and matter accretes onto the planet following the field lines. As noted by Batygin (2018), this picture is similar to that of a magnetosphere around young stars, with the difference that in the latter, the mass comes from the circumstellar disk. In the case of planets, matter coming from the circumstellar disks and falling vertically onto the CPD is deflected towards the planet as it reaches the field line that has truncated the CPD. The rest of the infalling matter falls onto the CPD and is eventually expelled back towards the circumstellar disk (Batygin 2018).

In this Chapter, we use planetary parameters inferred from observations of PDS 70b and c and calculate the Hα fluxes and line profiles for a range of suitable mass accretion rates and temperatures. In § 7.2, we describe the magnetospheric model and in § 7.3, the results of our exploration. Finally, we give a brief discussion and conclusions in § 7.4.

Table 7.1. Range of Model Parameters

Parameters	Min.	Max.	Step
log($\dot{M}/M_{\rm Jup}\,{\rm yr}^{-1}$)	-11	-5	1
$T_{\rm max}$ (K)	8000	11000	200
$R_{\rm i}$ ($R_{\rm p}$)	2	8	2
$W_{\rm r}$ ($R_{\rm p}$)		1, 2, 4, 6	
cos(i)	0.3	0.9	0.2

7.2 Magnetospheric Accretion Model

7.2.1 Model Description

To calculate the Hα line flux formed in a magnetosphere around a planet, we use the magnetospheric accretion model (Muzerolle et al. 2001) initially developed for T Tauri stars. The detailed description of the model can be found in Hartmann et al. (1994); Muzerolle et al. (1998a, 2001). Here we describe the main assumptions and parameters.

This model assumes an axisymmetric accretion flow arising from a co-rotating Keplerian gas disk on the same plane as the planet's equator. The material flows in the magnetic dipole geometry characterized by the truncation radius ($R_{\rm i}$) and the width at the based of the flow ($W_{\rm r}$). The density at a given point in the flow follows a steady flow prescription, parameterized by the total mass accretion rate $\dot{M}$. At each point in the flow, the temperature scales with the density; the maximum temperature $T_{\rm max}$, a free parameter, describes each model. The model uses a 16-level hydrogen atom and the mean intensities of each transition and level populations are calculated by adopting the extended Sobolev approximation. The line specific intensity is calculated using a ray-by-ray method for a given inclination angle (i) between the line of sight and the planet rotation/magnetic axis. The line flux density is calculated by spatially integrating the intensity. The final, continuum-subtracted line flux is calculated over the range of $\pm 500\ {\rm km\,s^{-1}}$ since the relevant range of velocities would be on the order of the planets' escape velocity $\sim 130\ {\rm km\,s^{-1}}$ for the planets' parameters.

7.2.2 Grids of Models

Calculating a grid of model for the magnetospheric parameters requires the mass, radius, and effective temperature of the accreting object. These parameters are poorly constrained for PDS 70 planets, especially the recently discovered PDS 70c (Haffert et al. 2019). For PDS 70b, the estimated mass range is as wide as $2 - 17\,\mathrm{M_{Jup}}$ (Müller et al. 2018), while the radius could be as small as $\sim 1.3\,\mathrm{R_{Jup}}$, with an effective temperature of $\sim 1200\,\mathrm{K}$ (Keppler et al. 2018). A similarly wide mass range, but slightly lower masses, has been given for PDS 70c (Haffert et al. 2019), although no estimate of the radius is available. The effective temperature of PDS 70c is currently unconstrained, but there is a possibility that it is lower than that of PDS 70b since it has a redder spectrum (Haffert et al. 2019). Given the uncertainty in the planet parameters, we adopt a set of parameters that is reasonable for both planets for our exploration of the magnetospheric model. Therefore, we adopted a planet mass of $\mathrm{M_p} = 6\,\mathrm{M_{Jup}}$, a radius $\mathrm{R_p} = 1.3\,\mathrm{R_{Jup}}$, and an effective temperature $\mathrm{T_{eff}} = 1200\,\mathrm{K}$. These values are also applicable to young Jupiter-mass planets in general.

We calculated a large grid of models with parameters covering the ranges shown in Table 7.1. In particular, the geometry of the magnetosphere covers the values predicted by Batygin (2018), and the mass accretion rate spans 6 orders of magnitude covering the values calculated for PDS 70b and c (Haffert et al. 2019; Wagner et al. 2018). The temperature in the flow $\mathrm{T_{max}}$ covers the range found to be relevant for T Tauri stars at low accretion rate (Thanathibodee et al. 2019b).

7.3 Results

7.3.1 Comparing the Models with Observations

We compared the measured Hα line fluxes of PDS 70b and PDS 70c with the line fluxes calculated in our grid of models. We did not take into account any extinction due to the disk (Wagner et al. 2018), and first considered the measurements of Haffert et al. (2019) as the intrinsic line fluxes for a consistent comparison between the two planets. Figures 7.1 and 7.2 show the scattered plots and histograms for combinations of the model parameters. For the models with Hα flux within the measurement uncertainties, the plots show flat distributions for $\mathrm{R_i}$, $\mathrm{W_r}$, and $\cos(i)$, suggesting that the uncertainty in geometric parameters have little effect on the final results. On the other hand, $\dot{M}$ has a narrow distribution, implying that it is the strongest predictor for the line flux. Nevertheless, there is a degeneracy between $\mathrm{T_{max}}$ and $\dot{M}$; similar line fluxes can be reproduced in high-T with low-$\dot{M}$ and low-T with high-$\dot{M}$. This degeneracy has been noted in the original paper on the magnetospheric accretion model for T Tauri stars (Muzerolle et al. 2001).

We calculated the mass accretion rates onto PDS 70b and c based on the models that predict Hα line fluxes within 3σ of the observed flux. By calculating the mean and standard deviation of the model log($\dot{M}$) we found log($\dot{M}$) = $-8.0 \pm 0.6\ \ M_{\mathrm{Jup}}\,\mathrm{yr}^{-1}$ and log($\dot{M}$) = $-8.1 \pm 0.6\ \ M_{\mathrm{Jup}}\,\mathrm{yr}^{-1}$ for PDS 70b and c, respectively. Although our mass accretion rate estimates are in agreement with those calculated by Haffert et al. (2019) within uncertainties, we caution that this agreement is not because $\mathrm{W_{10}}$-$\dot{M}$ relation based on TTS (Natta et al. 2004) is applicable to accreting protoplanets

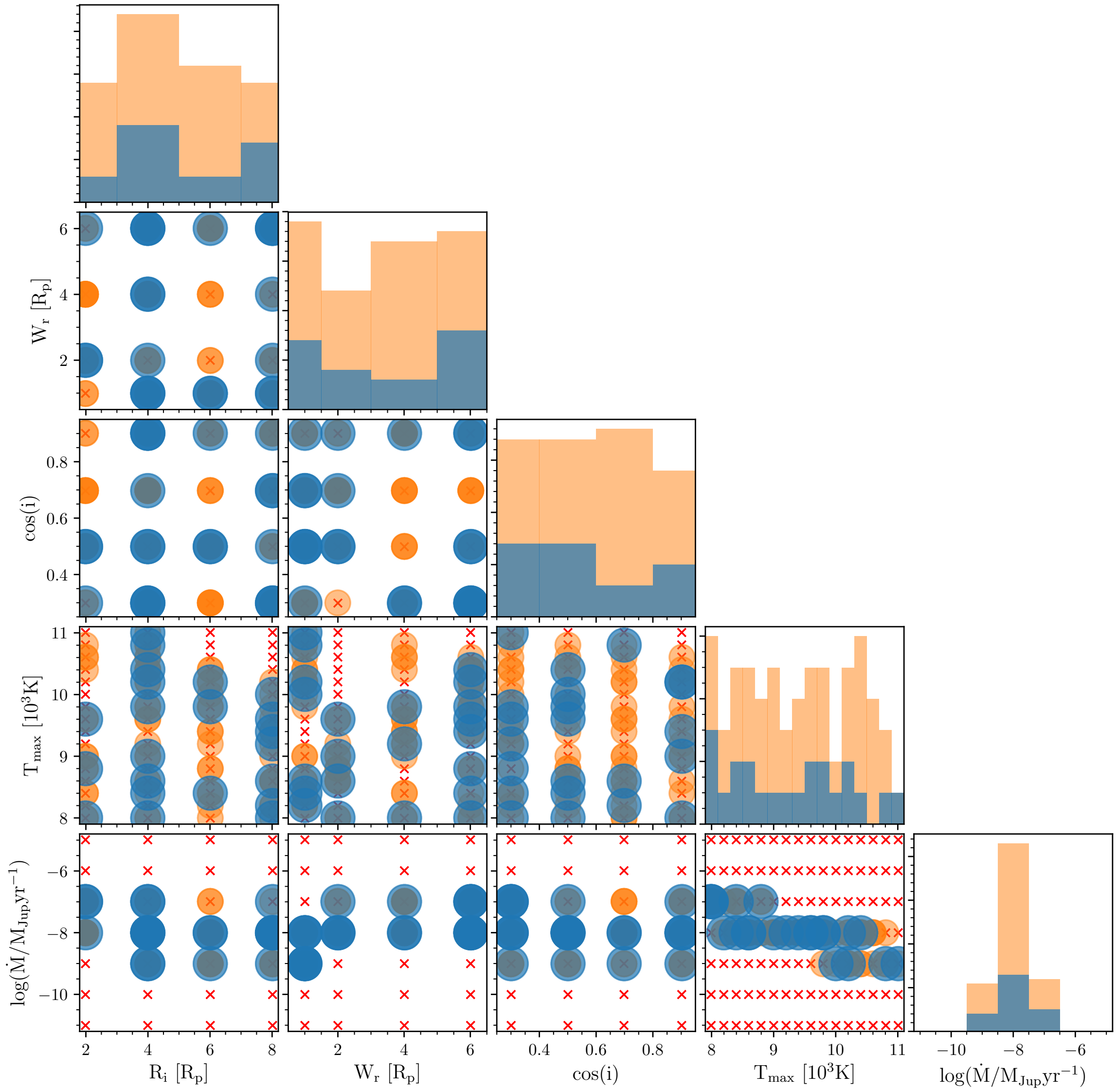

Figure 7.1 Corner plot showing regions in parameter space that are in agreement with the observed Hα flux of PDS 70b. Blue and orange points show the models which Hα line flux are within 1σ and 3σ of the measured line flux of the planet, respectively. Red crosses show models outside of 3σ. The histograms show the distribution of the parameters of the models that fit the observations, with the same color scheme as in scattered plots.

(§7.3.2), but because W_{10} from VLT/MUSE measurements are overestimated due to the low spectral resolution. Given the planet's escape velocity of $\sim 127\ \mathrm{km\,s^{-1}}$, the intrinsic line width would be on the same order, and it is much narrower than the instrumental broadened observed line width with a spectral resolution $\sim 110\ \mathrm{km\,s^{-1}}$ at 6562 Å.

As an illustration, Figure 7.3 shows the mean Hα line profiles from models with line flux within 3σ of the observed flux. We measured the W_{10} of the mean model profile to be $100\ \mathrm{km\,s^{-1}}$ and

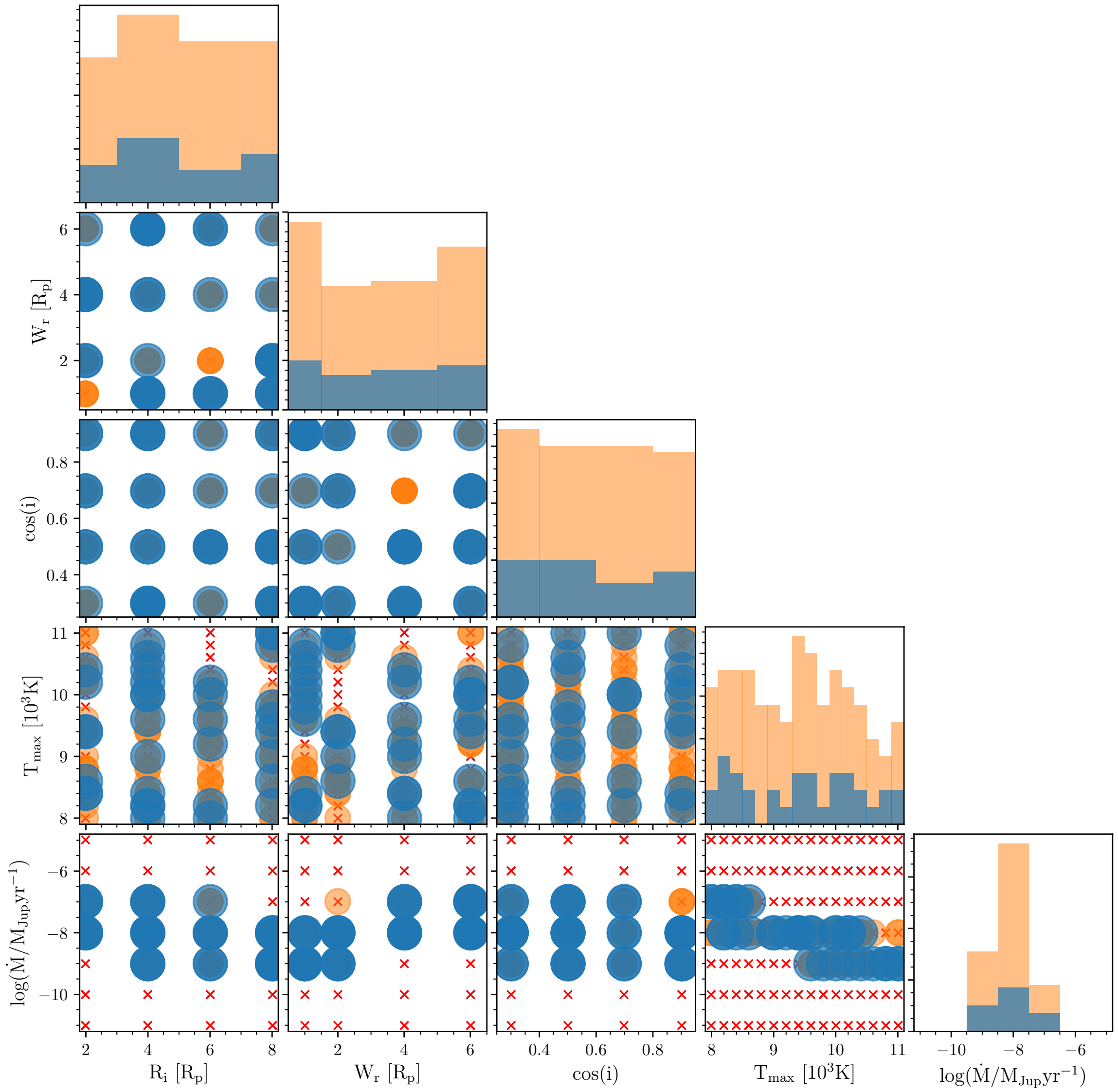

Figure 7.2 Corner plot showing regions in parameter space that are in agreement with the observed Hα flux of PDS 70c. The legends are the same as in Fig. 7.1.

96 $\mathrm{km\,s^{-1}}$ for PDS 70b and c, respectively. On the other hand, the W_{10} for the profiles taking into account the spectral resolution of MUSE (R∼2800 at 6560 Å), are 224 $\mathrm{km\,s^{-1}}$ and 219 $\mathrm{km\,s^{-1}}$ for the two planets. Although these values are in agreement with Haffert et al. (2019) measurements, they suggest that the instrumental broadening contributes significantly to the line width.

Another discrepancy between the results of our model and the observed Hα profiles of PDS 70b and c is that the model does not show a line-center redshift, while Haffert et al. (2019) reported a redshift of 25 ± 8 $\mathrm{km\,s^{-1}}$ and 30 ± 9 $\mathrm{km\,s^{-1}}$ for PDS 70b and c, respectively. One possibility is that this apparent line shift relative to the stellar Hα line center is due to a shift of the line center of the star itself. The redshifted absorption component in the stellar Hα line (Haffert et al. 2019) could cause the measured line center to be blueshifted. As a result, the line velocity measurement of the planet using the stellar Hα line as a reference would appear redshifted. Higher resolution observations are required to test this suggestion.

We also compare the mass accretion rates inferred from the Hα line fluxes of PDS 70b from MUSE with the Wagner et al. (2018) determination using MagAO. The value of the Hα flux was not explicitly reported by Wagner et al. (2018), so we followed the method outlined in Close et al. (2014) using the Hα contrast and found an Hα flux of $(3.3 \pm 1.8) \times 10^{-15}\,\mathrm{erg\,s^{-1}\,cm^{-2}}$ for PDS 70b. We assume no extinction for a consistent comparison with the results of Haffert et al. (2019). The Hα flux value from MagAO is an order of magnitude higher than that determined from the MUSE observations, which could imply that accretion onto PDS 70b could be variable. Using the method outlined above for models with fluxes within 1σ of the MagAO flux, we found that the mass accretion rate of PDS 70b at the epoch of the MagAO observation was log($\dot{M}$) = -7.8 ± 0.7 $M_{\mathrm{Jup}}\,\mathrm{yr}^{-1}$. This value of $\dot{M}$ is similar to that based on the MUSE observation (Haffert et al. 2019), mainly because the line flux is a steep function of $\dot{M}$ (c.f. Fig. 7.4). Although the observed variability of the Hα line flux could be due to variable accretion rate or extinction, detecting accretion variability is still challenging with the current assumptions of the model. Detailed modeling that is more sensitive to accretion variability of the planet is a subject of a future study.

7.3.2 Accretion Indicators for Planetary Mass Objects

Empirical relationships between Hα line luminosity (L$_{\mathrm{H}\alpha}$), or W$_{10}$ of the line, and $\dot{M}$ have been extensively used for T Tauri stars (Rigliaco et al. 2012; Ingleby et al. 2013; Natta et al. 2004), and they have been adopted to estimate the $\dot{M}$ of accreting planets (Wagner et al. 2018; Haffert et al. 2019). To examine the validity of those relationships in the planetary regime, we calculated the mean and standard deviation of L$_{\mathrm{H}\alpha}$ and W$_{10}$ for a given value of $\dot{M}$ in our model grid, shown in Figure 7.4. The shaded regions correspond to 1σ and 3σ from the mean. As expected, L$_{\mathrm{H}\alpha}$ increases as $\dot{M}$ increases. The relationship between $\dot{M}$ and L$_{\mathrm{H}\alpha}$ can be represented by a power law between $\sim 10^{-10}$ to $\sim 10^{-7}\,M_{\mathrm{Jup}}\,\mathrm{yr}^{-1}$, and the line flux seems to saturate at the high end of the accretion rate ($\dot{M}\sim 10^{-6}\,M_{\mathrm{Jup}}\,\mathrm{yr}^{-1}$); this trend has also been found in TTS (Ingleby et al. 2013). At the low $\dot{M}$ end, the relationship became nearly flat, which could be due to the weakness of the line at low density, essentially rendering it undetectable against the continuum.

Using simple linear regression, we fitted a power law to the L$_{\mathrm{H}\alpha}$ model results between $\dot{M}$ = $10^{-10} - 10^{-7}\,M_{\mathrm{Jup}}\,\mathrm{yr}^{-1}$, yielding the relationship

$$\log(\mathrm{L_{H\alpha}}) = (2.83 \pm 0.02)\log(\dot{\mathrm{M}}) + (15.7 \pm 0.2), \tag{7.1}$$

where L$_{\mathrm{H}\alpha}$ is in solar luminosities and $\dot{M}$ in $M_{\mathrm{Jup}}\,\mathrm{yr}^{-1}$. To aid the interpretation of future observa-

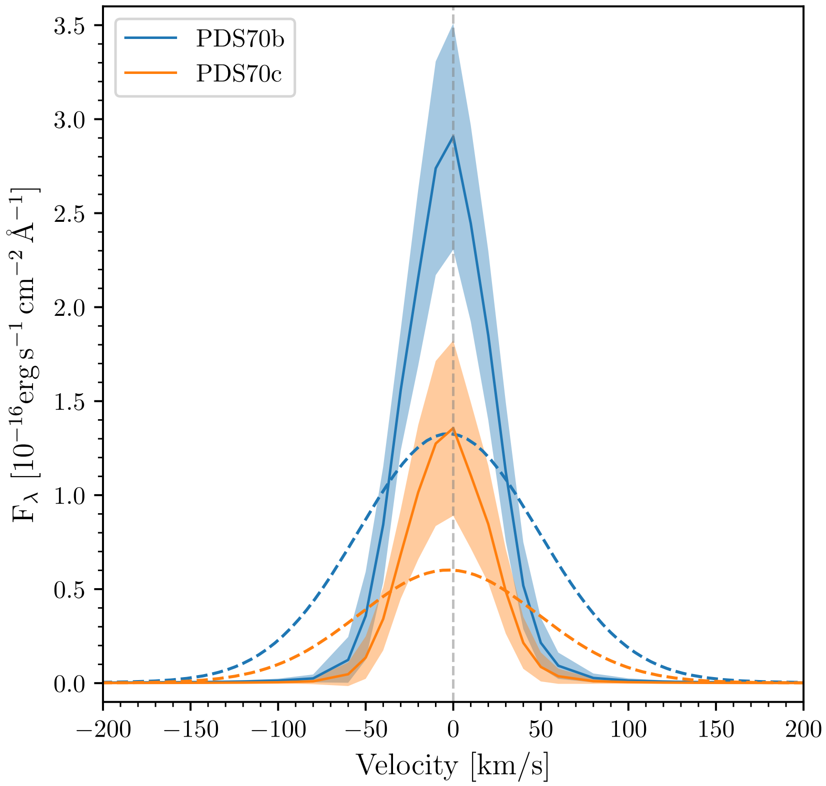

Figure 7.3 Hα line profiles of models that predicted line flux within 3σ of the observed flux. The solid lines are the mean intrinsic line profiles from the models; shaded areas show standard deviations of the profiles. The dashed lines are the mean model line profiles convolved with a Gaussian instrumental profile to $\mathrm{R} = 2800$, comparable to the resolution of MUSE at Hα wavelength.

tions of planets with similar parameters, we also fitted the inverse of this correlation, treating $\mathrm{L_{H\alpha}}$ as an independent variable, which yields

$$\log(\dot{\mathrm{M}}) = (0.280 \pm 0.002)\log(\mathrm{L_{H\alpha}}) - (6.14 \pm 0.02). \tag{7.2}$$

This relationship is different than the inverse of Eq. 7.1 since the dependent variable (i.e., $\dot{M}$) is not fully sampled.

As a comparison, in Figure 7.4 we plot the relationships between $\dot{M}$ and $\mathrm{L_{H\alpha}}$ from Ingleby et al. (2013) and Rigliaco et al. (2012), the latter derived from the correlation between $\mathrm{L_{acc}}$ and $\mathrm{L_{H\alpha}}$ using the parameters of the planets. The Ingleby et al. (2013) relationship is calculated from observations of a large number of T Tauri stars across a wide range of ages using contemporaneous UV and optical spectra, providing direct measurements of the accretion luminosity from the UV and of the line luminosity from the optical. Similarly, Rigliaco et al. (2012) used simultaneous observations, but for a lower mass range. As shown in Figure 7.4, the relationship found in this

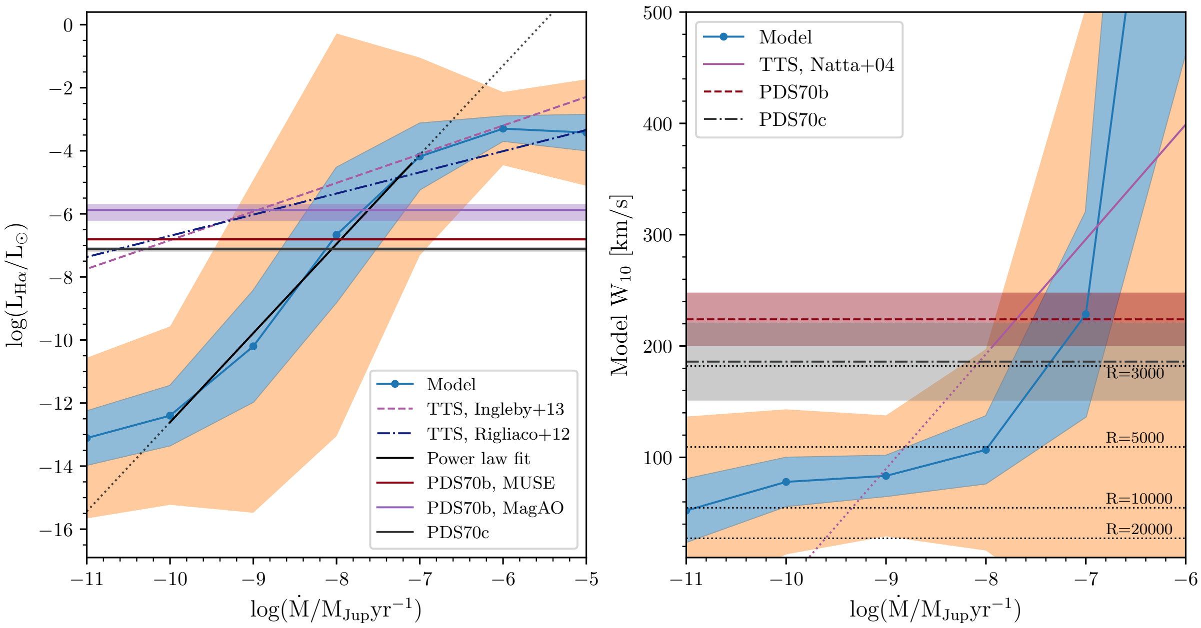

Figure 7.4 Predicted Hα line luminosity and line width as a function of mass accretion rate. *Left:* Hα luminosity as a function of mass accretion rate for planets with parameters similar to those of PDS 70b and c. The green and pink shaded regions show 1σ and 3σ, respectively, around the mean value (blue line) for a given $\dot{M}$. The line luminosity saturates once the accretion rate reaches the low end of mass accretion rate in pre-main sequence stars (T Tauri stars, TTS), $\dot{M} \sim 10^{-10}\, M_{\odot}\,\mathrm{yr}^{-1} \sim 10^{-7}\,\mathrm{M_{Jup}}\,\mathrm{yr}^{-1}$. The dashed purple line and the dash-dotted dark-blue line are extrapolation of empirical relationships between $\dot{M}$ and $\mathrm{L_{H\alpha}}$ for TTS. The relationships underestimate the $\dot{M}$ of the planets by ~2 orders of magnitude. The solid black line is the power law fit to the relationship for log($\dot{M}$) between -10 and -7; the dotted line is the extrapolation of the relationship outside the fitted range. Shaded horizontal lines show the line measurements of PDS 70 planets. *Right:* The $\mathrm{W_{10}}$ of the model Hα line as a function of log($\dot{M}$). The purple lines are the relationship for T Tauri stars from Natta et al. (2004), with extrapolation to $\mathrm{W_{10}} < 200\ \mathrm{km\,s^{-1}}$ in dotted line. The line width is a very weak function of $\dot{M}$. Horizontal dotted lines show $\mathrm{W_{10}}$ of Gaussian instrumental profiles for several spectral resolutions. The shaded crimson dashed line and dash-dotted gray line show the measured $\mathrm{W_{10}}$ of PDS 70b and PDS 70c, respectively.

study is steeper than those for T Tauri stars with up to two orders of magnitude difference in $\dot{M}$ for the parameters of the PDS 70 planets. The relationships are clearly different, even considering the intrinsic uncertainty in our modeling results, which as shown by the blue shaded region in Figure 7.4, can be as high as one order of magnitude in $\dot{M}$.

The right panel of Figure 7.4 shows the relationship between $\dot{M}$ and $\mathrm{W_{10}}$ for all models in our grid. At low accretion rates, $\dot{M} < 10^{-8}\, M_{\mathrm{Jup}}\,\mathrm{yr}^{-1}$, the line width is not sensitive to $\dot{M}$ even if it varies by orders of magnitude. In contrast, $\mathrm{W_{10}}$ increases steeply with $\dot{M}$ for $\dot{M} \gtrsim 10^{-8}\, M_{\mathrm{Jup}}\,\mathrm{yr}^{-1}$ with a scatter significantly increased. This happens because even though the mass accretion rates are comparable only to those of the lowest accretors among the TTS, with smaller spatial scales the density in the accretion flow becomes high enough for the line wings to become optically thick and pressure broadening to become effective (Muzerolle et al. 2001). The steep rise also reflects the high temperature in the model; $\mathrm{T}_{\mathrm{max}}$ is found to be $\sim 7000-8000\,\mathrm{K}$ for TTS magnetospheres in this range of $\dot{M}$ (Muzerolle et al. 2001), whereas our models have higher values of $\mathrm{T}_{\mathrm{max}}$, which are applicable at low $\dot{M}$ (Thanathibodee et al. 2019b). The large scatter of W_{10} at high $\dot{M}$ is due to the treatment of the continuum optical depth in the model. For the high-density cases, the continuum opacity of the magnetosphere can become so high that the continuum arises in the flow, and the photosphere of the planet is hidden. In this case, the Hα line emerging from the flow becomes very weak compared to the new continuum, and in some cases, the line appears in absorption. As a result, the measurements of W_{10} in this regime become meaningless since the continuum is now uncertain.

Plotted in purple line in the right panel of Figure 7.4 is the empirical relationship between W_{10} and $\dot{M}$ for T Tauri stars from Natta et al. (2004). Again, the relationship for T Tauri stars is different from our model results for planets. One possibility for this discrepancy is that the Natta et al. (2004) relationship is based on measurements of TTS covering a broad range of masses and radii, while our relationship is only applicable for a specific mass and radius. It is conceivable that one could fine-tune the model such that it reproduces the relationship, at least in the high $\dot{M}$ regime that is well-calibrated in TTS. Such a study is beyond the scope of this work, and the results would not be meaningful without calibrations with more planetary-mass accretors at their applicable accretion rates. At the moment, such a study is still challenging with the low-resolution of the existing planet spectrum. For example, the figure also shows the W_{10} of a purely Gaussian instrumental profile for different spectral resolutions. In order to extract geometric information from the line, sufficiently high signal-to-noise at the line wing is required. High-resolution spectra, comparable to the line width, will help to accurately measure W_{10} by suppressing the background noise from the star. With more detected planetary spectra, the relationship between $\dot{M}$ and W_{10} in the planetary mass regime can be revisited in the future.

7.4 Discussion and Conclusion

Following the detection of two accreting planets around the K7 star PDS 70, based in part on the measurement of Hα line emission from the planets (Wagner et al. 2018; Haffert et al. 2019), we applied the magnetospheric accretion model (Muzerolle et al. 2001) to the material accreting onto the planet to test if the model could explain the observed line flux with a reasonable range of parameters. Our study is the first to apply the full treatment of Hα line radiative transfer in a magnetospheric geometry for planetary-mass objects. The model can reproduce the observed fluxes, indicating that a magnetospheric model comparable to that of TTS can still be applicable in the planetary mass regime, as suggested by Batygin (2018). Our results also suggested that accretion can be the main source of Hα line emission from planets in circumstellar disks, and confirmed the use of Hα as a viable method to detect young planets.

Measuring the mass accretion rate of a planet from the flux of the Hα emission line is still challenging due to practical considerations, such as the low resolution of the IFU spectrographs used to detect the line, as well as the uncertainty in the line luminosity due to background subtraction and extinction (Wagner et al. 2018; Haffert et al. 2019). An additional challenge comes from the uncertain calibration between the Hα luminosity and the accretion rate in this very low-mass regime. Our results provide, for the first time, a correlation between the Hα line luminosity and $\dot{M}$ based on a physical model. In addition, we show that this correlation is different from the relationships applicable to T Tauri stars. However, we note the limitations of using our result since it requires knowledge of the planetary parameters, i.e., mass, radius, and effective temperature, from independent measurements. Large uncertainties in these values can change the final measured accretion rate in an uncertain way since the line emission properties depend on the dynamic of the gas in the accretion flow, which in turn depends on the mass of the object and the physical size of accretion flow; these also determine the optical depth of the line. Our provided relationship between $L_{H\alpha}$ and $\dot{M}$ is therefore only applicable for planets with mass and radius comparable to those of PDS 70b and c. Similar limitations apply to the calibrations of $\dot{M}$ with W_{10} since the line width is more sensitive to the planet parameters. The applicability of the magnetospheric accretion model in different ranges of planetary parameters will be the subject of future studies.

As in TTS, the highest uncertainty in measuring the mass accretion rate arises from the unknown temperature in the flow (Muzerolle et al. 2001). Magnetohydrodynamic simulations with a full treatment of magnetic and other heating sources in the flow are still needed to shed light onto the temperature problem. Observations of other hydrogen line transitions and other line species may also help to constrain the temperature empirically.

From an observational standpoint, modeling the velocity-resolved non-Gaussian Hα line profiles using the magnetospheric model (Muzerolle et al. 2001; Thanathibodee et al. 2019b) will provide much more accurate measurements of the mass accretion rates, since both the line flux and the line width can be simultaneously constrained. Such observations are still unavailable due to limitations of the current technology. High-resolution IFU spectrograph on a large telescope, such as HARMONI on the ELT will provide data necessary for such modeling study.

CHAPTER 8

Summary and Conclusions

In this Dissertation, we studied the last stages of accretion in low-mass pre-main sequence stars by applying accretion models to explain observations of stars accreting at very low rates – the low accretors. The main goal of our studies is to shed some light on the processes that make accretion stop in T Tauri stars. We approached this problem by studying a small set of objects at the critical age of disk evolution, modeling individual objects in detail, and conducting a survey to characterize the low accretors as a population. We found that the end of accretion is reached in diverse ways and that the disk – not the star – determines the fate of accretion onto the star. Further studies in both simulations and observations will be helpful to place constraints on the processes in the disk that starve the star out of material to accrete.

In this Chapter, we summarize our findings in Chapter 2-7, and suggest future research in Section 8.4.

8.1 The Last Stages of Primordial Disk Evolution

Previous studies (e.g., Ingleby et al. 2009, 2012) suggested that the inner region of (gas) disks are completely gas-free for stars that have transitioned from accreting (CTTS) to non-accreting (WTTS). However, the properties of the inner disk *during* the transition and how they relate to the dust is unclear. In Chapter 2, we directly probed the inner disk of three 5 Myr-old T Tauri stars using low-resolution spectroscopic observations in the UV obtained with the Hubble Space Telescope's Advanced Camera for Surveys. The targets, CVSO 114NE, CVSO 1335, and CVSO 114SW, showed different degrees of evolution in the dust disks; CVSO 114NE had a full disk, CVSO 1335 had a transitional disk (i.e., disk with a dust-poor hole), and CVSO 114SW had a debris disk. We probed the inner disk by detecting the bump at 1600 Å, thought to be from H_2 fluorescence (Herczeg et al. 2006) or H_2O dissociation (France et al. 2017); the presence of such feature provides information about the gas in the inner disks. We found that the non-accreting object, CVSO 114SW, showed no excess emission at 1600 Å, consistent with its disk being a gas-poor debris disk. CVSO 1335, while showing substantial dust depletion at NIR wavelengths, showed strong gas signatures at 1600 Å. Surprisingly, the full disk CVSO 114NE showed very weak H_2 emission, suggesting that the amount of gas in the inner disk could be low. These results provided evidence that the low accretors reach the final stages in different ways and that at the transition between accreting and non-accreting, the (dust) disks of low accretors are very diverse.

In Chapter 5, we performed a comparative study of low accretors taken from a large number of newly identified low accretors surrounded by disks to determine the properties of the dust disk. We used the 2MASS and WISE colors to classify the disks into several evolutionary stages: full, transitional, evolved, and debris disk. We found that low accretors showed higher excess over the photosphere in the WISE W4 band than the non-accretors, suggesting that their disks are less evolved. Moreover, our analysis of the inner disk dust, probed by the H-Ks color, suggests that stars are still accreting if dust is still present in the inner disk. However, not all accreting stars show evidence of dust in the inner disk, suggesting that the grains may have grown and emitted less in the near-IR.

From the observations using H_2 lines and the dust analysis, we concluded that at the last stages of disk evolution, the dust component of the disk could vary significantly from object to object. However, gas remains in the disk since the star is still accreting.

We probed the processes that could change the amount of gas in the inner disk by studying the disk of the T Tauri star PDS 70 in Chapter 4, wherein we measured the mass accretion rate onto the star using both Hα line modeling and accretion shock modeling. PDS 70 hosts two accreting protoplanets (Wagner et al. 2018; Haffert et al. 2019), with mass accretion rates measured in Chapter 7. Comparing these mass accretion rates with the disk observation from ALMA (Isella et al. 2019; Bae et al. 2019), we found that, although mass accretion onto the planets is small compared to that of the star, the mass accretion rate from the disk onto the star was too high for the outer disk to supply sufficient mass for the disk viscosity to be consistent with other studies, i.e., lower than $\alpha \sim 10^{-3}$. If this were the case, then an inner disk gas reservoir would be needed to supply the mass to be accreted (Hartmann & Bae 2018). The gas reservoir could play an important role in feeding low accretors once mass accretion from the outer disk is shut off (by, e.g., photoevaporation; Alexander et al. 2014). Further research to probe the inner disk gas reservoir is needed to test this hypothesis.

8.2 Identifying and Measuring Accretion Rates at the Lowest Limit

Identifying low accretors and measuring their mass accretion rates is challenging because the chromospheric emission contributes significantly to the flux of the lines traditionally used for detecting accretion, such as Hα (Manara et al. 2013, 2017b), or to continuum emission used for measuring accretion rates with shock modeling (Ingleby et al. 2011b). Therefore, the traditional methods used to identify accretors, such as the equivalent width of Hα and the width at the 10% flux (W_{10}) of Hα, have limitations for the lowest rates.

Here, we have confirmed that the He I λ10830 (Edwards et al. 2006; Fischer et al. 2008; Kwan & Fischer 2011) is a sensitive probe of accretion at low rates, as shown in Chapter 2 and Chapter 4. In Chapter 5, we used the He I λ10830 line to identify low accretors that were previously thought to have stopped accreting but were still hosting dust disks. We classified the He I line profiles into six types and argued that stars showing either redshifted or blueshifted absorption in the line were still accreting, while those showing emission or central absorption could still be accreting. We estimated that up to 30% of disk-bearing stars identified as non-accretors are actually still accreting. We showed, in Chapter 6, that both the equivalent width and W_{10} depend strongly on the inclination of the system and that using them as accretion indicators introduces biases in the sample's inclination.

We showed in Chapter 3 that measuring mass accretion rates using the continuum excess is not accurate at the low level, especially for early K-type stars. For later-type stars, measurements can be made if the NUV emission is known, as in PDS 70 (c.f., Chapter 4). Nevertheless, more accurate measurements of accretion rates can be achieved by magnetospheric accretion flow modeling, applied in Chapter 3, 4, and 6.

At low accretion rates, the standard magnetospheric accretion model faces difficulties in modeling Hα dominated by chromosphere or from multiple absorption components. In Chapter 3, we modified the magnetospheric model to have two geometrically separated flows; this new model can fit the observation of CVSO 1335 showing low-velocity redshifted component against the emission in Hα lines from multi-epoch observations. For other low accretors, we modeled the chromospheric emission by adding a Gaussian component at the line center with magnetospheric emission from the accretion flow model. As shown in Chapter 6, this procedure can be used to fit the observations reasonably well. This method can be used to fit other low accretors, but some improvements could be made, such as adding the chromospheric contribution directly into the model.

8.3 Accretion Properties of the Low Accretors

Using the magnetospheric accretion flow model outlined above, in Chapter 6 we inferred accretion properties of 20 newly identified low accretors to probe how accretion proceeds at very low rates and how accretion stops. We found that at low accretion rates, the dipolar magnetic fields or the efficiency for the magnetic field to truncate the disks are lower than expected from theory, numerical simulations, or observations. We also found an anti-correlation between the truncation radius and the mass accretion rate that is steeper than expected from theory and simulations. This suggests that in low accretors, the balance between the magnetic pressure and the gas pressure at the disk's inner edge is much more complicated than expected. Simulations are needed to explore this hypothesis.

A fraction of low accretors studied in Chapter 6 show low-velocity redshifted absorption features on weak Hα emission lines, similar to those analyzed in Chapter 3 for CVSO 1335. For that star, we used the magnetospheric accretion model to analyze its line profiles and found that the complex, variable profile requires a complex geometry to reproduce the observation in Hα and Hβ line. The results pointed to other processes modulating the accretion, such as the evolution of stellar magnetic field structure or a planetary companion. We have now observed several more stars exhibiting similar profiles, suggesting that the low-velocity feature is not uncommon among low accretors.

We compared the corotation and the truncation radius of 20 low accretors and found that essentially all of them are accreting in the unstable regime, and none of the stars are approaching the propeller regime of accretion. This suggests that accretion stops not because the stars "reject" mass; instead, the disk has stopped supplying material to the stars. The distribution of the mass accretion rates indicates a lower limit of accretion at $\sim 1 \times 10^{-10}\, M_{\odot}\, \mathrm{yr}^{-1}$ for K to mid-M type T Tauri stars. Since this rate is higher than the lower accretion rates detectable by the models, it is likely to be the physical lower limit in the applicable mass range. The rate is also in agreement with EUV-driven photoevaporation rates (Clarke et al. 2001), suggesting photoevaporation as a possible driver for stopping accretion. Detailed studies of disks and searches for evidence of photoevaporating winds in these systems are needed to explore this hypothesis.

8.4 Directions for Future Studies

As much as the work in this Dissertation has revealed some secrets of the universe regarding the accretion processes of young objects at the last stages of their evolution, it also raises questions for future studies. In particular, we now know that accretion stops because no gas is left in the inner disk, but the processes that modulate the gas content in the inner disk are unclear. One possible observational approach to this problem is to use high-resolution spectroscopic observation provided by HST/COS to probe the inner disks of low accretors in the FUV by modeling H_2 lines excited by their high-energy radiation field (France et al. 2012). HST/ACS instruments used in Chapter 3 does not provide enough resolution for such studies. As we have ruled out X-ray and FUV photoevaporation in favor of EUV photoevaporation based on the low accretion limit, this conclusion should be confirmed by observing the X-ray and FUV luminosities of these stars to verify whether they are sufficient to evaporate the disks.

Observations and simulations are essential to understand the interplay between the star's magnetic fields and the disk across a wide range of mass accretion rates. The steeper than expected exponent for the relationship between the mass accretion rates and the disk truncation radius could be pointing to additional physics or complex magnetic configurations in that interacting region (Ireland et al. 2021). Observations of more low accretors are needed to confirm this trend. In addition, spectropolarimetric observations directly measuring the magnetic fields of low accretors are needed to constrain parameter space.

Although the magnetospheric accretion flow modeling is well-developed, improvements can be made to expand its use to further study the properties of accreting T Tauri stars. In particular, the current version of the model only supports hydrogen and sodium lines (Muzerolle et al. 2001). Additional lines, such as Ca II and He I in the optical and NIR and C IV in the FUV, could be explored. In this regard, the Hubble *UV Legacy Library of Young Stars as Essential Standards* (ULLYSES) Program and its associated *Outflows and Disks around Young Stars: Synergies for the Exploration of ULLYSES Spectra* (ODYSSEUS) Project would provide crucial data for such study. These programs have been observing T Tauri stars across a wide range of stellar parameters in contemporaneous observations from the FUV to the NIR at high resolution (Manara et al. 2021, Espaillat et al., 2021, in prep). The mass accretion rates from the NUV shock modeling provide constraints on the magnetospheric flow modeling of the Balmer lines, which in turn provide constraints on the geometric parameters for other atomic lines. The regions where the line form and/or the abundance of the elements can be inferred from fitting the observations from the model.

The field of planet formation has had exciting developments following the discovery of two protoplanets in the disk of T Tauri star PDS 70. Forming giant planets accreting mass from their circumplanetary disks produce emission in the $H\alpha$ line as well as in the UV continuum (Zhou et al. 2021). As we have shown in Chapter 7, the $H\alpha$ line can be reproduced by magnetospheric accretion, among other processes (Aoyama et al. 2018; Aoyama & Ikoma 2019). However, the model producing the line is highly dependent on the planet parameters. Therefore, it is crucial to understand the effect of mass, radius, and effective temperature in the $H\alpha$ line formation in the magnetosphere. Calculating other hydrogen lines with a wide range of parameters would provide crucial prediction to confirm that giant planets accrete their mass through magnetosphere (Batygin

2018), and give a reference point in the search for more protoplanets (Zurlo et al. 2020; Xie et al. 2020).

APPENDIX A

Appendix of Chapter 5

A.1 Stellar Parameters of Low Accretor Candidates

Here we compiled the properties of the observed targets. The references in the table refer to: (1) Briceño et al. (2019); (2) Hernández et al. (2014); (3) Ansdell et al. (2017); (4) this study; (5) Frasca et al. (2015); (6) Hernández et al. (2008); (7) Esplin et al. (2017); (8) Sacco et al. (2017); (9) Luhman (2004); (10) Nguyen et al. (2012); (11) Pecaut & Mamajek (2016); (12) Frasca et al. (2017); (13) Esplin et al. (2018).

Stars marked with A are those with the equivalent width larger than the threshold of White & Basri (2003) but are included as they are classified as type CW by Briceño et al. (2019), weak accretor candidates by Hernández et al. (2014), or if their W_{10} are smaller than $200\ \mathrm{km\,s^{-1}}$ (Jayawardhana et al. 2006). Those marked with B are stars that are classified as non-accretors using the $270\ \mathrm{km\,s^{-1}}$ criterion of White & Basri (2003) but are classified as accretors using the $200\ \mathrm{km\,s^{-1}}$ of Jayawardhana et al. (2006).

Table A.1: Properties of Observed Targets

Name	SpT	SpT.r	EW	EW.r	W_{10}	W_{10}.r	Teff	Av	Av.r	$M_\star$	$R_\star$	Note
CVSO 267	K7	(1)	1.81	(1)	···	···	3970	0.00	(1)	0.71	1.34	–
CVSO 288	M1	(1)	10.7	(1)	···	···	3630	1.03	(1)	0.39	2.44	A
CVSO 298	M0	(1)	9.79	(1)	···	···	3770	1.27	(1)	0.56	1.33	–
CVSO 378	K7	(1)	2.54	(1)	···	···	3970	0.05	(1)	0.74	1.27	–
CVSO 415	M0	(1)	2.79	(1)	···	···	3770	0.00	(1)	0.59	1.06	–
CVSO 418	M4	(1)	6.08	(1)	···	···	3190	0.00	(1)	0.17	0.84	–
CVSO 456	M5	(1)	22.3	(1)	···	···	2980	0.83	(1)	0.10	0.86	A
CVSO 491	M3	(1)	6.16	(1)	···	···	3360	0.83	(1)	0.29	0.97	–
CVSO 535	M2	(1)	3.7	(1)	···	···	3490	0.00	(1)	0.36	1.22	–
CVSO 604	M3	(1)	12.0	(1)	···	···	3360	0.92	(1)	0.29	0.85	–

Continued on next page

Table A.1 – continued

Name	SpT	SpT.r	EW	EW.r	W_{10}	W_{10}.r	Teff	Av	Av.r	$M_\star$	$R_\star$	Note
CVSO 662	K5	(1)	0.93	(1)	···	···	4140	0.00	(1)	0.88	1.39	–
CVSO 746	M3	(1)	18.5	(1)	···	···	3360	0.92	(1)	0.28	1.09	–
CVSO 40	M0	(1)	10.36	(1)	···	···	3770	0.80	(1)	0.53	1.47	A
CVSO 932	K7	(1)	3.9	(1)	···	···	3970	0.75	(1)	0.75	1.21	–
CVSO 952	M4	(1)	7.18	(1)	···	···	3190	0.24	(1)	0.17	1.17	–
CVSO 982	K1	(1)	0.6	(1)	···	···	4920	0.00	(1)	1.42	1.80	–
CVSO 985	M0	(1)	4.37	(1)	···	···	3770	0.00	(1)	0.51	1.73	–
CVSO 1043	M0	(1)	3.1	(1)	···	···	3770	0.64	(1)	0.59	1.04	–
CVSO 1231	K7.5	(1)	4.1	(1)	···	···	3910	0.09	(1)	0.68	1.16	–
CVSO 1232	M4	(1)	10.2	(1)	···	···	3190	0.55	(1)	0.17	0.93	–
CVSO 1261	M4	(1)	9.8	(1)	···	···	3190	0.00	(1)	0.17	0.90	–
CVSO 1262	M1	(1)	3.0	(1)	···	···	3630	0.00	(1)	0.44	1.43	–
CVSO 1295	K7.5	(1)	3.3	(1)	···	···	3910	0.44	(1)	0.59	1.54	–
CVSO 82	K7	(1)	8.1	(1)	···	···	3970	4.11	(1)	0.60	2.03	–
CVSO 95	M5	(1)	8.9	(1)	···	···	2980	0.00	(1)	0.10	1.10	–
CVSO 1320	K3	(1)	2.92	(1)	···	···	4550	0.00	(1)	1.11	1.36	–
CVSO 239	K5	(1)	1.2	(1)	···	···	4140	0.19	(1)	0.85	1.43	–
CVSO 1338	M1	(1)	6.96	(1)	···	···	3630	0.00	(1)	0.43	1.55	–
CVSO 2065	M2	(1)	7.78	(1)	···	···	3490	2.02	(1)	0.36	1.31	–
CVSO 1348	M2	(1)	14.43	(1)	···	···	3490	0.00	(1)	0.32	2.83	A
CVSO 2067	M2	(1)	3.18	(1)	···	···	3490	1.14	(1)	0.36	1.10	–
CVSO 2084	M3	(1)	9.63	(1)	···	···	3360	1.52	(1)	0.27	1.19	–
CVSO 111	M1	(1)	2.9	(1)	···	···	3630	0.30	(1)	0.45	1.13	–
CVSO 2071W	M3	(1)	7.31	(1)	···	···	3360	1.16	(1)	0.27	1.30	–
CVSO 2071E	M3	(1)	7.31	(1)	···	···	3360	1.16	(1)	0.28	1.14	–
CVSO 1381	M4	(1)	8.7	(1)	···	···	3190	0.00	(1)	0.17	1.43	–
CVSO 1388	K3.5	(1)	1.63	(1)	···	···	4440	0.40	(1)	1.06	1.32	–
CVSO 115	M0	(1)	2.4	(1)	···	···	3770	0.31	(1)	0.52	1.45	–
CVSO 248	K7	(1)	3.3	(1)	···	···	3970	0.00	(1)	0.78	1.09	–
CVSO 2080	M3	(1)	2.22	(1)	···	···	3360	0.07	(1)	0.28	1.01	–
CVSO 1415B	M0.5	(1)	7.3	(1)	···	···	3700	0.00	(1)	0.50	1.24	–
CVSO 1415A	M0.5	(1)	7.3	(1)	···	···	3700	0.00	(1)	0.49	1.31	–
CVSO 119	K7	(1)	2.2	(1)	···	···	3970	0.24	(1)	0.77	1.13	–
CVSO 1424	M4	(1)	5.5	(1)	···	···	3190	0.00	(1)	0.17	0.88	–
CVSO 1427	M4	(1)	8.9	(1)	···	···	3190	0.00	(1)	0.16	0.97	–
CVSO 1432	K4.5	(1)	1.01	(1)	···	···	4240	0.00	(1)	0.95	1.37	–
CVSO 1439	M4	(1)	17.59	(1)	···	···	3190	0.00	(1)	0.17	0.94	–
CVSO 1442	K7	(1)	2.45	(1)	···	···	3970	0.76	(1)	0.74	1.25	–
CVSO 1446	M0	(1)	7.56	(1)	···	···	3770	1.84	(1)	0.46	2.32	–
CVSO 1461	K7	(1)	3.93	(1)	···	···	3970	0.67	(1)	0.71	1.41	–

Continued on next page

Table A.1 – continued

Name	SpT	SpT.r	EW	EW.r	W_{10}	W_{10}.r	Teff	Av	Av.r	$M_\star$	$R_\star$	Note
CVSO 1513	K7	(1)	5.49	(1)	···	···	3970	0.00	(1)	0.66	1.58	–
CVSO 135	M1	(1)	4.4	(1)	···	···	3630	0.00	(1)	0.43	1.67	–
CVSO 1545	M4	(1)	18.06	(1)	···	···	3190	0.00	(1)	0.17	1.58	–
CVSO 1567SW	M4	(1)	22.65	(1)	···	···	3190	0.27	(1)	0.17	1.20	A
CVSO 1567NE	M4	(1)	22.65	(1)	···	···	3190	0.27	(1)	0.18	1.38	A
CVSO 1575	K7.5	(1)	8.4	(1)	···	···	3910	0.40	(1)	0.57	1.65	–
CVSO 1579	M5	(1)	14.0	(1)	···	···	2980	0.58	(1)	0.10	1.04	–
CVSO 1586	M4	(1)	20.13	(1)	···	···	3190	0.48	(1)	0.17	0.98	A
CVSO 1588	M0	(1)	3.73	(1)	···	···	3770	0.00	(1)	0.52	1.53	–
CVSO 1600W	M3	(1)	9.03	(1)	···	···	3360	0.44	(1)	0.27	1.54	–
CVSO 1600E	M3	(1)	9.03	(1)	···	···	3360	0.44	(1)	0.27	1.65	–
CVSO 1608	M0	(1)	4.61	(1)	···	···	3770	1.45	(1)	0.54	1.43	–
CVSO 1653	K4.5	(1)	2.21	(1)	···	···	4240	0.57	(1)	0.93	1.47	–
CVSO 1655	M0	(1)	1.52	(1)	···	···	3770	0.37	(1)	0.52	1.55	–
CVSO 1672	K7.5	(1)	1.93	(1)	···	···	3910	0.55	(1)	0.61	1.37	–
CVSO 1678	M0	(1)	1.67	(1)	···	···	3770	0.54	(1)	0.55	1.36	–
CVSO 1695	M0	(1)	7.05	(1)	···	···	3770	1.48	(1)	0.46	2.41	–
CVSO 1703	M0	(1)	4.47	(1)	···	···	3770	0.00	(1)	0.56	1.33	–
CVSO 1704	M3	(1)	6.5	(1)	···	···	3360	1.47	(1)	0.28	1.05	–
CVSO 1711	M0	(1)	9.88	(1)	···	···	3770	0.95	(1)	0.52	1.57	–
CVSO 1719	M6	(1)	14.4	(1)	···	···	2860	0.00	(1)	0.10	1.09	–
CVSO 1739	M5	(1)	18.4	(1)	···	···	2980	0.00	(1)	0.10	1.21	–
CVSO 1745	M4	(1)	12.23	(1)	···	···	3190	0.00	(1)	0.18	1.50	–
CVSO 1747A	M0	(1)	3.57	(1)	···	···	3770	1.37	(1)	0.52	1.53	–
CVSO 1747B	M0	(1)	3.57	(1)	···	···	3770	1.37	(1)	0.52	1.57	–
CVSO 1763	K3.5	(1)	3.01	(1)	···	···	4440	0.28	(1)	1.09	1.49	A
CVSO 1771	K3.5	(1)	1.27	(1)	···	···	4440	0.00	(1)	1.07	1.38	–
CVSO 1772	M3	(1)	16.5	(1)	···	···	3360	1.00	(1)	0.29	1.04	–
CVSO 1776	M5.5	(1)	9.8	(1)	···	···	2920	0.00	(1)	0.10	0.92	–
CVSO 156	M2	(1)	15.03	(1)	···	···	3490	0.24	(1)	0.34	1.96	A
SO247	M5.0	(2)	24.1	(2)	192.32	(2)	2980	0.00	(2)	0.10	1.02	A
CVSO 1790	M2	(1)	9.85	(1)	···	···	3490	0.83	(1)	0.36	1.15	–
SO435	M5.0	(2)	13.8	(2)	151.82	(2)	2980	0.00	(2)	0.10	1.20	–
SO451	M2.5	(2)	10.7	(2)	184.99	(2)	3420	0.40	(2)	0.32	1.27	A
SO467	M5.5	(2)	6.6	(2)	101.38	(2)	2920	0.00	(2)	0.10	1.31	–
CVSO 160	K6	(1)	7.2	(1)	···	···	4020	2.32	(1)	0.67	1.81	–
CVSO 1830	M5	(1)	16.02	(1)	···	···	2980	0.21	(1)	0.10	1.14	–
CVSO 1832	M4	(1)	8.89	(1)	···	···	3190	0.00	(1)	0.17	0.78	–
SO566	M5.0	(2)	6.9	(2)	···	···	2980	0.64	(2)	0.10	1.32	–
CVSO 1840	K7.5	(1)	7.15	(1)	···	···	3910	0.49	(1)	0.58	1.69	–

Continued on next page

Table A.1 – continued

Name	SpT	SpT.r	EW	EW.r	W$_{10}$	W$_{10}$.r	Teff	Av	Av.r	M$_\star$	R$_\star$	Note
SO662	K7.0	(2)	11.6	(2)	214.57	(2)	3970	1.53	(2)	0.59	2.12	A,B
CVSO 1841	M5	(1)	11.38	(1)	···	···	2980	0.43	(1)	0.10	1.36	–
SO674	M3.1	(3)	···	···	161.29	(2)	3390	0.54	(4)	0.26	1.20	–
CVSO 1842	M2.5	(1)	8.21	(1)	···	···	3420	0.52	(1)	0.32	1.03	–
SO682	M0.5	(2)	2.7	(2)	···	···	3700	0.34	(2)	0.46	1.83	–
SO697	K6.0	(2)	7.8	(2)	198.81	(2)	4020	0.00	(2)	0.67	1.85	–
CVSO 1844	M4.5	(1)	10.0	(1)	···	···	3080	0.83	(1)	0.13	1.58	–
SO738	M5.0	(3)	···	···	129.03	(2)	2980	0.39	(4)	0.10	0.65	–
SO823	M2.0	(2)	5.9	(2)	···	···	3490	1.71	(2)	0.35	3.23	–
SO967	M4.0	(2)	5.5	(2)	···	···	3190	0.15	(2)	0.17	1.07	–
CVSO 1884	M5	(1)	18.4	(1)	···	···	2980	0.39	(1)	0.10	1.18	–
CVSO 1886	M3	(1)	9.44	(1)	···	···	3360	0.52	(1)	0.28	1.02	–
CVSO 174	M2	(1)	4.99	(1)	···	···	3490	0.99	(1)	0.33	2.08	–
CVSO 175	K7	(1)	6.2	(1)	···	···	3970	0.74	(1)	0.71	0.80	–
CVSO 1920	M3	(1)	5.96	(1)	···	···	3360	0.18	(1)	0.26	2.27	–
CVSO 1923	M2	(1)	7.31	(1)	···	···	3490	0.16	(1)	0.34	1.72	–
CVSO 1928	M0.5	(1)	4.92	(1)	···	···	3700	0.55	(1)	0.47	1.54	–
CVSO 191	K5	(1)	1.1	(1)	···	···	4140	0.00	(1)	0.80	1.70	–
CVSO 1942	K6	(1)	1.3	(1)	···	···	4020	0.77	(1)	0.72	1.57	–
J08074647-4711495	M4	(5)	3.59	(5)	162.3	(5)	3190	0.17	(6)	0.17	0.84	–
J08075546-4707460	K3	(5)	4.73	(5)	196.5	(5)	4550	0.34	(6)	1.15	1.50	A
J08094701-4744297	K0	(4)	···	···	···	···	5030	0.00	(4)	1.39	1.70	–
ESO-Ha 553	M5.6	(7)	···	···	215.0	(8)	2910	0.00	(7)	0.10	0.80	B
SZ 4	M3.25	(7)	17.77	(5)	272.0	(8)	3360	1.18	(7)	0.24	2.06	B
Hn 1	M3	(7)	3.73	(5)	148.0	(8)	3360	1.63	(7)	0.27	1.39	–
ISO-ChaI 52	M4	(7)	6.4	(9)	126.0	(10)	3190	1.25	(7)	0.18	1.17	–
CHSM 9484	M5.25	(7)	5.5	(9)	···	···	2950	1.74	(7)	0.10	0.62	–
CHSM 10862	M5.75	(7)	18.0	(9)	···	···	2890	1.56	(7)	0.10	0.52	–
CHSM 13620	M2	(7)	3.04	(5)	275.0	(8)	3490	1.04	(7)	0.34	1.72	B
J11090915-7553477	M4	(7)	1.59	(5)	120.0	(8)	3190	0.94	(7)	0.17	1.31	–
Hn 13	M5.75	(7)	22.5	(9)	257.0	(8)	2890	0.80	(7)	0.10	1.38	B
Hn 17	M4	(7)	4.5	(9)	72.0	(10)	3190	0.31	(7)	0.17	0.88	–
Hn 18	M3.5	(7)	9.51	(5)	233.0	(8)	3300	0.49	(7)	0.22	0.98	B
Hn 21E	M5.75	(7)	7.5	(9)	···	···	2890	1.95	(7)	0.10	0.89	–
PDS 70	K7	(11)	2.2	(11)	···	···	3970	0.01	(11)	0.76	1.22	–
IM Lup	M0	(11)	4.9	(11)	260.5	(12)	3770	0.00	(11)	0.45	2.61	B
J15570146-2046184	M4.5	(13)	11.22	(4)	···	···	3080	1.37	(13)	0.11	0.99	–
J15574362-4143377	K6	(11)	5.5	(11)	···	···	4020	0.30	(11)	0.72	1.57	–
J16020757-2257467	M2.5	(13)	4.11	(4)	···	···	3420	0.17	(13)	0.32	1.03	–
J16023587-2320170	M4.25	(13)	13.98	(4)	···	···	3140	0.60	(13)	0.14	1.08	–

Continued on next page

Table A.1 – continued

Name	SpT	SpT.r	EW	EW.r	W_{10}	W_{10}.r	Teff	Av	Av.r	$M_\star$	$R_\star$	Note
J16024575-2304509	M5.5	(13)	13.77	(4)	···	···	2920	0.17	(13)	0.10	0.45	–
J16030161-2207523	M4.75	(13)	7.27	(4)	···	···	3030	0.34	(13)	0.10	0.54	–
J16031329-2112569	M4.75	(13)	6.74	(4)	···	···	3030	0.77	(13)	0.10	0.72	–
J16032625-2155378	M5	(13)	16.12	(4)	···	···	2980	0.94	(13)	0.10	0.62	–
J16041416-2129151	M4	(13)	9.05	(4)	···	···	3190	0.34	(13)	0.17	0.71	–
J16041740-1942287	M3.5	(13)	11.29	(4)	···	···	3300	0.51	(13)	0.23	0.96	–
J16041792-1941505	M5	(13)	12.61	(4)	···	···	2980	0.60	(13)	0.10	0.46	–
J16042165-2130284	K2	(11)	2.7	(11)	···	···	4760	5.03	(11)	1.39	1.98	–
J16044876-1748393	M3.5	(13)	10.45	(4)	···	···	3300	0.68	(13)	0.21	1.05	–
J16052076-1821367	M2	(13)	5.83	(4)	···	···	3490	0.43	(13)	0.35	1.65	–
J16052661-1957050	M4.5	(13)	10.32	(4)	···	···	3080	0.17	(13)	0.12	0.88	–
J16055863-1949029	M4	(13)	7.99	(4)	···	···	3190	0.00	(13)	0.17	0.81	–
J16060061-1957114	M4	(13)	4.15	(4)	···	···	3190	0.85	(13)	0.17	0.99	–
J16062898-2052167	M5.5	(13)	15.0	(4)	···	···	2920	0.43	(13)	0.10	1.28	–
J16064102-2455489	M4.5	(13)	9.48	(4)	···	···	3080	0.17	(13)	0.11	0.48	–
J16064115-2517044	M3.25	(13)	3.2	(4)	···	···	3360	0.17	(13)	0.26	0.71	–
J16070014-2033092	M2.75	(13)	1.13	(4)	···	···	3390	1.20	(13)	0.30	1.07	–
J16072625-2432079	M3.5	(13)	17.67	(4)	···	···	3300	0.68	(13)	0.22	1.15	–
J16072747-2059442	M4.75	(13)	7.29	(4)	···	···	3030	0.68	(13)	0.12	1.43	–
J16082870-2137198	M5	(13)	3.55	(4)	···	···	2980	0.85	(13)	0.10	0.94	–
J16084836-2341209	M5	(13)	13.99	(4)	···	···	2980	0.85	(13)	0.10	0.63	–
J16084894-2400045	M3.75	(13)	3.61	(4)	···	···	3240	0.43	(13)	0.19	0.72	–
J16093164-2229224	M2.75	(13)	5.65	(4)	···	···	3390	0.60	(13)	0.29	1.72	–
J16111534-1757214	M1	(11)	2.4	(11)	···	···	3630	0.75	(11)	0.45	1.35	–
J16113376-2027364	M3.5	(13)	9.99	(4)	···	···	3300	0.77	(13)	0.22	1.03	–
J16115091-2012098	M3.5	(13)	2.94	(4)	···	···	3300	0.34	(13)	0.23	0.86	–
J16115763-1926389	M5.25	(13)	15.02	(4)	···	···	2950	1.28	(13)	0.10	1.19	–
J16122737-2009596	M4.5	(13)	10.74	(4)	···	···	3080	0.43	(13)	0.11	0.59	–
J16123916-1859284	K2.5	(11)	-0.2	(11)	···	···	4660	2.57	(11)	1.05	1.18	–
J16132082-1757520	M4	(13)	5.83	(4)	···	···	3190	0.60	(13)	0.17	1.25	–
J16132125-1757487	M4	(13)	5.49	(4)	···	···	3190	0.85	(13)	0.17	1.15	–
J16145244-2513523	M3.5	(13)	3.15	(4)	···	···	3300	0.77	(13)	0.22	1.00	–
J16145928-2459308	M4.25	(13)	9.59	(4)	···	···	3140	1.03	(13)	0.15	0.84	–
J16150524-2459351	M5.25	(13)	5.28	(4)	···	···	2950	0.77	(13)	0.10	0.63	–
J16160602-2528217	M4.75	(13)	10.35	(4)	···	···	3030	1.20	(13)	0.10	0.64	–
J16162531-2412057	M5	(13)	9.86	(4)	···	···	2980	0.94	(13)	0.10	0.47	–
J16163345-2521505	M0.5	(13)	1.63	(4)	···	···	3700	0.85	(13)	0.53	0.99	–
J16171584-2255177	M4.75	(13)	8.61	(4)	···	···	3030	0.60	(13)	0.10	0.92	–
J16253849-2613540	K7	(11)	4.9	(11)	···	···	3970	0.39	(11)	0.56	2.46	–
J16265280-2343127	K1	(11)	2.6	(11)	···	···	4920	2.04	(11)	1.79	3.15	–

A.2 FIRE Observations of Low Accretor Candidates

Table A.2: Log of Observations

Name	RA	Dec	Obs. Date	Airmass	Exp. Time	SNR
CVSO 267	05:02:17.494	−04:08:25.83	2018-11-24	1.12	317.0	166.9
CVSO 288	05:06:49.879	−03:54:33.47	2020-01-09	1.32	422.8	120.2
CVSO 298	05:08:57.724	−01:29:16.11	2020-01-11	1.33	422.8	89.8
CVSO 378	05:17:37.154	+05:59:48.33	2020-01-11	1.35	422.8	79.4
CVSO 415	05:18:43.996	+00:53:45.34	2020-01-11	1.32	443.8	66.8
CVSO 418	05:18:48.862	−01:37:56.77	2020-12-30	1.35	613.0	50.0
CVSO 456	05:20:24.789	−00:14:20.28	2020-12-30	1.84	613.0	36.0
CVSO 491	05:21:39.868	−00:44:54.28	2020-12-29	1.15	549.6	77.3
CVSO 535	05:22:29.416	+00:19:27.60	2020-01-11	1.24	443.8	70.4
CVSO 604	05:23:15.525	+01:21:14.47	2018-12-29	1.17	486.2	58.8
CVSO 662	05:24:11.197	+03:35:21.60	2018-12-28	1.80	380.4	107.2
CVSO 746	05:25:06.735	+01:09:06.80	2020-01-11	1.23	401.6	57.6
CVSO 40	05:26:41.625	−00:40:52.44	2020-01-11	1.17	401.6	102.8
CVSO 932	05:27:16.762	+00:07:52.76	2020-01-11	1.16	380.4	92.0
CVSO 952	05:27:28.650	+01:17:39.13	2020-12-28	1.78	729.3	60.9
CVSO 982	05:27:43.395	+03:13:08.13	2018-11-24	1.21	211.4	187.3
CVSO 985	05:27:46.515	+03:12:15.51	2018-11-24	1.25	317.0	146.0
CVSO 1043	05:28:20.248	+01:21:15.96	2020-12-29	1.19	549.6	90.0
CVSO 1231	05:30:03.700	−01:55:46.81	2018-12-29	1.15	401.6	115.7
CVSO 1231	05:30:03.700	−01:55:46.81	2020-01-11	1.12	380.4	108.8
CVSO 1232	05:30:04.048	+03:50:52.15	2020-12-29	1.25	549.6	78.6
CVSO 1261	05:30:27.181	−01:14:31.15	2020-12-29	1.22	549.6	70.5
CVSO 1262	05:30:28.237	−01:53:30.71	2020-01-11	1.12	380.4	65.4
CVSO 1295	05:30:57.053	−04:12:56.51	2020-01-09	1.31	422.8	149.9
CVSO 1295	05:30:57.053	−04:12:56.51	2018-12-28	1.47	317.0	117.0
CVSO 82	05:30:57.849	−00:40:37.77	2020-01-11	1.14	380.4	97.9
CVSO 95	05:31:38.998	−01:27:45.96	2018-12-29	1.25	486.2	60.8
CVSO 1320	05:31:49.372	−06:00:19.35	2018-11-23	1.11	380.4	185.0
CVSO 239	05:32:03.471	−01:56:32.12	2018-12-28	1.40	359.4	119.7
CVSO 1338	05:32:15.134	−05:35:00.24	2018-12-28	1.23	359.4	122.7
CVSO 2065	05:32:16.820	−02:56:25.50	2020-12-29	1.26	549.6	84.6
CVSO 1348	05:32:24.014	−05:05:23.48	2020-01-09	1.25	317.0	153.3
CVSO 2067	05:32:28.245	−00:41:36.61	2020-12-29	1.35	549.6	72.2
CVSO 2084	05:32:43.464	−00:48:44.58	2020-12-29	1.43	549.6	73.0

Continued on next page

Table A.2 – continued

Name	RA	Dec	Obs. Date	Airmass	Exp. Time	SNR
CVSO 111	05:32:47.425	−00:40:34.13	2020-12-28	1.58	486.2	87.4
CVSO 2071W	05:32:48.635	−00:49:45.10	2020-12-28	1.38	486.2	48.9
CVSO 2071E	05:32:48.728	−00:49:44.65	2020-12-28	1.32	486.2	58.4
CVSO 1381	05:32:55.414	−01:32:51.75	2018-12-29	1.19	401.6	72.9
CVSO 1388	05:33:04.328	−05:19:41.03	2018-12-28	1.17	359.4	112.2
CVSO 115	05:33:06.239	−00:42:19.79	2018-11-23	1.14	380.4	140.4
CVSO 248	05:33:22.726	−01:43:42.21	2020-12-30	1.37	549.6	97.4
CVSO 248	05:33:22.726	−01:43:42.21	2020-12-28	1.25	380.4	89.8
CVSO 2080	05:33:23.659	−00:33:33.44	2020-12-28	1.23	486.2	82.7
CVSO 1415B	05:33:25.084	−04:03:31.22	2020-01-11	1.12	380.4	68.9
CVSO 1415A	05:33:25.114	−04:03:29.53	2020-01-11	1.11	380.4	95.8
CVSO 119	05:33:30.839	−01:27:34.08	2020-01-11	1.17	380.4	104.3
CVSO 1424	05:33:31.950	−01:25:38.26	2020-12-30	1.88	613.0	36.6
CVSO 1427	05:33:34.194	−01:32:12.42	2020-12-29	1.56	549.6	57.7
CVSO 1432	05:33:35.904	−06:06:41.47	2020-01-09	1.20	380.4	124.7
CVSO 1439	05:33:42.466	−00:07:38.97	2020-12-30	1.72	549.6	39.2
CVSO 1442	05:33:45.196	−04:37:08.65	2020-01-11	1.15	380.4	109.6
CVSO 1446	05:33:47.716	−04:52:07.98	2018-12-28	1.11	422.8	56.0
CVSO 1461	05:34:01.090	−06:02:26.71	2020-01-11	1.21	359.4	123.0
CVSO 1513	05:34:38.556	−05:47:35.16	2018-12-28	1.09	380.4	148.2
CVSO 1513	05:34:38.556	−05:47:35.16	2020-01-09	1.16	401.6	128.6
CVSO 135	05:34:40.977	−01:22:44.10	2018-11-24	1.21	317.0	181.8
CVSO 1545	05:34:59.570	−00:18:59.89	2020-12-28	1.16	380.4	104.1
CVSO 1567SW	05:35:11.085	+02:28:23.50	2020-12-28	1.17	401.6	84.5
CVSO 1567NE	05:35:11.102	+02:28:24.21	2020-12-28	1.17	401.6	43.6
CVSO 1575	05:35:15.799	−05:33:12.39	2018-12-28	1.17	380.4	155.7
CVSO 1575	05:35:15.799	−05:33:12.39	2020-01-09	1.12	380.4	141.0
CVSO 1579	05:35:18.522	−01:52:10.92	2020-12-30	1.47	613.0	43.6
CVSO 1586	05:35:22.442	−00:40:03.26	2020-12-30	1.57	549.6	51.8
CVSO 1588	05:35:23.490	−06:01:25.23	2020-01-09	1.36	422.8	123.0
CVSO 1600W	05:35:28.466	−01:25:31.54	2020-12-28	1.15	401.6	42.3
CVSO 1600E	05:35:28.559	−01:25:31.44	2020-12-28	1.14	401.6	84.2
CVSO 1608	05:35:31.982	−05:59:41.63	2020-12-28	1.15	380.4	100.3
CVSO 1653	05:35:56.078	−04:56:55.23	2018-12-28	1.60	401.6	114.2
CVSO 1655	05:35:57.513	−04:39:09.14	2020-12-28	1.56	380.4	104.5
CVSO 1672	05:36:14.437	−04:35:48.48	2020-12-29	1.64	380.4	67.7
CVSO 1672	05:36:14.437	−04:35:48.48	2020-12-28	1.90	401.6	81.4
CVSO 1678	05:36:25.802	−04:50:19.94	2020-12-29	1.52	380.4	99.5
CVSO 1695	05:36:37.035	−05:04:41.09	2018-12-27	1.71	317.0	125.8
CVSO 1703	05:36:42.049	−06:07:06.12	2020-12-29	1.30	380.4	102.2

Continued on next page

Table A.2 – continued

Name	RA	Dec	Obs. Date	Airmass	Exp. Time	SNR
CVSO 1704	05:36:42.888	−00:45:08.29	2020-12-30	1.33	549.6	68.9
CVSO 1711	05:36:51.865	−05:08:35.89	2020-12-29	1.38	380.4	108.9
CVSO 1719	05:36:58.495	−01:45:22.96	2020-12-30	1.20	549.6	42.2
CVSO 1739	05:37:09.916	−01:10:50.36	2020-12-30	1.17	549.6	53.1
CVSO 1745	05:37:14.786	−00:49:31.90	2020-12-29	1.30	380.4	90.4
CVSO 1747A	05:37:15.855	−04:37:48.35	2020-12-29	1.14	380.4	84.2
CVSO 1747B	05:37:15.965	−04:37:48.79	2020-12-29	1.16	380.4	77.4
CVSO 1763	05:37:26.014	−05:34:01.33	2018-12-28	1.97	401.6	140.7
CVSO 1771	05:37:33.172	−05:58:21.18	2018-12-29	1.34	380.4	151.2
CVSO 1772	05:37:33.386	−00:02:43.64	2020-12-30	1.15	919.5	44.6
CVSO 1776	05:37:37.356	−00:28:27.84	2020-12-30	1.14	613.0	38.4
CVSO 156	05:37:47.019	−00:20:07.23	2020-01-09	1.38	380.4	114.6
SO247	05:37:54.866	−02:41:09.24	2020-01-09	1.12	528.4	61.5
CVSO 1790	05:37:59.047	−00:46:14.41	2020-12-30	1.15	613.0	60.3
SO435	05:38:17.785	−02:40:50.10	2020-01-09	1.13	486.2	71.0
SO451	05:38:18.859	−02:51:38.95	2020-01-08	1.14	570.6	75.1
SO467	05:38:21.194	−02:54:11.14	2020-01-08	1.12	570.6	68.3
CVSO 160	05:38:26.569	−02:12:17.47	2020-01-09	1.13	380.4	114.9
CVSO 160	05:38:26.569	−02:12:17.47	2018-12-29	1.30	380.4	120.2
CVSO 1830	05:38:31.368	−00:39:56.68	2020-12-29	1.15	486.2	73.1
CVSO 1832	05:38:32.003	−01:43:17.20	2020-12-30	2.05	369.9	23.2
SO566	05:38:32.136	−02:32:43.12	2020-01-09	1.12	486.2	69.8
CVSO 1840	05:38:39.819	−02:56:46.24	2018-11-23	1.29	570.6	203.7
SO662	05:38:40.273	−02:30:18.56	2020-01-08	1.20	422.8	118.4
CVSO 1841	05:38:41.365	−01:35:58.45	2020-12-29	1.87	549.6	79.3
SO674	05:38:41.598	−02:30:28.93	2020-01-08	1.13	570.6	79.0
CVSO 1842	05:38:41.681	−00:02:34.44	2020-12-30	1.17	613.0	51.7
SO682	05:38:42.280	−02:37:14.82	2020-01-08	1.17	422.8	122.3
SO697	05:38:44.235	−02:40:19.77	2020-01-08	1.25	422.8	138.2
CVSO 1844	05:38:47.237	−00:50:41.97	2020-12-29	1.26	380.4	106.3
SO738	05:38:48.099	−02:28:53.68	2020-01-09	1.18	676.4	40.7
SO823	05:38:59.101	−02:47:13.43	2020-01-08	1.33	380.4	88.9
SO967	05:39:15.830	−02:36:50.76	2020-01-09	1.15	528.4	72.8
CVSO 1884	05:39:37.324	−01:25:29.47	2020-12-29	2.08	274.8	43.8
CVSO 1886	05:39:41.025	−00:17:16.81	2020-12-29	1.14	486.2	56.9
CVSO 174	05:39:57.971	−01:31:55.41	2018-12-29	1.24	412.2	47.5
CVSO 175	05:40:09.059	−01:34:08.67	2020-12-29	1.13	486.2	75.0
CVSO 1920	05:42:06.793	−02:46:35.13	2020-01-09	1.61	422.8	124.6
CVSO 1923	05:42:11.930	−02:45:21.48	2020-01-09	1.73	486.2	105.1
CVSO 1928	05:42:48.600	−03:24:47.62	2018-12-29	1.13	401.6	124.0

Continued on next page

Table A.2 – continued

Name	RA	Dec	Obs. Date	Airmass	Exp. Time	SNR
CVSO 1928	05:42:48.600	−03:24:47.62	2020-01-09	1.12	380.4	113.8
CVSO 191	05:43:36.304	−00:02:30.05	2018-11-23	1.23	570.6	200.1
CVSO 1942	05:45:41.951	−00:12:05.42	2018-12-29	1.15	380.4	127.1
J08074647-4711495	08:07:46.485	−47:11:49.58	2020-01-09	1.11	613.0	64.4
J08075546-4707460	08:07:55.471	−47:07:46.02	2019-04-27	1.13	274.8	113.4
J08075546-4707460	08:07:55.471	−47:07:46.02	2018-12-29	1.07	253.6	165.0
J08094701-4744297	08:09:47.018	−47:44:29.83	2018-12-28	1.14	317.0	168.1
ESO-Ha 553	10:56:16.377	−76:30:53.12	2019-04-26	1.57	507.2	66.8
ESO-Ha 553	10:56:16.377	−76:30:53.12	2020-01-09	1.48	507.2	83.0
SZ 4	10:57:42.098	−76:59:35.64	2019-04-25	1.69	338.2	96.4
Hn 1	11:02:32.605	−77:29:13.03	2019-04-26	1.72	317.0	115.0
ISO-ChaI 52	11:04:42.599	−77:41:57.17	2019-04-25	1.61	380.4	76.5
CHSM 9484	11:07:11.807	−76:25:50.02	2019-04-26	1.52	613.0	53.4
CHSM 10862	11:07:46.586	−76:15:17.40	2019-04-27	1.48	655.2	43.2
CHSM 13620	11:08:52.425	−75:19:02.79	2019-04-25	1.62	338.2	138.5
J11090915-7553477	11:09:09.147	−75:53:47.83	2019-04-26	1.66	359.4	127.3
Hn 13	11:10:55.978	−76:45:32.65	2019-04-25	1.61	317.0	109.3
Hn 17	11:12:48.611	−76:47:06.61	2019-04-26	1.49	380.4	79.4
Hn 18	11:13:24.452	−76:29:22.87	2020-01-09	1.48	422.8	118.0
Hn 18	11:13:24.452	−76:29:22.87	2019-04-25	1.54	380.4	92.6
Hn 21E	11:14:26.107	−77:33:04.44	2019-04-26	1.52	380.4	51.9
PDS 70	14:08:10.155	−41:23:52.57	2019-04-26	1.28	253.6	228.3
PDS 70	14:08:10.155	−41:23:52.57	2020-01-09	1.23	126.8	217.7
PDS 70	14:08:10.155	−41:23:52.57	2020-01-11	1.51	126.8	149.9
IM Lup	15:56:09.207	−37:56:06.13	2019-04-27	1.77	105.6	246.0
J15570146-2046184	15:57:01.470	−20:46:18.43	2019-04-26	2.04	338.2	90.1
J15574362-4143377	15:57:43.621	−41:43:37.83	2019-04-27	1.69	105.6	159.0
J16020757-2257467	16:02:07.577	−22:57:46.88	2019-04-26	1.88	274.8	124.0
J16023587-2320170	16:02:35.877	−23:20:17.06	2019-04-26	1.49	274.8	98.9
J16024575-2304509	16:02:45.755	−23:04:50.97	2019-04-27	1.01	380.4	97.3
J16030161-2207523	16:03:01.614	−22:07:52.47	2019-04-27	1.01	422.8	81.5
J16031329-2112569	16:03:13.301	−21:12:56.96	2019-04-27	1.03	380.4	115.8
J16032625-2155378	16:03:26.257	−21:55:37.92	2019-04-27	1.01	401.6	100.5
J16041416-2129151	16:04:14.166	−21:29:15.28	2019-04-27	1.05	295.8	101.6
J16041740-1942287	16:04:17.405	−19:42:28.82	2019-04-26	1.01	295.8	104.8
J16041792-1941505	16:04:17.926	−19:41:50.72	2019-04-27	1.09	613.0	80.1
J16042165-2130284	16:04:21.655	−21:30:28.55	2019-04-27	1.08	126.8	186.5
J16044876-1748393	16:04:48.773	−17:48:39.67	2019-04-26	1.02	295.8	128.3
J16052076-1821367	16:05:20.773	−18:21:36.98	2019-04-26	1.47	126.8	146.1
J16052661-1957050	16:05:26.594	−19:57:05.45	2019-04-26	1.05	359.4	111.1

Continued on next page

Table A.2 – continued

Name	RA	Dec	Obs. Date	Airmass	Exp. Time	SNR
J16055863-1949029	16:05:58.642	−19:49:02.98	2019-04-27	2.01	359.4	114.4
J16060061-1957114	16:06:00.606	−19:57:11.25	2019-04-26	1.11	359.4	82.9
J16062898-2052167	16:06:28.968	−20:52:17.20	2019-04-26	1.06	274.8	127.0
J16064102-2455489	16:06:41.022	−24:55:49.05	2019-04-27	1.11	570.6	99.1
J16064115-2517044	16:06:41.161	−25:17:04.56	2019-04-27	1.58	380.4	96.7
J16070014-2033092	16:07:00.147	−20:33:09.31	2019-04-26	1.05	295.8	137.0
J16072625-2432079	16:07:26.254	−24:32:07.91	2019-04-26	1.12	253.6	125.7
J16072747-2059442	16:07:27.460	−20:59:44.16	2019-04-26	1.03	317.0	144.7
J16082870-2137198	16:08:28.696	−21:37:19.95	2019-04-26	1.15	359.4	95.8
J16084836-2341209	16:08:48.372	−23:41:20.91	2019-04-27	1.23	507.2	107.3
J16084894-2400045	16:08:48.946	−24:00:04.57	2019-04-27	1.51	401.6	107.8
J16093164-2229224	16:09:31.652	−22:29:22.47	2019-04-26	1.20	126.8	124.3
J16111534-1757214	16:11:15.344	−17:57:21.43	2019-04-27	1.10	126.8	130.2
J16113376-2027364	16:11:33.767	−20:27:36.48	2019-04-26	1.43	274.8	115.1
J16115091-2012098	16:11:50.925	−20:12:09.86	2019-04-26	1.01	295.8	127.2
J16115763-1926389	16:11:57.638	−19:26:38.89	2019-04-26	1.02	295.8	143.0
J16122737-2009596	16:12:27.379	−20:09:59.66	2019-04-27	1.46	486.2	91.2
J16123916-1859284	16:12:39.167	−18:59:28.46	2019-04-26	1.18	148.0	145.1
J16132082-1757520	16:13:20.812	−17:57:52.09	2019-04-26	1.12	274.8	127.5
J16132125-1757487	16:13:21.238	−17:57:48.73	2019-04-26	1.14	274.8	116.2
J16145244-2513523	16:14:52.430	−25:13:52.57	2019-04-26	1.01	317.0	116.8
J16145928-2459308	16:14:59.282	−24:59:30.89	2019-04-26	1.16	380.4	92.3
J16150524-2459351	16:15:05.246	−24:59:35.23	2019-04-27	1.31	507.2	98.6
J16160602-2528217	16:16:06.022	−25:28:21.86	2019-04-27	1.02	465.0	83.8
J16162531-2412057	16:16:25.313	−24:12:05.76	2019-04-27	1.07	613.0	72.8
J16163345-2521505	16:16:33.447	−25:21:50.66	2019-04-26	1.35	274.8	108.3
J16171584-2255177	16:17:15.829	−22:55:18.16	2019-04-26	1.05	359.4	129.3
J16253849-2613540	16:25:38.498	−26:13:53.87	2019-04-27	1.10	105.6	220.7
J16265280-2343127	16:26:52.818	−23:43:12.71	2019-04-27	1.14	10.0	277.5

A.3 The Targets' Line Profiles and their Measurements

Here we show the He I λ10830 line profiles of all of the targets in our study in Figure A.1. Multiple observations of the same star are plotted in the same panel. Horizontal lines have the same meaning as in Figure 5.2.

Table A.3 shows the measurements of the components in the line profiles for all stars except those with type *f* profiles.

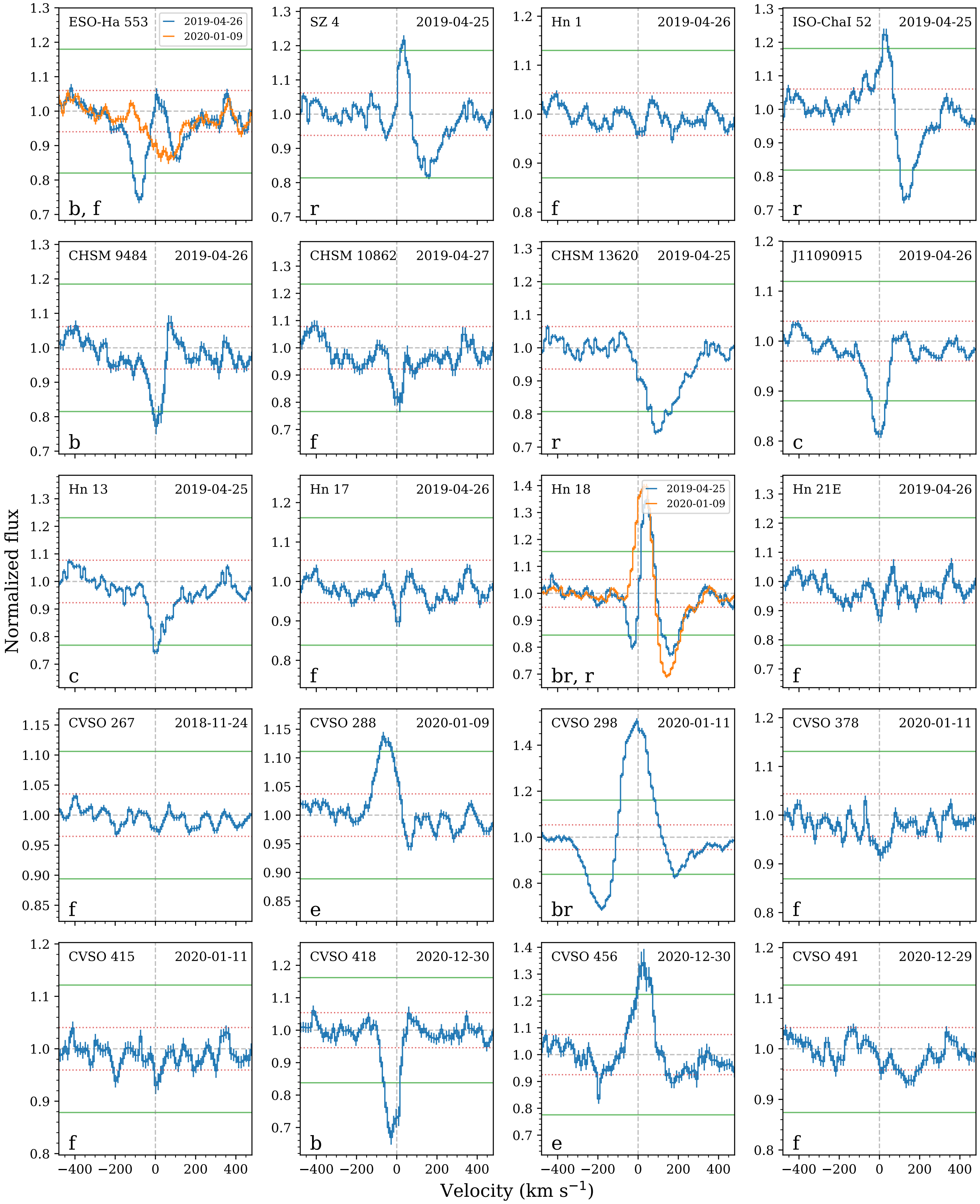

Figure A.1 The He I profiles of the targets. The profile classification is marked at the lower-left corner of each panel.

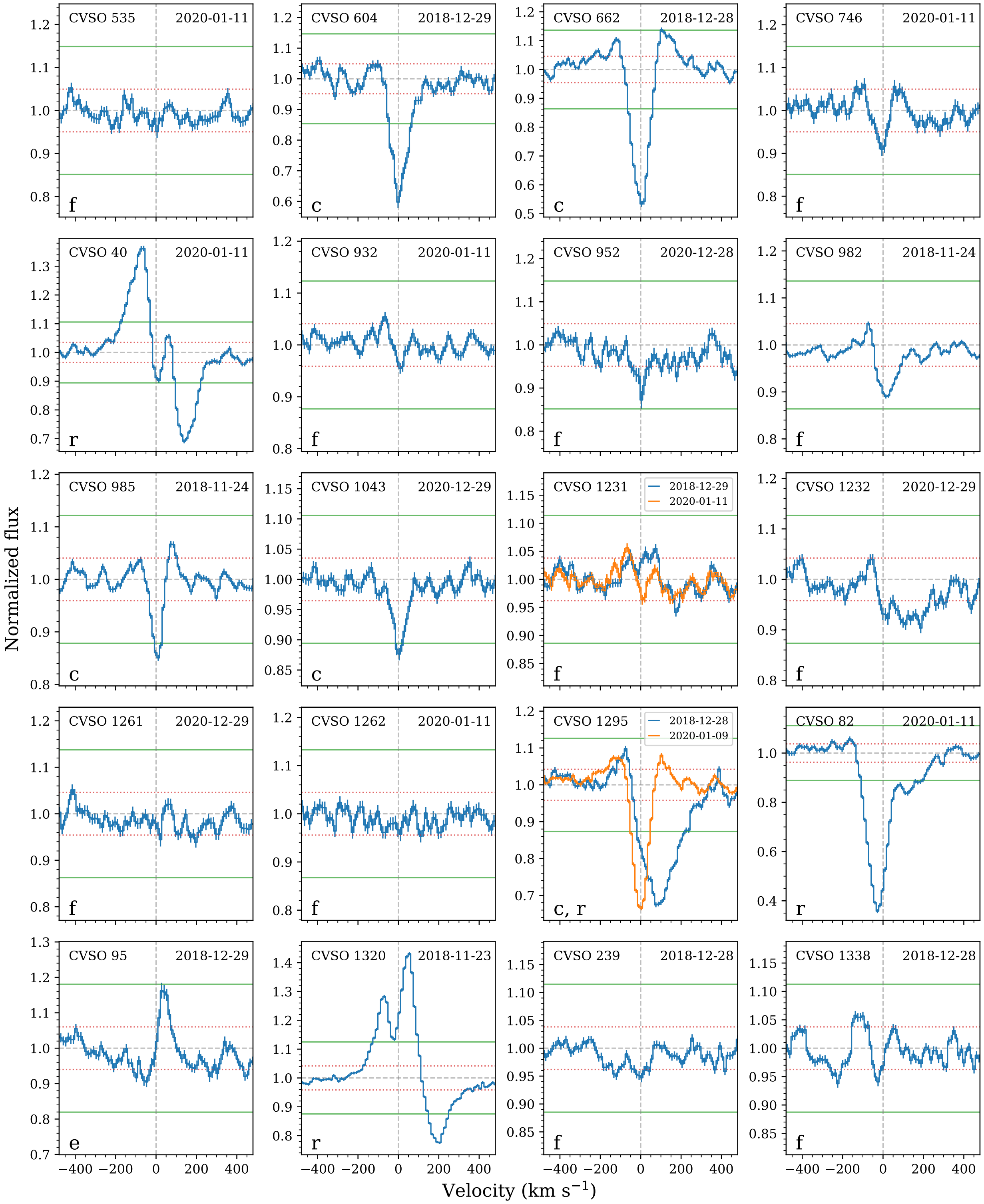

Figure A.1 – continued

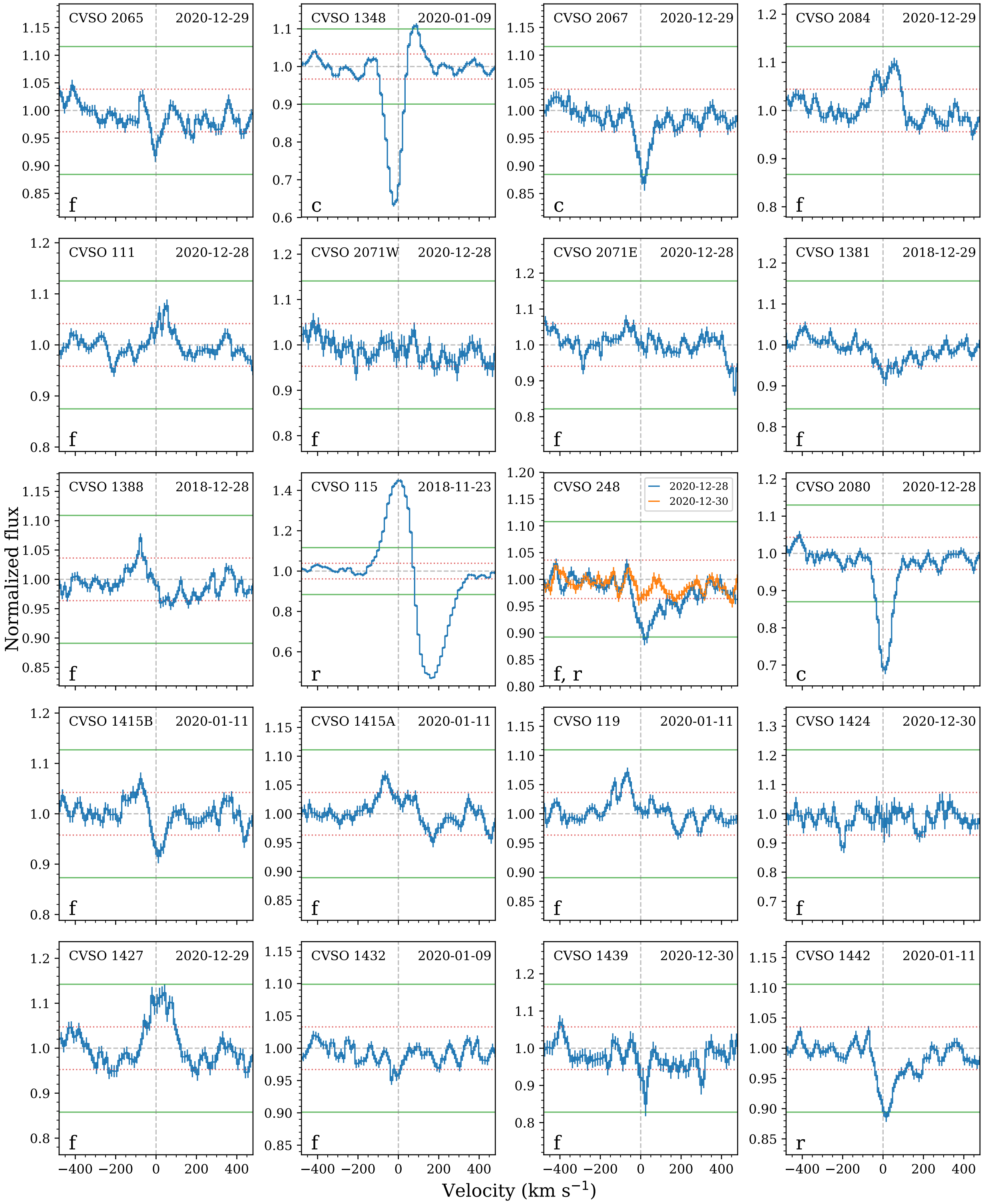

Figure A.1 – continued

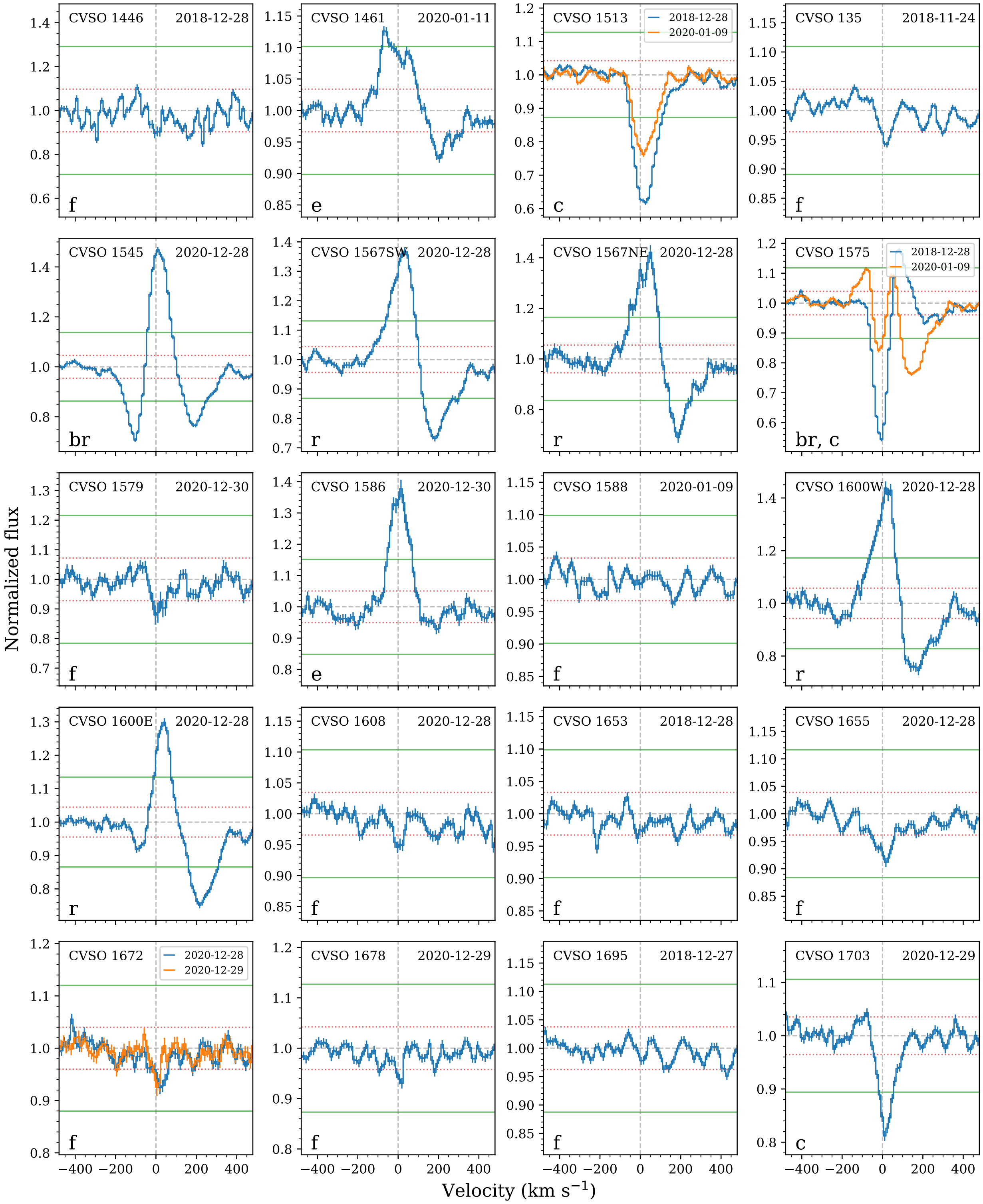

Figure A.1 – continued

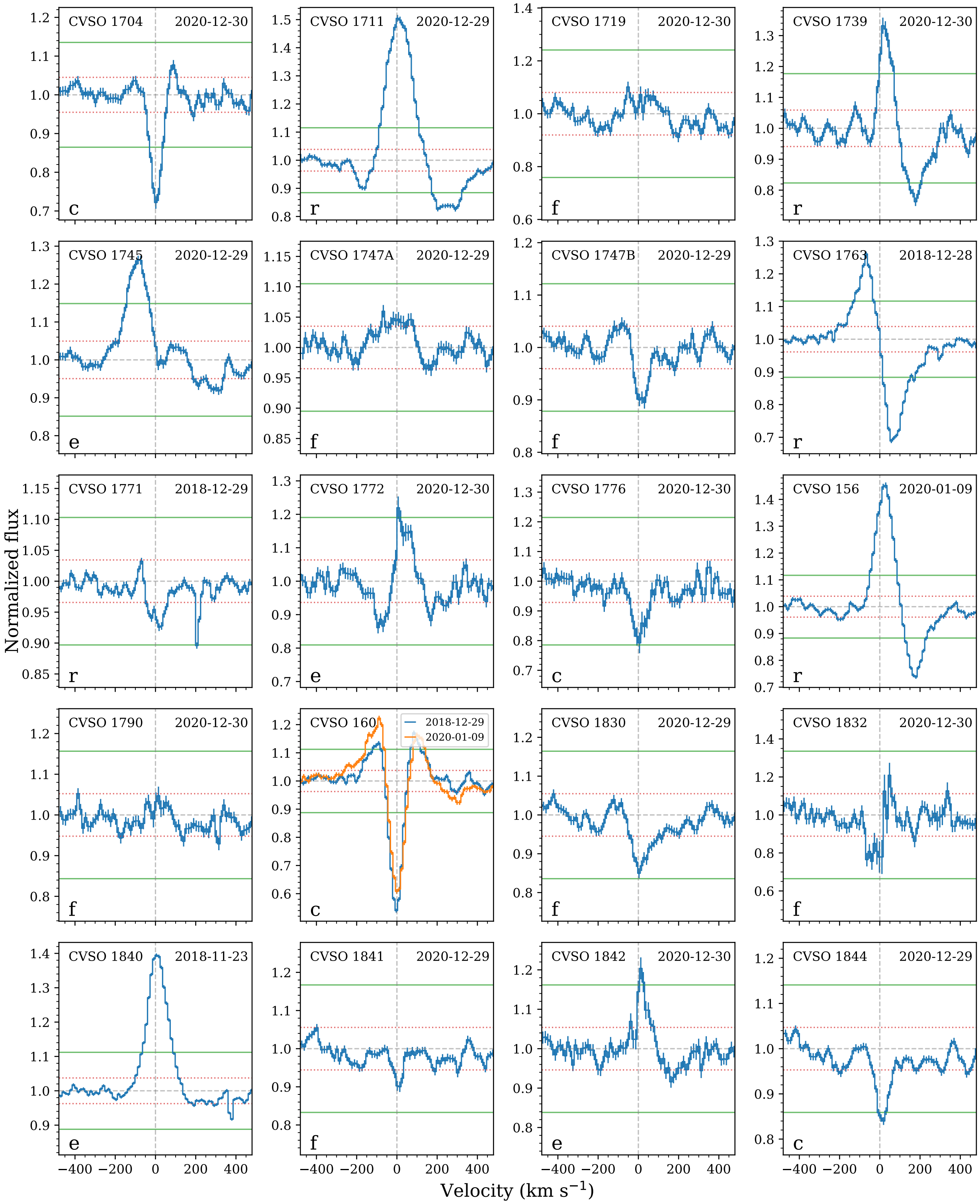

Figure A.1 – continued

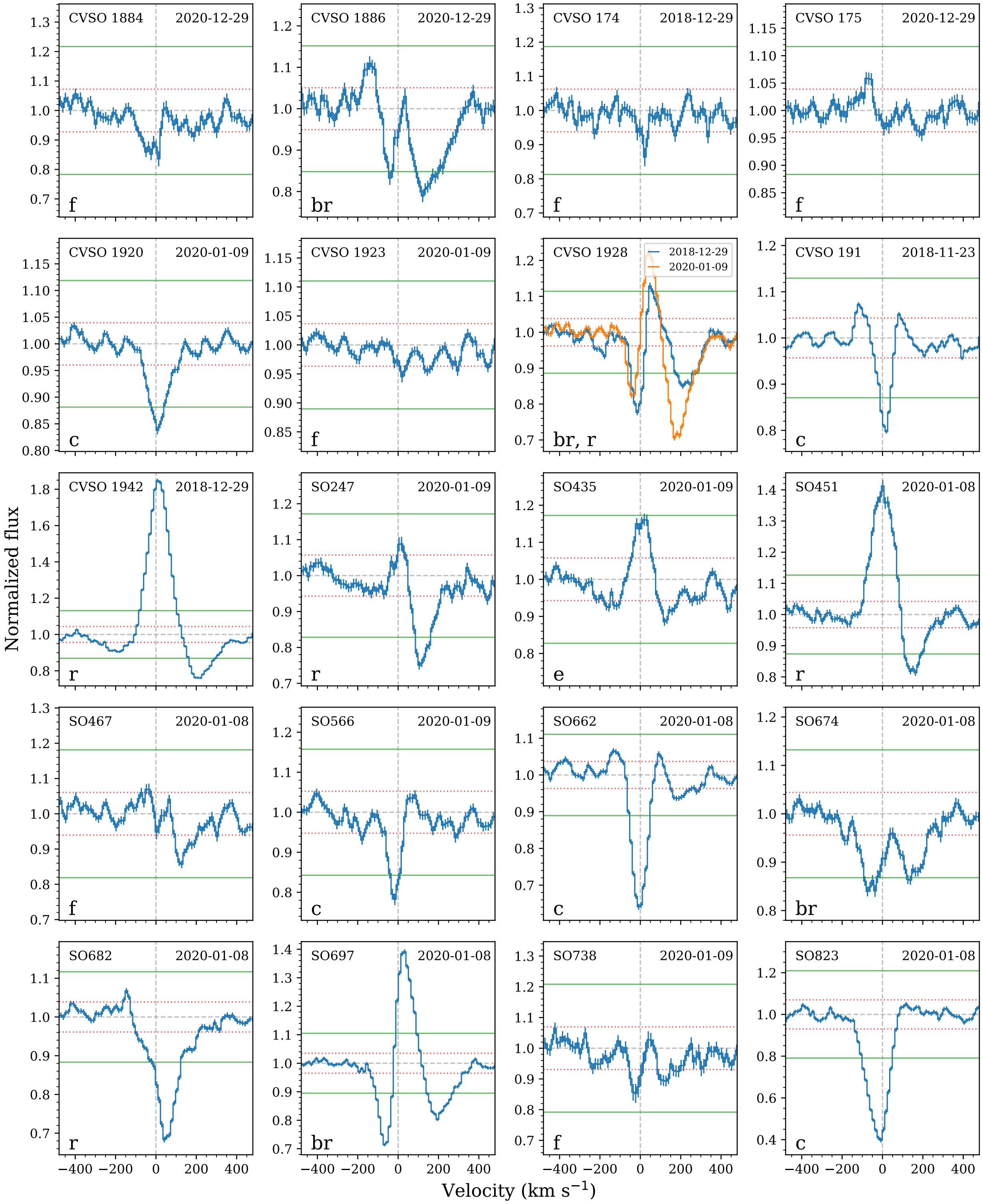

Figure A.1 – continued

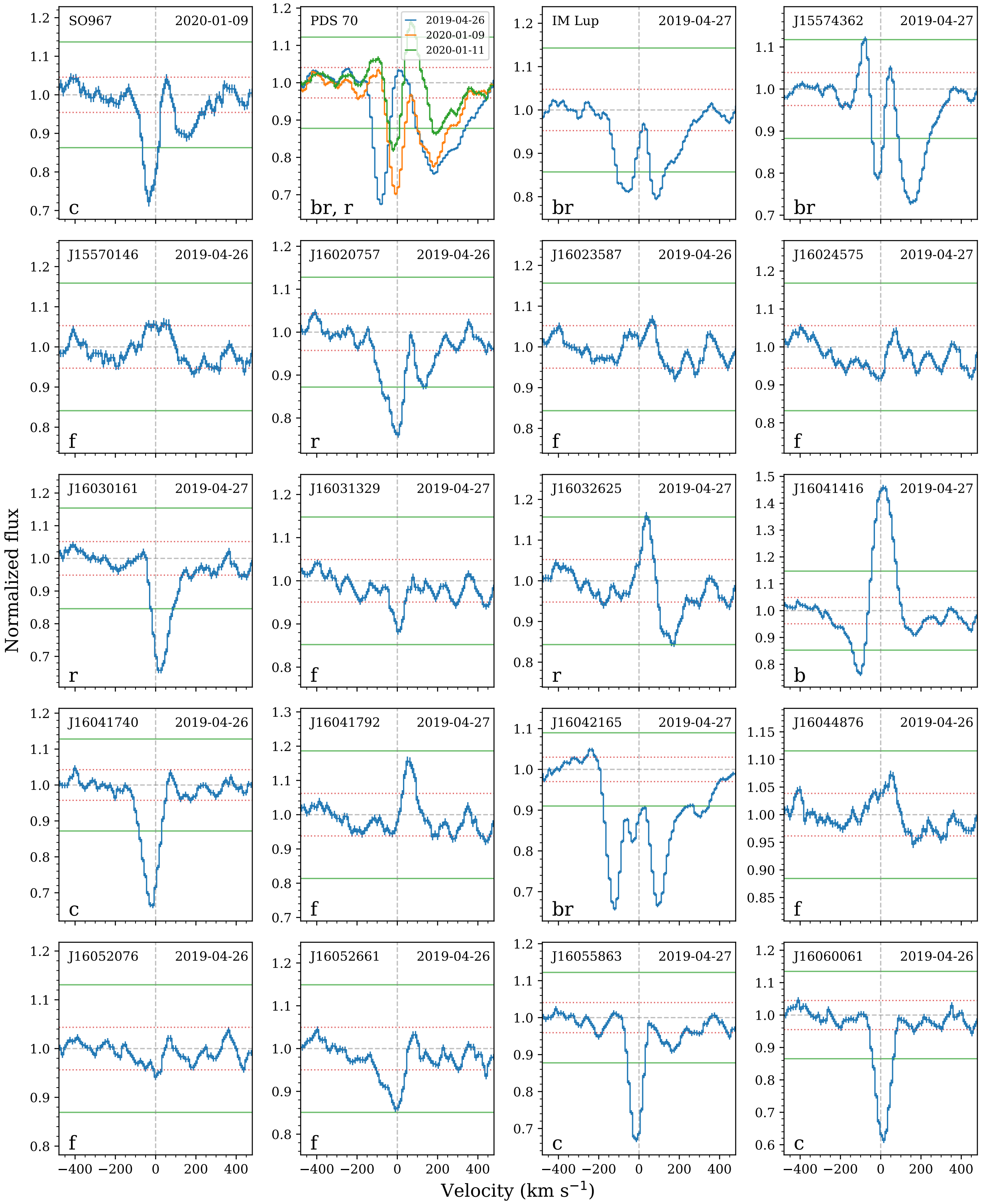

Figure A.1 – continued

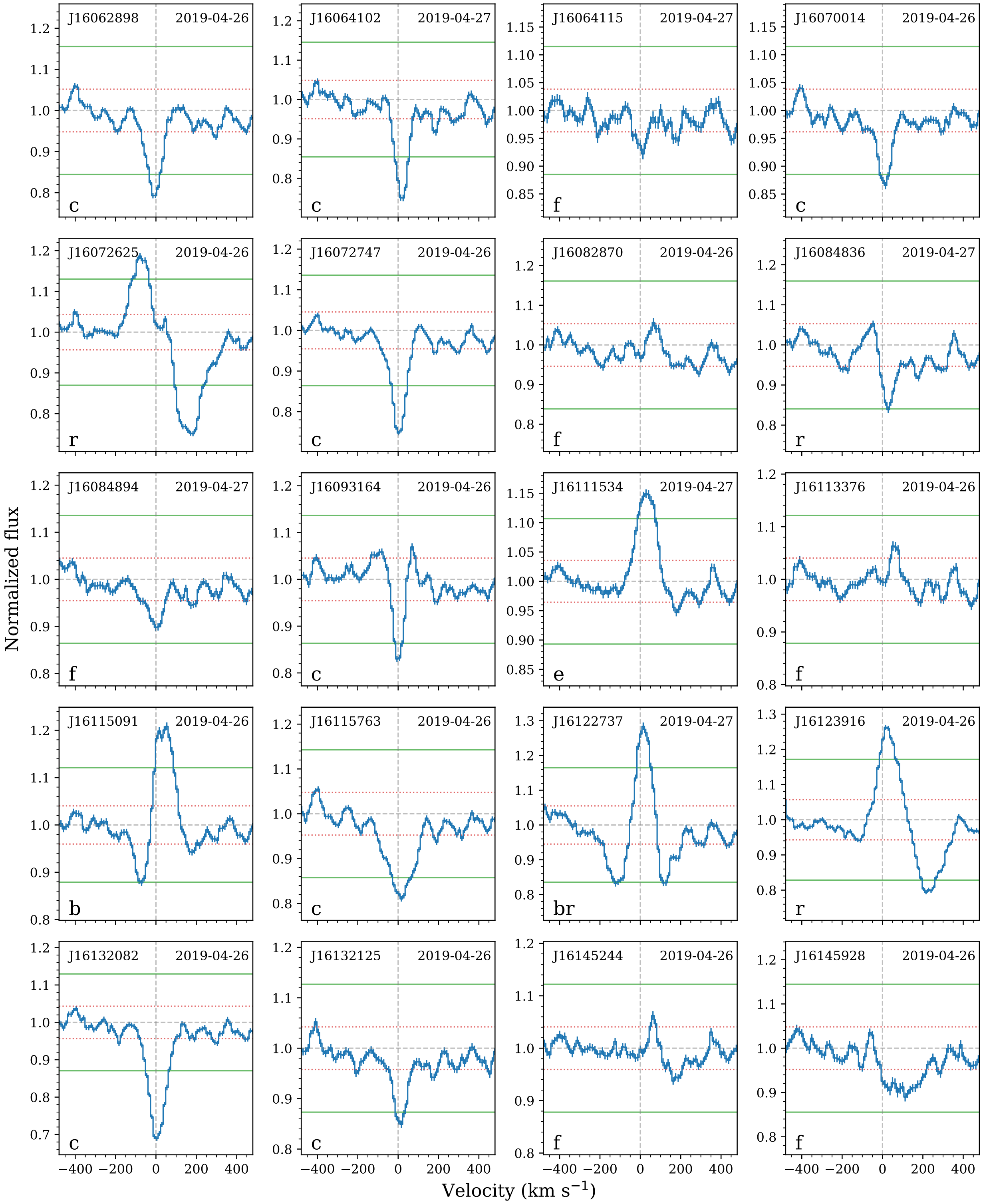

Figure A.1 – continued

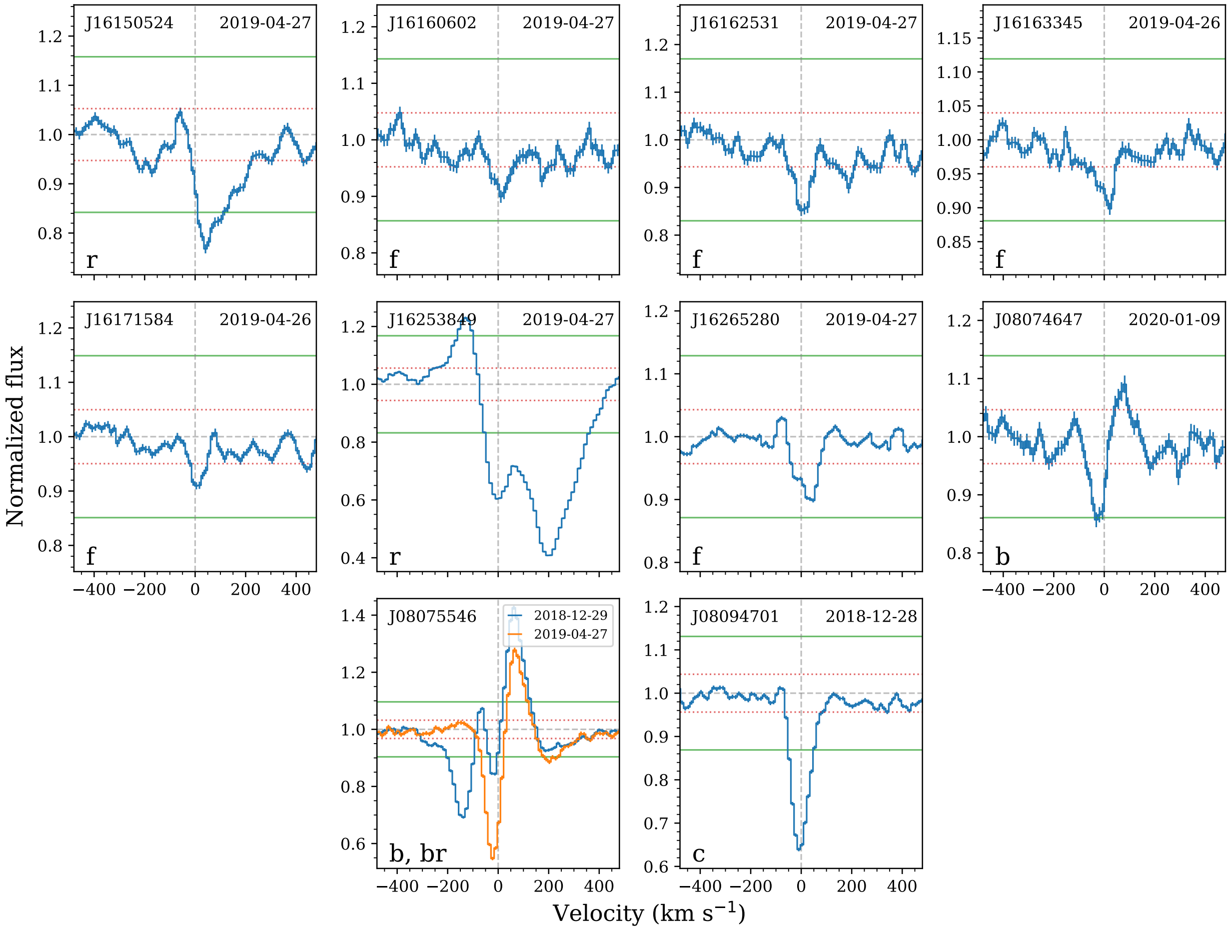

Figure A.1 – continued

Table A.3: Line Profile Measurements

Name	Obs. Date	Type	EW$_b$	EW$_c$	EW$_r$	$v_{b,b}$	$v_{0,b}$	$v_{r,b}$	$v_{b,c}$	$v_{0,c}$	$v_{r,c}$	$v_{b,r}$	$v_{0,r}$	$v_{r,r}$
CVSO 288	2020-01-09	e	0.5	⋯	⋯	-141.2	-66.5	29.0	⋯	⋯	⋯	⋯	⋯	⋯
CVSO 298	2020-01-11	br	-1.5	2.5	-0.9	-328.3	-181.3	-107.4	-107.4	-6.1	120.1	120.1	181.5	442.2
CVSO 418	2020-12-30	b	-0.9	⋯	⋯	-120.7	-27.7	48.7	⋯	⋯	⋯	⋯	⋯	⋯
CVSO 456	2020-12-30	e	⋯	1.2	⋯	⋯	⋯	⋯	-93.3	28.7	111.8	⋯	⋯	⋯
CVSO 604	2018-12-29	c	⋯	-1.4	⋯	⋯	⋯	⋯	-74.4	-1.4	135.6	⋯	⋯	⋯
CVSO 662	2018-12-28	c	⋯	-1.5	0.4	⋯	⋯	⋯	-83.9	3.3	74.7	74.7	103.7	227.4
CVSO 40	2020-01-11	r	1.5	-0.1	-1.3	-269.9	-61.5	-16.7	-16.7	14.0	42.2	78.8	139.4	323.7
CVSO 985	2018-11-24	c	⋯	-0.3	⋯	⋯	⋯	⋯	-52.9	11.0	48.4	⋯	⋯	⋯
CVSO 1043	2020-12-29	c	⋯	-0.4	⋯	⋯	⋯	⋯	-68.8	4.2	132.9	⋯	⋯	⋯
CVSO 1295	2020-01-09	c	⋯	-1.0	⋯	⋯	⋯	⋯	-68.7	2.7	69.9	⋯	⋯	⋯
CVSO 1295	2018-12-28	r	⋯	⋯	-2.4	⋯	⋯	⋯	⋯	⋯	⋯	-45.3	75.9	332.4
CVSO 82	2020-01-11	r	⋯	-3.4	⋯	⋯	⋯	⋯	-134.5	-27.3	265.7	⋯	⋯	⋯
CVSO 95	2018-12-29	e	⋯	⋯	0.3	⋯	⋯	⋯	⋯	⋯	⋯	-2.1	27.8	109.1
CVSO 1320	2018-11-23	r	2.3	⋯	-1.1	-329.8	54.6	116.0	⋯	⋯	⋯	116.0	204.0	417.4
CVSO 1348	2020-01-09	c	⋯	-1.1	0.3	⋯	⋯	⋯	-105.3	-23.1	42.5	42.5	89.0	156.2
CVSO 2067	2020-12-29	c	⋯	-0.4	⋯	⋯	⋯	⋯	-79.2	18.8	135.9	⋯	⋯	⋯
CVSO 115	2018-11-23	r	2.1	⋯	-3.0	-262.3	-0.8	75.6	⋯	⋯	⋯	75.6	161.9	409.3
CVSO 248	2020-12-28	r	⋯	-0.7	⋯	⋯	⋯	⋯	-265.4	18.6	254.4	⋯	⋯	⋯
CVSO 2080	2020-12-28	c	⋯	-1.0	⋯	⋯	⋯	⋯	-99.9	11.3	98.5	⋯	⋯	⋯
CVSO 1442	2020-01-11	r	⋯	⋯	-0.6	⋯	⋯	⋯	⋯	⋯	⋯	-50.7	15.8	317.1
CVSO 1461	2020-01-11	e	⋯	0.7	⋯	⋯	⋯	⋯	-152.6	-70.4	124.7	⋯	⋯	⋯
CVSO 1513	2018-12-28	c	⋯	-1.9	⋯	⋯	⋯	⋯	-151.5	26.1	265.3	⋯	⋯	⋯
CVSO 1513	2020-01-09	c	⋯	-1.0	⋯	⋯	⋯	⋯	-100.2	15.3	152.2	⋯	⋯	⋯
CVSO 1545	2020-12-28	br	-0.9	1.6	-0.7	-224.8	-103.6	-54.6	-54.6	9.3	102.3	102.3	196.2	225.2
CVSO 1567SW	2020-12-28	r	⋯	1.7	-1.1	⋯	⋯	⋯	-138.9	32.2	104.4	104.4	182.4	254.7
CVSO 1567NE	2020-12-28	r	⋯	1.8	-1.0	⋯	⋯	⋯	-146.7	50.1	107.4	107.4	187.9	243.5
CVSO 1575	2018-12-28	c	⋯	-1.2	0.4	⋯	⋯	⋯	-79.5	-4.8	49.2	49.2	82.4	163.7

Continued on next page

Table A.3 – continued

Name	Obs. Date	Type	EW$_b$	EW$_c$	EW$_r$	$v_{b,b}$	$v_{0,b}$	$v_{r,b}$	$v_{b,c}$	$v_{0,c}$	$v_{r,c}$	$v_{b,r}$	$v_{0,r}$	$v_{r,r}$
CVSO 1575	2020-01-09	br	0.3	-0.3	-1.2	-161.9	-81.4	-51.5	-51.5	-19.1	24.9	75.6	143.6	321.3
CVSO 1586	2020-12-30	e	· · ·	1.5	· · ·	· · ·	· · ·	· · ·	-140.3	14.2	106.3	· · ·	· · ·	· · ·
CVSO 1600W	2020-12-28	r	· · ·	1.8	-1.3	· · ·	· · ·	· · ·	-144.9	15.3	90.9	90.9	178.1	284.3
CVSO 1600E	2020-12-28	r	· · ·	· · ·	-1.0	· · ·	· · ·	· · ·	· · ·	· · ·	· · ·	112.8	216.5	274.7
CVSO 1703	2020-12-29	c	· · ·	-0.6	· · ·	· · ·	· · ·	· · ·	-58.2	10.7	117.0	· · ·	· · ·	· · ·
CVSO 1704	2020-12-30	c	· · ·	-0.6	· · ·	· · ·	· · ·	· · ·	-67.9	1.8	60.7	· · ·	· · ·	· · ·
CVSO 1711	2020-12-29	r	· · ·	2.6	-1.1	· · ·	· · ·	· · ·	-112.5	2.9	146.5	146.5	203.0	393.1
CVSO 1739	2020-12-30	r	· · ·	0.9	-0.6	· · ·	· · ·	· · ·	-31.3	15.2	92.4	92.4	177.9	195.3
CVSO 1745	2020-12-29	e	1.2	· · ·	· · ·	-232.7	-85.8	33.8	· · ·	· · ·	· · ·	· · ·	· · ·	· · ·
CVSO 1763	2018-12-28	r	1.0	· · ·	-1.6	-362.9	-68.2	-0.9	· · ·	· · ·	· · ·	-0.9	57.2	408.4
CVSO 1771	2018-12-29	r	· · ·	· · ·	-0.1	· · ·	· · ·	· · ·	· · ·	· · ·	· · ·	139.9	205.5	233.8
CVSO 1772	2020-12-30	e	· · ·	0.5	· · ·	· · ·	· · ·	· · ·	-23.6	6.3	115.9	· · ·	· · ·	· · ·
CVSO 1776	2020-12-30	c	· · ·	-0.6	· · ·	· · ·	· · ·	· · ·	-93.4	5.4	110.1	· · ·	· · ·	· · ·
CVSO 156	2020-01-09	r	· · ·	1.6	-1.0	· · ·	· · ·	· · ·	-115.9	29.4	105.7	105.7	178.8	281.8
SO247	2020-01-09	r	· · ·	· · ·	-0.9	· · ·	· · ·	· · ·	· · ·	· · ·	· · ·	47.6	104.9	212.9
SO435	2020-01-09	e	· · ·	0.5	· · ·	· · ·	· · ·	· · ·	-74.1	19.7	74.5	· · ·	· · ·	· · ·
SO451	2020-01-08	r	· · ·	1.8	-0.7	· · ·	· · ·	· · ·	-131.7	1.2	90.8	90.8	163.1	303.4
CVSO 160	2020-01-09	c	0.9	-1.0	0.4	-274.9	-88.1	-52.4	-52.4	-0.9	60.5	60.5	99.5	194.2
CVSO 160	2018-12-29	c	0.4	-1.1	0.5	-189.7	-90.9	-60.1	-60.1	-2.9	51.1	51.1	84.3	218.0
SO566	2020-01-09	c	· · ·	-0.6	· · ·	· · ·	· · ·	· · ·	-117.3	-16.9	37.1	· · ·	· · ·	· · ·
CVSO 1840	2018-11-23	e	· · ·	1.8	· · ·	· · ·	· · ·	· · ·	-118.6	4.3	138.0	· · ·	· · ·	· · ·
SO662	2020-01-08	c	· · ·	-1.1	· · ·	· · ·	· · ·	· · ·	-75.0	-8.6	71.1	· · ·	· · ·	· · ·
SO674	2020-01-08	br	· · ·	-1.4	· · ·	· · ·	· · ·	· · ·	-149.6	-74.0	297.9	· · ·	· · ·	· · ·
CVSO 1842	2020-12-30	e	· · ·	0.4	· · ·	· · ·	· · ·	· · ·	-109.1	12.2	93.5	· · ·	· · ·	· · ·
SO682	2020-01-08	r	· · ·	· · ·	-1.8	· · ·	· · ·	· · ·	· · ·	· · ·	· · ·	-117.6	40.9	325.7
SO697	2020-01-08	br	-0.7	· · ·	1.1	-155.4	-67.4	-22.6	· · ·	· · ·	· · ·	-22.6	32.2	117.7
CVSO 1844	2020-12-29	c	· · ·	-0.6	· · ·	· · ·	· · ·	· · ·	-97.6	18.7	195.5	· · ·	· · ·	· · ·
SO823	2020-01-08	c	· · ·	-2.7	· · ·	· · ·	· · ·	· · ·	-179.5	-7.7	82.0	· · ·	· · ·	· · ·

Continued on next page

Table A.3 – continued

Name	Obs. Date	Type	EW$_b$	EW$_c$	EW$_r$	$v_{b,b}$	$v_{0,b}$	$v_{r,b}$	$v_{b,c}$	$v_{0,c}$	$v_{r,c}$	$v_{b,r}$	$v_{0,r}$	$v_{r,r}$
SO967	2020-01-09	c	· · ·	-0.8	· · ·	· · ·	· · ·	· · ·	-145.7	-33.6	70.2	· · ·	· · ·	· · ·
CVSO 1886	2020-12-29	br	-0.3	· · ·	-1.2	-91.3	-40.7	25.7	· · ·	· · ·	· · ·	25.7	121.2	313.8
CVSO 1920	2020-01-09	c	· · ·	-0.7	· · ·	· · ·	· · ·	· · ·	-134.6	7.4	147.7	· · ·	· · ·	· · ·
CVSO 1928	2018-12-29	r	· · ·	-0.5	-0.7	· · ·	· · ·	· · ·	-119.2	-14.6	28.6	122.4	210.4	339.1
CVSO 1928	2020-01-09	br	-0.3	· · ·	-1.4	-97.8	-43.0	-0.7	· · ·	· · ·	· · ·	104.0	169.5	349.7
CVSO 191	2018-11-23	c	· · ·	-0.5	· · ·	· · ·	· · ·	· · ·	-58.8	19.2	64.1	· · ·	· · ·	· · ·
CVSO 1942	2018-12-29	r	· · ·	3.7	-1.4	· · ·	· · ·	· · ·	-105.2	7.7	129.0	129.0	219.5	457.7
J08074647-4711495	2020-01-09	b	-0.3	· · ·	· · ·	-136.0	-31.4	22.5	· · ·	· · ·	· · ·	· · ·	· · ·	· · ·
J08075546-4707460	2019-04-27	br	-1.0	· · ·	0.6	-311.0	-22.1	28.5	· · ·	· · ·	· · ·	28.5	65.1	143.9
J08075546-4707460	2018-12-29	b	-1.0	-0.2	1.1	-403.0	-138.2	-54.3	-54.3	-13.6	8.8	8.8	61.9	151.6
J08094701-4744297	2018-12-28	c	· · ·	-1.2	· · ·	· · ·	· · ·	· · ·	-259.4	-9.5	139.1	· · ·	· · ·	· · ·
ESO-Ha 553	2019-04-26	b	-0.9	· · ·	· · ·	-234.9	-81.3	34.9	· · ·	· · ·	· · ·	· · ·	· · ·	· · ·
SZ 4	2019-04-25	r	· · ·	· · ·	-0.7	· · ·	· · ·	· · ·	· · ·	· · ·	· · ·	72.3	159.4	231.7
ISO-ChaI 52	2019-04-25	r	· · ·	0.8	-1.0	· · ·	· · ·	· · ·	-146.2	21.5	74.7	74.7	122.0	266.5
CHSM 9484	2019-04-26	b	-0.9	· · ·	· · ·	-239.0	3.4	57.4	· · ·	· · ·	· · ·	· · ·	· · ·	· · ·
CHSM 13620	2019-04-25	r	· · ·	· · ·	-1.7	· · ·	· · ·	· · ·	· · ·	· · ·	· · ·	-46.1	87.5	302.6
J11090915-7553477	2019-04-26	c	· · ·	-0.7	· · ·	· · ·	· · ·	· · ·	-117.1	6.6	97.9	· · ·	· · ·	· · ·
Hn 13	2019-04-25	c	· · ·	-1.0	· · ·	· · ·	· · ·	· · ·	-79.8	-4.3	133.5	· · ·	· · ·	· · ·
Hn 18	2020-01-09	r	· · ·	1.2	-1.3	· · ·	· · ·	· · ·	-54.4	41.9	85.1	85.1	142.4	320.9
Hn 18	2019-04-25	br	-0.4	· · ·	-0.9	-127.1	-29.1	3.3	· · ·	· · ·	· · ·	93.0	158.5	304.7
PDS 70	2020-01-11	r	· · ·	-0.4	-0.6	· · ·	· · ·	· · ·	-68.2	-20.1	29.7	134.3	192.5	361.8
PDS 70	2020-01-09	r	· · ·	-0.8	-1.5	· · ·	· · ·	· · ·	-129.6	-7.5	67.2	67.2	180.1	459.9
PDS 70	2019-04-26	br	-0.9	· · ·	-2.1	-184.1	-81.1	-12.2	· · ·	· · ·	· · ·	49.2	182.1	468.5
IM Lup	2019-04-27	br	-0.8	· · ·	-1.0	-145.8	-52.8	23.6	· · ·	· · ·	· · ·	23.6	85.0	255.2
J15574362-4143377	2019-04-27	br	0.2	-0.4	-1.5	-126.2	-77.2	-54.0	-54.0	-14.2	47.3	47.3	148.6	385.2
J16020757-2257467	2019-04-26	r	· · ·	-1.0	-0.4	· · ·	· · ·	· · ·	-149.3	4.3	67.3	67.3	129.6	240.0
J16030161-2207523	2019-04-27	r	· · ·	· · ·	-1.5	· · ·	· · ·	· · ·	· · ·	· · ·	· · ·	-94.6	26.6	297.3
J16032625-2155378	2019-04-27	r	· · ·	· · ·	-0.6	· · ·	· · ·	· · ·	· · ·	· · ·	· · ·	86.1	173.3	274.6

Continued on next page

Table A.3 – continued

Name	Obs. Date	Type	EW$_b$	EW$_c$	EW$_r$	$v_{b,b}$	$v_{0,b}$	$v_{r,b}$	$v_{b,c}$	$v_{0,c}$	$v_{r,c}$	$v_{b,r}$	$v_{0,r}$	$v_{r,r}$
J16041416-2129151	2019-04-27	b	-0.8	1.7	···	-260.3	-100.9	-62.7	-62.7	12.1	105.0	···	···	···
J16041740-1942287	2019-04-26	c	···	-1.2	···	···	···	···	-132.4	-14.5	94.3	···	···	···
J16042165-2130284	2019-04-27	br	-1.5	···	-2.0	-200.7	-121.0	29.3	···	···	···	29.3	92.4	407.9
J16055863-1949029	2019-04-27	c	···	···	-1.4	···	···	···	···	···	···	-119.2	-12.9	313.4
J16060061-1957114	2019-04-26	c	···	-1.2	···	···	···	···	-100.2	15.2	92.5	···	···	···
J16062898-2052167	2019-04-26	c	···	-0.7	···	···	···	···	-127.6	-14.7	116.5	···	···	···
J16064102-2455489	2019-04-27	c	···	···	-1.1	···	···	···	···	···	···	-109.6	24.1	325.4
J16070014-2033092	2019-04-26	c	···	-0.5	···	···	···	···	-137.8	14.9	96.3	···	···	···
J16072625-2432079	2019-04-26	r	0.7	···	-1.3	-177.4	-79.4	29.4	···	···	···	29.4	183.0	295.0
J16072747-2059442	2019-04-26	c	···	-0.9	···	···	···	···	-114.3	1.9	113.2	···	···	···
J16084836-2341209	2019-04-27	r	···	···	-0.8	···	···	···	···	···	···	-26.4	28.4	272.5
J16093164-2229224	2019-04-26	c	···	-0.3	···	···	···	···	-47.2	-5.7	45.0	···	···	···
J16111534-1757214	2019-04-27	e	···	0.6	···	···	···	···	-61.4	28.3	121.3	···	···	···
J16115091-2012098	2019-04-26	b	-0.4	···	0.8	-231.8	-71.6	-27.6	···	···	···	-27.6	53.8	126.0
J16115763-1926389	2019-04-26	c	···	-1.1	···	···	···	···	-196.6	16.0	141.3	···	···	···
J16122737-2009596	2019-04-27	br	-0.7	0.8	-0.5	-237.0	-122.5	-51.1	-51.1	14.5	80.1	80.1	115.0	234.5
J16123916-1859284	2019-04-26	r	···	1.0	-1.1	···	···	···	-78.3	15.5	126.8	126.8	215.6	388.3
J16132082-1757520	2019-04-26	c	···	-1.2	···	···	···	···	-127.6	4.4	135.6	···	···	···
J16132125-1757487	2019-04-26	c	···	-0.7	···	···	···	···	-136.6	16.2	216.3	···	···	···
J16150524-2459351	2019-04-27	r	···	···	-1.3	···	···	···	···	···	···	-33.8	40.9	272.6
J16253849-2613540	2019-04-27	r	0.9	-1.5	-4.2	-296.2	-130.1	-76.1	-76.1	-4.7	58.4	58.4	195.3	324.0

REFERENCES

Alcalá, J. M., Natta, A., Manara, C. F., et al. 2014, A&A, 561, A2, doi: `10.1051/0004-6361/201322254`

Alcalá, J. M., Manara, C. F., Natta, A., et al. 2017, A&A, 600, A20, doi: `10.1051/0004-6361/201629929`

Alencar, S. H. P., Bouvier, J., Walter, F. M., et al. 2012, A&A, 541, A116, doi: `10.1051/0004-6361/201118395`

Alencar, S. H. P., Bouvier, J., Donati, J. F., et al. 2018, A&A, 620, A195, doi: `10.1051/0004-6361/201834263`

Alexander, R., Pascucci, I., Andrews, S., Armitage, P., & Cieza, L. 2014, in Protostars and Planets VI, ed. H. Beuther, R. S. Klessen, C. P. Dullemond, & T. Henning, 475, doi: `10.2458/azu_uapress_9780816531240-ch021`

ALMA Partnership, Brogan, C. L., Pérez, L. M., et al. 2015, ApJ, 808, L3, doi: `10.1088/2041-8205/808/1/L3`

Almeida, P. V., Gameiro, J. F., Petrov, P. P., et al. 2017, A&A, 600, A84, doi: `10.1051/0004-6361/201629749`

Andrews, S. M. 2020, ARA&A, 58, 483, doi: `10.1146/annurev-astro-031220-010302`

Andrews, S. M., Huang, J., Pérez, L. M., et al. 2018, ApJ, 869, L41, doi: `10.3847/2041-8213/aaf741`

Ansdell, M., Williams, J. P., Manara, C. F., et al. 2017, AJ, 153, 240, doi: `10.3847/1538-3881/aa69c0`

Antoniucci, S., Nisini, B., Giannini, T., et al. 2017, A&A, 599, A105, doi: `10.1051/0004-6361/201629683`

Aoyama, Y., & Ikoma, M. 2019, ApJL, 885, L29, doi: `10.3847/2041-8213/ab5062`

Aoyama, Y., Ikoma, M., & Tanigawa, T. 2018, ApJ, 866, 84, doi: `10.3847/1538-4357/aadc11`

Avenhaus, H., Quanz, S. P., Garufi, A., et al. 2018, ApJ, 863, 44, doi: `10.3847/1538-4357/aab846`

Bae, J., Zhu, Z., & Hartmann, L. 2017, ApJ, 850, 201, doi: `10.3847/1538-4357/aa9705`

Bae, J., Zhu, Z., Baruteau, C., et al. 2019, ApJL, 884, L41, doi: `10.3847/2041-8213/ab46b0`

Bailer-Jones, C. A. L., Rybizki, J., Fouesneau, M., Demleitner, M., & Andrae, R. 2021, AJ, 161, 147, doi: `10.3847/1538-3881/abd806`

Barenfeld, S. A., Carpenter, J. M., Sargent, A. I., et al. 2019, ApJ, 878, 45, doi: `10.3847/1538-4357/ab1e50`

Barrado y Navascués, D., & Martín, E. L. 2003, AJ, 126, 2997, doi: `10.1086/379673`

Batygin, K. 2018, AJ, 155, 178, doi: `10.3847/1538-3881/aab54e`

Bergin, E., Calvet, N., Sitko, M. L., et al. 2004, ApJL, 614, L133, doi: `10.1086/425865`

Biller, B. A., Males, J., Rodigas, T., et al. 2014, ApJ, 792, L22, doi: `10.1088/2041-8205/792/1/L22`

Blanco-Cuaresma, S., Soubiran, C., Jofré, P., & Heiter, U. 2014, A&A, 566, doi: `10.1051/0004-6361/201323153`

Blandford, R. D., & Payne, D. G. 1982, MNRAS, 199, 883, doi: `10.1093/mnras/199.4.883`

Blinova, A. A., Romanova, M. M., & Lovelace, R. V. E. 2016, MNRAS, 459, 2354, doi: `10.1093/mnras/stw786`

Bouvier, J., Chelli, A., Allain, S., et al. 1999, A&A, 349, 619

Bouvier, J., Grankin, K. N., Alencar, S. H. P., et al. 2003, A&A, 409, 169, doi: `10.1051/0004-6361:20030938`

Bouvier, J., Alencar, S. H. P., Boutelier, T., et al. 2007, A&A, 463, 1017, doi: `10.1051/0004-6361:20066021`

Briceño, C., Calvet, N., Hernández, J., et al. 2005, AJ, 129, 907, doi: `10.1086/426911`

—. 2019, AJ, 157, 85, doi: `10.3847/1538-3881/aaf79b`

Brittain, S. D., Carr, J. S., Najita, J. R., Quanz, S. P., & Meyer, M. R. 2014, ApJ, 791, 136, doi: `10.1088/0004-637X/791/2/136`

Caballero, J. A., de Burgos, A., Alonso-Floriano, F. J., et al. 2019, A&A, 629, A114, doi: `10.1051/0004-6361/201935987`

Calvet, N. 1997, in IAU Symposium, Vol. 182, Herbig-Haro Flows and the Birth of Stars, ed. B. Reipurth & C. Bertout, 417–432

Calvet, N., D'Alessio, P., Hartmann, L., et al. 2002, ApJ, 568, 1008, doi: `10.1086/339061`

Calvet, N., & Gullbring, E. 1998, ApJ, 509, 802, doi: `10.1086/306527`

Calvet, N., Muzerolle, J., Briceño, C., et al. 2004, AJ, 128, 1294, doi: `10.1086/422733`

Calvet, N., Patino, A., Magris, G. C., & D'Alessio, P. 1991, ApJ, 380, 617, doi: `10.1086/170618`

Calvet, N., D'Alessio, P., Watson, D. M., et al. 2005, ApJL, 630, L185, doi: `10.1086/491652`

Cardelli, J. A., Clayton, G. C., & Mathis, J. S. 1989, ApJ, 345, 245, doi: `10.1086/167900`

Carpenter, J. M., Mamajek, E. E., Hillenbrand, L. A., & Meyer, M. R. 2006, ApJL, 651, L49, doi: `10.1086/509121`

Carroll, J. A. 1933, MNRAS, 93, 478, doi: `10.1093/mnras/93.7.478`

Chen, W., & Johns-Krull, C. M. 2013, ApJ, 776, 113, doi: `10.1088/0004-637X/776/2/113`

Choi, J., Dotter, A., Conroy, C., et al. 2016, ApJ, 823, 102, doi: `10.3847/0004-637X/823/2/102`

Christiaens, V., Casassus, S., Absil, O., et al. 2019, MNRAS, 486, 5819, doi: `10.1093/mnras/stz1232`

Cieza, L. A., Olofsson, J., Harvey, P. M., et al. 2013, ApJ, 762, 100, doi: `10.1088/0004-637X/762/2/100`

Claret, A. 2000, A&A, 363, 1081

Clarke, C. J., Gendrin, A., & Sotomayor, M. 2001, MNRAS, 328, 485, doi: `10.1046/j.1365-8711.2001.04891.x`

Clemens, J. C., Crain, J. A., & Anderson, R. 2004, in Proc. SPIE, Vol. 5492, Ground-based Instrumentation for Astronomy, ed. A. F. M. Moorwood & M. Iye, 331–340, doi: `10.1117/12.550069`

Close, L. M., Follette, K. B., Males, J. R., et al. 2014, ApJL, 781, L30, doi: `10.1088/2041-8205/781/2/L30`

Costigan, G., Vink, J. S., Scholz, A., Ray, T., & Testi, L. 2014, MNRAS, 440, 3444, doi: `10.1093/mnras/stu529`

Currie, T., Cloutier, R., Brittain, S., et al. 2015, ApJ, 814, L27, doi: `10.1088/2041-8205/814/2/L27`

Currie, T., Marois, C., Cieza, L., et al. 2019, ApJL, 877, L3, doi: `10.3847/2041-8213/ab1b42`

Dahm, S. E., Slesnick, C. L., & White, R. J. 2012, ApJ, 745, 56, doi: `10.1088/0004-637X/745/1/56`

D'Alessio, P., Calvet, N., & Hartmann, L. 2001, ApJ, 553, 321, doi: `10.1086/320655`

D'Alessio, P., Calvet, N., Hartmann, L., Franco-Hernández, R., & Servín, H. 2006, ApJ, 638, 314, doi: `10.1086/498861`

David, T. J., Petigura, E. A., Hillenbrand, L. A., et al. 2017, ApJ, 835, 168, doi: `10.3847/1538-4357/835/2/168`

Dawson, R. I., & Johnson, J. A. 2018, ARA&A, 56, 175, doi: `10.1146/annurev-astro-081817-051853`

Donati, J. F., Jardine, M. M., Gregory, S. G., et al. 2007, MNRAS, 380, 1297, doi: `10.1111/j.1365-2966.2007.12194.x`

Donati, J. F., Bouvier, J., Walter, F. M., et al. 2011, MNRAS, 412, 2454, doi: `10.1111/j.1365-2966.2010.18069.x`

Dong, R., Hashimoto, J., Rafikov, R., et al. 2012, ApJ, 760, 111, doi: `10.1088/0004-637X/760/2/111`

Doppmann, G. W., Najita, J. R., & Carr, J. S. 2017, ApJ, 836, 242, doi: `10.3847/1538-4357/aa5c3c`

Dotter, A. 2016, ApJS, 222, 8, doi: `10.3847/0067-0049/222/1/8`

Edwards, S., Fischer, W., Hillenbrand, L., & Kwan, J. 2006, ApJ, 646, 319, doi: `10.1086/504832`

Edwards, S., Fischer, W., Kwan, J., Hillenbrand , L., & Dupree, A. K. 2003, ApJL, 599, L41, doi: `10.1086/381077`

Esau, C. F., Harries, T. J., & Bouvier, J. 2014, MNRAS, 443, 1022, doi: `10.1093/mnras/stu1211`

Espaillat, C., Calvet, N., D'Alessio, P., et al. 2007, ApJ, 664, L111, doi: `10.1086/520879`

Espaillat, C., Muzerolle, J., Hernández, J., et al. 2008, ApJL, 689, L145, doi: `10.1086/595869`

Espaillat, C., Muzerolle, J., Najita, J., et al. 2014, Protostars and Planets VI, 497, doi: `10.2458/azu_uapress_9780816531240-ch022`

Esplin, T. L., Luhman, K. L., Faherty, J. K., Mamajek, E. E., & Bochanski, J. J. 2017, AJ, 154, 46, doi: `10.3847/1538-3881/aa74e2`

Esplin, T. L., Luhman, K. L., & Mamajek, E. E. 2014, ApJ, 784, 126, doi: `10.1088/0004-637X/784/2/126`

Esplin, T. L., Luhman, K. L., Miller, E. B., & Mamajek, E. E. 2018, AJ, 156, 75, doi: `10.3847/1538-3881/aacce0`

Fedele, D., van den Ancker, M. E., Henning, T., Jayawardhana, R., & Oliveira, J. M. 2010, A&A, 510, A72, doi: `10.1051/0004-6361/200912810`

Ferland, G. J., Chatzikos, M., Guzmán, F., et al. 2017, RMxAA, 53, 385. `https://arxiv.org/abs/1705.10877`

Fischer, W., Kwan, J., Edwards, S., & Hillenbrand, L. 2008, ApJ, 687, 1117, doi: `10.1086/591902`

Follette, K. B., Rameau, J., Dong, R., et al. 2017, AJ, 153, 264, doi: `10.3847/1538-3881/aa6d85`

Fonseca, N. N. J., Alencar, S. H. P., Bouvier, J., Favata, F., & Flaccomio, E. 2014, A&A, 567, A39, doi: `10.1051/0004-6361/201323236`

France, K., Roueff, E., & Abgrall, H. 2017, ApJ, 844, 169, doi: `10.3847/1538-4357/aa7cee`

France, K., Schindhelm, E., Herczeg, G. J., et al. 2012, ApJ, 756, 171, doi: `10.1088/0004-637X/756/2/171`

Frasca, A., Biazzo, K., Alcalá, J. M., et al. 2017, A&A, 602, A33, doi: `10.1051/0004-6361/201630108`

Frasca, A., Biazzo, K., Lanzafame, A. C., et al. 2015, A&A, 575, A4, doi: `10.1051/0004-6361/201424409`

Fuhrmeister, B., Czesla, S., Hildebrandt, L., et al. 2020, A&A, 640, A52, doi: `10.1051/0004-6361/202038279`

Gaia Collaboration, Brown, A. G. A., Vallenari, A., et al. 2018, A&A, doi: `10.1051/0004-6361/201833051`

Ghosh, P., & Lamb, F. K. 1979a, ApJ, 232, 259, doi: `10.1086/157285`

—. 1979b, ApJ, 234, 296, doi: `10.1086/157498`

Ghosh, P., Lamb, F. K., & Pethick, C. J. 1977, ApJ, 217, 578, doi: `10.1086/155606`

Ginzburg, S., & Chiang, E. 2019, MNRAS, 487, 681, doi: `10.1093/mnras/stz1322`

Gómez de Castro, A. I., Loyd, R. O. P., France, K., Sytov, A., & Bisikalo, D. 2016, ApJL, 818, L17, doi: `10.3847/2041-8205/818/1/L17`

Gorti, U., & Hollenbach, D. 2009, ApJ, 690, 1539, doi: `10.1088/0004-637X/690/2/1539`

Gravity Collaboration, Garcia Lopez, R., Perraut, K., et al. 2017, A&A, 608, A78, doi: `10.1051/0004-6361/201731058`

Gregorio-Hetem, J., & Hetem, A. 2002, MNRAS, 336, 197, doi: `10.1046/j.1365-8711.2002.05716.x`

Gregory, S. G., Matt, S. P., Donati, J. F., & Jardine, M. 2008, MNRAS, 389, 1839, doi: `10.1111/j.1365-2966.2008.13687.x`

Gressel, O., Nelson, R. P., Turner, N. J., & Ziegler, U. 2013, ApJ, 779, 59, doi: `10.1088/0004-637X/779/1/59`

Gullbring, E., Hartmann, L., Briceño, C., & Calvet, N. 1998, ApJ, 492, 323, doi: `10.1086/305032`

Haffert, S. Y., Bohn, A. J., de Boer, J., et al. 2019, Nature Astronomy, 3, 749, doi: `10.1038/s41550-019-0780-5`

Hartigan, P., Edwards, S., & Ghandour, L. 1995, ApJ, 452, 736, doi: `10.1086/176344`

Hartmann, L. 1982, ApJS, 48, 109, doi: `10.1086/190770`

Hartmann, L., & Bae, J. 2018, MNRAS, 474, 88, doi: `10.1093/mnras/stx2775`

Hartmann, L., Calvet, N., Gullbring, E., & D'Alessio, P. 1998, ApJ, 495, 385, doi: `10.1086/305277`

Hartmann, L., Herczeg, G., & Calvet, N. 2016, ARA&A, 54, 135, doi: `10.1146/annurev-astro-081915-023347`

Hartmann, L., Hewett, R., & Calvet, N. 1994, ApJ, 426, 669, doi: `10.1086/174104`

Hashimoto, J., Dong, R., Kudo, T., et al. 2012, ApJ, 758, L19, doi: `10.1088/2041-8205/758/1/L19`

Hashimoto, J., Tsukagoshi, T., Brown, J. M., et al. 2015, ApJ, 799, 43, doi: `10.1088/0004-637X/799/1/43`

Herbst, W., Herbst, D. K., Grossman, E. J., & Weinstein, D. 1994, AJ, 108, 1906, doi: `10.1086/117204`

Herczeg, G. J., & Hillenbrand, L. A. 2008, ApJ, 681, 594, doi: `10.1086/586728`

—. 2015, ApJ, 808, 23, doi: `10.1088/0004-637X/808/1/23`

Herczeg, G. J., Linsky, J. L., Walter, F. M., Gahm, G. F., & Johns-Krull, C. M. 2006, ApJS, 165, 256, doi: `10.1086/503558`

Hernández, J., Calvet, N., Hartmann, L., et al. 2005, AJ, 129, 856, doi: `10.1086/426918`

Hernández, J., Hartmann, L., Calvet, N., et al. 2008, ApJ, 686, 1195, doi: `10.1086/591224`

Hernández, J., Hartmann, L., Megeath, T., et al. 2007, ApJ, 662, 1067, doi: `10.1086/513735`

Hernández, J., Calvet, N., Perez, A., et al. 2014, ApJ, 794, 36, doi: `10.1088/0004-637X/794/1/36`

Hill, C. A., Carmona, A., Donati, J. F., et al. 2017, MNRAS, 472, 1716, doi: `10.1093/mnras/stx2042`

Husser, T.-O., Wende-von Berg, S., Dreizler, S., et al. 2013, A&A, 553, A6, doi: `10.1051/0004-6361/201219058`

Ingleby, L., Calvet, N., Herczeg, G., & Briceño, C. 2012, ApJL, 752, L20, doi: `10.1088/2041-8205/752/2/L20`

Ingleby, L., Calvet, N., Hernández, J., et al. 2011a, AJ, 141, 127, doi: `10.1088/0004-6256/141/4/127`

Ingleby, L., Calvet, N., Bergin, E., et al. 2009, ApJL, 703, L137, doi: `10.1088/0004-637X/703/2/L137`

—. 2011b, ApJ, 743, 105, doi: `10.1088/0004-637X/743/2/105`

Ingleby, L., Calvet, N., Herczeg, G., et al. 2013, ApJ, 767, 112, doi: `10.1088/0004-637X/767/2/112`

Ireland, L. G., Zanni, C., Matt, S. P., & Pantolmos, G. 2021, ApJ, 906, 4, doi: `10.3847/1538-4357/abc828`

Isella, A., Benisty, M., Teague, R., et al. 2019, ApJL, 879, L25, doi: `10.3847/2041-8213/ab2a12`

James, D. J., Melo, C., Santos, N. C., & Bouvier, J. 2006, A&A, 446, 971, doi: `10.1051/0004-6361:20053900`

Jayawardhana, R., Coffey, J., Scholz, A., Brand eker, A., & van Kerkwijk, M. H. 2006, ApJ, 648, 1206, doi: `10.1086/506171`

Jayawardhana, R., Mohanty, S., & Basri, G. 2003, ApJ, 592, 282, doi: `10.1086/375573`

Jeffries, R. D., Jackson, R. J., Cottaar, M., et al. 2014, A&A, 563, A94, doi: `10.1051/0004-6361/201323288`

Johns-Krull, C. M., McLane, J. N., Prato, L., et al. 2016, ApJ, 826, 206, doi: `10.3847/0004-637X/826/2/206`

Jönsson, H., Holtzman, J. A., Allende Prieto, C., et al. 2020, AJ, 160, 120, doi: `10.3847/1538-3881/aba592`

Joyce, S. R. G., Pye, J. P., Nichols, J. D., et al. 2019, MNRAS, 491, L56, doi: `10.1093/mnrasl/slz169`

Karim, M. T., Stassun, K. G., Briceño, C., et al. 2016, AJ, 152, 198, doi: `10.3847/0004-6256/152/6/198`

Kelson, D. D. 2003, PASP, 115, 688, doi: `10.1086/375502`

Kelson, D. D., Illingworth, G. D., van Dokkum, P. G., & Franx, M. 2000, ApJ, 531, 159, doi: `10.1086/308445`

Kennedy, G. M., & Kenyon, S. J. 2009, ApJ, 695, 1210, doi: `10.1088/0004-637X/695/2/1210`

Keppler, M., Benisty, M., Müller, A., et al. 2018, A&A, 617, A44, doi: `10.1051/0004-6361/201832957`

Keppler, M., Teague, R., Bae, J., et al. 2019, A&A, 625, A118, doi: `10.1051/0004-6361/201935034`

Koenigl, A. 1991, ApJL, 370, L39, doi: `10.1086/185972`

Kounkel, M., Covey, K., Moe, M., et al. 2019, AJ, 157, 196, doi: `10.3847/1538-3881/ab13b1`

Koutoulaki, M., Garcia Lopez, R., Natta, A., et al. 2018, A&A, 614, A90, doi: `10.1051/0004-6361/201832814`

Kraus, A. L., & Ireland, M. J. 2012, ApJ, 745, 5, doi: `10.1088/0004-637X/745/1/5`

Kulkarni, A. K., & Romanova, M. M. 2009, MNRAS, 398, 701, doi: `10.1111/j.1365-2966.2009.15186.x`

—. 2013, MNRAS, 433, 3048, doi: `10.1093/mnras/stt945`

Kurosawa, R., Romanova, M. M., & Harries, T. J. 2011, MNRAS, 416, 2623, doi: `10.1111/j.1365-2966.2011.19216.x`

Kwan, J., Edwards, S., & Fischer, W. 2007, ApJ, 657, 897, doi: `10.1086/511057`

Kwan, J., & Fischer, W. 2011, MNRAS, 411, 2383, doi: `10.1111/j.1365-2966.2010.17863.x`

Larsen, S. S., Kümmel, M., & Walsh, J. R. 2006, in The 2005 HST Calibration Workshop: Hubble After the Transition to Two-Gyro Mode, ed. A. M. Koekemoer, P. Goudfrooij, & L. L. Dressel, 103

Lavail, A., Kochukhov, O., & Hussain, G. A. J. 2019, A&A, 630, A99, doi: `10.1051/0004-6361/201935695`

Lavail, A., Kochukhov, O., Hussain, G. A. J., et al. 2017, A&A, 608, A77, doi: `10.1051/0004-6361/201731889`

Lightkurve Collaboration, Cardoso, J. V. d. M., Hedges, C., et al. 2018, Lightkurve: Kepler and TESS time series analysis in Python, Astrophysics Source Code Library. `http://ascl.net/1812.013`

Lii, P. S., Romanova, M. M., Ustyugova, G. V., Koldoba, A. V., & Lovelace, R. V. E. 2014, MNRAS, 441, 86, doi: `10.1093/mnras/stu495`

Long, F., Pinilla, P., Herczeg, G. J., et al. 2018a, ApJ, 869, 17, doi: `10.3847/1538-4357/aae8e1`

Long, M., Romanova, M. M., & Lamb, F. K. 2012, NewA, 17, 232, doi: `10.1016/j.newast.2011.08.001`

Long, M., Romanova, M. M., & Lovelace, R. V. E. 2007, MNRAS, 374, 436, doi: `10.1111/j.1365-2966.2006.11192.x`

Long, Z. C., Akiyama, E., Sitko, M., et al. 2018b, ApJ, 858, 112, doi: `10.3847/1538-4357/aaba7c`

Lubow, S. H., & D'Angelo, G. 2006, ApJ, 641, 526, doi: `10.1086/500356`

Luhman, K. L. 2004, ApJ, 602, 816, doi: `10.1086/381146`

—. 2018, AJ, 156, 271, doi: `10.3847/1538-3881/aae831`

Luhman, K. L., Herrmann, K. A., Mamajek, E. E., Esplin, T. L., & Pecaut, M. J. 2018, AJ, 156, 76, doi: `10.3847/1538-3881/aacc6d`

Luhman, K. L., & Mamajek, E. E. 2012, ApJ, 758, 31, doi: `10.1088/0004-637X/758/1/31`

Luhman, K. L., Allen, L. E., Allen, P. R., et al. 2008, ApJ, 675, 1375, doi: `10.1086/527347`

Machida, M. N., Kokubo, E., Inutsuka, S.-i., & Matsumoto, T. 2008, ApJ, 685, 1220, doi: `10.1086/590421`

Manara, C. F., Fedele, D., Herczeg, G. J., & Teixeira, P. S. 2016, A&A, 585, A136, doi: `10.1051/0004-6361/201527224`

Manara, C. F., Frasca, A., Alcalá, J. M., et al. 2017a, A&A, 605, A86, doi: `10.1051/0004-6361/201730807`

Manara, C. F., Mordasini, C., Testi, L., et al. 2019, A&A, 631, L2, doi: `10.1051/0004-6361/201936488`

Manara, C. F., Testi, L., Natta, A., & Alcalá, J. M. 2015, A&A, 579, A66, doi: `10.1051/0004-6361/201526169`

Manara, C. F., Testi, L., Rigliaco, E., et al. 2013, A&A, 551, A107, doi: `10.1051/0004-6361/201220921`

Manara, C. F., Testi, L., Herczeg, G. J., et al. 2017b, A&A, 604, A127, doi: `10.1051/0004-6361/201630147`

Manara, C. F., Natta, A., Rosotti, G. P., et al. 2020, A&A, 639, A58, doi: `10.1051/0004-6361/202037949`

Manara, C. F., Frasca, A., Venuti, L., et al. 2021, arXiv e-prints, arXiv:2103.12446. `https://arxiv.org/abs/2103.12446`

Mann, A. W., Newton, E. R., Rizzuto, A. C., et al. 2016, AJ, 152, 61, doi: `10.3847/0004-6256/152/3/61`

Manzo-Martínez, E., Calvet, N., Hernández, J., et al. 2020, ApJ, 893, 56, doi: `10.3847/1538-4357/ab7ead`

Marshall, J. L., Burles, S., Thompson, I. B., et al. 2008, in Proc. SPIE, Vol. 7014, Ground-based and Airborne Instrumentation for Astronomy II, 701454, doi: `10.1117/12.789972`

Mateo, M., Bailey, J. I., Crane, J., et al. 2012, in Proc. SPIE, Vol. 8446, Ground-based and Airborne Instrumentation for Astronomy IV, 84464Y, doi: `10.1117/12.926448`

Maucó, K., Hernández, J., Calvet, N., et al. 2016, ApJ, 829, 38, doi: `10.3847/0004-637X/829/1/38`

Maucó, K., Briceño, C., Calvet, N., et al. 2018, ApJ, 859, 1, doi: `10.3847/1538-4357/aabf40`

Mayor, M., Pepe, F., Queloz, D., et al. 2003, The Messenger, 114, 20

Mendigutía, I., Oudmaijer, R. D., Schneider, P. C., et al. 2018, A&A, 618, L9, doi: `10.1051/0004-6361/201834233`

Meyer, M. R., Calvet, N., & Hillenbrand, L. A. 1997, AJ, 114, 288, doi: `10.1086/118474`

Miller, K. A., & Stone, J. M. 1997, ApJ, 489, 890, doi: `10.1086/304825`

Mohanty, S., Jankovic, M. R., Tan, J. C., & Owen, J. E. 2018, ApJ, 861, 144, doi: `10.3847/1538-4357/aabcd0`

Mordasini, C., Alibert, Y., & Benz, W. 2009, A&A, 501, 1139, doi: `10.1051/0004-6361/200810301`

Mordasini, C., Alibert, Y., Klahr, H., & Henning, T. 2012, A&A, 547, A111, doi: `10.1051/0004-6361/201118457`

Morton, D. C. 2000, ApJS, 130, 403, doi: `10.1086/317349`

Müller, A., Keppler, M., Henning, T., et al. 2018, A&A, 617, L2, doi: `10.1051/0004-6361/201833584`

Müller, T. W. A., & Kley, W. 2013, A&A, 560, A40, doi: `10.1051/0004-6361/201322503`

Muzerolle, J., Calvet, N., & Hartmann, L. 1998a, ApJ, 492, 743, doi: `10.1086/305069`

—. 2001, ApJ, 550, 944, doi: `10.1086/319779`

Muzerolle, J., Hartmann, L., & Calvet, N. 1998b, AJ, 116, 455, doi: `10.1086/300428`

Muzerolle, J., Hillenbrand, L., Calvet, N., Briceño, C., & Hartmann, L. 2003, ApJ, 592, 266, doi: `10.1086/375704`

Natta, A., Testi, L., Muzerolle, J., et al. 2004, A&A, 424, 603, doi: `10.1051/0004-6361:20040356`

Nguyen, D. C., Brandeker, A., van Kerkwijk, M. H., & Jayawardhana, R. 2012, ApJ, 745, 119, doi: `10.1088/0004-637X/745/2/119`

Owen, J. E., Ercolano, B., & Clarke, C. J. 2011, MNRAS, 412, 13, doi: `10.1111/j.1365-2966.2010.17818.x`

Papaloizou, J. C. B., & Nelson, R. P. 2005, A&A, 433, 247, doi: `10.1051/0004-6361:20042029`

Pecaut, M. J., & Mamajek, E. E. 2013, ApJS, 208, 9, doi: `10.1088/0067-0049/208/1/9`

—. 2016, MNRAS, 461, 794, doi: `10.1093/mnras/stw1300`

Petrov, P. P., Romanova, M. M., Grankin, K. N., et al. 2021, MNRAS, 504, 871, doi: `10.1093/mnras/stab904`

Pinte, C., Price, D. J., Ménard, F., et al. 2018, ApJ, 860, L13, doi: `10.3847/2041-8213/aac6dc`

Pollack, J. B., Hubickyj, O., Bodenheimer, P., et al. 1996, Icarus, 124, 62, doi: `10.1006/icar.1996.0190`

Potravnov, I. S., Mkrtichian, D. E., Grinin, V. P., Ilyin, I. V., & Shakhovskoy, D. N. 2017, A&A, 599, A60, doi: `10.1051/0004-6361/201628926`

Quanz, S. P., Amara, A., Meyer, M. R., et al. 2015, ApJ, 807, 64, doi: `10.1088/0004-637X/807/1/64`

—. 2013a, ApJ, 766, L1, doi: `10.1088/2041-8205/766/1/L1`

Quanz, S. P., Avenhaus, H., Buenzli, E., et al. 2013b, ApJ, 766, L2, doi: `10.1088/2041-8205/766/1/L2`

Rauscher, E., & Marcy, G. W. 2006, PASP, 118, 617, doi: `10.1086/503021`

Reggiani, M., Quanz, S. P., Meyer, M. R., et al. 2014, ApJ, 792, L23, doi: `10.1088/2041-8205/792/1/L23`

Reggiani, M., Christiaens, V., Absil, O., et al. 2018, A&A, 611, A74, doi: `10.1051/0004-6361/201732016`

Reipurth, B., Pedrosa, A., & Lago, M. T. V. T. 1996, A&AS, 120, 229

Riaud, P., Mawet, D., Absil, O., et al. 2006, A&A, 458, 317, doi: `10.1051/0004-6361:20065232`

Ribas, Á., Bouy, H., & Merín, B. 2015, A&A, 576, A52, doi: `10.1051/0004-6361/201424846`

Rigliaco, E., Natta, A., Testi, L., et al. 2012, A&A, 548, A56, doi: `10.1051/0004-6361/201219832`

Robinson, C. E., & Espaillat, C. C. 2019, ApJ, 874, 129, doi: `10.3847/1538-4357/ab0d8d`

Romanova, M. M., Blinova, A. A., Ustyugova, G. V., Koldoba, A. V., & Lovelace, R. V. E. 2018, NewA, 62, 94, doi: `10.1016/j.newast.2018.01.011`

Romanova, M. M., Kulkarni, A. K., & Lovelace, R. V. E. 2008, ApJL, 673, L171, doi: `10.1086/527298`

Romanova, M. M., Long, M., Lamb, F. K., Kulkarni, A. K., & Donati, J. F. 2011, MNRAS, 411, 915, doi: `10.1111/j.1365-2966.2010.17724.x`

Romanova, M. M., Ustyugova, G. V., Koldoba, A. V., & Lovelace, R. V. E. 2004, ApJ, 610, 920, doi: `10.1086/421867`

—. 2009, MNRAS, 399, 1802, doi: `10.1111/j.1365-2966.2009.15413.x`

—. 2012, MNRAS, 421, 63, doi: `10.1111/j.1365-2966.2011.20055.x`

Romanova, M. M., Ustyugova, G. V., Koldoba, A. V., Wick, J. V., & Lovelace, R. V. E. 2003, ApJ, 595, 1009, doi: `10.1086/377514`

Sacco, G. G., Spina, L., Randich, S., et al. 2017, A&A, 601, A97, doi: `10.1051/0004-6361/201629698`

Saha, A., & Vivas, A. K. 2017, AJ, 154, 231, doi: `10.3847/1538-3881/aa8fd3`

Sallum, S., Follette, K. B., Eisner, J. A., et al. 2015, Nature, 527, 342, doi: `10.1038/nature15761`

Sanz-Forcada, J., & Dupree, A. K. 2008, A&A, 488, 715, doi: `10.1051/0004-6361:20078501`

Schlafly, E. F., Meisner, A. M., & Green, G. M. 2019, ApJS, 240, 30, doi: `10.3847/1538-4365/aafbea`

Schneider, P. C., France, K., Günther, H. M., et al. 2015, A&A, 584, A51, doi: `10.1051/0004-6361/201425583`

Shakura, N. I., & Sunyaev, R. A. 1973, A&A, 500, 33

Siess, L., Dufour, E., & Forestini, M. 2000, A&A, 358, 593

Silverberg, S. M., Wisniewski, J. P., Kuchner, M. J., et al. 2020, ApJ, 890, 106, doi: `10.3847/1538-4357/ab68e6`

Simcoe, R. A., Burgasser, A. J., Schechter, P. L., et al. 2013, PASP, 125, 270, doi: `10.1086/670241`

Simón-Díaz, S., & Herrero, A. 2007, A&A, 468, 1063, doi: 10.1051/0004-6361:20066060

Siwak, M., Ogloza, W., Moffat, A. F. J., et al. 2018, MNRAS, 478, 758, doi: 10.1093/mnras/sty1220

Skrutskie, M. F., Cutri, R. M., Stiening, R., et al. 2006, AJ, 131, 1163, doi: 10.1086/498708

Sung, H., Stauffer, J. R., & Bessell, M. S. 2009, AJ, 138, 1116, doi: 10.1088/0004-6256/138/4/1116

Szulágyi, J., Dullemond, C. P., Pohl, A., & Quanz, S. P. 2019, MNRAS, 487, 1248, doi: 10.1093/mnras/stz1326

Szulágyi, J., Masset, F., Lega, E., et al. 2016, MNRAS, 460, 2853, doi: 10.1093/mnras/stw1160

Szulágyi, J., & Mordasini, C. 2017, MNRAS, 465, L64, doi: 10.1093/mnrasl/slw212

Tang, Y.-W., Guilloteau, S., Dutrey, A., et al. 2017, ApJ, 840, 32, doi: 10.3847/1538-4357/aa6af7

Tanigawa, T., Ohtsuki, K., & Machida, M. N. 2012, ApJ, 747, 47, doi: 10.1088/0004-637X/747/1/47

Teague, R., Bae, J., Bergin, E. A., Birnstiel, T., & Foreman-Mackey, D. 2018, ApJ, 860, L12, doi: 10.3847/2041-8213/aac6d7

Thanathibodee, T., Calvet, N., Bae, J., Muzerolle, J., & Hernández, R. F. 2019a, ApJ, 885, 94, doi: 10.3847/1538-4357/ab44c1

Thanathibodee, T., Calvet, N., Muzerolle, J., et al. 2019b, ApJ, 884, 86, doi: 10.3847/1538-4357/ab4127

Thanathibodee, T., Calvet, N., Herczeg, G., et al. 2018, ApJ, 861, 73, doi: 10.3847/1538-4357/aac5e9

Thanathibodee, T., Molina, B., Calvet, N., et al. 2020, ApJ, 892, 81, doi: 10.3847/1538-4357/ab77c1

Tokovinin, A., & Briceño, C. 2020, AJ, 159, 15, doi: 10.3847/1538-3881/ab5525

Tokovinin, A., Cantarutti, R., Tighe, R., et al. 2016, PASP, 128, 125003, doi: 10.1088/1538-3873/128/970/125003

Tokovinin, A., Petr-Gotzens, M. G., & Briceño, C. 2020, AJ, 160, 268, doi: 10.3847/1538-3881/abc2d6

van Eyken, J. C., Ciardi, D. R., von Braun, K., et al. 2012, ApJ, 755, 42, doi: 10.1088/0004-637X/755/1/42

Vasconcelos, M. J., & Bouvier, J. 2015, A&A, 578, A89, doi: `10.1051/0004-6361/201525765`

Venuti, L., Bouvier, J., Flaccomio, E., et al. 2014, A&A, 570, A82, doi: `10.1051/0004-6361/201423776`

Venuti, L., Bouvier, J., Cody, A. M., et al. 2017, A&A, 599, A23, doi: `10.1051/0004-6361/201629537`

Villebrun, F., Alecian, E., Hussain, G., et al. 2019, A&A, 622, A72, doi: `10.1051/0004-6361/201833545`

Wagner, K., Stone, J. M., Spalding, E., et al. 2019, ApJ, 882, 20, doi: `10.3847/1538-4357/ab32ea`

Wagner, K., Follete, K. B., Close, L. M., et al. 2018, ApJ, 863, L8, doi: `10.3847/2041-8213/aad695`

White, R. J., & Basri, G. 2003, ApJ, 582, 1109, doi: `10.1086/344673`

Williams, J. P., & Cieza, L. A. 2011, ARA&A, 49, 67, doi: `10.1146/annurev-astro-081710-102548`

Winn, J. N., & Fabrycky, D. C. 2015, ARA&A, 53, 409, doi: `10.1146/annurev-astro-082214-122246`

Wright, E. L., Eisenhardt, P. R. M., Mainzer, A. K., et al. 2010, AJ, 140, 1868, doi: `10.1088/0004-6256/140/6/1868`

Wyatt, M. C. 2008, ARA&A, 46, 339, doi: `10.1146/annurev.astro.45.051806.110525`

Xie, C., Haffert, S. Y., de Boer, J., et al. 2020, A&A, 644, A149, doi: `10.1051/0004-6361/202038242`

Yang, H., Herczeg, G. J., Linsky, J. L., et al. 2012, ApJ, 744, 121, doi: `10.1088/0004-637X/744/2/121`

Zarro, D. M., & Zirin, H. 1986, ApJ, 304, 365, doi: `10.1086/164170`

Zhang, K., Blake, G. A., & Bergin, E. A. 2015, ApJ, 806, L7, doi: `10.1088/2041-8205/806/1/L7`

Zhou, Y., Bowler, B. P., Wagner, K. R., et al. 2021, AJ, 161, 244, doi: `10.3847/1538-3881/abeb7a`

Zhu, Z., Nelson, R. P., Hartmann, L., Espaillat, C., & Calvet, N. 2011, ApJ, 729, 47, doi: `10.1088/0004-637X/729/1/47`

Zurlo, A., Cugno, G., Montesinos, M., et al. 2020, A&A, 633, A119, doi: `10.1051/0004-6361/201936891`